Universidade de São Paulo
Instituto de Física

Transistor spintrônico: *descoberta e caracterização de isolantes topológicos*

Carlos Augusto Mera Acosta

Orientador: Prof. Dr. Adalberto Fazzio

Tese de doutorado apresentada ao Instituto de Física da Universidade de São Paulo, como requisito parcial para a obtenção do título de Doutor em Ciências.

Banca Examinadora:
Prof. Dr. Adalberto Fazzio - Orientador (Universidade de São Paulo)
Prof. Dr. Luis Gregório Godoy de Vasconcellos Dias da Silva (Universidade de São Paulo)
Prof. Dr. Gennady Gusev (Universidade de São Paulo)
Prof. Dr. Gustavo Martini Dalpian (Universidade Federal do ABC)
Prof. Dr. Tomé Mauro Schmidt (Universidade Federal de Uberlandia)

São Paulo
2018

FICHA CATALOGRÁFICA
Preparada pelo Serviço de Biblioteca e Informação do Instituto de Física da Universidade de São Paulo

Mera Acosta, Carlos Augusto

Transistor spintrônico: descoberta e caracterização de isolantes topológicos / Spintronic transistor: discovery and characterization of topological insulators. São Paulo, 2018.

Tese (Doutorado) – Universidade de São Paulo. Instituto de Física. Depto. de Física dos Materiais e Mecânica.

Orientador: Prof. Dr. Adalberto Fazzio
Área de Concentração: Física da Matéria Condensada.

Unitermos: 1. Spintrônica; 2. Transistores; 3. Topologia; 4. Efeito Hall; 5. Aprendizado de máquina.

USP/IF/SBI-067/2018

University of Sao Paulo
Physics Institute

Spintronic transistor: *discovery and characterization of topological insulators*

Carlos Augusto Mera Acosta

Supervisor: Prof. Dr. Adalberto Fazzio

Thesis submitted to the Physics Institute of the
University of São Paulo in partial fulfillment of the
requirements for the degree of Doctor of Science

Examining Committee:
Prof. Dr. Adalberto Fazzio - Supervisor (University of Sao Paulo)
Prof. Dr. Luis Gregório Godoy de Vasconcellos Dias da Silva (University of Sao Paulo)
Prof. Dr. Gennady Gusev (University of Sao Paulo
Prof. Dr. Gustavo Martini Dalpian (ABC University)
Prof. Dr. Tomé Mauro Schmidt (University of Uberlandia)

Sao Paulo
2018

道場訓

一、人格完成に努むること
一、誠の道を守ること
一、努力の精神を養うこと
一、礼儀を重んずること
一、血気の勇を戒むること

Dedicado a mis papás, Gina y Matias.
A todos aquellos que ven la ciencia como una expresión de libertad.
A todos aquellos que creen en un mundo diferente y en el amor como el catalizador para alcanzarlo.

Acknowledgments

I want to thank the São Paulo Research Foundation for the financial support: Doctorate Scholarship (14/12357-3) and Research Internships Abroad - BEPE (16/04496-9).

Special thanks to the Fritz Haber Institute of the Max Planck Society (FHI) for the computational support and the facilities purchased in the thematic project led by Prof. Dr. Adalberto Fazzio - the cluster Josephson.

I deeply thank my supervisor, Prof. Dr. Adalberto Fazzio, my colleagues in Brazil and Germany, my friends, my family and my wife Gina Polo for all the support.

I also would like to thank Prof. Dr. Matthias Scheffler, Prof. Dr. Antônio José Roque da Silva, and Prof. Dr. Caio Lewenkopf for their valuable contributions to this thesis.

ABSTRACT

MERA ACOSTA, Carlos Augusto. **Spintronic transistor: *discovery and characterization of topological insulators*** [Transistor spintrônico: *descoberta e caracterizão de isolantes topológicos*] 2018. 146 f. Tese (Doutor em Ciências) - Instituto de Física, Universidade de São Paulo, São Paulo, 2018.

The main goal of spintronics is to understand the mechanisms to efficiently control both spin configurations and spin currents, aiming the use of the spin degree of freedom as the basic element of digital devices, e.g., the ”spintronic transistor” in which the ON and OFF are defined by the spin electron orientation. Many of the most promising proposed mechanisms are based on spin current generation in Rashba and/or topological semiconductors mainly mediated by the spin-orbit coupling and electric fields. However, despite topological insulators (TIs) are predicted to feature boundary (surface/edge for three/two dimensional systems) states protected by a given symmetry against disorder, the proposed TI candidates are extremely sensible to fabrications processes, impurities and temperature effects; indeed, it is difficult to observed the current known phenomena or even to experimentally achieve the spin transport regime governed by the topologically protected boundary states. In this thesis, based on first-principle calculation, tight-binding models and topological invariant calculations we propose possible solutions for these problems, not only systematically predicting new topological insulator candidates with suitable conditions to achieve the boundary states transport regime, but also suggesting novel phenomena allowing for the spin current control. Specifically, we have *i*) explored the honeycomb-lattice family proposing a new kind of band inversion; *ii*) used machine learning to systematically predict new two-dimensional TIs; *iii*) proposed that instead of focused on finding TIs exhibiting large band gaps, the bulk states can be intrinsically protected by the time-reversal symmetry; *iv*) found that an external electric field breaking the mirror symmetry in dual topological insulators can be used to control the spin polarization, leading to a non-dynamic spin-polarization generation and allowing the construction of a spintronic transistor; and *v*) studied the influence of the bulk states in the surface electronic transport. To address this issues we have also implemented the topological invariants: Chern Number C_n and the Z_2 invariant within the SIESTA, VASP and AIMS codes which are used to performed first-principles calculations, and we made a model for the electronic transport considering spin-orbit coupling. We believe that our work advances the understanding of the properties of TIs, the external field effects in these systems, and their potential for device applications. We also believe that our proposal, i.e., the spin-polarization controlled by the mirror symmetry breaking, could open a new research area in TIs.

Key words: Spintronic, transistor, density functional theory, nontrivial topological phases, electronic transport.

RESUMO

MERA ACOSTA, Carlos. **Spintronic transistor: *discovery and characterization of topological insulators*** [Transistor spintrônico: *descoberta e caracterizão de isolantes topológicos*] 2018. 146 f. Tese (Doutor em Ciências) - Instituto de Física, Universidade de São Paulo, São Paulo, 2018.

O principal objetivo da spintrônica é entender os mecanismos que permitem controlar de forma eficiente tanto a configuração de spin quanto as correntes de spin, orientando ao uso do grau de liberdade do spin como o elemento básico de dispositivos digitais. Por exemplo, o “transistor spintrônico”, no qual o ”ON” e o ”OFF” são definidos pela orientação do spin. Muitos destes mecanismos propostos estão baseados na geração de corrente de spin em semicondutores tipo Rashba e isolantes topológicos (TIs) usando a interação spin-orbita e campos elétricos. No entanto, embora os TIs apresentam estados de borda ou superfície protegidos contra a desordem por uma certa simetria, os sistemas que têm sido propostos são muito sensíveis aos processos de fabricação, impurezas e efeitos de temperatura; de fato, não é trivial observar os fenômenos conhecidos ou inclusive obter experimentalmente o transporte de spin dominado pelos estados topologicamente protegidos. Nesta tese, usando cálculos de primeiros princípios, modelos ”tight-binding” e cálculos de invariantes topológicos, foi proposta uma possível solução para estes problemas, não somente para predizer novos TIs de forma sistemática, mas também para sugerir novos fenômenos que permitam controlar as correntes de spin. Especificamente, i) exploramos a família de sistemas similares ao grafeno, propondo uma nova classe de inversão de banda; ii) usando aprendizado de máquina prevemos de forma sistemática novos TIs; iii) encontramos que os estados de bulk poderiam também ser protegidos pela simetria de reversão temporal, e não necessariamente a procura deve ser focada em encontrar matérias com gap grande; iv) encontramos que um campo elétrico quebrando a simetria de espelho em isolantes topológicos duais permite controlar a polarização de spin, levando a uma geração não dinâmica de spin o qual permitiria a construção de um transistor spintrônico; e v) estudamos a influencia dos estados de Bulk no transporte de estados de superfície. Neste estudo, implementamos os invariantes topológicos: número de Chern e invariante Z_2 nos códigos SIESTA, VASP e AIMS usados para cálculos de primeiros princípios. Também implementamos um modelo para o transporte eletrônico usando spin-órbita. Acreditamos que nosso trabalho ajuda no entendimento das propriedades dos TIs, dos efeitos de campos elétricos externos e as possíveis aplicações para dispositivos. Também acreditamos que nossa proposta, o controle da polarização de spin quebrando a simetria de espelho, poderia abrir uma nova área de estudo em TIs.

Palavras Chave: Spintrônica, transistor, teoria do funcional da densidade, fases topológicas não triviais, transporte eletrônico.

Contents

Introduction

Linking all the physical aspects of the universe into a single equation would encode the answer to the greatest enigmas of human history in a unique theory. Although this reductionist idea known as "the theory of everything" has been the goal of several greatest scientists, nowadays it is still one of the most important unsolved "problems" in physics. Curiously, even within the current areas in which physical problems could be divided, an equivalent "equation of everything" is rarely found, in some way suggesting that the paradigm of a universal equation could be just an idealization without a strong *a priori* demonstration [1]. Remarkable, in materials science, there is a general description from which all effects, material properties, and phenomena could in principle be derived. Specifically, in quantum mechanic, the different known material phases, e.g., gases (molecules) and condensed (bulk, surfaces, and wires), can be described without any ambiguity as a conglomerate of M atomic nucleus and N electrons interacting each other via electrostatic forces. The quantum mechanic equation covering this "reductionist vision" of the condensed matter is not more than the Schrodinger equation

$$\hat{\mathcal{H}}\Psi_n(\boldsymbol{R},\boldsymbol{r}) = \varepsilon_n \Psi_n(\boldsymbol{R},\boldsymbol{r}), \tag{1.1}$$

where $\boldsymbol{R} = \{\boldsymbol{R}_A, \quad A = 1,2,...,M\}$ are the nuclear coordinates, $\boldsymbol{r} = \{\boldsymbol{r}_\alpha, \quad A = 1,2,...,N\}$ is the set of N electronic coordinates, and $\Psi_n(\boldsymbol{R},\boldsymbol{r})$ is the wave function depending on nuclear and electronic coordinates. From this point of view, the Hamiltonian $\hat{\mathcal{H}}$ accounts for all interaction contributing to the total energy of the systems ε_n. This contributions are essentially defined by the follow operators: $i)$ the nuclear kinetic energy $\hat{T}_N$, electronic kinetic energy $\hat{T}_N$, electron-nucleus Coulomb interaction $\hat{V}_{Ne}$, electron-electron Coulomb interaction $\hat{V}_e$, and nucleus-nucleus Coulomb interaction $\hat{V}_N$. In this order, the non-relativistic Hamiltonian describing any material can be written as

$$\hat{\mathcal{H}} = \hat{T}_N + \hat{T}_e + \hat{V}_{Ne} + \hat{V}_e + \hat{V}_N, \tag{1.2}$$

The explicit form of these operators leads to

$$\begin{aligned}\hat{\mathcal{H}} = &-\sum_{A=1}^{P}\frac{\hbar^2}{2M_A}\nabla_A^2 - \sum_{\alpha=1}^{N}\frac{\hbar^2}{2m}\nabla_\alpha^2 - \frac{e^2}{2}\sum_{A=1}^{P}\sum_{\alpha}^{N}\frac{Z_A}{|\boldsymbol{r}_\alpha - \boldsymbol{R}_A|}\\ &+\frac{e^2}{2}\sum_{\alpha=1}^{N}\sum_{\beta\neq\alpha}^{N}\frac{1}{|\boldsymbol{r}_\alpha - \boldsymbol{r}_\beta|} + \frac{e^2}{2}\sum_{A=1}^{P}\sum_{B\neq A}^{P}\frac{Z_A Z_B}{|\boldsymbol{R}_A - \boldsymbol{R}_B|},\end{aligned} \tag{1.3}$$

where m and M_A are the nuclear and electronic masses, respectively, and Z_A is the atomic number of the nucleus A. The term $\hat{V}_{Ne}$ accounting for the interaction of different classes of particles does not allow to write the total wavefunction as a product between functions describing the electronic and nuclear part. Therefore, in practice, the total energy calculation is a problem almost impossible to solve using the quantum mechanic techniques. Indeed, using numerical approaches this equation has been solved only for few systems formed by a very small number of atoms. This undoubtedly reinforces the assumptions presented by Anderson [1]: even if there is an equation of everything, it would be impossible to solve it. Consequently, in the condensed matter physics history, many approximations based on experimental results and theoretical approaches have been done in order to solve the discussed many-body problem without losing information related to the electronic structure of the systems, which is the focus of this work. For instance, surprisingly, the molecular energy spectrum is usually separated in terms of the frequency of the excited modes into three regions, microwaves, infrared, and ultraviolet, which are associated with the rotational, vibrational, and electronic spectrum, respectively. This bring a theoretical framework known as Born-Oppenheimer approximation [2]: based on the difference between the electron and nucleus masses, Born and Oppenheimer proposed the decoupled of the electronic and nuclear movements.

Trying to solve the "equation of everything" in condensed matter

In a classical vision, since the electron velocity is greater than the nucleus velocity, the nuclear dynamics can be treated as in the inertia state, i.e., the electrons are moving respect to the static nucleus. Thus, the kinetic energy term $\hat{T}_N$ can be neglected and hence, the interacting many-body system problem is reduced to solve the Schrodinger equation for a set of interacting electrons in the presence of an external potential arising from the nuclear part. In the original proposal, Born and Oppenheimer introduce the nuclear movement effect in the electronic wavefunction by considering new nuclear variables $\boldsymbol{R} = \boldsymbol{R}_0 + \boldsymbol{u}$, where $\boldsymbol{u}$ stands for the displacement of the nucleus respect to the equilibrium position $\boldsymbol{R}_0$. In this way, the Hamiltonian is written as an expansion in terms of $k = (m_e/M_N)^{\frac{1}{4}}$, i.e., keeping terms of the fourth order expansion onwards, there is no mixing between stationary electronic states due to the interaction with the cores [2]. Therefore, under appropriate conditions [1], the electrons do not undergo transitions between stationary states. In a schematic view, we can imagine that the electrons instantaneously change their wavefunction following the movement and wavefunction of the nuclei, i.e., for a particular nuclear configuration $\boldsymbol{R}_i$, the potential V_{Ne} is not more than an external electrostatic potential V_{ext}. Naturally, this external potential can also

---

[1] The nucleus movement effect can be neglected if the energy distance between electronic states musts be greater than the energy required to obtain transitions between vibrational states.

Since metals are characterized by a zero bandgap, this approximation is not suitable to described them. However, the electronic excitations are usually confined to a small region near the Fermi surface.

account not only for the nucleus-nucleus Coulomb interaction, but also for any single-particle external potential. This is equivalent to write a single Hamiltonian describing the electronic part,

$$\hat{\mathcal{H}}_e\psi_n(\boldsymbol{R}_i,\boldsymbol{r}) = E_n\psi_n(\boldsymbol{R}_i,\boldsymbol{r}), \tag{1.4}$$

where $\hat{\mathcal{H}}_e = \hat{T}_e + \hat{V}_{Ne} + \hat{V}_e$. In this way, the electrons are always in the same stationary states described by this electronic Hamiltonian.

Let's introduce this previous discussion by writing the wavefunction of the systems as,

$$\Psi(\boldsymbol{R},\boldsymbol{r}) = \sum_m \varphi_m(\boldsymbol{R})\psi_m(\boldsymbol{R},\boldsymbol{r}), \tag{1.5}$$

where $\psi_m(\boldsymbol{R},\boldsymbol{r})$ is the electronic wavefunction for a given nuclear configuration, and $\varphi_m(\boldsymbol{R})$ describes the evolution of the nuclear subsystem. This leads to the Schrodinger equation,

$$\begin{aligned}\left[i\hbar\frac{\partial}{\partial t} + \sum_{A=1}^{P}\frac{\hbar^2}{2M_A}\nabla_A^2 - V_N - E_n(\boldsymbol{R})\right]\varphi_n(\boldsymbol{R},t) = -\sum_m\sum_{A=1}^{P}\frac{\hbar^2}{2M_A}\langle\psi_n|\nabla_A^2|\psi_m\rangle\varphi_m(\boldsymbol{R},t)\\ - 2\sum_m\sum_{A=1}^{P}\frac{\hbar^2}{2M_A}\boldsymbol{\nabla}_A\varphi_m(\boldsymbol{R},t)\langle\psi_n|\boldsymbol{\nabla}_{\boldsymbol{A}}|\psi_m\rangle.\end{aligned} \tag{1.6}$$

The wavefunction can be written as decoupled stationary states,

$$\Psi(\boldsymbol{R},\boldsymbol{r}) = \varphi_m(\boldsymbol{R})\psi_m(\boldsymbol{R},\boldsymbol{r}), \tag{1.7}$$

by disregarding the off-diagonal terms $\langle\psi_n|\boldsymbol{\nabla}_{\boldsymbol{A}}|\psi_m\rangle$ and $\langle\psi_n|\nabla_A^2|\psi_m\rangle$, which introduce an effective coupling between states associated with the electronic Hamiltonian. Formally, this implies that the equations describing the electronic contributions and the evolution of the nuclear subsystem can be written separately: the electronic Hamiltonian is

$$\hat{\mathcal{H}}_e = -\sum_{\alpha=1}^{N}\frac{\hbar^2}{2m}\nabla_\alpha^2 - \frac{e^2}{2}\sum_{A=1}^{P}\sum_{\alpha}^{N}\frac{Z_A}{|\boldsymbol{r}_\alpha - \boldsymbol{R}_A|} + \frac{e^2}{2}\sum_{\alpha=1}^{N}\sum_{\beta\neq\alpha}^{N}\frac{1}{|\boldsymbol{r}_\alpha - \boldsymbol{r}_\beta|}, \tag{1.8}$$

while the evolution of the nuclear subsystem is given by

$$i\hbar\frac{\partial\varphi_n(\boldsymbol{R},t)}{\partial t} = \left(-\sum_{A=1}^{P}\nabla_A^2 + \widetilde{E}_m(\boldsymbol{R},t)\right)\varphi_n(\boldsymbol{R},t), \tag{1.9}$$

where

$$\widetilde{E}_m = E_m(\boldsymbol{R}) + \sum_{A=1}^{P}\langle\varphi_m|\nabla_A^2|\varphi_m\rangle. \tag{1.10}$$

This suggests that the effective potential felt by the nuclei is equivalent to the electronic total energy. In the modern version, the Born-Oppenheimer approximation considers the off-diagonal terms as zero [3], i.e., $\sum_{A=1}^{P}\langle\varphi_m|\nabla_A^2|\varphi_m\rangle = 0$. Thus, the electronic structure is completely decoupled from the nuclear movement and the equation describing the nuclear temporal evolution is

$$i\hbar\frac{\partial\varphi_n(\boldsymbol{R},t)}{\partial t} = \left(-\sum_{A=1}^{P}\nabla_A^2 + E_m(\boldsymbol{R},t)\right)\varphi_n(\boldsymbol{R},t). \tag{1.11}$$

The study of the electronic properties given by the Hamiltonian 1.8 is not an easy task: even within the Born-Oppenheimer framework, the electronic wavefunction $\psi_n(\boldsymbol{R},\boldsymbol{r})$ depending on the N coordinates of the interacting electrons should be calculated for each nuclear configuration.

The biggest challenge is contained in the treatment of the electron-electron coupling, since this term implies that the Eq. 1.4 is essentially a many-body problem. To elucidate that, we rewrite the electronic Hamiltonian as,

$$\hat{\mathcal{H}}_e = \sum_{\alpha=1}^{N}\left[h_\alpha + \frac{e^2}{2}\sum_{\beta\neq\alpha}^{N}\frac{1}{r_{\alpha\beta}}\right], \tag{1.12}$$

where $r_{\alpha\beta} = |\boldsymbol{r}_\alpha - \boldsymbol{r}_\beta|$ and

$$h_e = -\frac{\hbar^2}{2m}\nabla_\alpha^2 + V_{eff}(\boldsymbol{r}) \tag{1.13}$$

is the single-particle electronic Hamiltonian. Here, we include the nuclear effect in an effective potential, i.e., $V_{eff}(\boldsymbol{r}) = -\frac{e^2}{2}\sum_{A=1}^{P}\frac{Z_A}{|\boldsymbol{r}_\alpha - \boldsymbol{R}_A|}$. If the electron-electron interaction is neglected, the electronic Hamiltonian is just the sum of the single-particle contribution of each electron. The solution of this single-particle problem is relatively trivial respect to the initial problem considering all interaction. However, this mean field theory is enough to capture many of the known phenomena and material properties. The solution of the single particle Schrodinger equation $h_e\psi_n(\boldsymbol{r}) = E_n\psi_n(\boldsymbol{r})$, is usually addressed using tight-binding models. This concept becomes evident when the Hamiltonian is written in a specific basis. Since all the systems studied here are periodic solids, the natural basis to address this problem are atomic orbitals. The electronic wavefunction is then written as

$$\psi_n(\boldsymbol{r}) = \sum_{\mu}C_n^\mu\phi_\mu(\boldsymbol{r} - \boldsymbol{R}) \tag{1.14}$$

where $\phi_\mu(\boldsymbol{r} - \boldsymbol{R})$ are atomic orbitals centered at the atom in the position $\boldsymbol{R}$. Thus, the single-particle Schrodinger equation is $\sum_{\mu}\left[\hat{h}_e\phi_\mu(\boldsymbol{r} - \boldsymbol{R})\right]C_n^\mu = E_n\sum_{\mu}C_n^\mu\phi_\mu(\boldsymbol{r} - \boldsymbol{R})$.

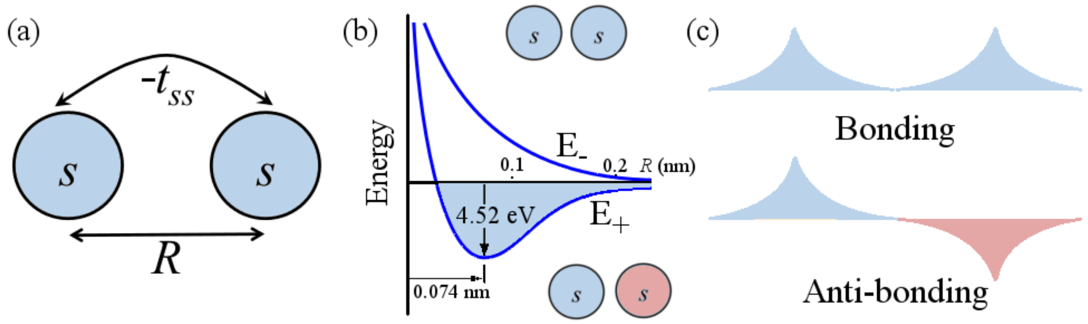

Figure 1.1 - Representation of the (a) s-orbitals separated by the distance R, (b) bonding and anti-bonding energies, and (c) bonding and anti-bonding states.

Multiplying by the atomic orbital $\phi_{\nu}^{*}(\boldsymbol{r}-\boldsymbol{R})$ and integrating in the real space, we have

$$\sum_{\mu}[t_{\nu\mu}-E_{n}S_{\nu\mu}]C_{n}^{\mu}=0, \tag{1.15}$$

where the hopping and the overlap terms are given by

$$t_{\nu\mu}=\int d^{3}r\phi_{\nu}^{*}(\boldsymbol{r}-\boldsymbol{R})\,\hat{h}_{e}\phi_{\mu}(\boldsymbol{r}-\boldsymbol{R})=\int d^{3}r\phi_{\nu}^{*}(\boldsymbol{r}-\boldsymbol{R})\left(-\frac{\hbar}{2m}\nabla^{2}+V_{eff}(\boldsymbol{r})\right)\phi_{\mu}(\boldsymbol{r}-\boldsymbol{R}) \tag{1.16}$$

and

$$s_{\nu\mu}=\int d^{3}r\phi_{\nu}^{*}(\boldsymbol{r}-\boldsymbol{R})\,\phi_{\mu}(\boldsymbol{r}-\boldsymbol{R}), \tag{1.17}$$

respectively. The Hamiltonian matrix elements are then given by

$$[h_{e}]_{ij}=\varepsilon_{0}^{ij}\delta_{ij}+t_{a_{n}}^{ij}, \tag{1.18}$$

where a_n is the index of the n-th nearest neighbors, i and j are the indexes of the atomic orbitals used to write the Hamiltonian, and ε_0 is the on-site energy.

The functions $\phi_{\mu}(\boldsymbol{r}-\boldsymbol{R})$ are not restricted to be atomic orbital. In general, any set of linear combination of localized functions is suitable to write the wavefunction. For instance, orthogonal functions are usually used, since the overlap matrix become diagonal, i.e $s_{\nu\mu}=\delta_{\nu\mu}$. It is specially instructive to consider a simple example: The Hydrogen molecule ion H_2^+, whose wavefunction is written in terms of a linear combination of s-orbitals, i.e., $|\psi_n\rangle=C_n^1|s_1\rangle+C_n^2|s_2\rangle$, as represented in Fig. 1.1a. The wavefunctions and energies are then given by the Eq. 1.15, $|\psi_\pm\rangle=(|s_1\rangle\pm|s_2\rangle)/\sqrt{2}$ and $E_\pm=\varepsilon_0\mp|t_{ss}|$, respectively. Here, $\varepsilon_0=t_{11}$ is the on-site energy and $t_{ss}=t_{12}$ is the interaction between s-orbitals. The $|\psi_+\rangle$ and $|\psi_-\rangle$ states are the bonding and anti-bonding wavefunctions (See Fig. 1.1). In the bonding (anti-bonding) state the spherically symmetric s-orbitals have the same (opposite) quantum phase, as represented in Fig. 1.1b. Since the hopping term depends on the electron-nucleus electrostatic interaction, the energies associated with the (anti-) and bonding states varies with respect to the inter-atomic distance R. This also suggests that the orbital interaction could effectively be represented by a repulsive interaction for the anti-bonding states, i.e., in the specific case of s-orbitals, $t_{22} > 0$. In the next section, this will be discussed in more details.

The Hydrogen molecule ion H_2^+ is a very simple example to show how the Schrodinger equation can be solve for atomic systems, however, even for this case, if the electron-electron interaction is taken into account, the analytical solution is not trivial and hence, computational approaches are needed. Specifically, since this interaction leads to a many-body description, the wavefunction can not be written as a linear combination of orbitals, but as a Slater determinant. If we use the previously described procedure, it is clear that the term $\hat{V}_e = \frac{e^2}{2}\sum_{\alpha=1}^{N}\sum_{\beta\neq\alpha}^{N}\frac{1}{r_{\alpha\beta}}$ is a two-body operator written as [3]

$$[\hat{V}_e]_{\nu\mu} = \mathcal{J}_{\nu\mu} + \mathcal{K}_{\nu\mu} \tag{1.19}$$

where

$$\mathcal{J}_{\nu\mu} = \int\int \phi_\nu^*(r_\alpha)\phi_\mu^*(r_\beta)\phi_\nu(r_\alpha)\phi_\mu(r_\beta)\frac{1}{r_{\alpha\beta}}dr_\alpha dr_\beta \tag{1.20}$$

and

$$\mathcal{K}_{\nu\mu} = \int\int \phi_\nu^*(r_\alpha)\phi_\mu^*(r_\beta)\phi_\mu(r_\alpha)\phi_\nu(r_\beta)\frac{1}{r_{\alpha\beta}}dr_\alpha dr_\beta. \tag{1.21}$$

Here, the term $\mathcal{J}_{\nu\mu}$ is usually called Hartree potential and it stands for the interaction between electronic densities $|\phi_\nu^*(r_\alpha)\phi_\nu(r_\alpha)|$ and $|\phi_\mu^*(r_\beta)\phi_\mu(r_\beta)|$; the term $\mathcal{K}_{\nu\mu}$ is known as exchange-correlation term and has no classical analog. There are many methods and approximations to include the exchange-correlation term in the Schrodinger equation solution; the most remarkable approach is known as density functional theory (DFT) [4, 5, 6]. The exact solution via the numeric self-consistent convergence of the population matrix $P_{\nu\mu} = 2\sum_i C_{\nu i}^* C_{\mu i}$ is usually called as Hartree-Fock-Roothan method [7].

1.1.1 *Density functional theory*

Formally, the DFT proposes to write the energy of the N-interacting electrons as a functional of the total electronic density. In other words, since the density is a scalar field in the three-dimensional space, the electronic problem can be treated using only the coordinates of the electronic density, instead of the $3N$ coordinates of the total wavefunction. Thus, the Eq. 1.8 leads to the energy of the ground state [5],

$$E_s[\rho] = T_s[\rho] + \int d^3r\rho(\boldsymbol{r})V_{eff}(\boldsymbol{r}) + V_{Hartree}(\boldsymbol{r}) + V_{ext}(\boldsymbol{r}). \tag{1.22}$$

This energy can be minimized with the restriction $N = \int d^3 r \rho(\boldsymbol{r})$ using the variational principle,

$$\frac{\delta}{\delta \rho}\left[E[\rho] - \mu\left(\int d^3 r \rho(\boldsymbol{r}) - N\right)\right], \tag{1.23}$$

which in turns leads to

$$\frac{\delta T_s[\rho]}{\delta \rho} + V_{Hartree}(\boldsymbol{r}) + V_{ext}(\boldsymbol{r}) + \frac{E_{xc}[\rho]}{\delta \rho} - \mu = 0. \tag{1.24}$$

Kohn and Sham proposed the mathematical foundations of the DFT, from which is established that the electronic densities of the non- and interacting systems should be the same. This implies that the electron-electron and electron-nucleus interactions could be approximated by an effective potential,

$$V_{eff}(\boldsymbol{r}) = V_{Hartree}(\boldsymbol{r}) + V_{ext}(\boldsymbol{r}) + \frac{\delta E_{xc}[\rho]}{\delta \rho}. \tag{1.25}$$

Therefore, the interacting problem is reduced to the solution of the Schrodinger equation for N non-interacting particles in an effective potential, i.e., the Kohn-Sham equation,

$$\left[-\frac{1}{2}\nabla^2 - V_{eff}(\boldsymbol{r})\right]\psi_\alpha^{KS}(\boldsymbol{r}) = \epsilon_\alpha^{KS}\psi_\alpha^{KS}(\boldsymbol{r}), \tag{1.26}$$

where it has been used the functional form of the kinetic energy contribution of the non-interacting systems $T_s[\rho]$, which is written in terms of the Kohn-Sham wavefunctions $\psi_\alpha^{KS}(\boldsymbol{r})$,

$$T_s[\rho] = \sum_{\alpha=1}^{N} \psi_\alpha^{KS*}(\boldsymbol{r})\left[-\frac{1}{2}\nabla^2\right]\psi_\alpha^{KS}(\boldsymbol{r}) \tag{1.27}$$

In this way, the electronic density is

$$\rho(\boldsymbol{r}) = \sum_{\alpha=1}^{N} \psi_\alpha^{KS*}(\boldsymbol{r})\psi_\alpha^{KS}(\boldsymbol{r}). \tag{1.28}$$

The electronic density and the Kohn-Sham energies ϵ_α^{KS} are obtained from the self-consistent solution of the Kohn-Sham equation. Please note that these energies are just the eigenvalues of an equation describing effective particles, which give the exact electronic density of the ground state. Naturally, the electronic density satisfies the symmetries of the particular studied system and hence, the Kohn-Sham equation should be solved by imposing the symmetry of the problem, as done for tight-binding models. For instance, crystalline solids have translational symmetry, which allow to write the wavefunction as a linear combination of only atomic orbitals in the unit cell defining the periodicity. As we will discuss in the next section, this has remarkable consequences in the electronic states description.

The band structures as a consequence of the translation symmetry breaking

The breaking symmetry principle is one of the most important theoretical frameworks in the condensed matter physics [8]. Although other principles, theories and mathematical elements are required to described and understand some emerging phenomena, e.g., the integer and fractional quantum spin Hall effect, the spatial and translational symmetry breaking is the base of the band theory, which along with group theory allows the discrimination of periodic systems into metals, semiconductors, insulators, and even novel topological phases. Since this classification is one of the focuses of this work, it is convenient to discuss how it appears as a consequence of the translational symmetry and the number of electrons in the system. Using a study case, i.e., the one-dimensional chain of atoms with only one orbital per site, we will described how the band structure is a natural consequence of the translation symmetry breaking. Specifically, instead of discussed the general approximations to solve the "equation of everything" for a general system, here we used an inductive approach to define the required concepts for this thesis. Although the general description can be find in the literature, here we will give a phenomenological explanation when needed.

The effect of the periodic potentials $V(\boldsymbol{r} + \boldsymbol{R}_m)$ can be introduced in the electronic Hamiltonian by considering scattering centers separated by constant translations, i.e.,

$$\boldsymbol{R}_m = \sum_{i=1}^{3} l_{m,i}\boldsymbol{a}_i \tag{1.29}$$

where $\boldsymbol{a}_i$ are vectors defining the topology of the system, i.e., the geometry of the scattering centers.

The periodic distribution of the scattering centers implies the existence of a reciprocal space (whose origin has the crystal symmetry). This reciprocal space is also periodic and defined by the set of vectors $\{\boldsymbol{G}_m\}$ satisfying $\boldsymbol{G}_m \cdot \boldsymbol{R}_n = 2\pi n$ (with $n \in \mathbb{Z}$) for all translation vectors in the real space. The vectors $\{\boldsymbol{G}_m\}$ are essentially the translation vectors in the reciprocal space, also defining the equivalent "reciprocal scattering centers",

$$\boldsymbol{G}_m = \sum_{i=1}^{3} g_{m,i}\boldsymbol{b}_i, \tag{1.30}$$

where $g_{m,i}$ are integers and the vector b_i satisfies: $a_i \cdot b_j = 2\pi\delta_{ij}$. Two vectors in the reciprocal space (for example $\boldsymbol{k'}$ and $\boldsymbol{k}$) are equivalent if they are connected through a reciprocal translational vector, i.e., $\boldsymbol{k'} = \boldsymbol{k} + G$. This leads to the relation $e^{i\boldsymbol{k'}\cdot\boldsymbol{R}_n} = e^{i\boldsymbol{k}\cdot\boldsymbol{R}_n}e^{i\boldsymbol{G}_m\cdot\boldsymbol{R}_n} = e^{i\boldsymbol{k}\cdot\boldsymbol{R}_n}$, suggesting that the wave function in the reciprocal space

$$|\psi(\boldsymbol{k})\rangle = \int e^{-i\boldsymbol{k}\cdot\boldsymbol{r}}\,|\psi(\boldsymbol{r})\rangle\,, \tag{1.31}$$

that encodes the quantum mechanic behavior of the system, only needs to be defined for a set of non-equivalente k-points. This set of points is in principle arbitrary, but it is usually defined by the Wigner-seitz cell in the reciprocal space, which is determined by the k-points satisfying

$$k^2 = (\boldsymbol{k} + \boldsymbol{G}_1)^2. \tag{1.32}$$

Since this cell, the first Brillouin Zone (BZ), is centered at the origin, it contains all the symmetry properties of the crystal. The $\boldsymbol{k}$-vector can be interpreted as the momentum of the electron in the periodic potential, i.e., $\boldsymbol{p} = \hbar\boldsymbol{k}$.

The periodicity is introduced in the Hamiltonian by means of the periodic potential, $\mathcal{H}_e(\boldsymbol{r}) = -\frac{\hbar}{2m}\boldsymbol{\nabla}^2 + V(\boldsymbol{r})$, where the nucleus-electron interaction could be intrinsically included, i.e., $V(\boldsymbol{r}) = \tilde{V}(\boldsymbol{r}) - \frac{e^2}{2}\sum_{A=1}^{P}\sum_{\alpha}^{N}\frac{Z_A}{|\boldsymbol{r}_\alpha - \boldsymbol{R}_A|}$. By definition this Hamiltonian is invariant under the translation symmetry operator T_m, i.e.,

$$T_m\mathcal{H}(\boldsymbol{r}) = \mathcal{H}(\boldsymbol{r} + \boldsymbol{R}_m) = \mathcal{H}(\boldsymbol{r}). \tag{1.33}$$

This implies that the translation symmetry operator commutes with the Hamiltonian $[T_m, \mathcal{H}(\boldsymbol{r})]$ and hence, both operators can be simultaneously diagonalized. In other words, the translated wavefunction $T_m\left|\psi_n(\boldsymbol{r})\right\rangle = \left|\psi_n(\boldsymbol{r} + \boldsymbol{R}_m)\right\rangle$ is also a Hamiltonian eigenvector,

$$\begin{aligned} \mathcal{H}_e(\boldsymbol{r})T_m\left|\psi_n(\boldsymbol{r})\right\rangle &= T_m\mathcal{H}_e(\boldsymbol{r})\left|\psi_n(\boldsymbol{r})\right\rangle \\ \mathcal{H}_e(\boldsymbol{r})\left|\psi_n(\boldsymbol{r} + \boldsymbol{R}_m)\right\rangle &= E_n\left|\psi_n(\boldsymbol{r} + \boldsymbol{R}_m)\right\rangle \end{aligned} \tag{1.34}$$

There are two important consequences that emerge from this equation:

- The Hamiltonian matrix elements are the same in both the non-translated and translated representation,

$$\begin{aligned} \left\langle\psi_n(\boldsymbol{r})\right| T_m^\dagger\mathcal{H}_e(\boldsymbol{r})\left|\psi_n(\boldsymbol{r} + \boldsymbol{R}_m)\right\rangle &= \left\langle\psi_n(\boldsymbol{r})\right| \mathcal{H}_e(\boldsymbol{r})T_m^\dagger\left|\psi_n(\boldsymbol{r} + \boldsymbol{R}_m)\right\rangle \\ \left\langle\psi_n(\boldsymbol{r} + \boldsymbol{R}_m)\right| \mathcal{H}_e(\boldsymbol{r})\left|\psi_n(\boldsymbol{r} + \boldsymbol{R}_m)\right\rangle &= \left\langle\psi_n(\boldsymbol{r})\right| \mathcal{H}_e(\boldsymbol{r})\left|\psi_n(\boldsymbol{r})\right\rangle. \end{aligned}$$

- Both non-translated and translated system have the same energy spectrum.

This formally shows that the spatial distribution of the electronic density should also be periodic, i.e., $\left\langle\psi_n(\boldsymbol{r} + \boldsymbol{R}_m)\right|\left.\psi_n(\boldsymbol{r} + \boldsymbol{R}_m)\right\rangle = \left\langle\psi_n(\boldsymbol{r})\right|\left.\psi_n(\boldsymbol{r})\right\rangle$.

To better understand the relation between the periodic Hamiltonian and the reciprocal space, it is convenient to analyze the eigenvalues of the translation position operator α_m, i.e, $T_m\left|\psi_n(\boldsymbol{r})\right\rangle = \alpha_m\left|\psi_n(\boldsymbol{r})\right\rangle = \left|\psi_n(\boldsymbol{r} + \boldsymbol{R}_m)\right\rangle$. Since T_m is a unitary operator, the eigenvalues should satisfy that $\alpha_m^2 = \pm1$ and hence, $\alpha_m = e^{i\xi_m}$. The parameter ξ_m can

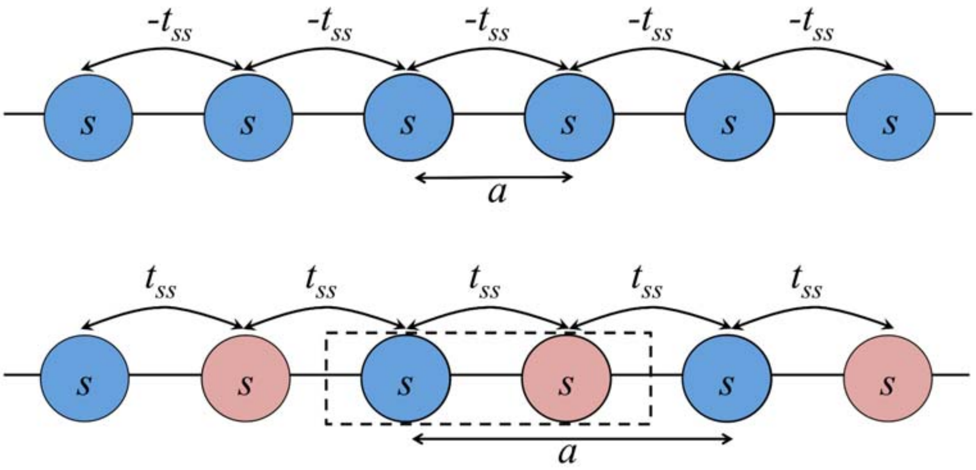

Figure 1.2 - (top) One-dimensional chain of s-orbitals with only one orbital per unit cell. The hopping terms are taking as negative (See text). (b) One-dimensional chain formed by s-orbitals with different phases. This required two orbital per unit cell, which is represented by the dashed line.

be determined by applying to successive translations, i.e., $T_m T_n |\psi_n(\boldsymbol{r})\rangle = \alpha_m \alpha_n |\psi_n(\boldsymbol{r})\rangle$. This means that $\alpha_{m+n} = \alpha_m \alpha_n$; the product of two eigenvalues of the translational symmetry operator is equal to the combined translation, indicating that ξ_n should be proportional to $\boldsymbol{R}_n$. This equivalence between these parameters is achieved through the wave-vectors of the BZ, $\boldsymbol{k}$. The eigenvalues is then written as

$$\alpha_n = e^{i\boldsymbol{k}\cdot\boldsymbol{R}_n}. \tag{1.35}$$

This relation leads to one of the most import results in physics, the Bloch theorem [9],

$$T_m |\psi_n(\boldsymbol{r})\rangle = |\psi_n(\boldsymbol{r} + \boldsymbol{R}_m)\rangle = e^{i\boldsymbol{k}\cdot\boldsymbol{R}_m} |\psi_n(\boldsymbol{r})\rangle\,, \tag{1.36}$$

which is the main constrained imposed by the periodic potential to the Schrodinger equation. This relation implies that the Hamiltonian is block diagonal in the k-space and hence, it can be separately diagonalized for each k-point, i.e., the wavefunction and energies are also indexed with the momentum of the electron, e.g., $E_{n,k}$ and $|\psi_{n,k}(\boldsymbol{r})\rangle$. Based on the initially derived form for the Hamiltonian matrix elements (Eq. 1.18), the periodic boundary conditions leads to the matrix elements

$$[h_e]_{ij} = \varepsilon_0^{ij}\delta_{ij} + \sum_n t_{a_n}^{ij} e^{i\boldsymbol{k}\cdot\boldsymbol{R}_n)}. \tag{1.37}$$

Since the symmetry of the Hamiltonian does not abruptally change from $\boldsymbol{k}$ to $\boldsymbol{k} + \delta k$ (with $\delta k \to 0$), the energies adiabatically change through the BZ, giving rise to the concept

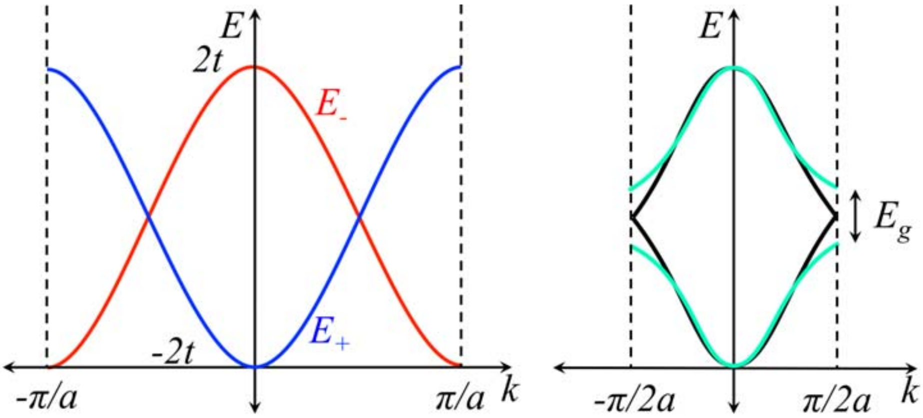

Figure 1.3 - (left) Bands for positive and negative hopping parameters in a one-dimensional chain with only one orbital per unit cell. (right) The bands for a one-dimensional chain with two orbital per unit cell is represented in black. The gaped band structure for the SSH model is shown in green, with $E_g = 2\delta$ being the bandgap.

of bands, i.e., the lines joining successive eigenvalues. To make this evident and study and specific problem, it is convenient to rewrite the Hamiltonian in terms of a specific basis, e.g., plane waves or atomic orbitals. Here, we are going to discuss a simple toy model for a periodic chain of Hydrogen atoms, since it can be understood by extrapolating the previous discussion about the molecule H_2^+ , as schematically represented in Fig. 1.2.

Designing a one-dimensional band inverted insulator

In this work, some mathematical artifices are used to differentiate the phase of the orbitals forming the chain; if they have the same phase we impose an attractive interaction by taking $t_{ss} < 0$, as represented in Fig. 1.2a. Meanwhile, the chains formed by intercalated atoms with different quantum phases are described by a repulsive effective interaction, i.e., $t_{ss} > 0$; this is essentially an anti-bonding states. In this case, the periodicity of the chain requires an unit cell formed by two atoms, as show in Fig. 1.2b. We would like to emphasize that the sign of the hopping term must be understood as a mathematical artifice, since the physical interpretation is not as simple as in the case of the discussed molecule. However, it can be verified that for a chain with only one atom per unit cell and $t_{ss} < 0$ ($t_{ss} > 0$), the energy dispersion described the well known nearly-free-electron model with a non-zero periodic interaction, which seems like a s-orbital (anti-bonding) bonding-state (See Fig. 1.3). Using the Hamiltonian matrix elements given by the tight-binding approximation (Eq. 1.37), the energy dispersion is written as

$$E_{\pm}^{ss} = \varepsilon_0 \mp \sum_{\nu=1} t_{ss} e^{i\boldsymbol{k}\cdot\boldsymbol{R}_\nu} = \varepsilon_0 \mp (t_{ss}e^{ika} + t_{ss}e^{-ika}) = \varepsilon_0 \mp 2t_{ss}\cos ka \tag{1.38}$$

for $t_{ss} < 0$ and $t_{ss} > 0$, corresponding to the bonding E_+ and anti-bonding E_- states, respectively. On the other hand, if the unit cell is formed by two atoms, the band structure is exactly the same for $t_{ss} < 0$ and $t_{ss} > 0$, as represented in Fig. 1.3. This is a manifestation of the folding of the band structure into the first BZ. Specifically, the Hamiltonian reads

$$\mathcal{H}(\boldsymbol{k}) = \begin{pmatrix} \varepsilon_0 & t + te^{ika} \\ t + te^{-ika} & \varepsilon_0 \end{pmatrix}, \tag{1.39}$$

which leads to the energies $E_{\pm}^{ss} = \varepsilon_0 \mp t_{ss}\sqrt{2(1+\cos ka)}$ (See Fig. 1.3). Since the bands are totally occupied, this chain is electrically inert. The last toy model studied here is a system in which the distance between the atoms forming the unit cell decrease. This can be introduced by considering that inter-atomic hopping between atoms in the same unit cell is different from the hopping term between adjacent atoms in different unit cells. Such a effective Hamiltonian is known as Su-Schrieffer–Heeger (SSH) Model [11].

1.3.1 *Su-Schrieffer–Heeger Model*

The SSH model is usually written in terms of the second quantization operators c_{in} and $c_{in}^{\dagger}$. This formalism is completely equivalent to the previous discussed formalism, which we make explicit by considering the SSH Hamiltonian in its usual form [11, **?**],

$$H = -\sum_{n=1}^{N} (t_{ss} + \delta)(c_{An}^{\dagger} c_{Bn} + h.c) + (t_{ss} - \delta)(c_{An+1}^{\dagger} c_{Bn} + h.c), \tag{1.40}$$

where $n_{in} = c_{in}^{\dagger} c_{in}$ is the particle number operator. To simplify the discussion we consider two different kids of s-orbitals: s_A and s_B, as represented in Fig. 1.2. Thus, $t_{ss} + \delta$ is called the long hopping parameter (atoms in the same unit cell), $t_{ss} - \delta$ is the short hopping parameter (atoms in the different unit cells), and (A, B) are the two sublattices. By computing the Fourier transform of the annihilation operators for these sublattices, i.e.,

$$a_k = \frac{1}{\sqrt{N}} \sum_n \exp(-ikna) c_{An} \tag{1.41}$$

and

$$b_k = \frac{1}{\sqrt{N}} \sum_n \exp(-ikna) c_{Bn}, \tag{1.42}$$

we obtain the Bloch Hamiltonian given by the function $h(k) = d_x \sigma_x + d_y \sigma_y$[2],

$$H = \sum_k \psi_k^{\dagger} h(k) \psi_k, \tag{1.44}$$

---

[2] Here, we have used the orthogonality of exponential function

$$\sum_n e^{-ina(k-q)} = N\delta_{kq}. \tag{1.43}$$

where $\psi_k^\dagger = (a_k \quad b_k)$ is a spinor, σ_x and σ_y are the Pauli matrices, and

$$d_x = (t_{ss} + \delta) + (t_{ss} - \delta)\cos k, \tag{1.45}$$

and

$$d_y = (t_{ss} - \delta)\sin k. \tag{1.46}$$

Naturally, this is essential the same Hamiltonian obtained in Eq. 1.39 with $a = 1$. Remarkably, in the low-energy limit $k \to 0$, we have $(d_x, d_y) = (2t_{ss}, (t_{ss} - \delta)k)$, which is the Dirac theory in $(1 + 1)$ dimensions.

As computed in the last section, the energies for the Bloch Hamiltonian of the SSH model are given by

$$E_\pm(k) = \pm\sqrt{d_x^2 + d_y^2} = \pm 2\sqrt{t_{ss}^2 \cos^2\left(\frac{k}{2}\right) + \delta^2 \sin^2\left(\frac{k}{2}\right)} \tag{1.47}$$

Therefore, at the $k = \pi$ point, there is a non-zero energy gap of 2δ, as represented in Fig. 1.3. Thus, the band-gap only closes if $\delta \to 0$, which correspond with the case studied in the last section. For this case, we break the adiabatic condition in the Hamiltonian, hence there exist a topological phase transition, i.e., the Bloch wavefunction gain a non-zero phase when it is adiabatically deformed in a close path defined by changing of momentum (the reciprocal space). In the next chapter we will discus this this in more details and show how to computed this phase, known as Berry phase, for three- and two-dimensional materials. For one-dimensional systems, the Berry phase is essentially the winding number [12],

$$\nu_{SSH} = -\frac{i}{2\pi}\int_{B.Z} dk\ \hat{d}^{-1}(k)\partial_k \hat{d}(k), \tag{1.48}$$

where $\hat{d}(k) \equiv d(k)/|d(k)|$ with $d(k) = d_x(k) + i d_y(k)$. It is instructive to explicitly compute this integral. After some simplifications, we have

$$\nu_{SSH} = -\frac{i}{2\pi}\int_{B.Z} dk\ d(k)\mathcal{K}(k, t_{ss}, \delta), \tag{1.49}$$

with

$$\mathcal{K} = i\frac{(t_{ss} - \delta)^2 + (t_{ss}^2 - \delta^2)\cos k}{[t_{ss} + \delta + (t_{ss} - \delta)\cos k]^2 + (t_{ss} - \delta)^2 \sin^2 k}. \tag{1.50}$$

Finally, integrating over k for $t_{ss} > 0$, we obtain that the winding number in the SSH model is

$$\nu_{SSH} = \frac{1}{2}\left[1 - \mathrm{sgn}(\delta)\right] = \begin{cases} 1, & \delta < 0, \\ 0, & \delta > 0. \end{cases}. \tag{1.51}$$

This number is known as topological invariant and also gives the number of zero-enery states for systems with open-boundary conditions. The transformation $\delta \to -\delta$ changes the phase of the system, because the long hopping parameters become the short one. Although *a priori* these phases are equivalent, the difference appears when we look at the behavior for open boundary conditions [12]. Indeed, it is relatively easy to show this for $N = 4$ (where N is the number of unit cells); the Hamiltonian reads

$$H = C^\dagger \begin{pmatrix} 0 & -(t+\delta) & 0 & 0 \\ -(t+\delta) & 0 & -(t+\delta) & 0 \\ 0 & -(t+\delta) & 0 & -(t+\delta) \\ 0 & 0 & -(t+\delta) & 0 \end{pmatrix} C, \tag{1.52}$$

where $C^\dagger = (c^\dagger_{A,1}\ c^\dagger_{B,1}\ c^\dagger_{A,2}\ c^\dagger_{B,2})$ is the basis. The generalization for any N is straightforward. It is relatively simple to show that this solution can have a zero-energy state. The existence of zero-energy states implies the existence of a ground state with fractional charge [12]. Indeed, we write the decomposition of the field operator as

$$\psi(x) = \sum_E b_E \psi_E(x) + d^\dagger_E \psi_{-E}(x) + a\psi_0(x), \tag{1.53}$$

where b_E creates an electron with positive energy, $d^\dagger_E$ creates a hole with negative energy, and a creates the zero-energy mode. These fermionic operators obey: $b_E, b^\dagger_E = 1$, $d_E, d^\dagger_E = 1$, and $a, a^\dagger = 1$. From the particle-hole symmetry, we conclude that for each sate with energy E, there is other state with energy $-E$. Therefore, the zero-energy mode $E = 0$ must be double degenerate. We represent these zero-energy states by $|G\pm\rangle$, hence, $\{a, a^\dagger\}|G\pm\rangle = |G\pm\rangle$. This allow us to obtain the algebra of these operators given by

$$a|G_+\rangle = |G_-\rangle, a|G_-\rangle = 0, a^\dagger|G_-\rangle = |G_+\rangle, a^\dagger|G_+\rangle = 0 \tag{1.54}$$

Next, we define the fermion number operator Q. This is given by

$$Q = \frac{1}{2}\int d^2x(\psi^\dagger\psi - \psi\psi^\dagger) \tag{1.55}$$

We then find that,

$$Q = \sum_E = (b^\dagger_E b_E - d^\dagger_E d_E) + a^\dagger a - \frac{1}{2}. \tag{1.56}$$

It is easy to show that

$$Q|G\pm\rangle = \pm\frac{1}{2}|G\pm\rangle \tag{1.57}$$

This zero-energy states are usually known as topological states[3], since they appear when-

---

[3] In the particular case of the SSH model, the states with fractional quantum numbers are known as solitons.

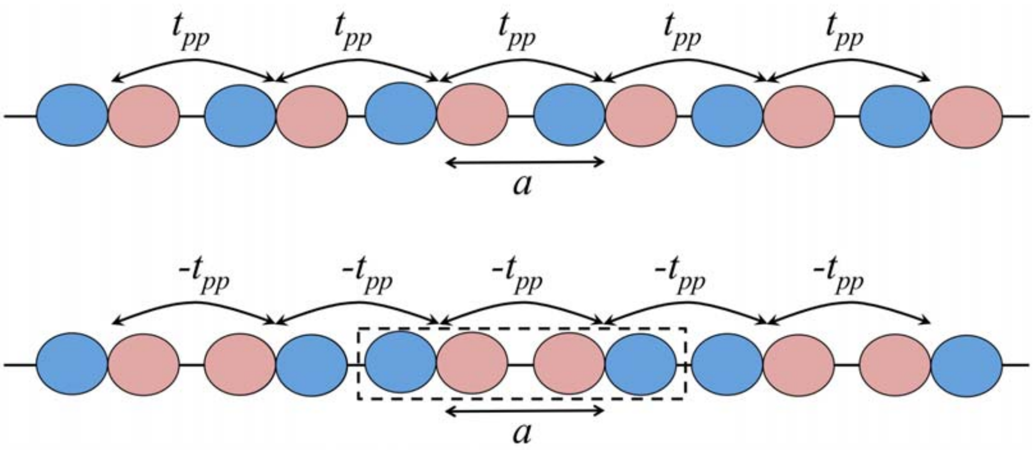

Figure 1.4 - One-dimensional chain formed by p_x-orbitals with (top) the same phase and (bottom) different phases. The chain formed by orbitals with different phases (a bonding-like state) requires two orbitals per unit cell, which is represented by the dashed line.

ever the topological invariant is different from zero. Here, the symmetry imposing this condition is the particle-hole symmetry, but in principle any symmetry (except the inversion symmetry) can lead to a equivalent behavior. Topological transitions, i.e., the changing in the topological invariant, are usually related to band-inversion, as we discuss in the next section.

1.3.2 *Band inversion*

In a periodic chain formed by p_x-orbitals with only one orbital per unit cell, two successive orbitals intrinsically form an anti-bonding state (See Fig. 1.4). Consequently, in this chain, the eigenvalues become $E_{-}^{pp} = \varepsilon_0 + 2t_{pp}\cos ka$, and the hopping term can be considered as an effective repulsion, i.e., $t_{pp} > 0$. As represented in Fig. 1.4, two atoms per unit cell are required to obtain a bonding-like state ($t_{pp} < 0$) in a chain form by p_x-orbitals, i.e., two successive orbitals with opposite phase. The energies are essentially the same as the obtained for s-orbitals, but usually the hopping terms are extremely different, e.g., the s-s orbital interaction is usually stronger than the p-p orbital interaction. Summarizing, except for the change of the interaction term sign ($t_{pp} > 0$ and $t_{ss} < 0$), which in turns change the concavity of the band, the descriptions of both p_x- and s-orbitals one-dimensional chains is similar. This gives us information about the how to model systems formed by s- and p_{xy}-orbitals around the Γ point. For instance, in the Zinc blende structure the minimum of the conduction band is usually formed by s-orbitals, while the maximum of the valence band by p_{xy}-orbitals (See Fig. 1.5). Near the Γ point the band structure can be then approximated by the simple model similar to the Eq. 1.39. Specifically, by taking the approximation $\boldsymbol{k} \rightarrow \Gamma$, the energies describing the electrons confined in an one-dimensional chain form by either s- or p-orbitals are $E^{pp} = \varepsilon_0 + 2t_{pp} - t_{pp}(ka)^2$ and $E^{ss} = \varepsilon_0 - 2t_{pp} + t_{pp}(ka)^2$, respectively.

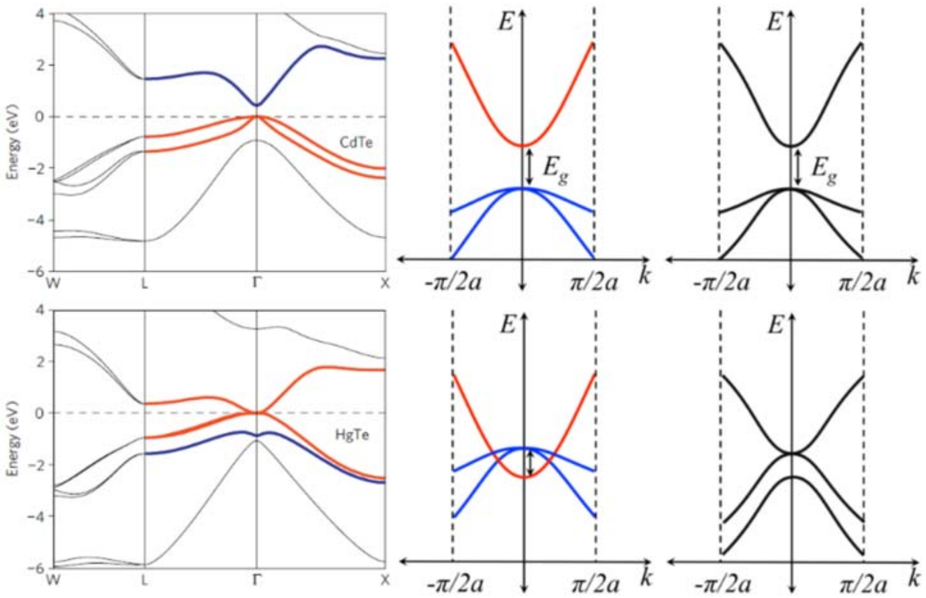

Figure 1.5 - Band structure for (top) CdTe and (bottom) HgTe semiconductors calculated using (left) density functional theory [20] and (right) the tight-binding model (only for k-points near the Γ point). We first show the bands without the interaction term between s- and p-orbitals and then showing the effect of this interaction.

Curiously, this is consistent with the expected s- and p_{xy}-orbital energy dispersion at the Γ point for Zinc blend semiconductors, e.g., CdTe, as represented in Fig. 1.5. This does not support the proposed criterion for the hopping term, but it demonstrates that we can effectively describe the band structure and chemical bonds dominated by an specific set of orbitals by modifying the hopping term. For instance, as already mentioned, the Γ_6 band (s-character) has an effective kinetic energy proportional to k^2, while in the Γ_7 and Γ_8 bands (p-character) the kinetic energy is proportional to $-k^2$, which is easily capture by our simple model. Naturally, a symmetry analysis is required to find the interaction term between these bands. Although in Zinc blende semiconductors the bands whose wavefunction is dominated by s-orbitals are typically above the bands formed by p-orbitals, the inverse order is also possible, e.g., in HgTe the relativistic correction leave the p-orbital contribution above the states formed by s-orbitals. In semiconductors featuring inverted bands, the quantum confinement can revel remarkable properties of the energy spectrum, as we discuss below.

Based on the previous discussion, we construct an effective model describing a simple one-dimensional band inverted insulator, i.e., a unit cell formed by p_x and s-orbitals. We discriminate again the hopping in terms of effective bonding and anti-bonding states depending on the phases of the orbitals involved in the interaction, as shown in Fig. 1.6. Using the tight-binding approximation including next nearest neighbors (Eq. 1.37), we

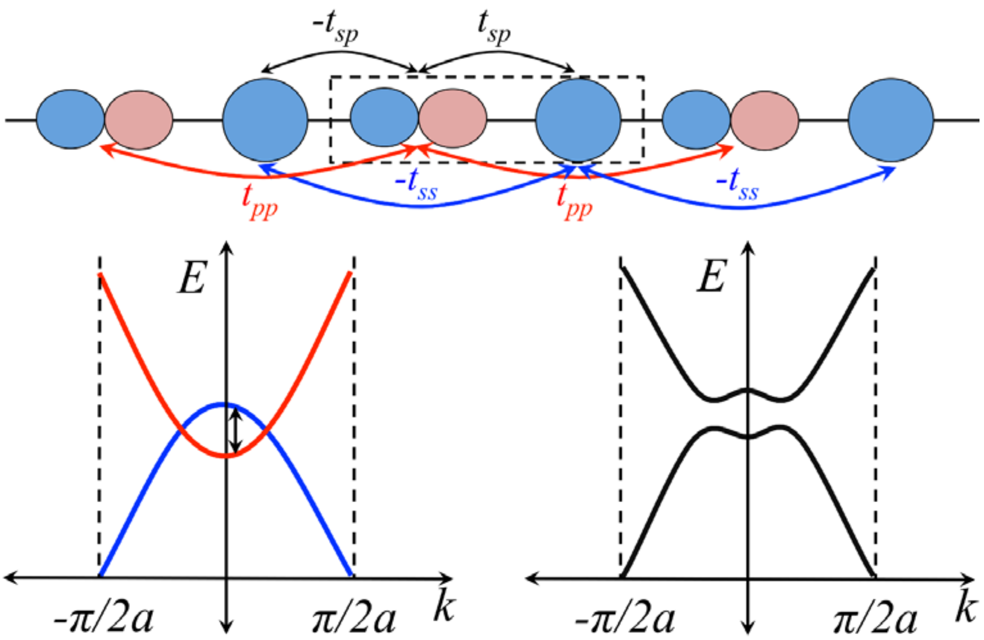

Figure 1.6 - (top) One-dimensional chain formed by s- and p_x-orbitals. (Bottom) Band structure without and with the interaction term between s- and p_x-orbitals, t_{sp}.

obtain the Hamiltonian,

$$\mathcal{H}(\boldsymbol{k}) = \begin{pmatrix} \varepsilon_0 - t_{ss}e^{ika} - t_{ss}e^{-ika} & t_{sp} + t_{sp}e^{ika} \\ t_{sp} + t_{sp}e^{-ika} & \varepsilon_0 + t_{pp}e^{ika} + t_{pp}e^{-ika} \end{pmatrix}. \tag{1.58}$$

By taking the approximation $\boldsymbol{k} \to \Gamma$ and considering the on-site energy equal to zero ($\varepsilon_0 = 0$), this Hamiltonian can be rewritten as

$$\mathcal{H}(\boldsymbol{k}) = \begin{pmatrix} -2t_{ss} - 2t_{ss}(ka)^2 & t_{sp} + t_{sp}e^{ika} \\ t_{sp} + t_{sp}e^{-ika} & 2t_{pp} + 2t_{pp}(ka)^2 \end{pmatrix}, \tag{1.59}$$

where a is the lattice constant. It is very instructive to note that a null hopping interaction term t_{sp} results in two parabolic inverted bands, as represented in Fig. 1.6. The role of the interaction term is then opening the bandgap, leading to an insulator behavior (depending on the position of the Fermi energy). Using the Eq. 1.48, we verify that the winding number - the topological invariant - for the proposed system is $\nu = 1$, which suggest that in the finite chain, topological states should exist, exactly in the same way discussed for the SSH model. In the rest of this introduction, we will discuss how the topological states are protected by a specific symmetry of the crystal.

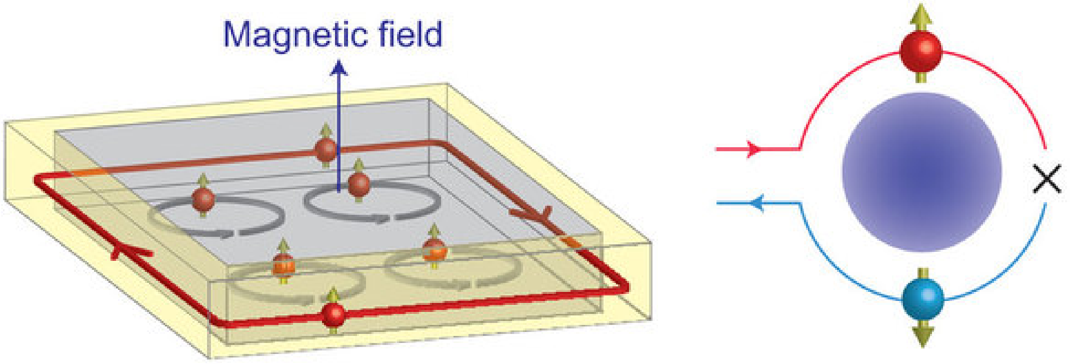

Figure 1.7 - Integer quantum Hall effect and Backscattering in systems with non-trivial topological phases [20].

Band inverted insulators: Topological insulators

The surface of an "infinite" crystal introduces evanescent states. These surface states (edge estates for 2D systems) are connected with the Bloch states of the bulk-crystal. From the band theory viewpoint, the insulating state is characterized by an energy band gap, which separates electronic completely filled bands from a set of completely empty bands. In an insulating material, the surface states are easily modified through impurities, defects or by the reconstruction itself, such that the material remains in the insulating state. Consequently, within either a semiclassical or any transport model, insulators do not respond to an electric field, i.e., the insulating state is defined as electrically inert, as previously discussed for a one-dimensional chain.

The physics of condensed matter of the twentieth century has been revolutionized with the discovery of a new state, called Quantum Hall Effect (QHE). This state is characterized by an insulating bulk with stable metallic edge states, which are robust to the disorder. Thus, although the QHE presents an energy gap separating the different conduction levels, it also has a transverse magneto-conductance (σ_{xy}). This conductance is quantized in an extremely accurate way in terms of integers of $e^2/\hbar$. This conductance is localized at the edges of the system, i.e., whereas the bulk behaves as an insulator, the electrons describe cyclotron orbit, as shown in Fig 1.7.

The QHE seemed to violate the understanding in which a system with energy gap have no electronic transport, and therefore, it opened a fundamental question about the way in which an insulating state is characterized: can we classify insulators as materials that does not respond to the action of the electric field?, or as one that has occupied levels separated from unoccupied states by an energy gap?. This apparent paradox was solved by Laughlin [13], who noted that the wave function plays a fundamental role in the electronic transport, i.e., the transport is a coherence property of the many-body wave functions phase. Later, Thouless, Kohmoto, Nighting e Nijs (TKNN) [14] showed explicitly the relation between this phase and the conductance σ_{xy}, bringing the concept of topology for the characterization of the insulator state.

The first BZ of the QH system can be understood as a closed manifold. Similarly as is done in mathematics, using the Gauss-Bonnet theorem for a compact two-dimensional Riemannian manifold, QH systems could be characterized by a topological invariant. When a quantum state varies adiabatically in a closed path in the BZ, there is a topological invariant in terms of the Berry phase that characterizes the system, the first Chern number,

$$C_n = \frac{1}{2\pi}\sum_m \int_{BZ} f_m \left[\boldsymbol{\nabla}_{\boldsymbol{k}} \times \boldsymbol{A}(\boldsymbol{k})\right]_m d^2k, \tag{1.60}$$

where the Berry curvature $\boldsymbol{B}_{m\alpha\beta}(\boldsymbol{k})$ is defined as:

$$\boldsymbol{B}_{m\alpha\beta}(\boldsymbol{k}) = \left[\boldsymbol{\nabla}_{\boldsymbol{k}} \times \boldsymbol{A}(\boldsymbol{k})\right]_m = -2\mathrm{Im}\sum_{n\neq m}^{N'} \frac{\langle u_{m\boldsymbol{k}}|\partial_{k_\alpha}\mathcal{H}(\boldsymbol{k})|u_{n\boldsymbol{k}}\rangle\langle u_{n\boldsymbol{k}}|\partial_{k_\beta}\mathcal{H}(\boldsymbol{k})|u_{m\boldsymbol{k}}\rangle}{(E_{m\boldsymbol{k}} - E_{n\boldsymbol{k}})^2}, \tag{1.61}$$

where $\mathcal{H}(\boldsymbol{k})$ is the Hamiltonian describing the system, $|u_{m\boldsymbol{k}}\rangle$ and $E_{m\boldsymbol{k}}$ represents the Bloch function and the energy for a given $\boldsymbol{k}$ point and a band index m. Remarkable, although the Chern number is a property that involves all bulk states below the Fermi level, this topological invariant corresponds to the number of one-dimensional edge channels. This is typically known as bulk-edge correspondence. In the edge channels, the electrons can not be backscattered (See Fig. 1.7), leading to a perfect quantized conductivity.

The Hall conductance is intrinsically only related to the number of edge states, which are unidirectional due to the time-reversal symmetry breaking caused by an external magnetic field, explicitly $\sigma_{xy} = C_n e^2/\hbar$. In the case of a normal insulator (also known as trivial insulator) $C_n = 0$ and $\sigma_{xy} = 0$. Before considering an external magnetic field, edge states are observed and therefore, $C_n \neq 0$. Whereas metals have an Ohmic current (derived from the non-equilibrium Fermi-Dirac distribution function for states near the Fermi level), the Hall current is a topology current that involves all states below the Fermi level.

The time reversal symmetry breaking due to an intrinsic magnetic moment, together with Rashba spin-orbit coupling, can produce a topological current at the edges with a particular spin direction (spin-polarized current). This effect is known as Quantum Anomalous Hall Effect (QAHE), which is also characterized by the first Chern number. This phenomenon has been studied experimentally in the 80s, but it was theoretically explained only after the theoretical discovery of a new topological phase baptized as Quantum Spin Hall Effect (QSH). This effect is essentially a two-dimensional analog of

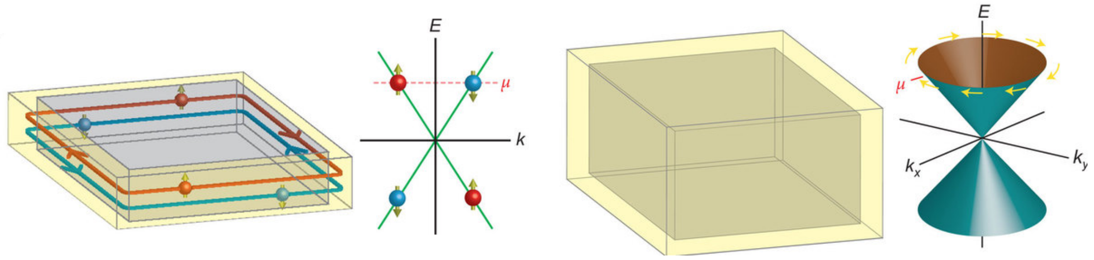

Figure 1.8 - (left) Quantum spin Hall effect. (right) 3D Topological insulator. [20]

the band inverted one-dimensional chain discussed in the last section.

In the QSH effect, predicted by Kane and Mele [15] in graphene[4], the role of the magnetic field is provided by the spin-orbit coupling and therefore, the time reversal symmetry is preserved. This unique feature results in a bulk insulator system with a pair of anti-propagated edge states with opposite spin. These states have a linear dispersion (Dirac cone) with helical spin texture, as show in Fig. 1.8. The edge spin currents associated with these helical states have no dissipation, suppressing the backscattering. Naturally, this property is ideal for spintronic devices. Consequently, the metallic edge states are robust against disorder and the topological protection is governed by the time reversal symmetry. The topological band dispersion has been experimentally characterized via angle-resolved photoemission spectroscopy (ARPES) and local scanning tunneling microscopy (STM) in 3D topological insulators, and via transport measurements in HgTe/CdTe quantum wells [18, 19]. The 3D generalization of these systems is known as *Topological Insulators* (TI) [16, 17]. The QSH is characterized by a new topological invariant known as Z_2, which is similar to the Chern number for the QAHE,

$$Z_2 = \frac{1}{2\pi i}\left[\oint_{EBZ} d\boldsymbol{k}\cdot\boldsymbol{A} - \int_{EBZ} d^2\boldsymbol{k}\cdot\boldsymbol{B}\right]\mathrm{mod}(2). \tag{1.62}$$

The effective BZ (EBZ)is not more than the half of the Brillouin zone with the appropriate boundary conditions, i.e., preserving the time-reversal symmetry.

The description of periodic systems through the Bloch theorem and the band theory is not incorrect, nevertheless a suitable description and characterization of the insulator state requires the introduction of concepts related to topology. In this theory, known as topological band theory, the symmetry preserved by the crystal can provide a topological protection. Whenever this symmetry is preserved, the metallic states inside the bulk-gap will be protected against the backscattering. If the Hamiltonian describing an insulating

---

[4] Formally, the little intrinsic SOC of carbon atoms does not allowed the experimental observation of this effect in graphene. However, much work has been developed in finding a way to increase the graphene SOC.

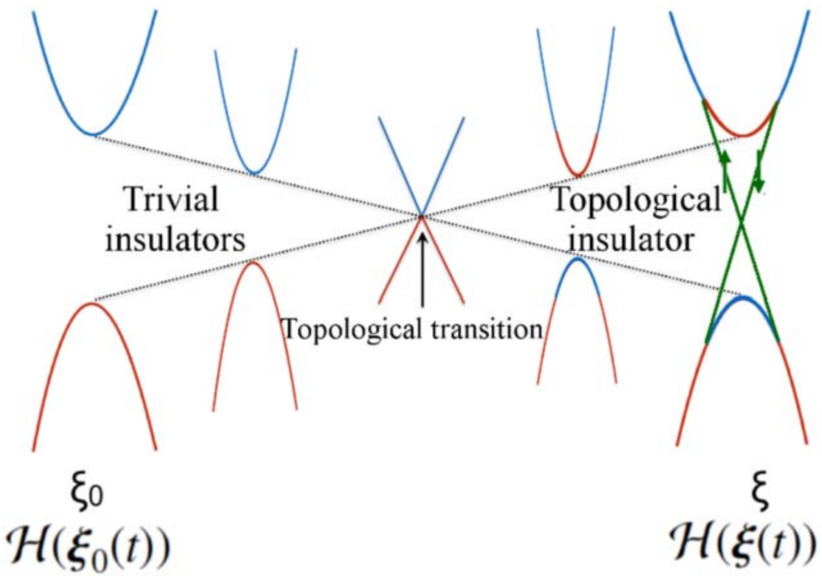

Figure 1.9 - Topological transition and boundary states in trivial and topological insulators.

commutes with the time reversal symmetry operator, the time reversal invariant momenta points exhibit degenerated states. In the case of a topological insulator, if the energy gap occurs at these points, the surface states connecting the valence band and conduction bands form a Dirac cone, as show in the Fig. 1.9. The discovery of these systems and their theoretical and experimental study has opened a new area of research in condensed matter physics, which covers all insulators classified by a non-zero topological invariant: Chern insulating, QAHIs, QSHIs, and TIs.

Topological insulators and spintronics

The spintronic is based on a simple idea: "A future spintronics device would perform calculations and store information using the spin-degree of freedom of electrons with a vision to eventually replace conventional electronics" [22, 23]. The central objective of spintronics is to understand the mechanisms by which it is possible to achieve efficient electrical control of spin currents and spin configurations. It has been proposed several mechanisms for the simultaneous control of both the electronic transport and the spin currents. The phenomena of interest in spintronic could be classify according to the spin transport control mechanisms: *i*) electric field (See Fig. 1.10) and *ii*) spin-orbit coupling (See Fig. 1.11). These phenomena are typically found in two groups of systems: *i*) conductor systems with magnetic order and *ii*) semiconductor systems or paramagnetic metals. In this thesis, we study both spin control mechanisms, but we always focus on systems with strong intrinsic SOC.

- QAH systems, which are conductors with magnetic order where the SOC generates

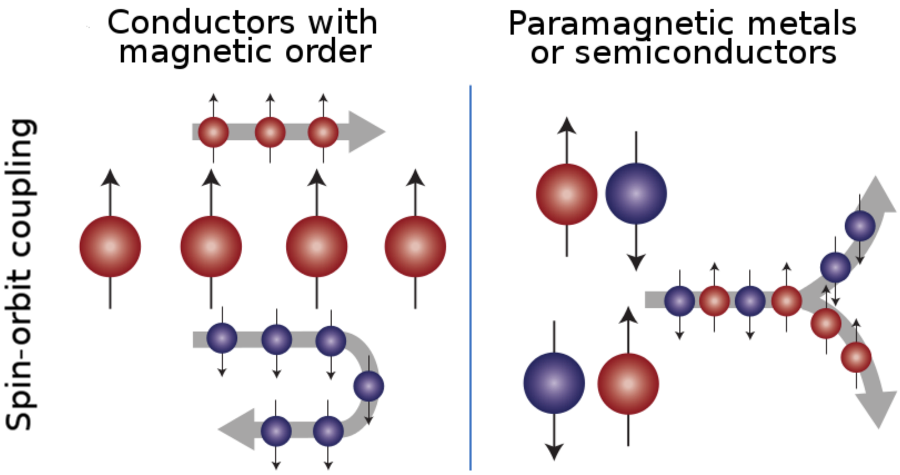

Figure 1.10 - The two panels in this figure schematically illustrate (left) giant magnetoresistance in which variation in magnetization direction increases backscattering and hence resistance and (right) Andreev reflection of spins in non-collinear magnetic systems that leads to spin-transfer torques and current-induced spin reversal [21].

a band inversion that results in a spatial breaking of the conductivity channels with spin polarized current, as previously mentioned.

- QSH systems, which are non-magnetic. As discussed above, in these systems, the electronic states physics depends on the SOC.

Even though the systems exhibiting protected boundary states are not the unique class of systems that present phenomena of interest in spintronic, these are the most developed in terms of theoretical understanding.

We would like to highlight an effect that has been the subject of intense theoretical and experimental research activity, since it allows the control of the magnetization of a thin layer of material through a spin-polarized current, i.e., the spin-transfer torque. Spintronics in semiconductors is richer scientifically than spintronics in metals because doping, gating, and heterojunction formation can be used to engineer material properties. In highmobility two-dimensional electron systems that have substantial Rashba spin-orbit coupling, the spin-torque implies that spin currents always accompany charge currents, leading to the spin Hall effect (See Fig. 1.11): the charge accumulated at the edges has a spin orientation preference. A similar recently proposed effect known as spin-orbit torque, which is produced by the flow of an electric current in a crystalline structure lacking inversion symmetry, transfers orbital angular momentum from the lattice to the spin system. Spin-orbit torques are found to be prominent in both ferromagnetic metal and semiconducting systems, allowing for great flexibility in adjusting their orientation and magnitude by proper material engineering. In this work, we explore spin-orbit torque-

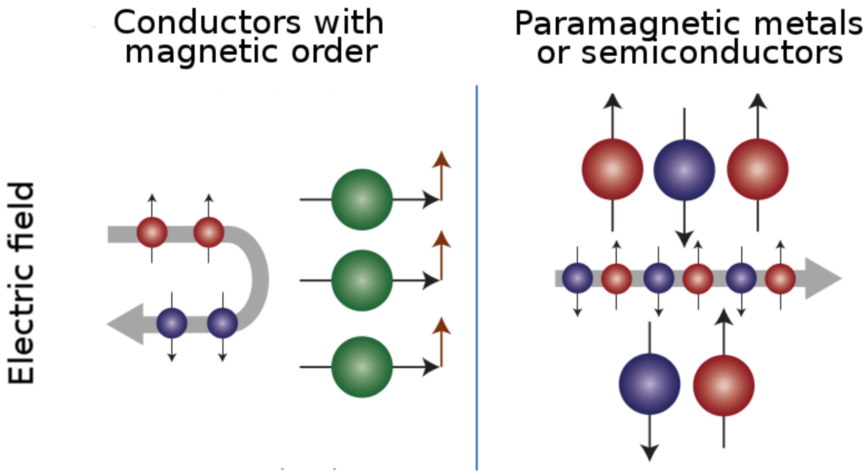

Figure 1.11 - The two panels in this figure schematically illustrate (left) the spin Hall effect and spin currents in paramagnetic conductors and (right) current-induced spin polarization in paramagnetic conductors; Spin-transport effects in paramagnetic conductors always require spin-orbit interactions [21].

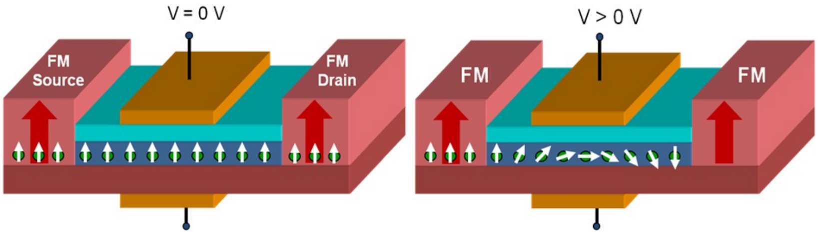

Figure 1.12 - Elemental model of a digital spintronic transistor [22, 23].

like effects for the equilibrium carrier spin density configuration.

The current silicon-based semiconductor devices are reaching the miniaturization limit, which is a feature associated with minimum distance traveled by electrons in a device and hence, the performance of the same. Since in systems featuring non-zero topological invariants, the conductivity channels exhibit dissipationless spin-polarized electronic states, the spin relaxation time is usually greater than the electronic relaxation time. We believe that it is possible to construct topological insulator based spintronic devices with an efficiency significantly higher than the common electronic devices.

The digital transistor is a fundamental device model that uses an external electric field as a mechanism to control the spin transport properties (See Fig 1.12). In this system, the spin degree of freedom is used as the basic element to obtain 1 (spin $\uparrow$) or 0 (spin $\downarrow$), required for a digital device system. The realization of spintronic devices with these characteristics using topological insulator materials is not trivial, because there are intrinsic difficulties in the electronic transport measurements, i.e., the experimental results characterized by ARPES techniques show that the samples present [20]: *i)* an intrinsic n-type and p-type doping due to intrinsic defects or impurities; *ii)* the presence of residual continuous bulk states (main difficulty); *iii)* the lack of a mechanism to control the surface state without obtaining emergent phenomena originating from the bulk states; *iv)* low SOC bandgaps and therefore, intrinsic difficulties in the observation of topologically protected edge metallic states. Since the countless experimental works searching for the electronic behavior expected by the predicted model have not been satisfactory, the electronic transportation measurements are still a challenge. This suggest that the search for either novel topological insulators with a sizable bandgap or novel phenomena allowing the spin-polarization control is still an open problem,

Objectives

Our research group has been studied the electronic properties of topological insulators, showing that:

(a) 3D transition metals when adsorbed on the Bi_2Se_3 and Bi_2Te_3 surface provide a mechanism to control the magnetic moment of these systems. This magnetic moment is associated predominantly with the spin configuration and the spin direction of the adsorbed atom. The intrinsic magnetic moment breaks the time-reversal symmetry, eliminating the spin degeneration at the high symmetry points and thus, opening a gap at the Dirac cone. There is a dependence of this gap in relation to the magnetic moment direction. the Dirac cone is broken when the magnetic moment induced by the adsorbed atom is out-plane in relation to the TI surface. Whereas if the magnetic moment is in-plane two effects appear: i) the Dirac cone moves and ii) the break of degeneracy results in a smaller gap compared with the gap in the out-plane magnetic moment case [24].

(b) It is possible to eliminate the contribution of the bulk states near the Dirac cone via stacking faults in the atomic layers that form the Bi_2Se_3 and Bi_2Te_3 TI [25].

(c) The topological properties can be controlled by hydrogenating and doping the QSH systems; increasing or decreasing the contribution of the SOC and thus, allowing experimental observations [26].

Unifying these results, which resolved separately one of the problems described above, we have some ideas about the conditions satisfied by systems that could be suitable for the construction of a spintronic device. The general objective of this project is:

Propose systems and phenomena with the electronic properties that enable the construction of a digital transistor using the spin as a basic element for the control of transport properties.

In the prediction and the design of new topological materials and devices, the computational simulations have played a fundamental role. Indeed, from a theoretical point of view, the $ab-initio$ methods based on the density functional theory have been the most used framework for the characterization of topological states, the prediction of novel materials and the study of the spin texture consequences in these materials. However, for the study of the electronic transport in QSH systems is necessary a computational code that takes into account the SOC. Within the computer codes of first principles calculations, our group frequently use the SIESTA code, in which, in order to enrich the theoretical treatment, we have implemented: *i)* the spin-orbit interaction (developed in my Masters project), *ii)* the self-interaction correction (SIC) and *iii)* the ballistic electronic transport via non-equilibrium Green's functions (TRANSAMPA-code), etc. In the present work, using the formalism of non-equilibrium Green's functions and norm-conserving relativistic pseudopotentials, we will implement the SOC in the TRANSAMPA code, fundamental to understanding the electronic transport properties and the spin transport properties of nontrivial topological states.

According to the theoretical and experimental development described above, the present work initially aims a dense implementation work to study the transport properties of 2D and 3D pristine topological insulators. Below we list some of our specific objectives necessary to achieve a general framework in the understanding of topological insulators materials and the way to predict suitable systems and phenomena for the construction of novel spintronic devices:

1. Implement the topological invariants: Chern Number C_n and the Z_2 invariant for the characterization of topological insulators in the SIESTA, VASP and AIMS codes used to perform first-principles calculation.

2. Make a model for the electronic transport of these materials. Although our research group have expertise in the treatment of transport based on the Landauer model, our technique does not include in the Hamiltonian the spin-orbit effects fundamental to the correct description of topological insulators. So that, our model based on the DFT coupled to Green's functions techniques should be modified. In the search for 2D materials that may present a QSH behavior, initially our study is focused on bidimensional layers of Silicon (Si), Germanium (Ge) and alloys. With the methodology proposed for the inclusion of SOC in the ballistic transport, we have an appropriate tool to spin current calculations in nanoribbons.

3. Using DFT simulations as a tool for prediction of systems with nontrivial topological phases, we propose to look for new two-dimensional systems with strong SOC by implementing machine learning algorithms. Specifically, we have computed the

topological Z_2 invariant for 220 functionalized honeycomb-lattices that are isoelectronic to functionalized graphene. Besides confirming the TI character of well-known materials, e.g., functionalized stanene, our study identifies several other yet unreported QSHIs. We applied a compressed-sensing approach to identify a physically meaningful descriptor for the Z_2 invariant that only depends on the properties of the material's constituent atoms. First, this yields fundamental insights in the mechanisms driving topological transitions, especially in the atypical case of QSHIs with low spin-orbit coupling. Second, this allows us to predict 74 new QSHIs that are not part of the original set of 220 graphene-type materials used to identify the descriptor.

4. Evaluate two possible ways for the construction of a transistor based on either the spin conservation or spin generation:

   i) Protected bulk states: we proposed that the simultaneous presence of both Rashba and band inversion can lead to a Rashba-like spin-splitting formed by two bands with the same in-plane helical spin texture. Because of this unconventional spin texture, the backscattering is forbidden in edge and bulk conductivity channels. We propose a new non-centrosymmetric honeycomb-lattice quantum spin Hall (QSH) insulator family formed by the IV, V, and VII elements with this property. The system formed by Bi, Pb and I atoms is mechanically stable and has both a large Rashba spin-splitting of 60 meV and a large nontrivial band gap of 0.14 eV. Since the edge and the bulk states are protected by the TR symmetry, contrary to what happens in most doped QSH insulators, the bulk states do not contribute to the backscattering in the electronic transport, allowing the construction of a spintronic device with less energy loss.

   ii) Spintronic transistor: we show that half-functionalized honeycomb lattice materials can exhibit a dual topological character, which required that the spin texture of the edge states is oriented perpendicular to the mirror plane that protects them. Remarkably, we find that an external electric field breaking the mirror symmetry in dual topological insulator nanoribbons induces a spin-polarization parallel to the mirror plane. Based on this, we propose a transistor model using the spin-direction as a switch. We also find that the in-plane magnetic fields, breaking the time reversal symmetry and preserving the mirror symmetry, lead to a displacement of the Dirac point formed by the edge states in the reciprocal space, confirming the topological mirror symmetry protection. The proposed transistor essentially corresponds to the device shown in Fig.1.12.

5. We studied the influence of the bulk states in the surface electronic transport. First, we put forward a tight-binding model for rhombohedral topological insulators materials with the space group $D_{3d}^5(R\bar{3}m)$. The model describes the bulk band structure

of these materials over the whole Brillouin zone. Within this framework, we also describe the topological nature of surface states, characterized by a Dirac cone-like dispersion and the emergence of surface projected bulk states near to the Dirac-point in energy. We find that the breaking of the R_3 symmetry as one moves away from the Γ point has an important role in the hybridization of the p_x, p_y, and p_z atomic orbitals. In our tight-binding model, the latter leads to a band mixing matrix element ruled by a single parameter. We show that our model gives a good description of the strategies/mechanisms proposed in the literature to eliminate and/or energy shift the bulk states away from the Dirac point, such as stacking faults and the introduction of an external applied electric field.

Computer simulations allow the study of different systems varying its parameters and characteristics in a controlled manner. In this project, using computer simulations based on the Density Functional Theory (DFT) and non-equilibrium Green functions within the Ladauer formalism, we implemented of the electronic transport taking into account the SOC. This implementation allows the study of electronic transport in nanostructures, and therefore, it is a powerful tool for the study of spin currents and the problems associated with the construction of digital transistors using topological-protected materials. Thus, we studied the conditions required to eliminate the aforementioned problems and subsequently, proposing a system that has the electronic conditions to enable the construction of a digital transistor in the most basic elemental model.

Bibliography

[1] P. W. Anderson Science, **177**, 4047 393 (1972).

[2] Max Born, and J. Robert Oppenheimer Annalen der Physik (in German), **389** (20), 457 (1927).

[3] Adalberto Fazzio, Jose David M. Vianna, and Sylvio Canuto Teoria Quântica de Moléculas e Sólidos: Simulação Computacional, (2004)

[4] Hohenberg Pierre, and Walter Kohn Inhomogeneous electron gas, Physical Review, **136** (1964).

[5] Kohn W, and Sham L. J. Self-consistent equations including exchange and correlation effects, Physical Review, **140** A1133, (1965).

[6] Parr Robert G, and Yang Weitao Density-Functional Theory of Atoms and Molecules. Oxford: Oxford University Press. (1994).

[7] Roothaan, C. C. J. New Developments in Molecular Orbital Theory", Reviews of Modern Physics, **23**, 69 (1951).

[8] Brading, Katherine and Castellani, Elena and Teh, Nicholas Symmetry and Symmetry Breaking, The Stanford Encyclopedia of Philosophy. (2017).

[9] Felix Bloch Yber die Quantenmechanik der Elektronen in Kristallgittern. Z. Phys. **52**, 555 (1928).

[10] W.P. Su, J.R. Schrieffer, and A.J. Heeger, Phys. Rev. Lett. **42**, 1698 (1979).

[11] W.P. Su, J.R. Schrieffer, and A.J. Heeger, Phys. Rev. B **22**, 2099 (1980).

[12] J. K. Asboth, L. Oroszlany, and A. Palyi, A Short Course on Topological Insulators, Band-structure topology and edge states in one and two dimensions. Arxiv 1509.02295 (2015).

[13] Liang Fu, and A.C. Kane, Physical Rev B **74**, 195312 (2006).

[14] Thouless, Kohmoto, Nighting e Nijs, Physical Rev Letter **49**, 405 (1982).

[15] C.L. Kane and E.J. Mele, Physical Rev. Letters **95**, 226801 (2005).

[16] Liang Fu, C.L. Kane, and E.J. Mele, Physical Rev Lett. **98**, 106803 (2007).

[17] Haijun Zhang, et al., Nature Physics **5**, 438 (2009).

[18] Markus Konig, et al., Science **318**, 5851, 766 (2017).

[19] E. B. Olshanetsky, et al., Phys. Rev. Lett. **114**, 126802 (2015).

[20] D. Hsieh, et al., Nature physics **452**, 970 (2008).

[21] Dmytro Pesin and Allan H. MacDonald, Nature Material **11**, 409 (2012).

[22] Péter Boross, et al., Nature, Scientific Reports **3**, 3233, (2013).

[23] Zhou, W, et al., Phys. Rev. B **84**, 125323, (2011).

[24] Abadalla, et al., Physical Rev B **88**, 045312-1-045312-12, 2013.

[25] Seixas, L, et al., Journal of Applied Physics, **113**, 023705 4, 2013.

[26] L. Seixas, J. E. Padilha, and A. Fazzio, Physical Rev. B **89**, 195403, 2014.

[27] C. Mera Acosta, et al., Phys. Rev. B **89**, 155438, 2014.

2. Implementations

Geometric phase in band theory

In recent years, the band theory of solids has been augmented by new chapters to account for geometric and topological effects that had not been considered previously[1]. The introduction of the Berry phase [3] allowed the systematic description of many observable effects of purely geometric origin, such as the Aharonov-Bohm effect [11], and its applications in the band-theory context have included the theory of electric polarization [5, 6] and the anomalous Hall conductance [7, 8].

The adiabatic theorem is a fundamental concept in quantum mechanics and is essential to the understanding of quantum phase transitions. Even the geometric phase that the wave function gains in an adiabatic process - the Berry phase - is ubiquitous in physics and its discussion is included in most of the contemporary quantum mechanics textbooks. The initial formulation of the adiabatic theorem reads as follows: *"A physical system remains in its instantaneous eigenstate if a given perturbation is acting on it slowly enough and if there is a gap between the eigenvalue and the rest of the Hamiltonian's spectrum."*[2]. Which means that: if we consider the hamiltonian system $\mathcal{H}(\boldsymbol{R}(t))$ that depends on some external parameter $\boldsymbol{R}$, then in a process of adiabatic evolution, a system initially in a Hamiltonian eigenstate $|\psi_n(0)\rangle = |n(\boldsymbol{R}(0))\rangle$ will remain in this instantaneous eigenstate, gaining a phase in this process. The parameter $\boldsymbol{R} = \{R_1(t), R_2(t), ...\}$ may vary with the time.

Fock presented an argument [12] that the phase of a quantum state accumulated in the process of adiabatic evolution can always be taken to be unity. However, this result was derived with the assumption of non-cyclic evolution. Surprisingly, a general theory of cyclic evolution was not considered until 1984, when Berry, in his seminal paper[3], proved that a cyclic evolution of a quantum state results in a phase factor of a purely geometric origin and, in principle, is observable. Explicitly, the eigenvalue equation is written as:

$$\mathcal{H}(\boldsymbol{R}(t))|n(\boldsymbol{R}(t))\rangle = E_n(\boldsymbol{R}(t))|n(\boldsymbol{R}(t))\rangle, \tag{2.1}$$

and the time evolution of the system is given by the equation, $i\hbar\partial_t|n(\boldsymbol{R}(t))\rangle = \mathcal{H}(\boldsymbol{R}(t))|n(\boldsymbol{R}(t))\rangle$. The phase factor of the wave function in an adiabatic cyclic evolution, that is $|\psi_n\rangle = e^{i\theta}|n(\boldsymbol{R}(t))\rangle$, can be written in terms of two contributions,

$$\theta = -\frac{1}{\hbar}\int_0^t dt' E_n(\boldsymbol{R}(t)) - i\gamma_n, \tag{2.2}$$

where the first term is associated with the dynamic phase and the second term is a geometric phase known as the Berry phase,

$$\gamma_n = -i \int_{\mathcal{C}} d\boldsymbol{R}(t) \cdot \langle n(\boldsymbol{R}(t)) | \boldsymbol{\nabla}_{\boldsymbol{R}} n(\boldsymbol{R}(t)) \rangle. \tag{2.3}$$

The $\mathcal{C}$ path is the contour traversed by the adiabatic parameter $\boldsymbol{R}$ during the evolution. Interpreting the Berry phase in the configuration space of the parameter $\boldsymbol{R} = \{R_1(t), R_2(t), ...\}$, analogously to the magnetic flux in the real space, we can define a "magnetic vector potential" $\boldsymbol{\mathcal{A}}_n(\boldsymbol{R}(t))$, which is known in the literature as Berry connection,

$$\boldsymbol{\mathcal{A}}_n(\boldsymbol{R}(t)) = -i \langle n(\boldsymbol{R}(t)) | \boldsymbol{\nabla}_{\boldsymbol{R}} n(\boldsymbol{R}(t)) \rangle. \tag{2.4}$$

The Berry connection $\boldsymbol{\mathcal{A}}_n(\boldsymbol{R}(t))$ is obviously gauge-dependent. A gauge transformation $|n'(\boldsymbol{R})\rangle = e^{i\phi}|n(\boldsymbol{R})\rangle$, changes it to:

$$\boldsymbol{\mathcal{A}}'_n(\boldsymbol{R}(t)) = \boldsymbol{\mathcal{A}}_n(\boldsymbol{R}(t)) - \boldsymbol{\nabla}_{\boldsymbol{R}} \phi(\boldsymbol{R}).$$

If we consider a cyclic evolution $\boldsymbol{R}(0) = \boldsymbol{R}(t_f)$, the wavefunction has to be singlevalued $|n'(\boldsymbol{R})\rangle = |n(\boldsymbol{R})\rangle$, therefore we have,

$$\phi(\boldsymbol{R}(0)) - \phi(\boldsymbol{R}(t_f)) = 2\pi\sigma, \tag{2.5}$$

where $\sigma \in \mathbb{Z}$. Thus, the Berry phase can not be removed anymore.

Using the Stocks theorem, we can rewritten the Berry phase in terms of the Berry field (or as it is commonly known Berry curvature) in analogy with the magnetic field,

$$\gamma_n = \int_S d\boldsymbol{s} \cdot \boldsymbol{\Omega}_n(\boldsymbol{R}(t)), \tag{2.6}$$

where S is any surface bounded by the $\mathcal{C}$ path. Once the Berry connection is defined at less than a gradient function, the Berry curvature, $\boldsymbol{\Omega}_n(\boldsymbol{R}(t)) = \boldsymbol{\nabla}_{\boldsymbol{R}} \times \boldsymbol{\mathcal{A}}_n(\boldsymbol{R}(t))$, is gauge-invariant.

The components of the Berry phase can be written as,

$$\Omega^n_{\mu\nu}(\boldsymbol{R}(t)) = i(\langle \partial_\mu n(\boldsymbol{R}) | \partial_\nu n(\boldsymbol{R}) \rangle - \langle \partial_\nu n(\boldsymbol{R}) | \partial_\mu n(\boldsymbol{R}) \rangle) \tag{2.7}$$

where ∂_ν represent ∂_{R_ν}.

Hall conductivity and Chern number

In band theory the Bloch states have an explicit $\boldsymbol{k}$-dependence, which gives a natural parameter to study Berry phase effects [4]. As commented earlier, the conductivity hall is one of the most interesting results so far discovered in condensed matter physics, because allows the observation of a non-zero Berry phase via the conductivity Hall measure. The quantized behavior of this conductivity can not be understood at models that usually describe the electron transport in metals, for instance, the Drude model. Whereas, in the Berry formulation this behavior appears naturally, expressing the topological nature of the insulating state. Used the Kubo formula, which is described in the context of the linear response theory, TKNN found the explicit form of the Hall conductivity[13],

$$\sigma_{Hall} = \xi \sum_{n<E_f} \int_{BZ} \frac{dk_x k_y}{(2\pi)^2} \{\langle \partial_x n_{\boldsymbol{k}} | \partial_y n_{\boldsymbol{k}} \rangle - \langle \partial_y n_{\boldsymbol{k}} | \partial_x n_{\boldsymbol{k}} \rangle\}. \tag{2.8}$$

Using the Eq. 8, the Hall conductivity may be rewrite in terms of the Berry curvature,

$$\sigma_{Hall} = \xi \sum_{n} \int_{BZ} \frac{dk_x k_y}{(2\pi)^2} f_n \boldsymbol{\Omega}^n_{xy}. \tag{2.9}$$

The relation between the Berry curvature and the Berry phase (eq. 6) allows to find the conductivity Hall via a simple calculation,

$$\sigma_{Hall} = \frac{e^2}{2\pi hi} \sum_n f_n \gamma_n = \frac{e^2}{2\pi hi} i2\pi\sigma = \frac{e^2}{h}\sigma = \frac{e^2}{h} C_n$$

where the eq. (5) was used. C_n is knowing as Chern number and the conductivity Hall calculations reduces to finding this topological invariant[16],

$$C_n = \sum_n \frac{f_n}{2\pi} \int_{BZ} d^2k \boldsymbol{\Omega}^n(\boldsymbol{k}) \tag{2.10}$$

In addition to the usual band theory, the band gaps in the insulating state are topologically characterized by the Chern number ($\mathcal{C}$) calculation. This number is necessary to identify the topological class induced by the SOC in magnetic systems and is related to non-trivial Hall conductivity, as already mentioned. Using the expression,

$$\langle \partial_\alpha n'_{\boldsymbol{k}} | n_{\boldsymbol{k}} \rangle = \frac{\langle n'_{\boldsymbol{k}} | \partial_\alpha \mathcal{H}(\boldsymbol{k}) | n_{\boldsymbol{k}} \rangle}{(E_{n'\boldsymbol{k}} - E_{n\boldsymbol{k}})}, \tag{2.11}$$

and introducing a completeness relation ($\sum_{n'} |n'\rangle\langle n'|$) in the eq. (8), the calculation of the Berry phase is reduced to finding the derived of the Hamiltonian operator, eigenvalues and eigenvectors of all bands below the Fermi level,

$$\Omega^{n}_{xy}(\boldsymbol{k}) = -2\text{Im}\sum_{n'\neq n}\frac{\langle n_{\boldsymbol{k}}|\partial_{\boldsymbol{k_x}}\mathcal{H}(\boldsymbol{k})|n'_{\boldsymbol{k}}\rangle\langle n'_{\boldsymbol{k}}|\partial_{\boldsymbol{k_y}}\mathcal{H}(\boldsymbol{k})|n_{\boldsymbol{k}}\rangle}{(E_{n\boldsymbol{k}}-E_{n'\boldsymbol{k}})^2}, \tag{2.12}$$

which is relatively easy to apply to periodic materials described by effective Hamiltonian or even studies via DFT calculations.

In the first-principles calculations, the reciprocal space is discretized by building a grid of $\boldsymbol{k}$-points. In this sense, the calculation of the Chern number using the information obtained from these calculations (Hamiltonian, charge density and wave functions) is not trivial. The Eq. 13 needs to be rewritten to take into account *i*) the discrete space of $\boldsymbol{k}$-points and *ii*) possible degeneracies in the band structure. The Berry curvature written in Eq. 13 is called Abelian Berry curvature, which assumes that the bands are separated between each other by an energy gap. Therefore, if the band structure have degeneracies, the Berry curvature diverges. Such divergences are eliminated by introducing the so-called non-Abelian Berry curvature $\boldsymbol{B}(\boldsymbol{k})$.

In two dimensional systems the Chern number can be calculated within a non-Abelian formulation[16] by the following expression:

$$\mathcal{C} = \frac{1}{2\pi}\int_{BZ}\text{Tr}[\boldsymbol{B}(\boldsymbol{k})]d^2k. \tag{2.13}$$

Where the trace is a summation over the band index, and only the occupied bands are taken into account. The integration is done over the whole Brillouin Zone (BZ), and $\boldsymbol{B}(k)$ is a matrix representing the non-abelian momentum-space Berry curvature, whose diagonal elements can be written as [16]:

$$\begin{aligned}\boldsymbol{B}_n(\boldsymbol{k}) = \lim_{\Delta_{k_y}\to 0}\lim_{\Delta_{k_x}\to 0}\frac{-i}{\Delta_{k_x}\Delta_{k_y}}\text{Im}\ \log[\langle u_{n\boldsymbol{k}}|u_{n\boldsymbol{k}+\Delta_{k_x}}\rangle\langle u_{n\boldsymbol{k}+\Delta_{k_x}}|u_{n\boldsymbol{k}+\Delta_{k_x}+\Delta_{k_y}}\rangle \\ \langle u_{n\boldsymbol{k}+\Delta_{k_x}+\Delta_{k_y}}|u_{n\boldsymbol{k}+\Delta_{k_y}}\rangle\langle u_{n\boldsymbol{k}+\Delta_{k_y}}|u_{n\boldsymbol{k}}\rangle],\end{aligned} \tag{2.14}$$

where Δ_{k_x} (Δ_{k_y}) is the grid displacement in the k_x (k_y) direction of the reciprocal space, $|u_{n\boldsymbol{k}}\rangle$ is the cell-periodic Bloch functions in the ($\boldsymbol{k}$) point of the BZ, and n indicates the band index. This expression is quite adequate to perform calculations in systems with band crossing, and was implemented using a discrete grid in the reciprocal space.

Regarded as the first material in which it was predicted to occur the QSH, the graphene has played an important role in the development of theories that allow the understanding of some phenomena in materials with nontrivial topological phases. We will use this material as an example of the results obtained from the non-abelian Berry curvature implementation and subsequent calculation of the Chern number. In the QSH,

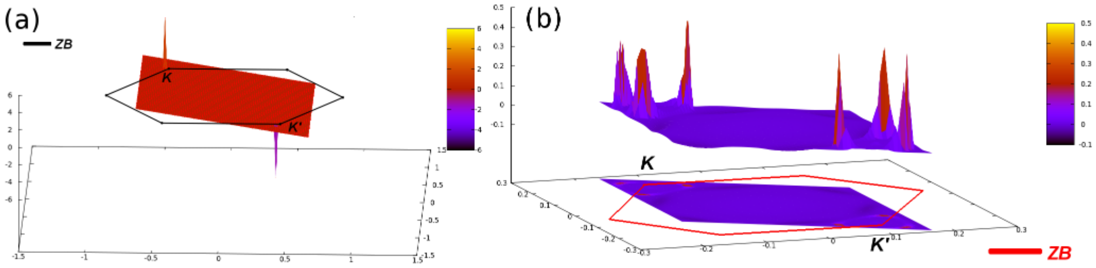

Figure 2.1 - (a) Berry curvature for the pristine graphene. (b) Berry curvature for the Ru@Gr system using a 4×4 graphene supercell. We used arbitrary units.

whereas the charge conductivity is zero, the spin conductivity is non-zero. Thus, as the Chern number corresponds with the number of charge conductivity channels, it is expected that for the graphene, the Chem number is zero. This is verified on the Fig.2.1(a), in which it is evident that the Berry curvature contribution at the points K and K' to the Chern number are cancel each other, resulting in $C_n = 0$. This value was obtained using the implementation done in the SIESTA code associated with the activity 3 of this project.

The transition metals when adsorbed in graphene may be generate a magnetic moment, breaking the time reversal symmetry. It is expected that if there is a spin-orbit transfer via transition metals deposition, the QAH topological phase may be appear with a non-zero Chem number.

In the test stage of the implementation performed, various metals were considered, as an example we present the result of ruthenium atom when adsorbed on a graphene supercell (Ru@Gr). With the implementation developed, it was verified the time reversal symmetry breaking, as shown in the Berry curvature (Fig.2.1(b)). Additionally, a $C_n = -2$ was obtained, which characterize our Ru@Gr system as a QAH. We shown that it is possible to change the topological phase of the graphene through the change of the Ru atoms concentration. This finding has already been published in the Physical Rev B [27].

Time reversal invariant and the quantum spin Hall effect

The easiest way of discovering new topological materials, is the evaluation of an invariant number always associated with a particular symmetry. For systems protected by Time Reversal (TR) symmetry, the invariant characterizing the system is called as Z_2 invariant. How discussed above, when this number is not zero, the system has TR protected metallic edge states. Thus, the presence of an external magnetic field or of magnetic impurities destroys the metallic edge states. In this system the charge conductivity is zero, that is, $C_n = 0$. However, the spin conductivity is not zero, indicating a non-zero Z_2 number.

Likewise the number of Chern, the Z_2 invariant is a bulk property of the system.

The formulation of the Z_2 number follows many differents formulations, being the most famous, via the parity eigenvalues for system with inversion symmetry [22], the formulation via Resta polarization [21], by an integration of the Berry phase over the effective Brillouin zone [17, 18](eq. 1.2), and by the switching of Wannier center of Charges [24] and in another work [25]. When the materials are non-centrosymmetric, the *Ab initio* calculation can give a generic gauge [24] on the states. Therefore, we chosen to calculate Z_2 via the switching of Wannier Center of Charges (WCCs). In that manner, we know that the invariant Z_2 can be written as:

$$Z_2 = P_\Theta(t = T/2) - P_\Theta(t = 0), \tag{2.15}$$

where t represents an adiabatic time. Now we want to rewrite equation (2.15) in terms of the WCCs. For that, we need to define Wannier functions (WF). The WFFs belonging the the same unit cell R have the following format:

$$|Rn\rangle = \frac{1}{2\pi}\int_{-\pi}^{\pi} dk e^{-ik(R-x)}|u_{nk}\rangle. \tag{2.16}$$

A WCC $\overline{x}_n$ is defined as the mean value of $\langle 0n|\hat{X}|0n\rangle$ where $\hat{X}$ is the position operator and $|0n\rangle$ is the state corresponding to a WF in the cell with $R = 0$. So we have:

$$\overline{x}_n = \frac{i}{2\pi}\int_{-\pi}^{\pi} dk\langle u_{nk}|\partial_k|u_{nk}\rangle. \tag{2.17}$$

Assuming that we got $\sum_\alpha \overline{x}_\alpha^S = \frac{1}{2\pi}\oint_{BZ} A^S$ with $S = I, II$, where sumation in α represents occupied states and A the Berry connection, we finally have:

$$Z_2 = \sum_\alpha \left[\overline{x}_\alpha^I(T/2) - \overline{x}_\alpha^{II}(T/2)\right] - \sum_\alpha \left[\overline{x}_\alpha^I(0) - \overline{x}_\alpha^{II}(0)\right]. \tag{2.18}$$

With the smooth gauge condition between $t \in [0, T/2]$ it is possible to track the evolution of WCCs during a half cycle, which is also smooth. It is important to note that this argumentation is only valid when some properties are valid for the construction of the Wannier Functions as pointed by [?]. Now if we have an even or odd number of crossing between half cycle of the WCCs, we are dealing with a trivial or a topological material, i.e Z_2 equal 0 or 1.

Electronic transport in topological insulators: SOC implementation

The SOC is essential for describing systems with NTP, thus our density functional theory and the electronic transport description must take into account this interaction. So the formalism used in the SIESTA code and TRANSAMPA code must also change.

The SOC in the SIESTA code: In order to investigate the NTP systems, in a previous work, we implemented the Spin-Orbit Coupling in the SIESTA code within the on-site approximation[14, 27]. Within this approach, the Kohn-Sham Hamiltonian $\boldsymbol{H}$ is a sum of the kinetic energy $\boldsymbol{T}$, the Hartree potential $\boldsymbol{V}^H$, the exchange and correlation potential $\boldsymbol{V}^{xc}$, the scalar relativistic ionic pseudopotential $\boldsymbol{V}^{sc}$, and the spin-orbit interaction $\boldsymbol{V}^{SOC}$. $\boldsymbol{H}$ can be written as a 2×2 matrix in the spin space as:

$$\boldsymbol{H} = \boldsymbol{T} + \boldsymbol{V}^H + \boldsymbol{V}^{xc} + \boldsymbol{V}^{sc} + \boldsymbol{V}^{SOC} = \left[\begin{array}{cc} \boldsymbol{H}^{\uparrow\uparrow} & \boldsymbol{H}^{\uparrow\downarrow} \\ \boldsymbol{H}^{\downarrow\uparrow} & \boldsymbol{H}^{\downarrow\downarrow} \end{array} \right]. \tag{2.19}$$

All terms contribute to the diagonal elements, however only the $\boldsymbol{V}^{xc}$ and the $\boldsymbol{V}^{SOC}$ potentials have off-diagonal coupling terms due to the non-collinear spin.

From the self-consistent solution of the all-electron Dirac equation for an atom, the procedure to generate the non-relativistic pseudopotential can be extended to take into account the first order relativistic effects. Using projection operators in terms of angular wave function, the relativistic pseudopotential is written as:

$$\begin{aligned} \hat{V}_{ps}^{ion} &= \hat{V}_{sc} + \hat{V}_{SO} \\ &= \sum_{l,m} \left[V_{sc}^l(\boldsymbol{r}) \boldsymbol{I}_\sigma + V_{SO}^l(\boldsymbol{r}) \boldsymbol{L} \cdot \boldsymbol{S} \right] |l, m\rangle \langle l, m| \, , \end{aligned}$$

where $\boldsymbol{I}_\sigma$ is the identity operator in the spin space,

$$V_{SOC}^l(\boldsymbol{r}) = \frac{2}{2l+1} \left[V_{ps}^{(l+\frac{1}{2})}(r) - V_{ps}^{(l-\frac{1}{2})}(r) \right] \tag{2.20}$$

and

$$V_{sc}^l(\boldsymbol{r}) = \frac{1}{2l+1} \left[(l+1) V_{ps}^{(l+\frac{1}{2})}(r) + l V_{ps}^{(l-\frac{1}{2})}(r) \right]. \tag{2.21}$$

The spin-orbit matrix elements are written as:

$$V_{ij}^{SOC} = \frac{1}{2} V_{l_i,n_i,n_j}^{SOC} \langle l_i, M_i | \boldsymbol{L} \cdot \boldsymbol{S} | l_i, M_j \rangle \delta_{l_i l_j}, \tag{2.22}$$

where $|l_i, M_j\rangle$ are the real spherical harmonics[15]. The radial contributions $V_{l_i,n_i,n_j}^{SOC} = \langle R_{n_i,l_i} | V_{l_i}^{SOC} | R_{n_j,li} \rangle$ are calculated with the solution of the Dirac equation for each atom. The angular contribution $\boldsymbol{L} \cdot \boldsymbol{S}$, considering the spin operator in terms of the Pauli matrices, can be written as:

$$\boldsymbol{L} \cdot \boldsymbol{S} = \left[\begin{array}{cc} L_z & L_- \\ L_+ & -L_z. \end{array} \right]. \tag{2.23}$$

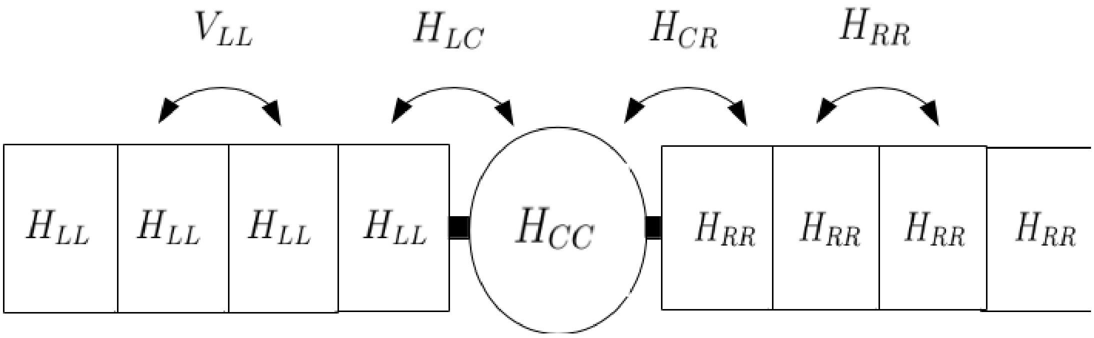

Figure 2.2 - Scheme of the electronic transport model in a common device.

The diagonal matrix elements for the SOC term $V_{ij}^{SOC,\sigma\sigma}$ (with $\sigma = \uparrow$ or $\downarrow$), are proportional to $\langle l_i, M_i|L_z|l_j, M_j\rangle$, which are different from zero only for $M_i = \pm M_j$. Thus, these terms couple orbitals with the same spins, and same $|M|$. On the other hand, the off-diagonal matrix elements $V_{ij}^{SOC,\sigma-\sigma}$ are proportional to $\langle l_i, M_i|L_\pm|l_j, M_j\rangle$, and thus couple orbitals with different spins and $M_i = M_j \pm 1$. These coupling terms could open bandgaps or generate the inversion of states that are essential to the physics of the topological insulators.

Electronic Transport

Typical devices are composed of a left and a right electrodes (L and R) interconnecting through a scattering region, exactly as shown in Fig2.2.

In the formalism that will be presented, it is necessary that all the electrons feel the same potential, as occurs in the KS equations. Thus, according to the diagram, the Hamiltonian has a local form given by:

$$H = \begin{bmatrix} H_L & H_{LC} & 0 \\ H_{LC}^\dagger & H_{CC} & H_{CR}^\dagger \\ 0 & H_{CR} & H_R \end{bmatrix}. \tag{2.24}$$

The matrices H_L and H_R are semi-infinite, and given by:

$$H = \begin{bmatrix} \ddots & & \vdots & \\ & H_{LL} & V_{LL}^\dagger & 0 \\ \vdots & V_{LL} & H_{LL} & V_{LL}^\dagger \\ & 0 & V_{LL} & H_{LL} \end{bmatrix};$$

$$H = \begin{bmatrix} H_{RR} & V_{RR}^{\dagger} & 0 & \\ V_{RR} & H_{RR} & V_{RR}^{\dagger} & \cdots \\ 0 & V_{RR} & H_{RR} & \\ & \vdots & & \ddots \end{bmatrix}$$

The equations above presuppose the use of a set of base functions located $\{\phi_\mu(\vec{r})\}$. The modelling of the problem considers that the distance between the right and left electrodes is higher than the cutoff of the radius, r_c, of these orbitals. The Hamiltonian matrix elements H_{LR} and the overlap S_{LR} that engaging the left electrode to the right electrode are null, as shown in eq. 25. At this point it is worth noting that the system has no translational symmetry, and thus is no longer possible to use the Bloch theorem, reducing the infinite problem to many finite problems. To address this problem is used the formalism of non-equilibrium Green's functions. Thus, it is defined the Green function $G(E)$ through the expression $[ES - H]G(E) = 1$, the matrix elements depends on the energy E. In this expression, $S \int \phi_\mu^*(\vec{r})\phi_\nu(\vec{r})d^3r$ is the overlap matrix.

In this formalism, the retarded and advance Green function are calculated using the equations

$$\begin{aligned} [E^+S - H]G^r(E) &= 1; \\ [E^-S - H]G^\alpha(E) &= 1, \end{aligned}$$

respectively. $E^\pm = E \pm i\delta$ is a complex numbers with a infinitesimal imaginary part δ. From the Hamiltonian we obtain the relations:

$$\begin{aligned} G_{LC}^r &= -g_L^r(E^+S_{LC} - H_{LC})G_{CC}^r \\ G_{RC}^r &= -g_R^r(E^+S_{CR} - H_{CR})G_{CC}^r, \end{aligned} \tag{2.25}$$

$g_{L(R)}^r = (E^+S_{L(R)} - H_{L(R)})^{-1}$ is the surface Green function of the left electrode (right) $H_{L(R)}$. Substituing the equations 10, it is obtain a expression for the central part of G^r, given by:

$$G_{CC}^r = [E^+S_{CC} - H_{CC} - \Sigma_L - \Sigma_R]^{-1}$$

where $\Sigma_{L(R)}$ are the auto-energies of the left (right) electrode, describe as:

$$\begin{aligned} \Sigma_L &= -(E^+S_{LC} - H_{LC}^\dagger)g_L^r(E^+S_{LC} - H_{LC}) \\ \Sigma_R &= -(E^+S_{CR} - H_{CR}^\dagger)g_R^r(E^+S_{CR} - H_{CR}) \end{aligned} \tag{2.26}$$

If instead of E^+ we used E^-, we will found the advance Green function G_{CC}^α in a simmilar way. G_{CC}^r is a fundamental quantity in the electronic transport theory using the non-equilibrium Green function. The auto-energies include in the central region the effect of the inifinite electrodes. These quantities are finite matrices, and in this manner the problem previously formulated is computationaly addressed.

Within the Landauer-Büttiker formalism using the Wingreen and Mei formula, the expression for the current is given by:

$$I = \frac{e^2}{h} \int_{E=-\infty}^{\infty} T(E)[f_{FD}(E-\mu_L) - f_{FD}(E-\mu_R)]dE \tag{2.27}$$

$f_{FD}(E)$ is the Fermi-Dirac function, and the transmittance $T(E)$ is written as:

$$T(E) = T_r[\Gamma_L(E) G^{\alpha}_{CC}(E) \Gamma_R(E) G^{r}_{CC}(E)], \tag{2.28}$$

where we use the definitions $\Gamma_{L(R)} = i(\Sigma_{L(R)} - \Sigma^{\dagger}_{L(R)})$. In the above equations it is assumed that the left electrode has a chemical potential μ_L, while the right electrode has a chemical potential μ_R. In this approach, the system is composed of non-interacting electrons. $\Sigma_{L(R)}$ are denominated coupling matrices and are a measure of the electrodes interaction with the scattering region. The function $T(E)$ is defined as the transmittance. This is interpreted as the probability of an electron that has energy E be transmitted from the left electrode to the right electrode through the central region (Fig.2.2). The most important energy region of $T(E)$ occurs when $\mu_L < E < \mu_R$, because in this energy region $f_{FD}(E-\mu_L) - f_{FD}(E-\mu_R) \neq 0$, with contribution to the current.

Currently, this formalism has been widely used in conjunction with the DFT, generating several relevant results to the scientific community. In this way, using the Khon-Sham Hamiltonian are calculated currents and transmittances. It is noteworthy that there is no formal support for using the Khon-Sham Hamiltonian for this type of calculation. But if it is done, the level of approximation is the same used in a energy bands calculation generated from the Khon-Sham spectrum. The SOC mixture the spin components, and therefore when considering the SOC, the Hamiltonian should be rewritten and the formalism is essentially analog, however, it is necessary to consider the presence of terms that allow the spin flip and the spin direction, which is done in this work.

From this theory, we implemented the interaction in the TRANSAMPA code for the electronic transport study. First tests were made in 3D topological insulator and in two-dimensional systems, including pristine graphene. As it is known the intrinsic SOC of carbon atoms is too small. However, in my master's work I developed a tool to study the change in the electronic properties of crystalline systems in relation to the variation of SOC. If we increase the SOC of the intrinsic triple carbon atoms, only as a way to test our implementation, the SOC opens a gap, though very little, sufficient to be observed in the transmittance of the system, as shown in Fig. 2.3a.

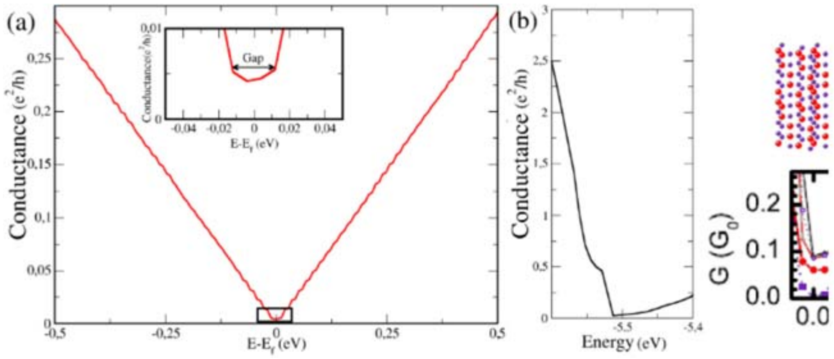

Figure 2.3 - (a) Transmittance of the pristine graphene with triple of the spin-orbit interaction. (b) Conductance of the Bi2Se3 - 4QL. On the right side the results obtained using the implementation made in this work, on the left side the geometry used and the results obtained in [26]. In the conductance obtained in this reference are shown several curves corresponding with the system qualitative behavior when the bulk is perturbed

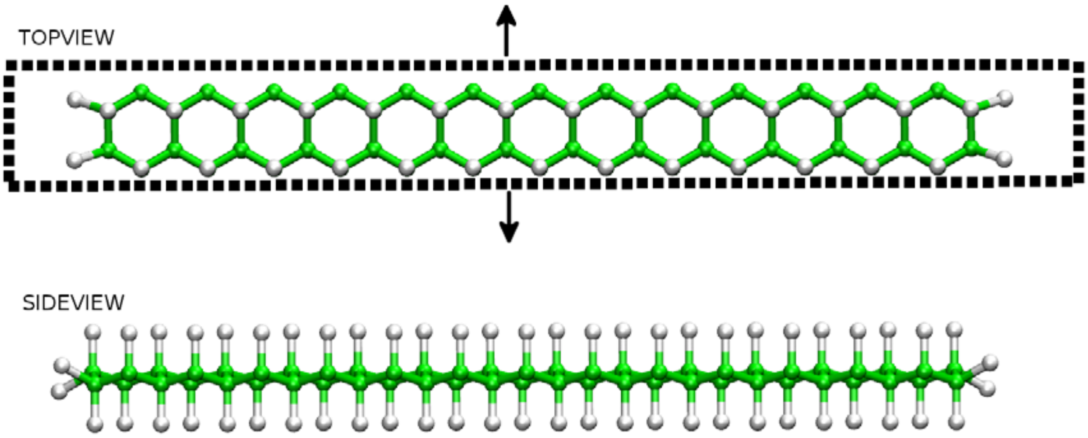

Figure 2.4 - Geometry of a Zig-zag nanoribbon of fluorized Germanene. The arrows indicate the nanoribbon periodicity direction.

As a test our implementation to study the electronic transport in systems with nontrivial topological phases, we make a qualitative comparison of the conductance curve using Bi2Se3 TRANSAMPA with SOC and the results reported in the literature. The conductance obtained with the TRANSAMPASOC code (right side) and the curve obtained in the reference [26] (left side) are shown in Fig. 2.3b. In these simulations, we used the same geometry illustrated in Fig. 2.3b.

Electronic transport in Germanene Nanoribbons:

Although it is an ongoing study, the most relevant preliminary results of the electronic transport in nanoribbons systems with nontrivial topological phases will be presented. In Fig. 2.4 it is shown the geometry of a nanoribbon germanene with fluorine. As expected, due to topological properties of the 2D bulk of the germanene and the increment the SOC

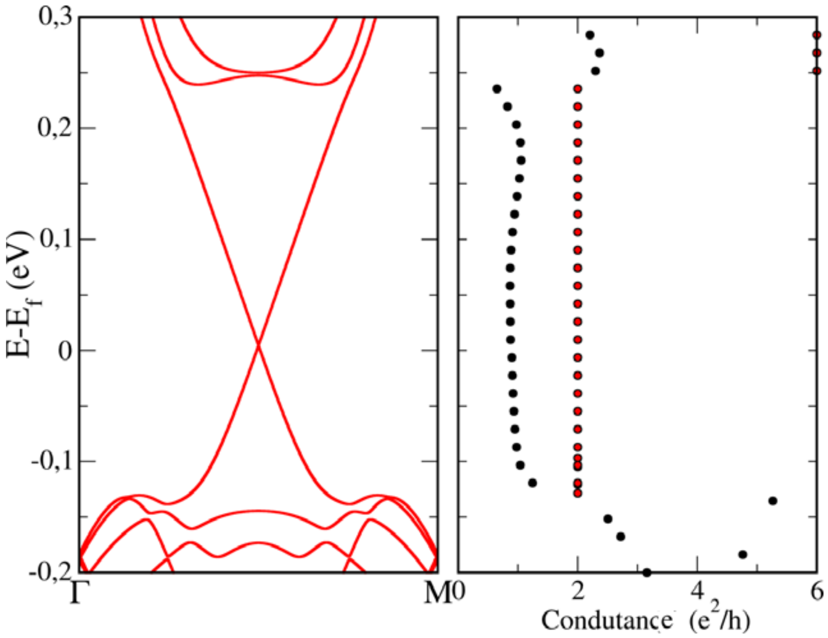

Figure 2.5 - Band structure of the Zig-zag nanoribbon of fluorized Germanene shown in Fig. 2.4 and the transmittance of the system. The black and red dots represent the transmittance associated with an edge and the total transmittance, respectively.

when including fluorine, it is clear the formation of a Dirac cone in the band structure of the system (Fig. 2.5). This Dirac cone is formed by an intersection of opposite spin bands, so that the Dirac cone is topologically different from Dirac cone in the pristine graphene.

We implemented a tool which allows to separate the transmittance-spatial regions in which the wave function is fully located. Thus, the conductivity channels can be separated (this remembering that the transmittance of the matrix only depends on trace). Using this tool, we get the transmittance to one of the edges systems (black dots in Fig. 2.5b), showing that there is one conductivity channel whose spin is well defined. This transmittance is half of the total transmittance (red dots in Fig. 2.5b).

Bibliography

[1] Soluyanov, Alexey A., Vanderbilt David Kalelkar, Mohan Rabe Karin, Wu Weida, Mele Eugene, Rutgers University, Graduate School - New Brunswick. Topological aspects of band theory. *xiv*, 159, 2012.

[2] C. L. Kane and E. J. Mele, “Z 2 topological order and the quantum spin Hall effect”, *Phys. Rev. Lett.*, **95**, 146802, 2005.

[3] M. V. Berry, “Quantal phase factors accompanying adiabatic changes”, *Proc. R. Soc. Lon. A*, **392** 1802, 45–57 (1984).

[4] J. Zak, “Berry’s phase for energy bands in solids”, *Phys. Rev. Lett.*, **62**, 2747–2750 (1989).

[5] R. D. King-Smith and David Vanderbilt, “Theory of polarization of crystalline solids”, *Phys. Rev. B*, **47**, 1651–1654 (1993).

[6] Raffaele Resta, “Macroscopic polarization in crystalline dielectrics: the geometric phase approach”, *Rev. Mod. Phys.*, **66**, 899–915 (1994).

[7] D. J. Thouless, M. Kohmoto, M. P. Nightingale, and M. den Nijs, “Quantized Hall conductance in a twodimensional periodic potential”, *Phys. Rev. Lett.*, **49**, 405–408 (1982).

[8] F. D. M. Haldane, “Berry curvature on the Fermi surface: Anomalous Hall effect as a topological Fermi-liquid property”, *Phys. Rev. Lett.*, **93**, 206602 (2004).

[9] F. D. M. Haldane, “Model for a quantum Hall effect without Landau levels: Condensed-matter realization of the parity anomaly”, *Phys. Rev. Lett.*, **61**, 2015–2018 (1988).

[10] C. L. Kane and E. J. Mele, “Quantum spin Hall effect in graphene”, *Phys. Rev. Lett.*, **95**, 226801 (2005).

[11] Y. Aharonov and D. Bohm, “Significance of electromagnetic potentials in the quantum theory”, *Phys. Rev.*, **115**, 485–491 (1959).

[12] A. Bohm, A. Mostafazadeh, H. Koizumi, Q. Niu, and J. Zwanziger, The Geometric Phase in Quantum Systems, Springer, 2003.

[13] Thouless, Kohmoto, Nightingale-den and Nijs (TKNN), *Phys. Rev. Lett.* **49**, 405–408 (1982).

[14] L. Fernandez-Seivane, M. A. Oliveira, S. Sanvito, and J. Ferrer, J. of Phys.: Condens. Matter 18, 7999 (2006).

[15] M. A. Blanco, M. Flrez, and M. Bermejo, *J. Mol. Struct.* **419**, 19 (1997).

[16] A. A. Soluyanov and D. Vanderbilt, *Phys. Rev. B* **85**, 115415 (2012).

[17] Fukui Takahiro and Hatsugai Yasuhiro 2007 *Journal of the Physical Society of Japan***76**, 053702.

[18] Fukui Takahiro, Fujiwara Takanori and Hatsugai Yasuhiro 2008 *Journal of the Physical Society of Japan***77**, 123705.

[19] Resta Raffaele and Vanderbilt David 2007 *Physics of Ferroelectrics* 31-68.

[20] Moore J. and Balents L. 2007 *Physical Review B***75** 121306

[21] Liang Fu and C. L. Kane 2006 *Physical Review B* **74**, 195312.

[22] Fu Liang and Kane C. 2007 *Physical Review B* **76**, 045302.

[23] Kane C. L. and Mele, E. J. 2005 *Physical Review Letters* **95**, 146802.

[24] Yu Rui, Qi Xiao Liang, Bernevig Andrei, Fang Zhong and Dai Xi 2011 *Physical Review B* **84**, 075119

[25] Liu Jianpeng and Vanderbilt David 2013 *Physical Review B* **88** 224202.

[26] Xue-Feng Wang, Yibin Hu, and Hong Guo. Robustness of helical edge states in topological insulators. *Phys. Rev. B* **85**, 241402(R).

[27] C. Mera Acosta, Matheus P. Lima, R. H. Miwa, Antônio J. R. da Silva, and A. Fazzio. Topological phases in triangular lattices of Ru adsorbed on graphene: Ab initio calculations. *Phys. Rev. B* **89**, 155438 (2014).

3. Completing the two-dimension honeycomb-lattice family: new kind of s-d type band inversion based materials

Introduction

The QSH effect was first proposed in a honeycomb lattice formed by carbon atoms: graphene [1, 2, 3, 4]. However, in graphene the band gap opened by the intrinsic spin-orbit coupling (SOC) is very small, making experimental observations extremely difficult [5]. Until now, the search for novel QSHIs has been focused on increasing the intrinsic SOC effects in graphene [6, 7, 8, 9] and finding alloy materials that present ions *i*) with high atomic number, *ii*) located between columns IIB to VIA of the Periodic Table, and *iii*) arranged on a network with hexagonal symmetry [10, 11, 12, 13, 14, 15]. Considering these three issues, those materials can be understood as systems with strong SOC effects, formed by atoms that in the pristine 3D structure are usually Zinc blende semiconductors described by s and p orbitals. Although these materials have been intensively studied, the complete family of binary honeycomb compounds formed by atoms that also stabilize the Zinc blende structure is still incomplete. In fact, this family can be extended to all possible atomic combinations that have eight electrons in the valence shells, and not only restricted to s-p semiconductors.

Much effort has been invested in the synthesis of graphene-type IV-materials, not only in the techniques but also in the control of intrinsic impurities (See Fig. 3.1) [16]. We believe that it is possible to extend the list of fabricated compounds of this material family. For instance, following the first experimental realization of graphene, other ultrathin materials have been studied, the most representative group is the heavy group-IV elements Si, Ge and Sn. Two-dimensional buckled Si-based silicene has been recently realized by molecular beam epitaxy growth [16], whereas germanene was obtained by molecular beam epitaxy and mechanical exfoliation [17]. The free-standing fabrication process is represented in Fig. 3.1. Recently, the fabrication of 2D stanene by molecular beam epitaxy has also been reported [18].

Naturally, honeycomb materials are an extremely good platform for novel phenomena and devices, not only because of the known topological properties but also because of the recent electric resistivity measurement suggesting superconductivity in graphene [19, 20, 21]. Indeed, grephene bylayer are also predicted to be superconductor [22, 23], and functionalized honeycomb compound can exhibit large topological band gaps [24]. As will be presented in the next chapters, a double topological protection can lead to interesting

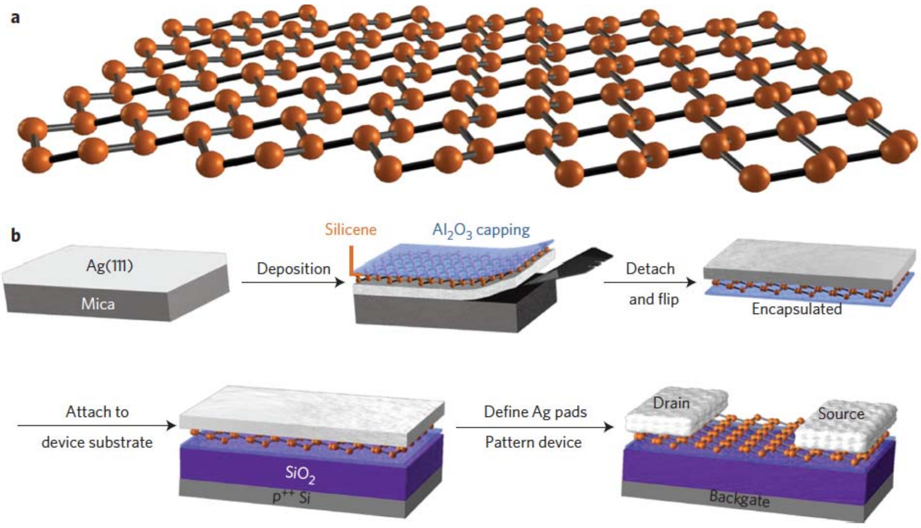

Figure 3.1 - Figure from Nature Nanotechnology 10, 227 (2015): (a) Buckled honeycomb lattice structure of silicene. (b) Silicene encapsulated delamination with native electrode process, which includes the following key steps: epitaxial growth of silicene on crystallized Ag(111) thin film, in situ Al2O3capping, encapsulated delamination transfer of silicene, and native contact electrode formation to enable back-gated silicene transistors.

phenomena for applications in spintronics. We find that these systems can also host this type of behavior, however, these results are not discussed in this thesis. Specifically, we will focus initially on the prediction of honeycomb-lattice material and the study of their electronic properties using DFT calculations and tight-binding models.

In this chapter, we extend the family of honeycomb-lattice materials: among all binary Zinc blend semiconductor AB there is only one mechanically stable system that have not been studied in the respective two-dimensional honeycomb-lattice. Specifically, we study binary compounds AB formed by coinage metals and halogens, i.e., $A =$ IB and $B =$ VIIA in the Periodic Table. Coinage metals are interesting due to their high reactivity at low dimensions, widely studied for catalysis purposes. According to the d-band center theory,[25] the reactivity trend is linked to the position of the d-band with respect to the Fermi energy: the closer the d-band center, the more reactive the metal. For the case of metals from the IB group, Ag is more inert than Cu and Au.[26] Based on the coinage metal reactivity and the mechanical stability of Zinc blende IB-VIIA compounds, e.g. AuI, the two-dimensional honeycomb lattice version of the IB-VIIA atomic combinations could exist. To the best of our knowledge, the band inversions reported until now in honeycomb lattice are those involving the following levels: a) s-p [27, 28, 29] b) p-p [30] c) d-p [31] d) d-f [32, 33] e) d-d [34, 35].

Here, we propose a new family of materials: coinage metal halides in single layer honeycomb structures. We found that most of these compounds are thermodynamically

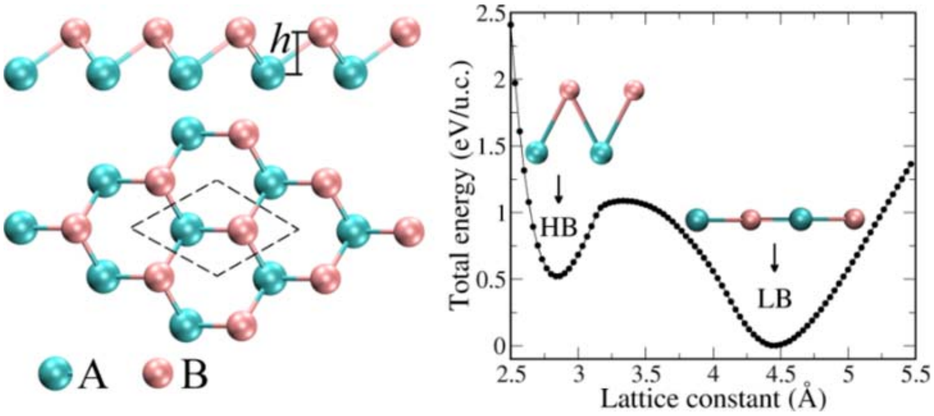

Figure 3.2 - (left) Side and top view of the coinage metal halides atomic structure; unit cell is marked with slash line. (right) Total energy as a function of the lattice parameter for the AuBr compound. The HB and LB structures are represented in the respective minimum energy.

and mechanically stable. All the systems containing Au atoms (AuF, AuCl, AuBr, and AuI), as well as CuF, feature protected edge states. As transition metals are involved, *d* orbitals play an important role: these new topological insulators present a band inversion of an unreported type: *s*-*d*, and have sizable band gaps between 0.03 eV and 0.29 eV. To better understand the *s*-*d* band inversion, we also develop an effective tight-binding model describing the IB-VIIA compounds, which allows band structure calculations for large nanoribbons.

Geometry and mechanical properties

All calculations were performed within the Density Functional Theory approach [36] as implemented in the Vienna Ab-initio Simulation Package (VASP).[37, 38] The interaction between valence electrons and ions was performed through the full-relativistic Projector Augmented Wave method,[39] and for the selection of the plain waves an energy cutoff of 450 eV was chosen to describe the atomic orbitals. For exchange and correlation, the Generalized Gradient Approximation in the Perdew-Burke-Ernzerhof [40] implementation was used. The sampling of the first Brillouin zone for the 2D structures was performed using a 40x40x1 grid centered at the Γ point. Phonon spectra were obtained by using DFT perturbation theory as implemented in the Phonopy code.[41] Z2 invariant of the materials were obtained following the methodology proposed by Vanderbilt et al.[42] as implemented in the Z2Pack code.[43]

In total, we have studied twelve systems, combining a coinage metal ion (A=Cu,Ag,Au) with an halogen (B=F,Cl,Br,I). They all are non-centrosymmetric, i.e., do not preserve the inversion symmetry, and have C_{3v} symmetry with two different atoms by unit cell, as depicted in Fig. 3.2. Graphene-like materials can have two structural phases, usually clas-

Material	a (Å)	E_f (eV/at)	E_c (eV/at)	E_g (eV)	MS	Z_2
CuF	3.49	-0.763	-3.177	0.10	yes	1
CuCl	3.89	-0.380	-2.890	1.09	yes	0
CuBr	4.12	-0.269	-2.652	1.01	yes	0
CuI	4.38	-0.175	-2.490	1.34	yes	0
AgF	3.94	-0.833	-2.754	1.04	yes	0
AgCl	4.37	-0.411	-2.427	1.73	yes	0
AgBr	4.56	-0.356	-2.245	1.65	yes	0
AgI	4.80	-0.292	-2.113	1.57	yes	0
AuF	3.95	-0.104	-2.273	0.29	no	1
AuCl	4.30	+0.068	-2.198	0.27	yes	1
AuBr	4.49	+0.035	-2.103	0.23	yes	1
AuI	4.71	-0.041	-2.111	0.03	yes	1

Table 3.1 - Structural and electronic properties of coinage metal halides. Values show lattice constant a, formation energy per atom, cohesion energy per atom, energy band gap, mechanical stability (MS) and Z2 invariant.

sified in terms of the length of the buckled format as high buckled (HB) and low buckled (LB). [44] Whereas HB graphene-like materials are usually metallic,[44] e.g., hexagonal tin and lead, LB compounds are generally insulator and always have a highest lattice constant, e.g., silicene, germanene, BN, AlAs, AlSb, GaP, InP, GaAs, InAs, GaSb, InSb and blue phosphorene.[45, 46, 47] All coinage metal halides stabilize the LB structure, as represented in Fig. 3.2 for the AuBr compound. The lattice parameters for the twelve structures are shown in Table 3.1. On these layers, negative charge is located near atom B, while positive densities are found around ion A.

To analyze the thermodynamic stability of the systems, the formation energy per atom was calculated as

$$E_f = \frac{E_{AB} - E_A - 1/2E_{B_2}}{2} \tag{3.1}$$

where E_{AB} is the total energy of the unit cell, E_A is the energy of a coinage metal atom in the most stable bulk phase and E_{B_2} is the energy of the diatomic halogen molecule in vacuum. Of all the systems, only AuCl and AuBr resulted with positive formation energy, which means that most of them would spontaneously form without the need of extra energy (see Table 3.1). However, kinetics may play a significant role in the growth process and even the materials with positive formation energy could be achieved with the proper synthesis method.

On the other hand, the cohesion energy could be estimated as

$$E_c = \frac{E_{AB} - E_A^{at} - E_B^{at}}{2} \tag{3.2}$$

where E_A^{at} and E_B^{at} are the energies of isolated atoms A and B, respectively. The fact that

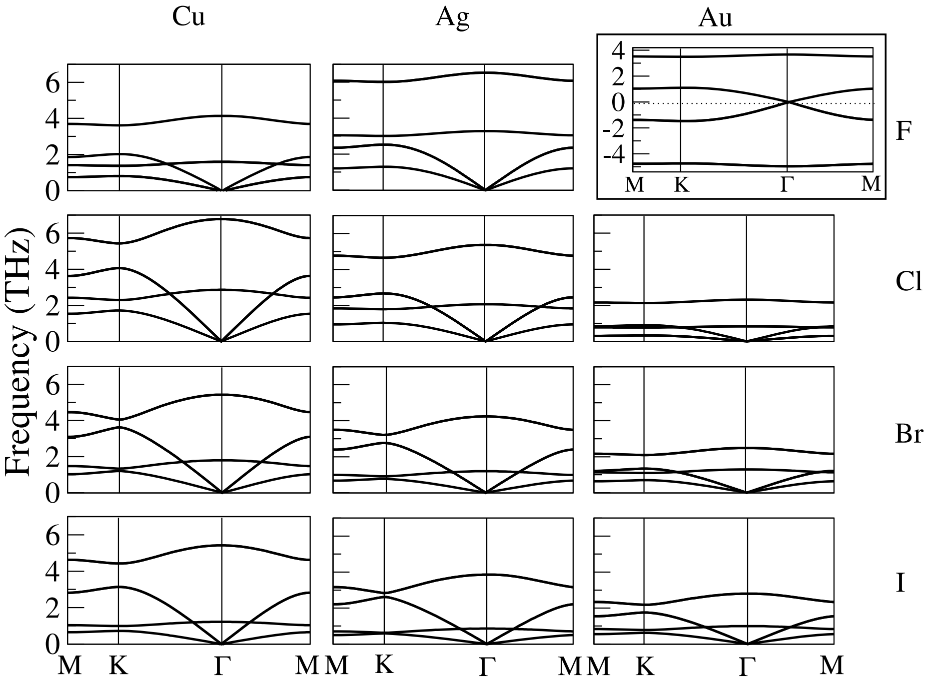

Figure 3.3 - Phonon spectra of coinage metal halides. The x-axis (y-axis) corresponds to the atoms A (B). Inset: AuF is the only material which is mechanically non-stable.

negative values are obtained for all the systems means that they are thermodynamically stable when compared to the atomized compounds. The mechanical stability can be studied through the calculation of the phonon spectra. Negative frequencies were not observed in most of the systems, indicating that the proposed materials are mechanically stable after formation. The only exception is AuF. The phonon spectra are shown in Fig. 3.3.

Electronic structure and band inversion

The first indication of the QSH effect comes from the inspection of the band structure of the bulk material (the 2D infinite sheet). We performed the corresponding calculations with and without SOC inclusion. According to our results, it is straightforward to separate the materials into two groups: *i*) large gaped semiconductors (in this group we include CuCl, CuBr, CuI and all silver halides); after SOC inclusion there are no relevant changes in the band structure, and *ii*) band inverted semimetals before including SOC (here we include CuF and all gold halides); SOC inclusion opens a band gap in Γ. To go deeper in this analysis, we have calculated the band structures projected on the atomic orbitals. In Fig. 3.4 we show the projected band structure for AuBr as an illustrative case of the band inversion, which takes place before including the SOC, i.e., the topological classification does not depend on the intrinsic atomic SOC.

The band inversion is dominated by orbitals belonging to the atom A, but the inter-

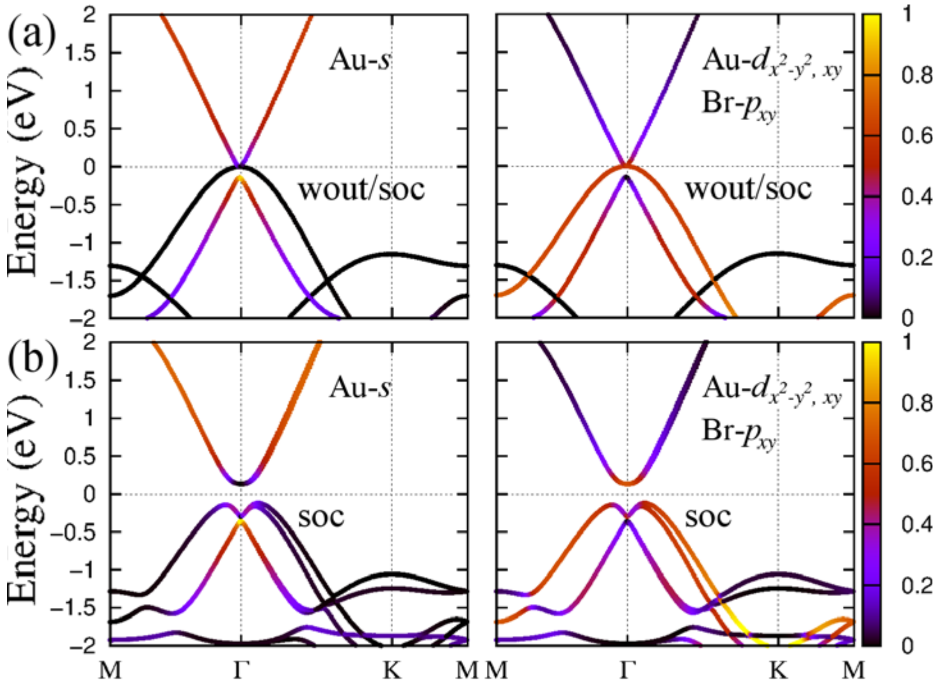

Figure 3.4 - Projected band structures without (a) and with (b) SOC for AuBr showing the levels near the Fermi energy. The color code stands for the weight of the atomic contribution of the p_{xy}^{Br} and $d_{xy,x^2-y^2}^{\mathrm{Au}}$ orbitals (right), and the s^{Au} orbitals (left) for each k-point and band index.

action between them is mediated by the atom B, as represented in Fig. 3.5. Specifically, the band inversion occurs between s orbitals and d_{xy,x^2-y^2} orbitals of the atom A (see Fig. 3.4) (with small contributions of $p_{x,y}$ levels of ion B). In the band inverted systems, the s level of A lies lower in energy than the d_{xy,x^2-y^2} levels (See Fig. 3.5). The SOC is then responsible for the band gap opening (see Fig. 3.4b), leading to the QSH effect. This band gap opens at Γ, different from other honeycomb materials, in which it is located at the K-point in the Brillouin zone. Regardless the high atomic SOC of the B atoms, this interaction is not strong enough to invert the band order in large gaped semiconductors of group i). The in-plane spin polarization due to the rotation symmetry R_3 and the Rashba SOC splitting due to the spacial symmetry breaking is obtained in all QSHIs, but the relatively low spin splitting avoids the unconventional spin texture protecting the bulk states [48].

Tight-binding effective model and protected edge states

Helical metallic edge states are the most interesting feature in the QSHIs. It is instructive to address the study of these states by using an effective tight-binding model that satisfies the symmetry operation of the Γ point, since it allows for insights on the s-d band inversion and the study of larger nanoribbons. According to the symmetry op-

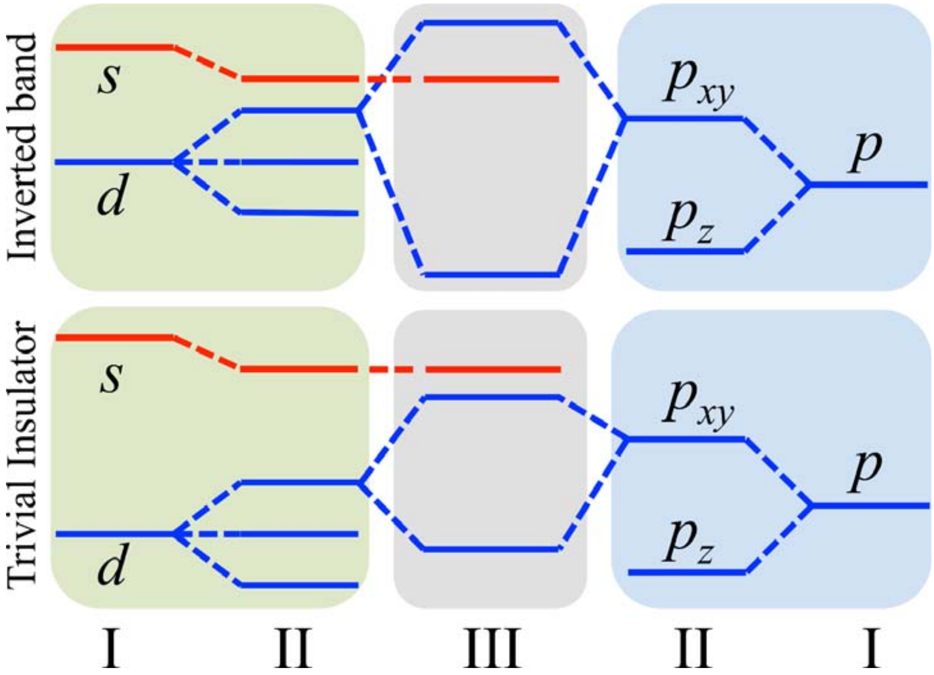

Figure 3.5 - Schematic representation of the atomic orbitals (I) and the two-dimensional confinement effects (II) for the atoms A (green area) and B (blue area). The interaction between orbitals involved in the band inversion (III) is shown in the gray area for trivial and QSH insulators before including SOC.

eration, the wavefunction at Γ is given by the $\{|\Lambda_J, j_z\rangle\}$ effective states, where J is the total angular momentum, j_z is the projection along the z axis, and Λ corresponds to the A and B atomic contributions. These states preserve the total angular momentum by construction. For instance, the $|\Lambda_{3/2}, \pm 3/2\rangle$ effective states are a linear combination of the $p_+ = p_x + ip_y$ and $p_- = p_x - ip_y$ effective orbitals.

The states involved in the band inversion at the Γ point are described by the effective states $\{|A_J, j_z\rangle\}$ (with J=1/2 for s-orbitals, and J=3/2 for states combining p- and d-orbitals) and hence, we wrote the tight-binding Hamiltonian using the full SOC basis $\{|A_{1/2}, \pm 1/2\rangle, |A_{3/2}, \pm 3/2\rangle\}, |A_{3/2}, \pm 1/2\rangle\}$. The tight-binding Hamiltonian matrix elements are then given by:

$$[\mathcal{H}(\vec{k})]_{ij} = \varepsilon_0^{ij}\delta_{ij} + \sum_{\nu=1}^{6} t_{\vec{a}_\nu}^{ij} e^{i\vec{k}\cdot\vec{a}_\nu}, \tag{3.3}$$

where $i = (A, J, j_z)$, $j = (A, J', j'_z)$ and ε_0 is the on-site energy. Since the contribution of the effective states $|B_J, j_z\rangle$ is not relevant near the Fermi energy, we omit terms associated with the nearest neighbors (atoms B). Hence, $t_{\vec{a}_\nu}^{ij} = \langle \vec{n}, A_J, j_z|H|\vec{a}_\nu, A_{J'}, j'_z\rangle$ represents the next nearest neighbor hopping terms, with $\vec{n}$ indicating the lattice site and $\vec{a}_\nu$ corresponding to the ν-th of the six next nearest neighbor vectors. These hopping terms

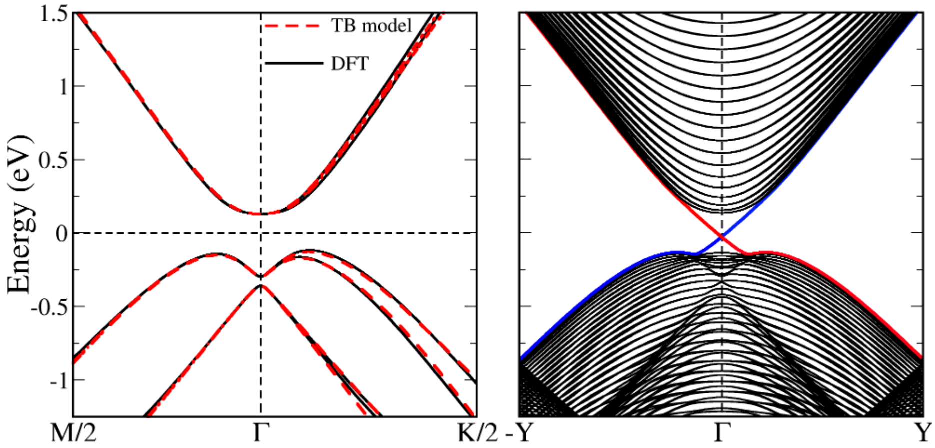

Figure 3.6 - (left) Tight-binding model (red) and DFT (black) band structures of the AuBr compound. (right) Band structure computed using the proposed tight-binding model for an armchair nanoribbon of 273.6 Å of thickness (60 unit cells). Up (down) spin projection is represented in red (blue).

are related to each other and are uniquely determined, through the relevant symmetry operations of the C_{3v} point group, namely: *i*) threefold rotation symmetry R_3 along the z axis, *ii*) reflection respect to the mirror plane $\mathcal{M}_x$ ($x \rightarrow -x$), and *iii*) the TR-symmetry $\mathcal{T}$. Specifically, the effective states $\{|\Lambda_J^\tau, j_z\rangle\}$ are transformed by the symmetry operators as

1. *Threefold rotation* R_3:

$$\begin{aligned} |\Lambda_J, \pm 1/2\rangle \rightarrow & e^{\pm \frac{i\pi}{3}} |\Lambda_J, \pm 1/2\rangle \,, \\ |\Lambda_J, \pm 3/2\rangle \rightarrow & - |\Lambda_J, \pm 3/2\rangle \,. \end{aligned}$$

2. *Mirror symmetry* $\mathcal{M}_x$:

$$\begin{aligned} \left|\Lambda_{J=1/2}, \pm 1/2\right\rangle \rightarrow & - i \left|\Lambda_{J=1/2}, \mp 1/2\right\rangle \,, \\ \left|\Lambda_{J=3/2}, \pm 1/2\right\rangle \rightarrow & i \left|\Lambda_{J=3/2}, \mp 1/2\right\rangle \,, \\ \left|\Lambda_{J=3/2}, \pm 3/2\right\rangle \rightarrow & i \left|\Lambda_{J=3/2}, \mp 3/2\right\rangle \,. \end{aligned}$$

3. *Time Reversal* $\mathcal{T}$:

$$\begin{aligned} |\Lambda_J, \pm 1/2\rangle \rightarrow \pm |\Lambda_J, \mp 1/2\rangle \,, \\ \left|\Lambda_{J=3/2}, \pm 3/2\right\rangle \rightarrow \mp \left|\Lambda_{J=3/2}, \mp 3/2\right\rangle \,. \end{aligned}$$

We simplified the matrix elements of the Hamiltonian by taking the limit $\vec{k} \rightarrow \Gamma$. Considering expansion in k up to second order, the Hamiltonian $\mathcal{H}(\vec{k} \rightarrow \Gamma)$ in the full

SOC basis $\{|A_{1/2}, \pm 1/2\rangle, |A_{3/2}, \pm 3/2\rangle\}, |A_{3/2}, \pm 1/2\rangle\}$ reads

$$\mathcal{H}(\vec{k}) = \begin{pmatrix} -\varepsilon_{11} + \xi_{11}k^2 & 0 & -\overline{\gamma}_{13}k_+ & i\gamma_{14}k_+ & 0 & \overline{\gamma}_{16}k_- \\ 0 & -\varepsilon_{11} + \xi_{11}k^2 & -i\gamma_{14}k_- & -\overline{\gamma}_{13}k_- & \overline{\gamma}_{16}k_+ & 0 \\ -\overline{\gamma}_{13}k_- & i\gamma_{14}k_+ & \varepsilon_{33} - \xi_{33}k^2 & i\alpha_R^{3/2}k_- & i\gamma_{35}k_- & -\overline{\gamma}_{36}k_- \\ -i\gamma_{14}k_- & -\overline{\gamma}_{13}k_+ & -i\alpha_R^{3/2}k_+ & \varepsilon_{33} - \xi_{33}k^2 & -\overline{\gamma}_{36}k_+ & -i\gamma_{35}k_+ \\ 0 & \overline{\gamma}_{16}k_- & -i\gamma_{35}k_+ & -\overline{\gamma}_{36}k_- & \varepsilon_{55} - \xi_{55}k^2 & 0 \\ \overline{\gamma}_{16}k_+ & 0 & -\overline{\gamma}_{36}k_+ & i\gamma_{35}k_- & 0 & \varepsilon_{55} - \xi_{55}k^2 \end{pmatrix},$$

where $k_\pm = k_x \pm ik_y$, $k^2 = k_x^2 + k_y^2$, $\gamma_{ij} = 3a\Re[t^{ij}]$, and $\overline{\gamma}_{ij} = 3a\Im[t^{ij}]$. Here, the band inversion is intrinsically introduced by the signs of the on-site term $\varepsilon_{ii} = \varepsilon_0^{ii} + 6\Re[t^{ii}]$ and the quadratic term $\xi_{ii} = 3a^2\Re[t^{ii}]/2$. Since the Rashba parameter for the effective states $\{|A_{1/2}, \pm 1/2\rangle$ and $|A_{3/2}, \pm 1/2\rangle\}$ is near zero, we select, without loss of generality, $\alpha_R^{1/2} = 0$. Thus, the spin splitting due to the breaking of the inversion symmetry is taken into account by the Rashba effect of the state $|A_{3/2}, \pm 3/2\rangle\}$. These parameters are obtained via least squares standard approach in order to match the DFT calculation. This simple model leads to a very well approximated description of the DFT band structure around the Γ point, as shown in Fig. 3.6.

In the known buckled honeycomb-lattice systems, such as germanene and silicene among others, the nearest neighbor hopping terms are essential for its description [11, 49]. However, in the proposed compounds, the atom B only mediates the interaction between the atoms A and its effect is successfully introduced within the next nearest neighbor hopping terms. Topological transitions can also arise as a consequence of atomic interactions [50]. Here, the atoms B modify the interatomic distance and hence, the interaction between the atoms A.

We verified the presence of edge states when cutting a one dimensional AuBr nanoribbon 273.6 Å width armchair terminated. Periodic boundary condition assures the infinity of the system in the other direction. When plotting the electronic band structure in the direction of the ribbon, gapless levels appear. The spin polarization on the metallic levels of the ribbon shows that the conduction is spin resolved: up and down spins propagate in opposite directions, assuring dissipationless transport.

The topological invariant Z2 was obtained through the computation of the Wilson loop by following the evolution of the Wannier Charge Centers (WCC), as explained in Chapter 2. The results confirm that the materials first included in group *ii*) (CuF and all gold halides) are topological Insulators with Z2=1. For the remaining layers Z2 is equal to zero. The most important results for the monolayers are summarized in Table 3.1. It is remarkable the fact that the size of some of the band gaps would allow room temperature functionality for these materials.

Conclusion

In conclusion, we have studied 2D coinage metals halides in a single layer honeycomb structure. Twelve systems were considered, which could be separated into two well defined groups: trivial insulators (CuCl, CuBr, CuI and silver halides) and five new Topological Insulators (CuF and gold halides). We focus on the fact that three of these materials have negative formation energies and could be synthesized without extra energy. However, many growing techniques would allow the formation of all of them, even those with endothermic processes. Moreover, if these systems are synthesized, the phonon spectra showed that four of them would be mechanically stable. Of particular interest is the size of the electronic bandgaps, which allow functionality even at room temperatures, an essential request for real electronic applications.

Bibliography

[1] M. Z. Hasan and C. L. Kane, Rev. Mod. Phys. **82**, 3045 (2010).

[2] L. Kou, Y. Ma, Z. Sun, T. Heine, and C. Chen, The Journal of Physical Chemistry Letters **8**, 1905 (2017).

[3] Y. Ren, Z. Qiao, and Q. Niu, Reports on Progress in Physics **79**, 066501 (2016).

[4] C. L. Kane and E. J. Mele, Phys. Rev. Lett. **95**, 226801 (2005).

[5] S. Konschuh, M. Gmitra, and J. Fabian, Phys. Rev. B **82**, 245412 (2010).

[6] C. Weeks, J. Hu, J. Alicea, M. Franz, and R. Wu, Phys. Rev. X **1**, 021001 (2011).

[7] J. Hu, J. Alicea, R. Wu, and M. Franz, Phys. Rev. Lett. **109**, 266801 (2012).

[8] Y. Li et al., Phys. Rev. B **87**, 245127 (2013).

[9] C. M. Acosta, M. P. Lima, R. H. Miwa, A. J. R. da Silva, and A. Fazzio, Phys. Rev. B **89**, 155438 (2014).

[10] C.-C. Liu, W. Feng, and Y. Yao, Phys. Rev. Lett. **107**, 076802 (2011).

[11] C.-C. Liu, H. Jiang, and Y. Yao, Phys. Rev. B **84**, 195430 (2011).

[12] F.-C. Chuang et al., Nano Letters **14**, 2505 (2014).

[13] L. Li, X. Zhang, X. Chen, and M. Zhao, Nano Letters **15**, 1296 (2015).

[14] X. Li et al., Nano Research **8**, 2954 (2015).

[15] S. Murakami, Phys. Rev. Lett. **97**, 236805 (2006).

[16] Guy Le Lay, Nature Nanotechnology volume **10**, 202 (2015).

[17] María Eugenia Dávila, and Guy Le Lay Scientific Reports **6**, 20714 (2016).

[18] Feng-feng Zhu, Wei-jiong Chen, Yong Xu, Chun-lei Gao, Dan-dan Guan, Can-hua Liu, Dong Qian, Shou-Cheng Zhang, and Jin-feng Jia Nature Materials **14**, 1020 (2015).

[19] D. Pesin and A. H. MacDonald, Nature Materials **11**, 409 EP (2012).

[20] Y. Fan and K. L. Wang, SPIN **06**, 1640001 (2016).

[21] A. Manchon, H. C. Koo, J. Nitta, S. M. Frolov, and R. A. Duine, Nature Materials **14**, 871 EP (2015).

[22] Yuan Cao, Valla Fatemi, Shiang Fang, Kenji Watanabe, Takashi Taniguchi, Efthimios Kaxiras, and Pablo Jarillo-Herrero Nature volume **556**, 43 (2018).

[23] Yuan Cao, Valla Fatemi, Ahmet Demir, Shiang Fang, Spencer L. Tomarken, Jason Y. Luo, Javier D. Sanchez-Yamagishi, Kenji Watanabe, Takashi Taniguchi, Efthimios Kaxiras, Ray C. Ashoori, and Pablo Jarillo-Herrero Nature volume **556**, 80 (2018).

[24] Yong Xu, Binghai Yan, Hai-Jun Zhang, Jing Wang, Gang Xu, Peizhe Tang, Wenhui Duan, and Shou-Cheng Zhang Phys. Rev. Lett. **111**, 136804 (2013).

[25] B. Hammer and J. Nørskov, Surface Science **343**, 211 (1995).

[26] C.-Y. Syu, H.-W. Yang, F.-H. Hsu, and J.-H. Wang, Phys. Chem. Chem. Phys. **16**, 7481 (2014).

[27] M. König et al., Science **318**, 766 (2007).

[28] C. Liu, T. L. Hughes, X.-L. Qi, K. Wang, and S.-C. Zhang, Phys. Rev. Lett. **100**, 236601 (2008).

[29] I. Knez, R.-R. Du, and G. Sullivan, Phys. Rev. Lett. **107**, 136603 (2011).

[30] H. Zhang et al., Nat. Phys. **5**, 438 (2009).

[31] M. Yang and W.-M. Liu, Scientific Reports **4**, 2045 (2014).

[32] M. Dzero, K. Sun, V. Galitski, and P. Coleman, Phys. Rev. Lett. **104**, 106408 (2010).

[33] X. Zhang, H. Zhang, J. Wang, C. Felser, and S.-C. Zhang, Science **335**, 1464 (2012).

[34] H. Weng et al., Phys. Rev. B **92**, 075436 (2015).

[35] C. Si, J. You, W. Shi, J. Zhou, and Z. Sun, J. Mater. Chem. C **4**, 11524 (2016).

[36] P. Hohenberg and W. Kohn, Phys. Rev. **136**, B864 (1964).

[37] G. Kresse and J. Hafner, Phys. Rev. B **47**, 558 (1993).

[38] G. Kresse and J. Furthmüller, Phys. Rev. B **54**, 11169 (1996).

[39] P. E. Blöchl, Phys. Rev. B **50**, 17953 (1994).

[40] J. P. Perdew, K. Burke, and M. Ernzerhof, Phys. Rev. Lett. **77**, 3865 (1996).

[41] A. Togo and I. Tanaka, Scr. Mater. **108**, 1 (2015).

[42] A. A. Soluyanov and D. Vanderbilt, Phys. Rev. B **83**, 235401 (2011).

[43] D. Gresch et al., Phys. Rev. B **95**, 075146 (2017).

[44] P. Rivero, J.-A. Yan, V. M. García-Suárez, J. Ferrer, and S. Barraza-Lopez, Phys. Rev. B **90**, 241408 (2014).

[45] S. Cahangirov, M. Topsakal, E. Aktürk, H. Şahin, and S. Ciraci, Phys. Rev. Lett. **102**, 236804 (2009).

[46] H. L. Zhuang, A. K. Singh, and R. G. Hennig, Phys. Rev. B **87**, 165415 (2013).

[47] Z. Zhu and D. Tománek, Phys. Rev. Lett. **112**, 176802 (2014).

[48] C. Mera Acosta, O. Babilonia, L. Abdalla, and A. Fazzio, Phys. Rev. B **94**, 041302 (2016).

[49] V. Zólyomi, J. R. Wallbank, and V. I. Fal'ko, 2D Materials **1**, 011005 (2014).

[50] Lei Wang, Xi Dai and X. C. Xie, EPL (Europhysics Letters) **98**, 5 57001 (2012).

4. Machine learning: understanding topological transitions in two-dimensional half-functionalized materials using compressed-sensing

Introduction: Compressed-sending and materials science

The predicted honeycomb-lattice QSH insulators in the last chapter are an example of the fundamental role of the computational simulations in the prediction of new materials and the devices design. Indeed, nowadays the computational simulations based on DFT calculations is at the heart of the material sciences. This approximation has been essentially used to understand physical and chemical phenomena in real materials that can potentially be utilized for a certain function. One of the usual approaches starts with a trial-and-error learning process to find new materials and then, employing DFT calculations, verify if the proposed materials satisfy the required property. These calculations typically have a high computational cost, and hence, the trial-and-error learning process is not usually feasible. For instance, nowadays the prediction of new stable TIs through DFT calculations requires to verify the inverted band gap and to calculate the topological invariant for each TI candidate. For its part the verification of the inverted bandgap require the electronic structure calculation with and without SOC, and finding the topological invariants involves the wavefunction computation for all filled electronic states. Thus, it is evident that this trial-and-error learning process have a high computational cost.

Physical intuition and experience suggest that many important material properties are primarily determined by just a few key variables. From my point of view, the phenomena satisfying this premise can be classified into three groups in terms of how these key variables are determined. *i*) Numerical correlations found when analyzing the limits of phenomenologically established theories. An example that has taken on great relevance in recent years is the BCS theory, from which the correlation between the superconducting gap and the critical temperature of these systems is derived. This relation presented in Fig. 4.1a is one of the most impressive and strong result in condensed matter physics. *ii* Feature spaces that separate different phases of the same system, e.g., solid, liquid and gas phases of water (See Fig. 4.1b). This example also includes systems that have different behaviors in relation to the same property, e.g., non-superconductors and superconductors. An relevant example of that is the classification of the water phases in terms of two features: temperature and pressure. Obviously, this is different from the numerically correlation discussed above. *iii* Finally, the last class of properties considered here is the

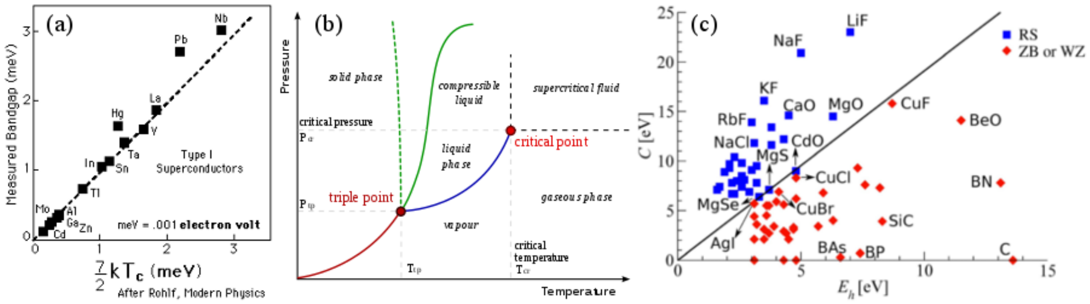

Figure 4.1 - (a) Experimental superconductor of the band gap as a function of the critical temperature. The dashed line represents the predicted values from BCS theory. Some homopolar compounds are indicated by the labels. (b) Classification of the matter stable phases in terms of the temperature and pressure. The critical temperatures and pressures given the phase transitions are indicated by the dashed lines. The solid lines stand for the divided the map of phases according to experimental results. The triple point, i.e., the state in which the solid, liquid and vapor can simultaneously exist, is indicated by the red dot. (c) Experimental ground-state structures of 68 octet binary compounds, arranged according to the two-dimensional descriptor introduced by Phillips. C and E_h are the the experimental dielectric constant and nearest-neighbor distance in the crystal, respectively [1].

derived relations from numerical or experimental results. One of the most illustrative examples of this class (that is no part of material science) is the Keppler's laws, derived from the observation of Thycho Brahe. In material science, the classification of structure according to the most stable phase for a given combination of atoms is one of the most representative examples of this third class. This particular problem was first addressed by Phillips in 1970, proposing that binary systems can be classified by visual inspection of the 2D plot into Zinc blend and Rocksalt structures. The axes of this plot are defined by the experimental dielectric constant and nearest-neighbor distance in the crystal, as represented in Fig. 4.1c. Clearly, these properties require the experimental measurement and in many cases, they also require *a priori* knowledge of the most stable structure, which naturally does not allow a systematic classification of the binary structures.

In the ideal scenario a systematic research of TI materials would allow to build models involving a few atomic variables to predict new inverted bandgap systems without additional DFT calculations. However, with some exceptions, the key variables determining the behavior of a certain property are not known. For instance, the relations between atomic properties and a non-trivial bandgap are not known, if they exist. Although the SOC is fundamental to obtain TI systems, the relation between the atomic SOC and the inverted bandgap behavior is not clear.

Since the amount of calculated data to find systems with a specific property increase exponentially with time, the "big-data of materials science" is a good strategy to over-come the problem of computational cost and to build predictive models. This statistical learning focuses on finding the actuating mechanisms of a certain property or function and describing it in terms of a set of physically meaningful parameters (henceforth termed descriptor). Ghiringhelli et. al., put forward the requirements for a suitable descriptor and demonstrated how a meaningful descriptor can be systematically found[1]:

a) A descriptor uniquely characterizes the material as well as property-relevant elementary processes.

b) Materials that are very different (similar) should be characterized by very different (similar) descriptor values.

c) The determination of the descriptor must not involve calculations as intensive as those needed for the evaluation of the property to be predicted.

d) The dimension of the descriptor should be as low as possible (for a certain accuracy request).

In order to find the descriptors, $d_{p_j,i}$, correlated with a certain property, P_j, associated with the j-th material within a group of N systems, we can use simple relations between the vector of properties, $\boldsymbol{P} = \{P_1, P_2, ..., P_N\}$, and the matrix represented the values of the descriptors, $\boldsymbol{D}$. In this matrix, the elements of the N rows are the possible descriptors $\boldsymbol{d}_{p_j} = \{d_{p_j,1}, d_{p_j,2}, ..., d_{p_j,\Omega}\}$ for the property P_j. Since usually the number of possible descriptors, Ω, is greater than N (the number of samples of material property P), even in the most simple relation, $\boldsymbol{P} = \boldsymbol{Dc}$, we need to solve an underdetermined linear system of equations. Remarkably, in many situations of practical relevance, solve this problem is still possible, in sharp contrast to conventional wisdom. Resolve this problem is the role of a recent theory formulated for sensing and compressing signals (e.g. data) simultaneously - the *compressed sensing* theory.

Compressed sensing relies on two principles[2]: sparsity and incoherence. The sparsity means that when data have a sparse expansion, one can discard the small coefficients without much perceptual loss. Formally, in our example, consider P_S obtained by keeping only the terms corresponding to the S largest values of (c_i) in the expansion. A vector is sparse in a strict sense when all but a few of its entries are zero; we will call S-sparse such objects with at most S nonzero entries[2]. On the other hand, the coherence measures the largest correlation between any two elements of $\boldsymbol{P}$ and $\boldsymbol{d}_{p_j}$. If $\boldsymbol{P}$ and $\boldsymbol{d}_{p_j}$ contain correlated elements, the coherence is large. Otherwise, it is small. As for how large and how small, it follows from linear algebra that $\mu(\boldsymbol{P}, \boldsymbol{d}_{p_j}) \in [1, \sqrt{n}]$. Compressed sensing is mainly concerned with low coherence pairs. For example, the time-frequency pair have the maximal incoherence[2]. Thus, the sinusoids signals and the Fourier coefficients obtained in a magnetic resonance (MR) spectroscopy are one of the most relevant applications of the compressed sensing theory. The returning MR spectroscopy signal is composite of many different signals of, for example, neuronal metabolites, which is resolved into individual resonance frequencies and their relative amplitudes (abundance) by the Fourier transform[3]. In practice to recover a signal from noisy data we use l_1 minimization with relaxed constraints for reconstruction[4]:

$$\min \quad \|\boldsymbol{c}\|_{l_1} \qquad \text{subject to} \quad \|\boldsymbol{Dc}-\boldsymbol{P}\|_{l_2} \leq \varepsilon, \tag{4.1}$$

where ε bounds the amount of noise in the data and the l_p norm is defined as:

$$\|\boldsymbol{A}\|_{l_p} = \left(\sum_i |\boldsymbol{A}|^p\right)^{1/p}. \tag{4.2}$$

Problem (3) is often called the least absolute shrinkage and selection operator (LASSO) problem and can be rewritten as[5]:

$$\arg\min \quad \|\boldsymbol{Dc}-\boldsymbol{P}\|_{l_2} + \lambda\|\boldsymbol{c}\|_{l_1}. \tag{4.3}$$

The larger we choose $\lambda > 0$, the smaller the l_1 norm of the solution of Eq. (3) and vice versa.

Quite generally, a mathematical theorem proven by Candes et al.,[6] guarantees that with an overwhelming probability, any sparse signal with S nonzero components can be recovered from $M \sim S\ln N$ random measurements, where N is the total number of sensing basis functions[4]. This very powerful result is the mathematical foundation of compressed sensing. For this reason such concept has a wide range of applications in various fields of signal processing. Based on the compressive sensing concepts, Prof. Scheffler's group has developed a code to systematically find the adequate descriptor associated with a certain material property.

The main goal of this work is finding suitable descriptors for TI based on the compressed sensing concepts to construct predictive models for these systems. K. Yang, et al.[7] propose the descriptor $\mathcal{X}_{TI} = -\frac{E_k^{SOC}(a_0)/a_0}{\delta E_k^{noSOC}(a)/\delta a|_{a_0}}$ to systematically find TIs, where E_k^{SOC} and E_k^{SOC} are the bandgap with and without SOC, respectively, and a and a_0 are the lattice constant and the equilibrium lattice constant, respectively. Calculating the value of this descriptor for a material requires the same DFT calculations than the evaluation of the inverted bandgap in a trial-and-error learning process. Therefore, the descriptor $\mathcal{X}_{TI}$ does not satisfy c), and hence, does not represent a gain. Additionally, this descriptor does not uniquely characterizes the topological insulator phase, because it ignores the among of band inversions[1]. Thus, the problem of finding an meaningful descriptor for TIs and the causality of the learned descriptor-inverted bandgap (i.e. SOC-inverted band gap) relation is an unsolved problem. Using compressed sensing concepts

---

[1] An even number of band inversion can results in a trivial topological insulator.

would be a novel approach in topological materials field.

Delimitation of the problem

The crossing of energy bands in condensed matter has been theoretically studied since the formulation of quantum mechanics [8]. Now with the experimental realization of graphene and topological insulators, the fundamental physics and possible applications that are hosted in linear band crossings have been intensively studied. Already in 1985, Volkow and Pankratov [9] showed that interfacing two semiconductors with mutually inverted bands can lead to massless Dirac fermions, i.e., linear electronic dispersion relations that cross (inversion) and connect conduction and valence bands. If this inversion occurs at a reciprocal space point that obeys time reversal (TR) symmetry, the respective boundary states associated to different spins must exhibit opposite momentum, which in turn forbids backscattering [10, 11, 12]. Quantum spin Hall insulators (QSHI) are two-dimensional topological insulators (TIs) [13, 14] that intrinsically exhibit this property, i.e., that feature a band inversion at TR-symmetry protected reciprocal-space points. In graphene, for instance, this band inversion is driven by spin-orbit coupling (SOC), which formally leads to a minute band-gap opening [15, 16]. In close analogy to charge pumping in the integer quantum Hall effect [17], the spin-charge pumped through the edge states is quantized in QSHIs [18]. The respective integer quantum, i.e., the topological Z_2 invariant, is 1 in QSHIs and 0 in trivial insulators. Formally, this Z_2 invariant is defined via the half Brillouin zone integral

$$Z_2 = \frac{1}{2\pi}\left[\oint_{\partial\tau} \mathcal{A}(\boldsymbol{k})dl - \int_{\tau} \mathcal{F}(\boldsymbol{k})d\tau\right] \mod (2) \tag{4.4}$$

over the Berry connection $\mathcal{A}(\boldsymbol{k})$ and Berry curvature $\mathcal{F}(\boldsymbol{k})$ [19, 18]. This can be interpreted as the effective magnetic flux of a self-induced magnetic field, the Berry curvature, through the half BZ τ. Here, $\partial\tau$ is the contour of τ. Although theory predicted a wide variety of QSHIs [11, 10], only few of them feature a large enough intrinsic bulk bandgap at finite temperatures to allow for an experimental characterization, e.g., bilayer Bi [20, 21] as well as HgTe/CdTe [22, 23, 24] and InAs/GaSb quantum wells [25, 26]. So far, the computational search for new QSHIs has been a numerically costly trial-and-error process that required to compute the Z_2 invariant for each individual compound, since no simple rule of thumb exists that allows to *a priori* distinguish trivial from topological insulators. Naturally, the search for new QSHIs was thus guided by experience and intuition, e.g., by focusing on heavy elements with high SOC [27, 28, 29, 30]. For instance, 17 potential TIs could be identified by carrying out high-throughput electronic band structure calculations for 60,000 materials [31]. In the same spirit, high-throughput studies in this field have been performed using semi-empirical descriptors as a guidance, e.g., the derivative of the bandgap with no SOC with respect to the lattice constant [32].

In this work, we first compute the Z_2-invariant for a representative set of materials from first principles, identifying 45 QSHI compounds that have not yet been reported in literature. Using a recently compressed sensing approach [33, 34, 35] based on compressed sensing, we then derive a “map” of these materials, in which metals, trivial insulators, and QSHIs are separated in different spatial domains. The axes of this map are given by a physically meaningful descriptor, i.e., a non-linear analytic function that only depends on the properties of the material’s constituent atoms, but not on the properties of the material itself. The identified descriptor is proportional to the ”matallicity”, revealing that orbital interaction can drive a band inversion in compounds with relatively light elements and thus low SOC. Furthermore, we are also able to predict the topological character of materials without performing any additional first-principles calculations, just by evaluating their position on the “map”. By this means, we predict 74 additional novel QSHI candidates.

First-principles Classification of Functionalized 2D Honeycomb-Lattice Materials

For each of these systems, we have first determined the equilibrium lattice constant by relaxing both the atomic positions and the unit-cell shape until the residual forces on the atoms were smaller than 0.01 eV/Å using the all electron, full potential numeric atom centered orbitals based electronic structure code *FHI-aims* [55, 56, 57, 58]. For the equilibrium configuration, the topological invariant Z_2 was computed from the evolution of the Wannier center of charge [59, 60, 61] that we implemented in FHI-aims using the band structures and wavefunctions. For these latter properties, SOC was accounted for using a second-variational, second-order perturbation approach recently implemented in FHI-aims [62] first used in Ref.[63]. For a qualitative analysis of the band inversion mechanism, projected band structures were computed. All calculations were performed using the Perdew-Burke-Ernzenhof (PBE) generalized gradient approximation[64], the Tkatchenko-Scheffler Van der Waals correction method (DFT-TS) [65], and with numerical settings that guarantee a convergence of <1 meV for the eigenvalues. Specifically, periodic boundary conditions were used: the 2D hexagonal monolayers lie in the xy-plane, and a vacuum of 20Å was used in the z-direction to avoid the undesirable interaction between the periodic images of sheets. Futhermore, “really tight” numerical settings and basis sets as well as a 40×40×1 $\vec{k}$ point grid for the Brillouin zone were used.

In a first step, we investigate the topological character of various functionalized 2D honeycomb-lattice materials ABX_2 (see Fig. 4.2) by computing their Z_2 invariant from first principles. Here, we consider all possible combinations AB that are isoelectronic with graphene (group IV-IV, III-V, and II-VI). For each compound AB, functionalization with four different group VII elements (X either Cl, Br, F, or I) is considered, so that 220 different honeycomb-lattice systems ABX_2 are investigated in total. This material

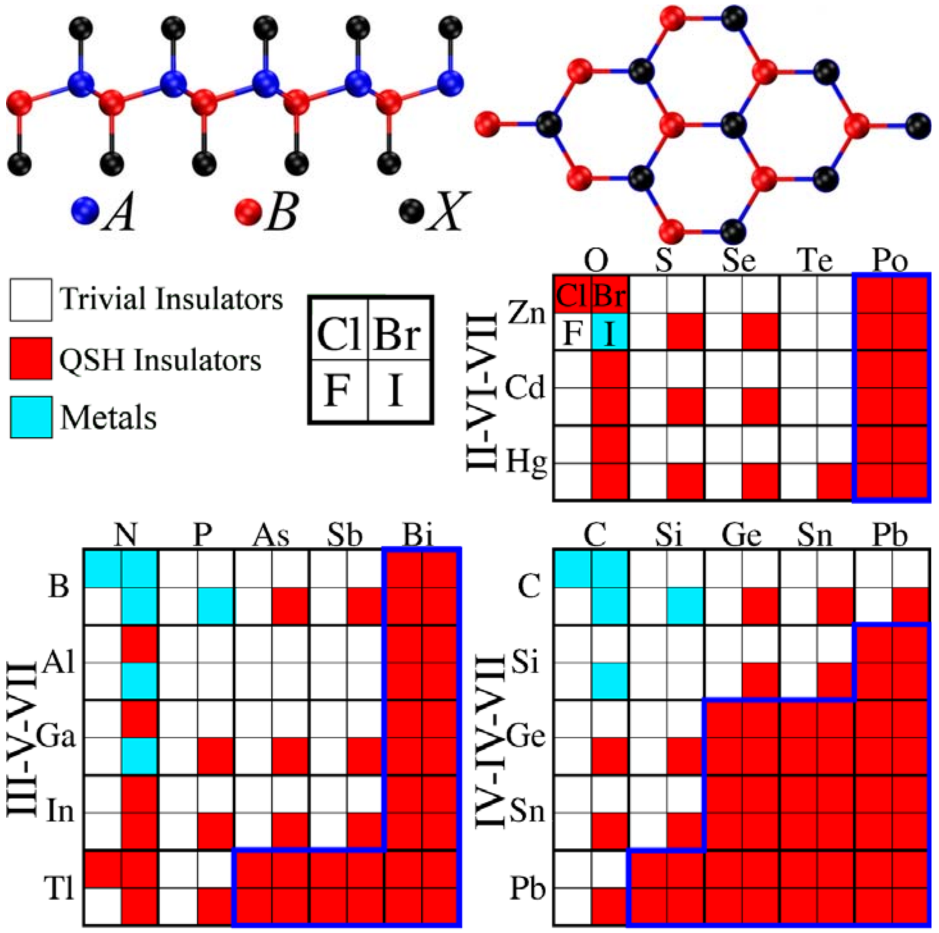

Figure 4.2 - Side and top view of the functionalized honeycomb-lattice system. Classification (trivial insulators: white; QSHIs: red; metals: cyan) of the 220 investigated ABX_2 compounds. The x and y axes denote the A and B atoms. For each combination AB, the four individual squares correspond to a different functionalization with a group VII element (see legend). Compounds for which the topological character is independent of X are grouped by a blue line.

class was chosen since compounds that form a diamond structure in 3D can potentially also behave like graphene in 2D. Accordingly, it has been topic of research in this field before [36, 37, 38], so that various QSHI candidates have been found in this material class already, e.g., functionalized stanene [39].

The resulting first-principles classification of these 220 compounds in metals (zero bandgap), trivial insulators (non-zero bandgap and $Z_2 = 0$), and QSHIs (non-zero bandgap and $Z_2 = 1$) is shown in Fig. 4.2. 103 compounds are identified to be QSHIs in our calculations: In most cases (66%), the TI character is independent of the actual functionalization, as highlighted in blue in Fig. 4.2. These 68 functionalization-independent (FI) QSHIs consist of relatively heavy elements, feature topological bandgaps between 5 meV and 2 eV, and include 15 new QSHIs and 53 QSHIs reported in literature before, e.g., functionalized stanene, germanene, Bi_2, GaBi, InBi, TlBi [38, 39, 40, 41, 42, 43, 44, 45, 46, 47, 48]. Additionally, we also identify 35 QSHIs (34% of all QSHIs), for which the TI character depends on the actual functionalization (mostly iodides). These functionalization-dependent (FD) QSHIs with topological bandgaps between 5 meV and 1 eV include 30 compounds that have not yet been reported in literature, e.g., $AlNBr_2$ and $GaAsI_2$. Quite surprisingly, these TIs consist of relatively light elements and thus defy the widespread reasoning that a strong SOC and thus heavy elements are required to induce a topological transition.

Descriptor Identification via Compressed Sensing

To learn a descriptor for the Z_2-invariant material property, we employed the compressed-sensing approach recently developed by Ouyang *et al.*[35], which mainly consists of two steps: *i*) construction of feature space (potential descriptors) by building analytical functions of the input parameters (atomic properties with SOC, in the case studied here), by iteratively applying a set of chosen algebraic operators, up to a certain complexity cutoff (number of applied operators). The used input atomic parameters are the eigenvalues of the highest occupied and lowest unoccupied Kohn-Sham states ϵ^{ho} ϵ^{lu}, the atomic number Z, the electron affinity EA, the ionization potential IP, and the size of the s, p, and d orbitals (r_s, r_p, and r_d), i.e., the radii where the radial probability density of the valence s, p, and d orbitals are maximal, for A, B and X. Consequently, the feature space is formed by N vectors $\boldsymbol{X}_n = (X_{n,1}, X_{n,2}, ..., X_{n,M})$, where $X_{n,m}$ is the n^{th} combination of atomic features, e.g., $(\epsilon_A^{ho} + \epsilon_B^{ho} + \epsilon_X^{ho})$, evaluated on the constituent atoms of the m^{th} ABX_2 compound. For more details about the feature space construction please refer to Ref. [34, 35]; *ii*) descriptor identification by a scheme combining sure independence screening and sparsifying operator, SISSO. SIS selects features $\boldsymbol{X}_n$, highly correlated with the Z_2 topological invariant property, which is formally written as a vector of the training values of Z_2-invariant. Starting from the features selected by SIS, the SO looks for the Ω-tuples of features that minimizes the overlap (or maximize the separation) [49], among convex hulls enveloping subsets of data. The dimensionality Ω of the representation is set as the minimal that yields perfect classification of all data in the "training" set. In this work $\Omega = 2$ was found sufficient. This procedure is performed for a "training" set (176 compounds randomly chosen from the total set of 220); the remaining 20% are used as a "test" set to validate the found model.

To identify descriptors that can **a priori** classify functionalized 2D honeycomb-lattice materials in metals, trivial insulators, and QSHI, we employed the SISSO (sure independence screening and sparsifying operator) approach recently developed by Ouyang **et al.**[35]. First, a pool of almost 10^7 different potential descriptors $\boldsymbol{X}_n$ is constructed by analytically combining the properties of the free atoms A, B and X computed with SOC (namely, the eigenvalues of the highest occupied and lowest unoccupied Kohn-Sham states ϵ^{ho} ϵ^{lu}, the atomic number Z, the electron affinity EA, the ionization potential IP, and the size r_s, r_p, and r_d of the s, p, and d orbitals, i.e., the radii where the radial probability density of the valence s, p, and d orbitals are maximal). Second, this compressed-sensing based technique identifies which low-dimensional combination of these descriptors represents the classification best, i.e., minimizes the overlap (or maximizes the separation) [49] among the convex hulls that envelope the individual classes (metals, trivial insulators, QSHIs). This procedure, which is performed for a "training" set (176 compounds randomly chosen from the total set of 220), reveals that the best descriptor for the classification of the investigated compounds is two-dimensional and features the components

$$\begin{aligned} X_1 &= (Z_A + Z_B)\,\frac{\epsilon_B^{ho}}{\mathrm{EA}_B} && (4.5)\\ X_2 &= \mathrm{EA}_X\,\mathrm{IP}_X\,\left(r_{s,A} + r_{p,B}\right)\ . && (4.6)\end{aligned}$$

For the remaining 20% of compounds, i.e., the so called "test" set used to validate the model, we find that all materials with a very well defined structural and topological character are correctly classified. Only $\mathrm{ZnOCl_2}$ and $\mathrm{AlNBr_2}$, which are both FD-QSHIs at the verge of a topological transition to a trivial insulator or metal (see Suppl. Mat.), are not correctly classified. This shows that the found descriptor, which exhibits a predictive power greater than 95%, is robust and transferable, i.e., not limited to the original training set used to identify X_1 and X_2

As shown in Fig. 4.3, we predict two trivial/QSHI transitions, which are defined by the boundary lines α_1 and β. All compounds with $X_1 > \alpha_1$ are FI-QSHIs (blue). For $X_1 < \alpha_1$, the descriptor X_2 matters as well: Trivial insulators (white) occur for values of $X_2 \gtrapprox \beta$, while for $X_2 \lessapprox \beta$ we find metals (cyan) in the region $X_1 < \alpha_2$ and FD-QSHIs (red) for $\alpha_2 < X_1 < \alpha_1$. Note that X_1 and X_2 do not only clearly discriminate between metals, insulators, and TIs, but also separate functionalization-independent and -dependent QSHIs (FI- and FD-QSHIs).

Qualitative Interpretation

The descriptors X_1 and X_2 do not only numerically and graphically sort the functionalized graphene-like materials, but also capture the fundamental parameters involved in the mechanism determining the topological phase transition. To understand this, it is necessary to clarify the character of the electronic states involved in the band inversion, schematically sketched in Fig. 4.4a: These are a $\sigma_{p_{xy}}$ state (blue), to which the highest occupied p_{xy}-orbitals from atoms B contribute, and a $\sigma^*_{sp_z}$ state (red), to which the s states from atoms A and the p_z states from atoms X contribute.As detailed below, the descriptors X_1 and X_2 actually describe the relative energetic positions of these states,

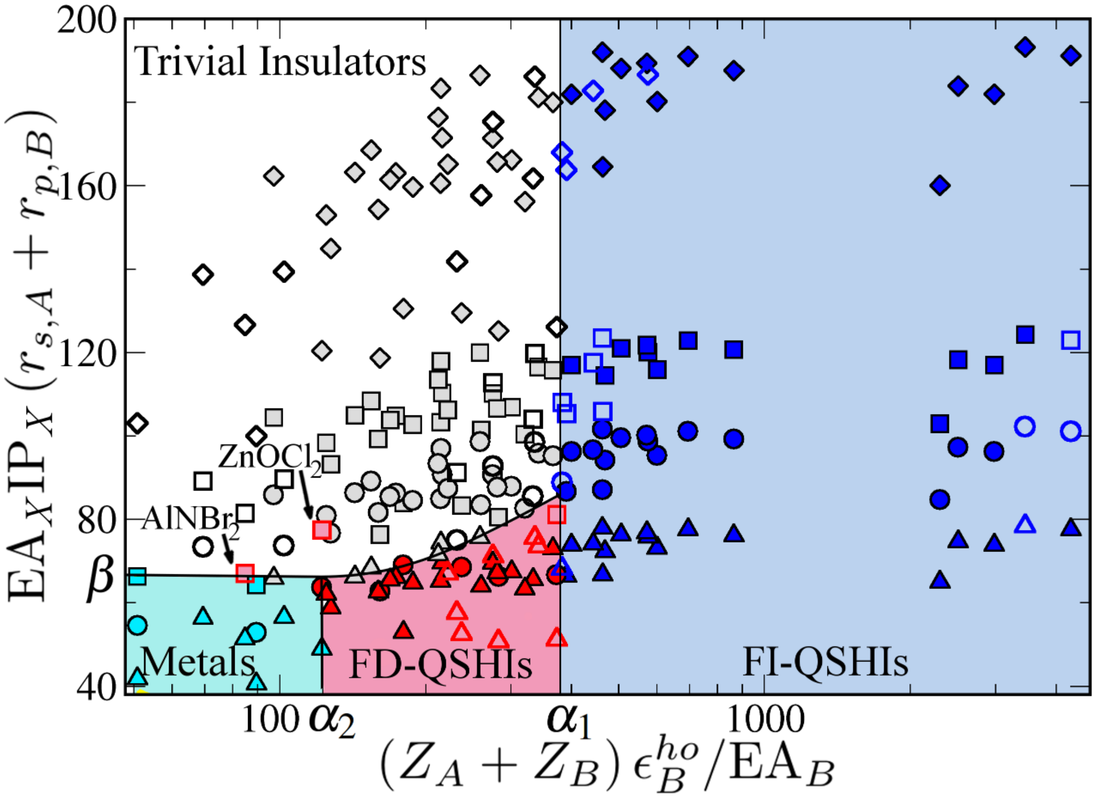

Figure 4.3 - Representation of DFT result for the training (filled) and test (unfilled symbols) set in the domain defined by the two-dimensional descriptors. A logarithmic scale is used for X_1. Compounds functionalized with F, Cl, Br, I are represented by diamonds, squares, circles and triangles, respectively. The symbols' color is used to distinguish between metalls (cyan), FD-QSHIs (red), FI-QSHIs (blue), and trivial insulators (white/grey). The same color-code is used to highlight the different regions identified by the SISSO descriptors. The boundaries of the map of materials are defined by $\alpha_1 \approx 379$, $\alpha_2 \approx 122.1$, and $\beta \approx 70$. The gap in the data points observed for $865 < X_1 < 2300$ is caused by the "jump" in Z_A and Z_B when switching from the 5th to the 6th row of the periodic system.

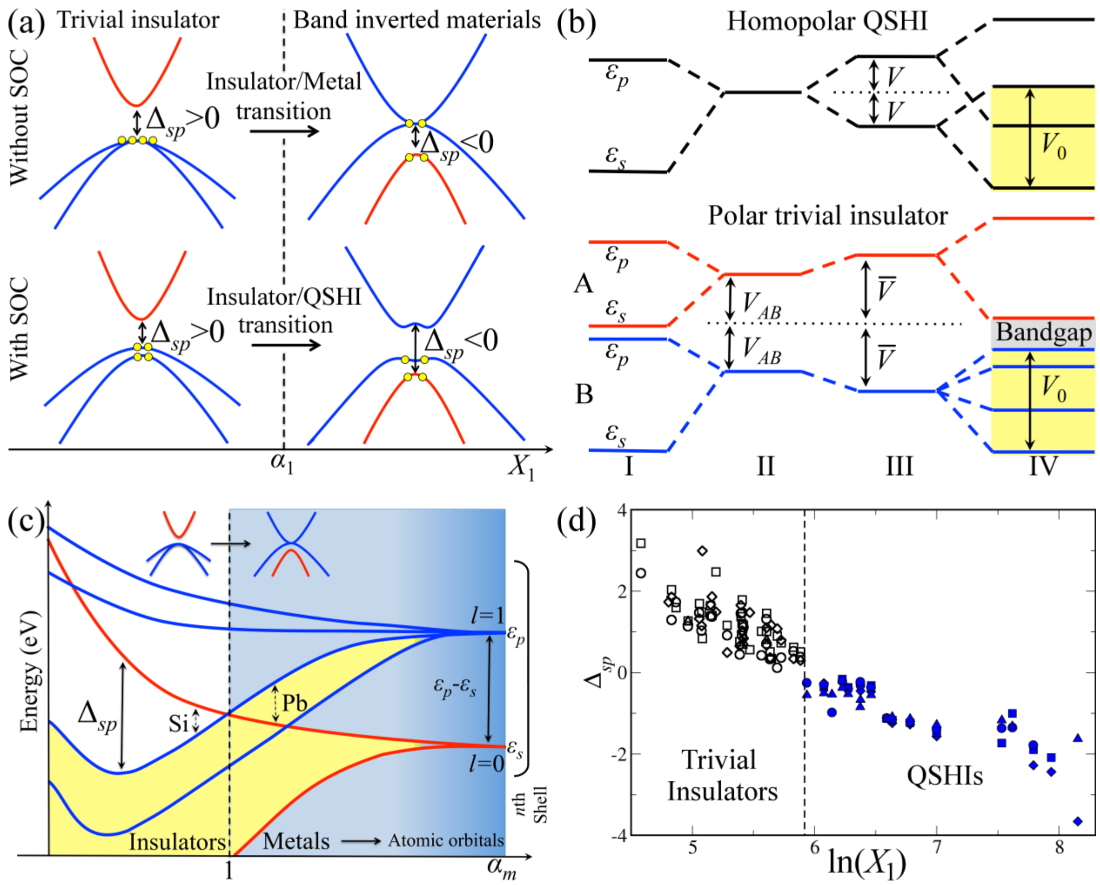

Figure 4.4 - (a) Representation of the band structure with and without SOC for trivial insulators and band-inverted materials. Semimetals become insulators after including the SOC, leading to the QSHI phase. States formed by p_{xy}- (blue lines) and sp_z-orbitals (red lines) are inverted in the QSHIs; the energy distance between them (Δ_{sp}) is related to the robustness of the topological states. Yellow dots represent the electrons. (b) Schematic representation of the evolution of atomic orbitals into bands for a homopolar band inverted system and polar trivial insulator: (I) s and p orbital, (II) sp^3 hybridization, (III) bonding-antibonding splitting, and (IV) conduction and valence bands. The yellow color stand for the occupied bands. (c) Evolution of the atomic orbitals (dark blue region) into band as a function of the metallicity. The energy distance between this states is given by Δ_{sp} and the bandgap represented by E_g. Blue (white) region represent the metallic (insulator) behavior. The insulator/metal transition takes place at $\alpha_m = 1$ (See text). (d) Δ_{sp} as a function of the logarithm of X_1.

$\Delta_{sp} = E_{\sigma^*_{sp_z}} - E_{\sigma_{p_{xy}}}$ **before** applying SOC. In trivial insulators ($\Delta_{sp} > 0$), the $\sigma^*_{sp_z}$ state lies higher in energy than the $\sigma_{p_{xy}}$ state, which is thus fully occupied. For $\Delta_{sp} < 0$, the $\sigma^*_{sp_z}$ state lies lower in energy, so that the $\sigma_{p_{xy}}$ state is only half-occupied: Before SOC, we thus observe an insulator/semi-metal transition at $X_1 = \alpha_1$ (See Fig. 4.4a), which indicates that the boundary at $X_1 = \alpha_1$ band inversion is essentially driven by atomic interactions and not by the strength of the SOC. The SOC itself is thus solely responsible for the band-gap opening in the semi-metals with $\Delta_{sp} < 0$, which leads to the QSHI state.

To qualitatively understand how the descriptor X_1 is able to describe the insulator/semi-metal transition at $X_1 = \alpha_1$, we employ the simplified tight-binding model proposed by Harrision [50], which is conceptually related to the metalization model proposed by Mooser and Pearson [51]. In this model, an insulator/semi-metal transition occurs at a "metallicity" $\alpha_m = 1$. This metallicity is defined via $\alpha_m = 4V_0/\sqrt{V^2 + V_{AB}^2}$, where V_0 is the metallic energy, V is the bonding-antibonding splitting and $V_{AB} = \epsilon^A_{sp^3} - \epsilon^B_{sp^3}$ is the energy distance between the sp^3 hybrid orbitals of atoms A and B (See Fig. 4.4b). As it is the case for tetrahedral seminconductors, the influence of V_0 is negligible, since V_0 is essentially constant for our compounds ($\approx 1.9 \pm 0.2 eV$). For homonuclear compounds, for which V_{AB} vasnishes, the hence dominant bonding-antibonding splitting V is quite well described by the approximation $V \propto d_{AB}^{-2}$, i.e., ($V \approx 18.6 d_{AB}^{-2}\text{eV}/\text{Å}^{-2}$) and, through that, by the atomic numbers [50], since the bonding length $d_{AB}^2 \propto Z_A + Z_B$ is proportional to the average atomic number, i.e, $Z_A + Z_B \approx 7.0\text{Å}^{-2} d_{AB}^2 - 57.1$ for $X = F$, a very accurate linear relation is obtained by including the change of d_{AB} due to the effect of the ionicity (polar compounds) and the functionalization. As sketched in Fig. 4.4c, compounds with heavy atoms feature large values of d_{AB} and thus a metallic electronic structure before including SOC ($\alpha_m > 1$). Conversely, light atoms feature low equilibrium distances d_{AB} and thus a finite gap before SOC.

For polar, heteronuclear compounds, the trend of $\overline{V}$ in the polar compounds is driven by the ability of the more electronegative atom B to attract electrons, i.e., its electrons affinity ($|EA_B|$). Accordingly, $\overline{V}$ decreases for same-column-atoms B as the row number in the periodic table increases, while it increases for same-row Bs from the left to the right, i.e., $V_{\text{GeGe}} < V_{\text{GaAs}} < V_{\text{ZnSe}}$. For large $|\text{EA}_B|$ (lower values of α_m), the atom B (anion) tends to take electrons from atom A (cation), thus leading to a completely occupation of the $\sigma_{p_{xy}}$ state, and hence to a trivial insulator state, as represented in Fig. 4.4b for a polar trivial insulator. Concretely, we consider the approximation $(Z_A + Z_B)/|EA_B| \approx 10.1 d_{AB}^2 \text{Å}^{-2}\text{eV}^{-1}$. Summarizing, the SISSO captures the property "encoded" in the topological phase transitions α_1, the metallicity,

$$\alpha_m = X_1/\alpha_1 = \frac{\epsilon_B^{ho}\,(Z_A + Z_B)}{\alpha_1 \text{EA}_B}, \tag{4.7}$$

with $\alpha_m = 1$ at the critical value $X_1 = \alpha_1$. Naturally, α_m increases as the lattice constant increases due to the functionalization. Thus, all of FI-QSHIs have a large enough atomic number (lattice constant always greater than 4.5 Å) to guaranteed $\alpha_m > 1$, making the topological phase independent of the actual functionalization. Here, ϵ_B^{ho} is a correction, like V_0, because it is almost the same in all compounds formed by atoms of the third, four and five row of the periodic table. Since bonding-antibonding splitting could be write as a logarithmic function either of the lattice constant or of the metallicity, a thorough demonstration of the equivalence between α_m and X_1 is that in materials with $X_2 \gtrapprox \beta$, the logarithm of X_1 does thus effectively linearly correlate with Δ_{sp} ($\Delta_{sp} \approx (-1.306 \pm 0.048) \ln(X_1) + (8.015 \pm 0.289)$), as show in Fig. 4.4d.

The descriptor X_2 at first appears to only group the compounds by functionalization, since it depends on the electron affinity and ionization potential of atom X and also on $(r_{s,A} + r_{p,B})$. This holds true for the region with $X_1 < \alpha_1$, but not for $X_1 > \alpha_1$, as apparent from Fig. 4.3. The lattice constant changes according to the functionalization, which is captured by the descriptor X_2: d_{AB} increases as X_2 decreases, i.e., for a given AB compound functionalized with I (F) we obtain the larger (lower) lattice constant. Specifically, we observe a general reduction of Δ_{sp} for heavier functionalization.

Graphene-like materials have two structural phases, usually classified in terms of the length of the buckled format as high bluckled (HB) and low buckled (LB) [52]. The functionalization stabilizes the LB phase in a large enough set of compounds, which are insulators (the 209 insulator discussed so far: Trivial insulators, FD-QSHIs, and FI-QSHIs) and always have a highest lattice constant ($a_{HB} < a_{LB}$). On the other hand, HB graphene-like materials are always metallic, even after including SOC [52], e.g., hexagonal tin and lead. This behavior is still the same in HB functionalized compounds, which are typically functionalized with I and Br (CX, BNX_2 (X=Cl, Br,I), $CSiI_2$, BPI_2, $AlNI_2$, $GaNI_2$ and $ZnOI_2$). The interaction between X and atoms A and B is meanly mediated by the Van der Waals interaction for smaller values of $\mathrm{EA}_X\mathrm{IP}_X$. In that case, the hexagonal AB compound is an insulator with metallic states formed by orbitals of the atom X inside the bandgap. Therefore, since the hexagonal AB compound in the HB structure remains in a trivial topological phase, the insulator/metal transition β with $X1 < \alpha_2$ is essentially a LB-HB structural phase transition and it is physically different from the topological transition α_1 (see Fig. 4.3). The transition FD-QSHI/metal at $X_1 \approx \alpha_2$ is dominated by the change of the bond length (also change of $Z_A + Z_B$), since HB compounds are formed by light atoms.

To showcase that the gained insights and identified descriptors are transferable, we have computed X_1 and X_2 for 140 less common honeycomb ABX_2 compounds (AB from groups V-V and IV-VI functionalized with a group VI element for X). For these compounds, the identified descriptor predicts 20 FI-QSHIs, 54 FD-QSHIs, 42 trivial insulators and 24 metals, as shown in Fig. 4.5. Since $\mathrm{EA}_x\mathrm{IP}_X$ for $X = VI$ is lower, we get that the functionalization stabilizes the HB phase for non-QSHI materials. We have verified the prediction for selected compounds (AsX, SbX, SnSeX_2, PSbX_2, BiX and PO with X:O,S,Se,Te). The VI-functionalized compounds are most feasible to realize the QSHI effect, since oxidation may be a spontaneous process. It has been shown that oxide blue-phosphorene is a trivial insulator, which can become a QSHI by applying ten-

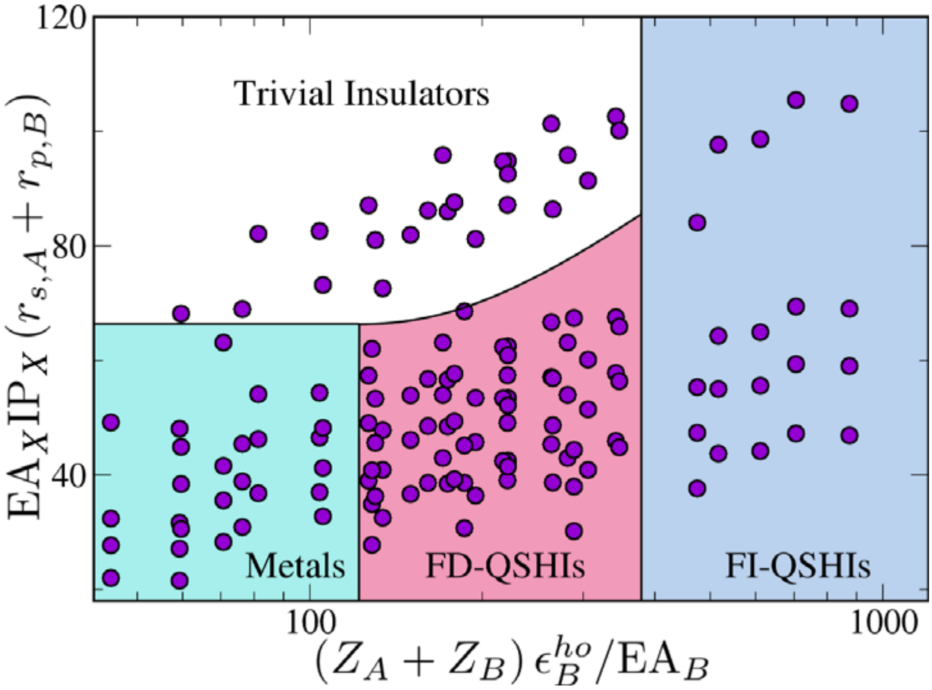

Figure 4.5 - Representation of proposed V-V-VI and IV-VI-VI compounds in the domain defined by the two-dimensional descriptor components.

sile strain [53]. Recently, only one compound has been reported as an intrinsic QSHI, AsO [54]. Different from the trial-and-error theoretical proposed systems, based on our SISSO we propose a complete family of 74 new QSHI candidates, opening a window for the potential observation of the theoretical expected protected edge states.

Bibliography

[1] L. M. Ghiringhelli, J. Vybiral, S. V. Levchenko, C. Draxl, and M. Scheffler, "Big Data of Materials Science : Critical Role of the Descriptor," **Physical Review Letters**, vol. 114, no. 10, p. 105503, 2015.

[2] E. Candes and M. Wakin, "An Introduction To Compressive Sampling," **IEEE Signal Processing Magazine**, vol. 25, no. 2, pp. 21–30, 2008.

[3] T. A. Gallagher, A. J. Nemeth, and L. Hacein-Bey, "An introduction to the Fourier transform: Relationship to MRI," **American Journal of Roentgenology**, vol. 190, no. 5, pp. 1396–1405, 2008.

[4] L. J. Nelson, G. L. W. Hart, F. Zhou, and V. Ozolins, "Compressive sensing as a paradigm for building physics models," **Physical Review B**, vol. 87, no. 3, p. 035125, 2013.

[5] R. Tibshirani, “Regression Selection and Shrinkage via the Lasso,” vol. 58, pp. 267–288, 1994.

[6] E. Candes, J. Romberg, and T. Tao, “Robust uncertainty principles: exact signal reconstruction from highly incomplete frequency information,” **Information Theory, IEEE Transactions on**, vol. 52, pp. 489–509, Feb 2006.

[7] K. Yang, W. Setyawan, S. Wang, M. Buongiorno Nardelli, and S. Curtarolo, “A search model for topological insulators with high-throughput robustness descriptors,” **Nature Materials**, vol. 11, no. 7, pp. 614–619, 2012.

[8] C. Herring, Phys. Rev. **52**, 365 (1937).

[9] B. Volkov and O. A. Pankratov, ZhETF Pisma Redaktsiiu **42**, 145 (1985).

[10] Y. Ren, Z. Qiao, and Q. Niu, Reports on Progress in Physics **79**, 066501 (2016).

[11] L. Kou, Y. Ma, Z. Sun, T. Heine, and C. Chen, The Journal of Physical Chemistry Letters **8**, 1905 (2017), PMID: 28394616.

[12] J. Maciejko, T. L. Hughes, and S.-C. Zhang, Annual Review of Condensed Matter Physics **2**, 31 (2011).

[13] M. Z. Hasan and C. L. Kane, Rev. Mod. Phys. **82**, 3045 (2010).

[14] X.-L. Qi and S.-C. Zhang, Rev. Mod. Phys. **83**, 1057 (2011).

[15] C. L. Kane and E. J. Mele, Phys. Rev. Lett. **95**, 226801 (2005).

[16] B. A. Bernevig and S.-C. Zhang, Phys. Rev. Lett. **96**, 106802 (2006).

[17] D. J. Thouless, M. Kohmoto, M. P. Nightingale, and M. den Nijs, Phys. Rev. Lett. **49**, 405 (1982).

[18] L. Fu and C. L. Kane, Phys. Rev. B **74**, 195312 (2006).

[19] C. L. Kane and E. J. Mele, Phys. Rev. Lett. **95**, 146802 (2005).

[20] Z. Liu et al., Phys. Rev. Lett. **107**, 136805 (2011).

[21] I. K. Drozdov et al., Nat Phys **10**, 664 (2014).

[22] B. A. Bernevig, T. L. Hughes, and S.-C. Zhang, Science **314**, 1757 (2006).

[23] M. König et al., Science **318**, 766 (2007).

[24] E. B. Olshanetsky et al., Phys. Rev. Lett. **114**, 126802 (2015).

[25] I. Knez, R.-R. Du, and G. Sullivan, Phys. Rev. Lett. **107**, 136603 (2011).

[26] C. Liu, T. L. Hughes, X.-L. Qi, K. Wang, and S.-C. Zhang, Phys. Rev. Lett. **100**, 236601 (2008).

[27] C. Weeks, J. Hu, J. Alicea, M. Franz, and R. Wu, Phys. Rev. X **1**, 021001 (2011).

[28] C.-C. Liu, H. Jiang, and Y. Yao, Phys. Rev. B **84**, 195430 (2011).

[29] C. M. Acosta, M. P. Lima, R. H. Miwa, A. J. R. da Silva, and A. Fazzio, Phys. Rev. B **89**, 155438 (2014).

[30] Zhou Miao et al., **4**, 7102 (2014).

[31] M. Klintenberg, J. T. Haraldse, and A. V. Balatsky, Applied Physics Research **6**, 31 (2014).

[32] Yang Kesong, Setyawan Wahyu, Wang Shidong, Buongiorno Nardelli Marco, and Curtarolo Stefano, Nat Mater **11**, 614 (2012), 10.1038/nmat3332.

[33] L. M. Ghiringhelli, J. Vybiral, S. V. Levchenko, C. Draxl, and M. Scheffler, Phys. Rev. Lett. **114**, 105503 (2015).

[34] L. M. Ghiringhelli et al., New. J. Phys. **19**, 023017 (2017).

[35] R. Ouyang, S. Curtarolo, E. Ahmetcik, L. M. Ghiringhelli, and M. Scheffler, To be publised (2017).

[36] M. C. Lucking et al., ArXiv e-prints (2016).

[37] Al Balushi Zakaria Y. et al., Nat Mater **15**, 1166 (2016).

[38] F.-C. Chuang et al., Nano Letters **14**, 2505 (2014), PMID: 24734779.

[39] Y. Xu et al., Phys. Rev. Lett. **111**, 136804 (2013).

[40] C. Si et al., Phys. Rev. B **89**, 115429 (2014).

[41] Y. ping Wang et al., Applied Physics Letters **108**, 073104 (2016).

[42] C. Niu et al., Phys. Rev. B **91**, 041303 (2015).

[43] C.-C. Liu et al., Phys. Rev. B **90**, 085431 (2014).

[44] Z. Song et al., ArXiv e-prints (2014).

[45] Jin Kyung-Hwan and Jhi Seung-Hoon, **5**, 8426 (2015).

[46] Y. Ma, Y. Dai, L. Kou, T. Frauenheim, and T. Heine, Nano Letters **15**, 1083 (2015), PMID: 25559879.

[47] L. Li, X. Zhang, X. Chen, and M. Zhao, Nano Letters **15**, 1296 (2015), PMID: 25625786.

[48] X. Li et al., Nano Research **8**, 2954 (2015).

[49] A. F. Bialon, T. Hammerschmidt, and R. Drautz, Chemistry of Materials **28**, 2550 (2016).

[50] W. A. Harrison, Phys. Rev. B **8**, 4487 (1973).

[51] E. Mooser and W. B. Pearson, Acta Crystallographica **12**, 1015 (1959).

[52] P. Rivero, J.-A. Yan, V. M. García-Suárez, J. Ferrer, and S. Barraza-Lopez, Phys. Rev. B **90**, 241408 (2014).

[53] G. Yang et al., The Journal of Physical Chemistry C **121**, 12945 (2017).

[54] Y. ping Wang et al., Applied Physics Letters **110**, 213101 (2017).

[55] V. Blum et al., Computer Physics Communications **180**, 2175 (2009).

[56] V. Havu, V. Blum, P. Havu, and M. Scheffler, Journal of Computational Physics **228**, 8367 (2009).

[57] F. Knuth, C. Carbogno, V. Atalla, V. Blum, and M. Scheffler, Comp. Phys. Comm. **190**, 33 (2015).

[58] K. Lejaeghere et al., Science **351** (2016).

[59] R. Yu, X. L. Qi, A. Bernevig, Z. Fang, and X. Dai, Phys. Rev. B **84**, 075119 (2011).

[60] A. A. Soluyanov and D. Vanderbilt, Phys. Rev. B **83**, 235401 (2011).

[61] A. A. Soluyanov and D. Vanderbilt, Phys. Rev. B **83**, 035108 (2011).

[62] Blum and Huhn, To be publised (2017).

[63] D. Shin et al., Chemistry of Materials **28**, 4771 (2016).

[64] J. P. Perdew, K. Burke, and M. Ernzerhof, Phys. Rev. Lett. **77**, 3865 (1996).

[65] A. Tkatchenko and M. Scheffler, Phys. Rev. Lett. **102**, 073005 (2009).

5. Time reversal protected bulk states

Introduction

The main objective of spintronics is to understand the mechanisms by which it is possible to achieve efficient control of both spin configurations and spin currents[1]. In the last decade, the way to achieve this objective has experienced a breakthrough due to *i*) the discovery and understanding of mechanisms to generate spin currents in conductors with magnetic order and in paramagnetic conductors/semiconductors[2, 3, 4], *ii*) the experimental observation of theoretically proposed spin injector systems[5, 6, 7], and *iii*) the synthesis of 2D materials with long spin relaxation time[1, 8]. The generation of spin currents, spin injections and spin conservation are mediated by the spin-orbit coupling (SOC) mainly via Rashba effect and/or nontrivial topological phases[9, 10, 11, 12], such as the quantum spin Hall (QSH) effect[13]. Therefore, the search for systems experiencing these properties is a primary concern for the development of spintronics.

QSH insulators support helical metallic edge states, forming topological Dirac fermions protected by the time-reversal (TR) symmetry on an insulating bulk[5, 6]. The topological transition from trivial insulating to topological insulators is evidenced as a band inversion at the TR invariant k-point mediated by the SOC. The topological band dispersion has been experimentally characterized via angle-resolved photoemission spectroscopy (ARPES) and local scanning tunneling microscopy (STM) in 3D topological insulators[5], and via transport measurements in HgTe/CdTe quantum wells[14, 15]. On the other hand, the Rashba effect, arising from the lack of inversion symmetry, leads to parallel spin-polarized band dispersion curves with opposite in-plane chiral spin texture[16], allowing the control of the spin direction through an electric field[9, 11, 12]. These dispersion curves and Fermi contours have been characterized by spectroscopic measurements for many surfaces and interfaces[17, 18, 19, 20]. Large Rashba spin-splitting are found in materials formed by heavy elements with strong intrinsic SOC such as Bi, Pb, W, among others[21, 22, 20, 23, 24]. In this work, we look at the consequences of the simultaneous presence of a Rashba spin-splitting and a inverted bandgap. Such properties appear simultaneously in thin films and heterostructures of 3D topological insulators[25, 26, 27, 28, 29, 30].

Here, we show that bulk states can be protected against backscattering in nanoribbons of QSH insulators with bulk inversion asymmetry. This behavior is a consequence of the simultaneous presence of both Rashba and band inversion in a QSH insulator. In our model, both the conduction and the valence bands are formed by two bands with the

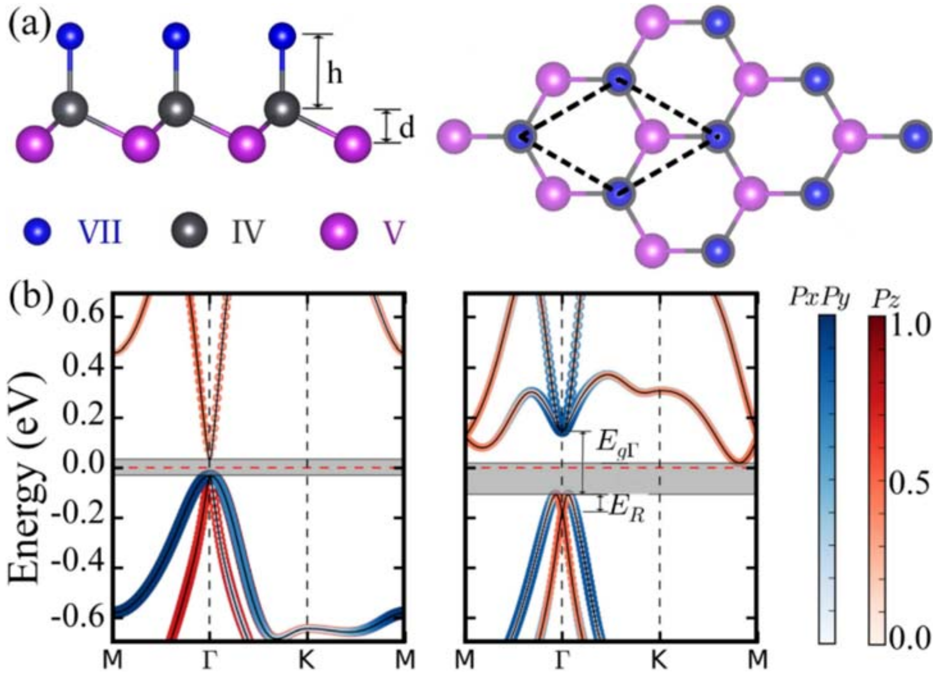

Figure 5.1 - (a) Top and side view of the PbBiI atomic structure. In the lowest energy configuration the buckled, d, has 1.3 Å in length and, the Bi-Pb and Pb-I (h) bounds have 3.04 Å and 1.35 Å in length, respectively. (b) Band structure without SOC (left) and with SOC (right). The color scales represent the weight of the orbital projection in the wavefunction $\psi_n(\vec{k})$. The projections in the $p_z(p_x$ and $p_y)$ Bi orbitals are indicated by red(blue). The Rashba spin-splitting and the band inversion are characterized by E_R and $E_{g\Gamma}$, respectively.

same in-plane helical spin texture and opposite $\langle S_z \rangle$ spin component. We propose a stable non-centrosymmetric honeycomb-lattice QSH insulator that presents this unconventional bulk spin texture. This system is formed by the Bi, Pb, and I elements and, has a large nontrivial band gap of 0.14 eV and a huge Rashba spin-splitting of 60 meV. To construct the Hamiltonian exhibiting the proposed spin texture we will use the PbBiI system.

Geometry and electronic band structure

Figure 5.1 summarizes the crystalline structure and the results we obtain from *ab initio* calculations, which are performed within the density functional theory (DFT) framework as implemented in the SIESTA code[31] and in the Vienna Ab Initio Simulation Package[32]. We consider the on-site approximation for the SOC[33, 34] in the SIESTA code. The Local Density Approximation[35] and the Perdew-Burke-Ernzenhof generalized gradient approximation[36] are used for the exchange-correlation functional. Interpreting the hexagonal lattice as two triangular sub-lattices A and B, the system has a V atom type on the sub-lattice A, and a IV-VII dimer in the sub-lattice B (Fig 5.1a). These non-centrosymmetry systems have a buckled format and fulfill the symmetry operations of the

C_{3v} symmetry: *i*) three-fold rotation symmetry R_3 along the z axis, *ii*) mirror symmetry M_x ($x \to -x$) in the yz plane, and *iv*) TR symmetry $\mathcal{T}$. We predict that the PbBiI system is mechanically stable, imaginary frequencies does not exist in the *ab initio* phonon spectrum (see Supplemental Material) and the formation energy ($E_F = E_{\text{PbBiI}} - \mu_{\text{Pb}} - \mu_{\text{Bi}} - \mu_{\text{I}}$) is about -0.77 eV.

At the Γ point, the top of the valence band is dominated by the $p_{x,y}$ Bi orbitals and the bottom of the conduction band mainly consists of the p_z Bi orbitals, as shown in Fig 5.1b. When the SOC is taken into account, the p orbitals are mixed to form effective orbitals preserving the total angular momentum and a band inversion occurs when $\lambda_{\text{SOC}} = 0.65$, where $\lambda_{\text{SOC}} = 0(1)$ means the absence (full presence) of SOC. We implemented the evolution of Wannier center of charges as an alternative method to the Z_2 invariant calculation using *ab-inito* simulations [37, 38, 39]. We find that there is no a horizontal reference line that crosses the evolution of the WCCs at least an odd number of times, as shown in Fig. 5.2. This suggests that $Z_2 = 1$[37, 39], confirming that the PbBiI system is a QSH insulator.

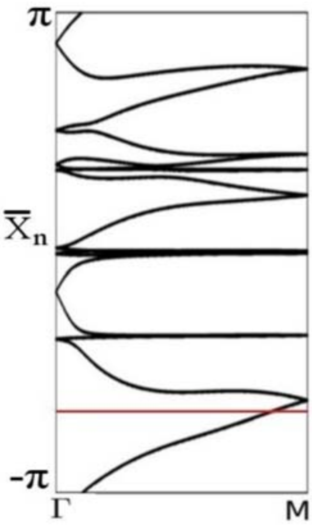

Figure 5.2 - The evolution of Wannier Center of Charges. If we draw a horizontal line of reference that crosses the picture, we would have at least an odd number of crossing, showing that the PbBiI system is a topological insulator.

According to the symmetry operation, the wavefunction at the Γ point is given by the $\{|\Lambda_J, j_z\rangle\}$ effective states, where J is the total angular momentum, j_z is the projection along the z axes, and Λ corresponds to the Bi and Pb-I contributions. To preserve the total angular momentum, the $|\Lambda_{3/2}, \pm 3/2\rangle$ effective states should be a linear combination of the $p_+ = p_x + ip_y$ and $p_- = p_x - ip_y$ effective orbitals and, the $|\Lambda_J, \pm 1/2\rangle$ effective states should be a linear combination of the p orbitals, mainly p_z orbitals. In this inverted band gap the conduction band mainly consists of $p_{x,y}$ Bi orbitals and the valence band is formed by the p orbitals, mainly dominated by p_z Bi orbitals, as shown in Fig 5.1b. Therefore, at the Γ point, the valence (conduction) band is described by the effective states $\{|\mathrm{Bi}_J, j_z\rangle\}$ with $J = 3/2$ ($J = 1/2$) and hence, we write the Hamiltonian using the full SOC basis $\{|\mathrm{Bi}_{1/2}, 1/2\rangle, |\mathrm{Bi}_{1/2}, -1/2\rangle, |\mathrm{Bi}_{3/2}, 1/2\rangle, |\mathrm{Bi}_{3/2}, -1/2\rangle\}$. This basis $\{|\mathrm{Bi}_J, j_z\rangle\}$ is transformed by the C_{3v} symmetries operations as,

(1) *Threefold rotation* R_3: $|\mathrm{Bi}_{J=1/2}, \pm1/2\rangle \rightarrow e^{\pm\frac{i\pi}{3}} |\mathrm{Bi}_{J=1/2}, \pm1/2\rangle$; $|\mathrm{Bi}_{J=3/2}, \pm1/2\rangle \rightarrow e^{\pm\frac{i\pi}{3}} |\mathrm{Bi}_{J=3/2}, \pm1/2\rangle$; $|\mathrm{Bi}_{J=3/2}, \pm3/2\rangle \rightarrow -|\mathrm{Bi}_{J=3/2}, \pm3/2\rangle$.

(2) *Twofold rotation* M_x: $|\mathrm{Bi}_{J=1/2}, \pm1/2\rangle \rightarrow -i\,|\mathrm{Bi}_{J=1/2}, \pm1/2\rangle$; $|\mathrm{Bi}_{J=3/2}, \pm1/2\rangle \rightarrow -i\,|\mathrm{Bi}_{J=3/2}, \pm1/2\rangle$; $|\mathrm{Bi}_{J=3/2}, \pm3/2\rangle \rightarrow -i\,|\mathrm{Bi}_{J=3/2}, \pm3/2\rangle$.

(3) *Time reversal* $\mathcal{T}$: $|\mathrm{Bi}_{J=1/2}, \pm1/2\rangle \rightarrow \pm\langle\mathrm{Bi}_{J=1/2}, \pm1/2|$; $|\mathrm{Bi}_{J=3/2}, \pm1/2\rangle \rightarrow \pm\langle\mathrm{Bi}_{J=3/2}, \pm1/2|$; $|\mathrm{Bi}_{J=3/2}, \pm3/2\rangle \rightarrow \mp\langle\mathrm{Bi}_{J=3/2}, \pm3/2|$.

This relations are extremely important to define the relation between the hopping terms in tight-binding model describing the proposed systems.

Band gap control

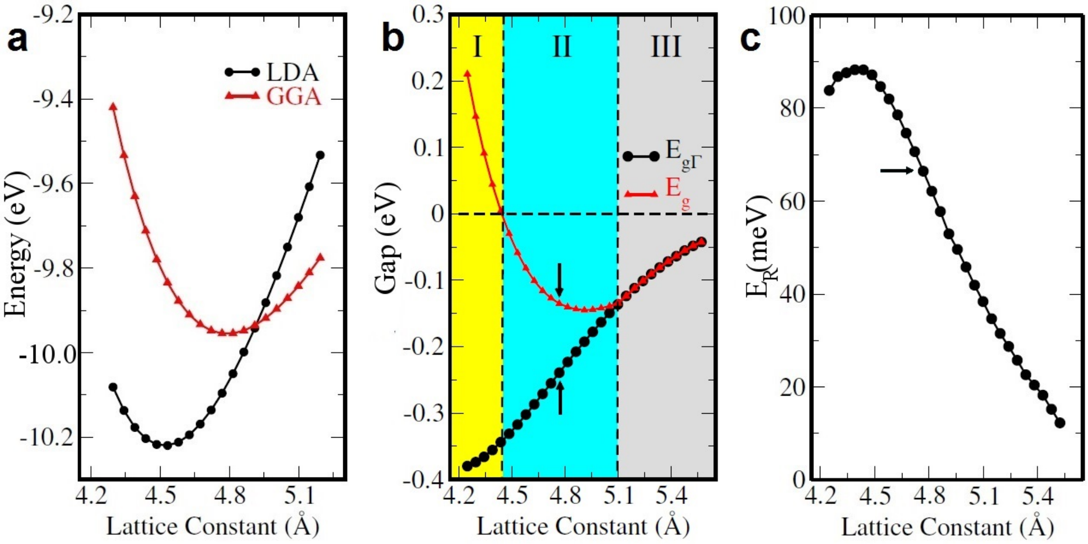

Figure 5.3 - (a) Energy in function of the lattice constant depending on the exchange-correlation functional used, i.e Local Density Approximation (LDA) or Generalized Gradient Approximation (GGA). (b) Band gap in function of the lattice constant, where E_g and $E_{g\Gamma}$ are the band gap of the system and the band gap at the Γ point, respectively. Below the dashed line at 0.0, the $E_{g\Gamma}$ is inverted. (c) Rashba spin splitting in function of the lattice constant. The arrows represent the equilibrium lattice constant for the GGA calculation.

Using GGA functional, we find that the lattice constant is 4.77 Å, whereas for LDA is 4.53 Å, as shown in Fig 5.3a. We find that the substitution of Pb atoms by Sn atoms (or changing the lattice constant) allows the control of both the band gap direction (see Fig 5.3b) and the lRashba spin-splitting in the valence band (see Fig 5.3c). The decrease (increase) of the lattice constant can be understood as a compressive (tensile) strain. We find three different behaviors depending on the intensity of the strain applied: semi-metal, indirect band gap semiconductor and direct band gap semiconductor, as represented in Fig 5.3b by the regions I, II and III, respectively. The equilibrium position is represented by arrows, shown as in the Fig 5.3.

As mentioned above, in the region II, in which the system is in the equilibrium lattice parameter, $E_{g\Gamma}$ is negative indicating a band inversion at the Γ point. The gap $E_{g\Gamma}$ is different from the indirect band gap E_g, which is also considered negative for comparison purposes. In the region I, when we apply compressive strain, the minimum of the conduction band, in $M \to K$ direction, begins to descend and cross the Fermi energy for $a = 4.3$ Å, forming a semi-metal. To represent this behavior, we change the sign of the band gap E_g. In the region III, we consider a tensile strain, E_g and $E_{g\Gamma}$ are equals and the system behaves as a semiconductor with a direct band gap at the Γ point. For any value of strain, the states near to the Fermi energy in the Γ point remain inverted, so if this band inversion is associated with a topological state, this state will be robust against strain, even for a tension of 20%(5.6 Å), as shown in Fig 5.3.

5.2.1 *Phonon spectrum*

Imaginary frequencies does not exist in the *ab initio* phonon spectrum of the PbBiI system, as shown in Fig 5.4, and the formation energy ($E_F = E_{\mathrm{PbBiI}} - \mu_{\mathrm{Pb}} - \mu_{\mathrm{Bi}} - \mu_{\mathrm{I}}$) is about -0.77 eV. Here, E_{PbBiI} is the energy of the system and $\mu_{\mathrm{Pb,Bi,I}}$ is the chemical potential from the more stable phase. These properties are necessary and sufficient to conclude that the PbBiI honeycomb lattice system is mechanically stable. Since the rest of compound in the proposed family are not QSH insulators, we do not show the phonon spectrum here. However, all of them are mechanically stables.

Effective tight-binding model

The tight-binding Hamiltonian matrix elements are given by:

$$[\mathcal{H}(\vec{k})]_{ij} = \varepsilon_{ij}\delta_{ij} + \sum_{\nu=1}^{6} t^{ij}_{\vec{a}_\nu} e^{i\vec{k}\cdot\vec{a}_\nu}, \tag{5.1}$$

where $i = (\mathrm{Bi}, J, j_z)$, $j = (\mathrm{Bi}, J', j'_z)$ and ε is the on-site energy. Since the $|(\text{Pb-I})_J, j_z\rangle$ effective states contribution is not relevant near the Fermi energy, we omit the terms associated with the nearest neighbors (Pb-I dimer) and hence, $t^{ij}_{\vec{a}_\nu} = \langle \vec{n}, \mathrm{Bi}_J, j_z | H | \vec{a}_\nu, \mathrm{Bi}_{J'}, j'_z \rangle$ represents the next nearest neighbor hopping terms, with $\vec{n}$ indicating the lattice site and

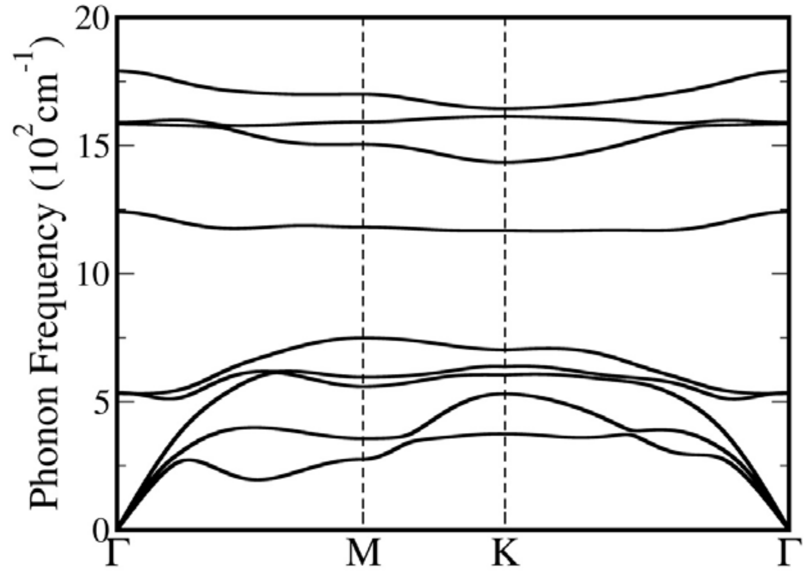

Figure 5.4 - Ab-initio phonons calculation for the PbBiI system. We use a 7×7 supercell.

$\vec{a}_\nu$ corresponding to the ν-th of the six next nearest neighbor vectors. Different form buckled honeycomb lattice systems, such as Germanene, Silicene among others, in which the nearest neighbor hopping terms are essential to its description, in the PbBiI the Pb-I dimer only mediates the interaction between Bi atoms and its effect is effectively introduced within the next nearest neighbor hopping terms. Therefore, the PbBiI Hamiltonian is striking different from the Kane-Mele model[13]. Using the relevant symmetry operations of the C_{3v} point group, these hopping terms can be related to each other and are uniquely determined (See tables 1-4), which leads to an approximate description of the DFT band structure (see Fig 5.5a).

Table 5.1 - Symmetry operation for $t^{11}_{a_i} = \langle 0, 1/2, 1/2|H|a_i, 1/2, 1/2\rangle$

	$t^{11}_{a_1}$	$t^{11}_{a_2}$	$t^{11}_{a_3}$	$t^{11}_{-a_1}$	$t^{11}_{-a_2}$	$t^{11}_{-a_3}$
$\mathcal{T}$	$t^{22*}_{a_1}$	$t^{22*}_{a_2}$	$t^{22*}_{a_3}$	$t^{22*}_{-a_1}$	$t^{22*}_{-a_2}$	$t^{22*}_{-a_3}$
R_3	$t^{11}_{a_3}$	$t^{11}_{a_1}$	$t^{11}_{a_2}$	$t^{11}_{-a_3}$	$t^{11}_{-a_1}$	$t^{11}_{-a_2}$
M_x	$t^{22}_{-a_1}$	$t^{22}_{-a_3}$	$t^{22}_{-a_2}$	$t^{22}_{a_1}$	$t^{22}_{a_3}$	$t^{22}_{a_2}$

Relations	$t^{11}_{a_i} = t^{22*}_{a_i} = t^{22}_{-a_i} = t^{11*}_{-a_i}$

The Hamiltonian describing the PbBiI system is written as

$$\mathcal{H} = \boldsymbol{\varepsilon} + \begin{pmatrix} \mathcal{H}_{1/2}(\vec{k}) & \mathcal{H}_{int}(\vec{k}) \\ \mathcal{H}^{\dagger}_{int}(\vec{k}) & \mathcal{H}_{3/2}(\vec{k}) \end{pmatrix}, \tag{5.2}$$

where $\mathcal{H}_{1/2}(\vec{k})$ and $\mathcal{H}_{3/2}(\vec{k})$ describe the $|\mathrm{Bi}_{1/2}, \pm 1/2\rangle$ and $|\mathrm{Bi}_{3/2}, \pm 3/2\rangle$ states, respec-

Table 5.2 - Symmetry operation for $t^{12}_{a_i} = \langle 0, 1/2, 1/2|H|a_i, 1/2, -1/2\rangle$

	$t^{12}_{a_1}$	$t^{12}_{a_2}$	$t^{12}_{a_3}$	$t^{12}_{-a_1}$	$t^{12}_{-a_2}$	$t^{12}_{-a_3}$
$\mathcal{T}$	$-t^{12}_{-a_1}$	$-t^{12}_{-a_2}$	$-t^{12}_{-a_3}$	$-t^{12}_{a_1}$	$-t^{12}_{a_2}$	$-t^{12}_{a_3}$
R_3	$e^{-i2\pi/3}t^{12}_{a_3}$	$e^{-i2\pi/3}t^{12}_{a_1}$	$e^{-i2\pi/3}t^{12}_{a_2}$	$e^{-i2\pi/3}t^{12}_{-a_3}$	$e^{-i2\pi/3}t^{12}_{-a_1}$	$e^{-i2\pi/3}t^{12}_{-a_2}$
M_x	$t^{12*}_{a_1}$	$t^{12*}_{a_3}$	$t^{12*}_{a_2}$	$t^{12*}_{-a_1}$	$t^{12*}_{-a_3}$	$t^{12*}_{-a_2}$
Relations	$t^{12}_{a_1} = t^{12}$; $t^{12}_{a_2} = -e^{i2\pi/6}t^{12}$; $t^{12}_{a_3} = -e^{-i2\pi/6}t^{12}$					

Table 5.3 - Symmetry operation for $t^{13}_{a_i} = \langle 0, 1/2, 1/2|H|a_i, 3/2, 1/2\rangle$

	$t^{13}_{a_1}$	$t^{13}_{a_2}$	$t^{13}_{a_3}$	$t^{13}_{-a_1}$	$t^{13}_{-a_2}$	$t^{13}_{-a_3}$
$\mathcal{T}$	$t^{24*}_{a_1}$	$t^{24*}_{a_2}$	$t^{24*}_{a_3}$	$t^{24*}_{-a_1}$	$t^{24*}_{-a_2}$	$t^{24*}_{-a_3}$
R_3	$t^{13}_{a_3}$	$t^{13}_{a_1}$	$t^{13}_{a_2}$	$t^{13}_{-a_3}$	$t^{13}_{-a_1}$	$t^{13}_{-a_2}$
M_x	- $t^{24}_{-a_1}$	-$t^{24}_{-a_3}$	-$t^{24}_{-a_2}$	-$t^{24}_{a_1}$	-$t^{24}_{a_3}$	-$t^{24}_{a_2}$
Relations	$t^{13}_{a_i} = t^{24*}_{a_i} = -t^{24}_{-a_i} = -t^{13*}_{-a_i}$					

Table 5.4 - Symmetry operation for $t^{14}_{a_i} = \langle 0, 1/2, 1/2|H|a_i, 3/2, -1/2\rangle$

	$t^{14}_{a_1}$	$t^{14}_{a_2}$	$t^{14}_{a_3}$	$t^{14}_{-a_1}$	$t^{14}_{-a_2}$	$t^{14}_{-a_3}$
$\mathcal{T}$	$-t^{23*}_{a_1}$	$-t^{23*}_{a_2}$	$-t^{23*}_{a_3}$	$-t^{23*}_{-a_1}$	$-t^{23*}_{-a_2}$	$-t^{23*}_{-a_3}$
R_3	$e^{-i2\pi/3}t^{14}_{a_3}$	$e^{-i2\pi/3}t^{14}_{a_1}$	$e^{-i2\pi/3}t^{14}_{a_2}$	$e^{-i2\pi/3}t^{14}_{-a_3}$	$e^{-i2\pi/3}t^{14}_{-a_1}$	$e^{-i2\pi/3}t^{14}_{-a_2}$
M_x	$t^{14*}_{-a_1}$	$t^{14*}_{-a_3}$	$t^{14*}_{-a_2}$	$t^{14*}_{a_1}$	$t^{14*}_{a_3}$	$t^{14*}_{a_2}$
Relations	$t^{14}_{a_1} = t_a$; $t^{14}_{a_2} = e^{-i2\pi/3}t^{14}_a$; $t^{14}_{a_3} = e^{-i4\pi/3}t^{14}_a$; $t^{14}_{-a_1} = t^*_a$; $t^{14}_{-a_2} = e^{-i4\pi/3}t^*_a$; $t^{14}_{-a_3} = e^{-i2\pi/3}t^*_a$					

tively. The $\mathcal{H}_{int}(\vec{k})$ term is the interaction between these states. Using the relations showed in tables 1-4, we found the matrix elements:

$$H^{11}_{J=1/2} = \sum_{j=1}^{6} t^{11}_{a_j} e^{ik\cdot a_j} = t^{11}\sum_{j=1}^{3}(\cos k_j + i\sin k_j) + t^{11*}\sum_{j=1}^{3}(\cos k_j - i\sin k_j) = 2\Re[t^{11}]\sum_{j=1}^{3}\cos k_j - 2\Im[t^{11}]\sum_{j=1}^{3}\sin k_j, \tag{5.3}$$

$$H^{22}_{J=1/2} = \sum_{j=1}^{6} t^{22}_{a_j} e^{ik\cdot a_j} = t^{11*}\sum_{j=1}^{3}(\cos k_j + i\sin k_j) + t^{11}\sum_{j=1}^{3}(\cos k_j - i\sin k_j) = 2\Re[t^{11}]\sum_{j=1}^{3}\cos k_j + 2\Im[t^{11}]\sum_{j=1}^{3}\sin k_j, \tag{5.4}$$

$$H^{11}_{J=3/2} = \sum_{j=1}^{6} t^{33}_{a_j} e^{ik\cdot a_j} = t^{33}\sum_{j=1}^{3}(\cos k_j + i\sin k_j) + t^{33*}\sum_{j=1}^{3}(\cos k_j - i\sin k_j) = 2\Re[t^{33}]\sum_{j=1}^{3}\cos k_j - 2\Im[t^{33}]\sum_{j=1}^{3}\sin k_j, \tag{5.5}$$

$$H^{22}_{J=3/2} = \sum_{j=1}^{6} t^{44}_{a_j} e^{ik\cdot a_j} = t^{33*}\sum_{j=1}^{3}(\cos k_j + i\sin k_j) + t^{33}\sum_{j=1}^{3}(\cos k_j - i\sin k_j) = 2\Re[t^{33}]\sum_{j=1}^{3}\cos k_j + 2\Im[t^{33}]\sum_{j=1}^{3}\sin k_j, \tag{5.6}$$

$$H^{12}_{J=1/2} = \sum_{j=1}^{6} t^{12}_{a_j} e^{ik\cdot a_j} = -2it^{12}[\sin k_1 + e^{-i2\pi/3}\sin k_2 + e^{i2\pi/3}\sin k_3], \tag{5.7}$$

$$H^{12}_{J=3/2} = \sum_{j=1}^{6} t^{34}_{a_j} e^{ik\cdot a_j} = -2it^{34}[\sin k_1 + e^{-i2\pi/3}\sin k_2 + e^{i2\pi/3}\sin k_3], \tag{5.8}$$

$$H^{11}_{int} = \sum_{j=1}^{6} t^{13}_{a_j} e^{ik\cdot a_j} = 2i\Im[t^{13}] \sum_{j=1}^{3} \cos k_j + 2i\Re[t^{13}] \sum_{j=1}^{3} \sin k_j, \tag{5.9}$$

$$H^{22}_{int} = \sum_{j=1}^{6} t^{13}_{a_j} e^{ik\cdot a_j} = -2i\Im[t^{13}] \sum_{j=1}^{3} \cos k_j + 2i\Re[t^{13}] \sum_{j=1}^{3} \sin k_j, \tag{5.10}$$

$$H^{12}_{int} = \sum_{j=1}^{6} t^{14}_{a_j} e^{ik\cdot a_j} = 2\Re[t^{14}](\cos k_1 + e^{-i2\pi/3}\cos k_2 + e^{-i4\pi/3}\cos k_3) + 2\Im[t^{14}](\sin k_1 + e^{-i2\pi/3}\sin k_2 + e^{-i4\pi/3}\sin k_3), \tag{5.11}$$

$$H^{21}_{int} = \sum_{j=1}^{6} t^{14}_{a_j} e^{ik\cdot a_j} = -2\Re[t^{14}](\cos k_1 + e^{i2\pi/3}\cos k_2 + e^{i4\pi/3}\cos k_3) - 2\Im[t^{14}](\sin k_1 + e^{i2\pi/3}\sin k_2 + e^{i4\pi/3}\sin k_3), \tag{5.12}$$

$$\boldsymbol{\varepsilon} = t^{ij}_0 \delta_{ij}. \tag{5.13}$$

The tight-binding effective Hamiltonian described above gives a very approximate description of the electronic structure, as shown in Fig ??(left). The hopping terms are obtained via a least squares standard approach in order to match the DFT calculation. We can simplify these expressions while maintaining accuracy in the description by taking the limit $\vec{k} \to \Gamma$. Thus, the reduced form for the tight-binding Hamiltonian matrix elements,

$$\mathcal{H}_J(\vec{k}) = (-1)^{2J+1}\varepsilon_J + (-1)^{2J} h_{J,0}(\vec{k}) + h_{J,R_3}(\vec{k}) + h_{J,R_1}(\vec{k}) \tag{5.14}$$

where $h^J_0(\vec{k}) = \xi\vec{k}^2$, $h^J_{R_3}(\vec{k}) = \alpha^J_{R_3}[(k_+)^3 + (k_-)^3]\sigma_z$, $h^J_{R_1}(\vec{k}) = \alpha^J_{R_1}(\vec{\sigma}\times\vec{k})\cdot\hat{z}$ and $\mathcal{H}_{int} = \gamma\vec{\sigma}\cdot\vec{k}$. Here, $\mathcal{H}_{1/2}(\vec{k})$ and $\mathcal{H}_{3/2}(\vec{k})$ are the effective terms that described the $|\mathrm{Bi}_{1/2}, \pm 1/2\rangle$ and $|\mathrm{Bi}_{3/2}, \pm 3/2\rangle$ states, respectively and $\mathcal{H}_{int}(\vec{k})$ is the interaction between these states. The parameters are related to the hopping terms and are obtained via a least squares standard approach in order to match the DFT calculation.

It is convenient to rewrite the Hamiltonian $\mathcal{H}(\vec{k} \to \Gamma)$ as a matrix fulfilling the symmetry operations of the C_{3v} point group,

$$\mathcal{H}(\vec{k}) = \begin{pmatrix} -\varepsilon_{1/2} + \xi_{1/2}k^2 & i\alpha^{1/2}_{R_1}k_- & 0 & \gamma k_- \\ -i\alpha^{1/2}_{R_1}k_+ & -\varepsilon_{1/2} + \xi_{1/2}k^2 & \gamma k_+ & 0 \\ 0 & \gamma k_- & \varepsilon_{3/2} - \xi_{3/2}k^2 & i\alpha^{3/2}_{R_1}k_- \\ \gamma k_+ & 0 & -i\alpha^{3/2}_{R_1}k_+ & \varepsilon_{3/2} - \xi_{3/2}k^2 \end{pmatrix}, \tag{5.15}$$

where $k_\pm = k_x \pm ik_y$ and $k^2 = k_x^2 + k_y^2$.

For simplicity in Eq. 5.16 we only consider terms up to second order in $\vec{k}$. In this model the parameters are related to the hopping terms: the on-site energy $\varepsilon_J = t^{ii}_0 + 6\Re[t^{ii}]$, free electron approximation term $\xi_J = \frac{\hbar^2}{2m^*_J} = \frac{3}{2}a^2\Re[t^{ii}]$, the first order Rashba parameter $\alpha_{R_1} = t^{12}3a$ and the interaction $\alpha_{in} = 3\Im[t^{14}]$ is the interaction parameter. We found that $t^{34} \approx 6\times 10^{-3}$, then we can make the approximation $\mathcal{H}^{12}_{J=3/2} = i\alpha^{3/2}_{R_1}k_- = \alpha_{R_1} =$

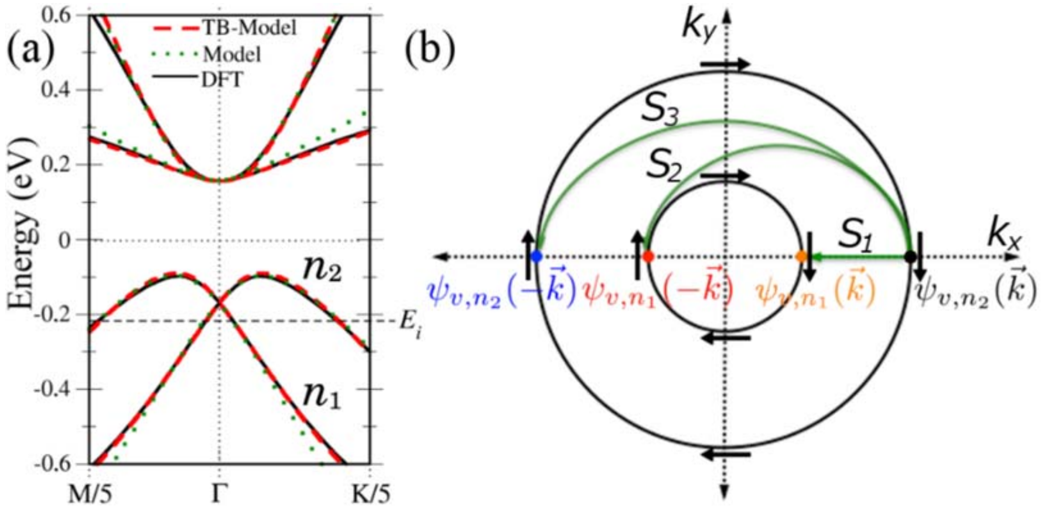

Figure 5.5 - (a) Band structure calculated with DFT, complete tight-binding model and simplified model. (b) Fermi contour at the energy plane E_i obtained from the simplified model. The backscattering processes and the spin textures are represented by green and black arrows, respectively.

$it^{12}3ak_- \approx 0$ and the Hamiltonian is expressed as

$$\mathcal{H}(\vec{k}) = \begin{pmatrix} -\varepsilon_{1/2} + \xi_{1/2}k^2 & i\alpha_{R_1}^{1/2}k_- & 0 & \gamma k_- \\ -i\alpha_{R_1}^{1/2}k_+ & -\varepsilon_{1/2} + \xi_{1/2}k^2 & \gamma k_+ & 0 \\ 0 & \gamma k_- & \varepsilon_{3/2} - \xi_{3/2}k^2 & 0 \\ \gamma k_+ & 0 & 0 & \varepsilon_{3/2} - \xi_{3/2}k^2 \end{pmatrix}. \tag{5.16}$$

Such toy model provides an approximate description of the DFT band structure, as shown in Fig 5.5. However, since the three order Rashba term is not considered ($h_{R_3}(\vec{k}) = \alpha_{R_3}(k_x^3 - 3k_x k_y^2)$, with $\alpha_{R_3} = \Im[t_a^{ii}]\frac{1}{4}a^3$), there are not any warping effect. Thus, the Fermi contour consists of two concentric circles, as represented in Fig 5.5 for the energy E_i.

For illustrative proposal and without loss of generality considering $\xi^{1/2} \approx \xi^{3/2} = \xi$, we then rewrite the Hamiltonian as

$$\mathcal{H}(\vec{k}) = \begin{pmatrix} -\varepsilon + \xi k^2 & i\alpha_{R_1}k_- & 0 & \gamma k_- \\ -i\alpha_{R_1}k_+ & -\varepsilon + \xi k^2 & \gamma k_+ & 0 \\ 0 & \gamma k_- & \varepsilon - \xi k^2 & 0 \\ \gamma k_+ & 0 & 0 & \varepsilon - \xi k^2 \end{pmatrix}. \tag{5.17}$$

We plot the Fermi contours obtained from this Hamiltonian and represent the backscattering processes in Fig 5.5b. In the valence band, an energy plane below(above) the band crossing consists of two concentric circles with the same(opposite) in-plane helical spin

$\epsilon_{1/2}$	$\epsilon_{3/2}$	$\xi_{1/2}$	$\xi_{3/2}$	γ	$\alpha_{R_1}^{1/2}$	$\alpha_{R_1}^{3/2}$
0.1685 eV	0.1575 eV	10 eV/Å^2	7.4 eV/Å^2	-3.5853 eV/Å	3.0919 eV/Å	0.1 eV/Å

Table 5.5 - Parameters of the effective tigh binding model.

texture. Likewise, in the conduction band, an energy plane consists of two concentric circles with the same in-plane helical spin texture. Because of this bulk spin texture, the elastic and inelastic backscattering processes represented by S_2 and S_3, respectively, are forbidden.

Phenomenological considerations

Through a phenomenological analysis of the electronic structure, we describe the effects required to reproduce the results obtained via DFT calculations. Although the Rashba effect and the surface states in 3D topological insulators arise as a result of different physical properties, the effective Hamiltonian that captures the Rashba M-shape in 2D semiconductors systems is also used to describe the surface states in a 3D topological insulator: $\mathcal{H}(\vec{k}) = h_0(\vec{k}) + h_{R_1}(\vec{k})$. The first term $h_0(\vec{k}) = \xi\vec{k}^2$ is the quasi-free electron approximation and the second term $h_{R_1}(\vec{k}) = \alpha_{R_1}(\vec{\sigma} \times \vec{k}) \cdot \hat{z}$ represents the interaction between the spin Pauli matrices vector $\vec{\sigma}$ and the momentum $\vec{k}$. Here α_{R_1} is the Rashba coefficient, and z the unit vector perpendicular to the plane in which lies the semiconductor. When the term ξ, which depends on the effective mass m^* and the electron mass m_e ($\xi = \frac{\hbar^2}{2m^* m_e}$), is sufficiently small relative to parameter α_R, states with linear dispersion and helical spin texture appears, describing the surface states in a 3D TI. Otherwise, the Rashba effect band dispersion appears. According to this reasoning, both the $|1/2, \pm 1/2\rangle$ and the $|3/2, \pm 1/2\rangle$ effective states have the $h_0(\vec{k})$ term, which introduces the band parabolic effect. The hexagonal warping in the conduction and valence bands is introduced considering the three order Rashba term $h_{R_3}(\vec{k}) = \alpha_{R_3}[(k_x + ik_y)^3 + (k_x - ik_y)^3]\sigma_z$ in both the $|1/2, \pm 1/2\rangle$ and the $|3/2, \pm 1/2\rangle$ effective states. Joining these terms, the effective Hamiltonian can be written as:

$$\mathcal{H} = \begin{pmatrix} \mathcal{H}_{1/2}(\vec{k}) & \mathcal{H}_{int}(\vec{k}) \\ \mathcal{H}_{int}^{\dagger}(\vec{k}) & \mathcal{H}_{3/2}(\vec{k}) \end{pmatrix}, \tag{5.18}$$

where $\mathcal{H}_{1/2}(\vec{k}) = h_0^{1/2}(\vec{k}) + h_{R_3}^{1/2}(\vec{k}) + h_{R_1}^{1/2}(\vec{k})$ and $\mathcal{H}_{3/2}(\vec{k}) = -h_0^{3/2}(\vec{k}) + h_{R_3}^{3/2}(\vec{k}) + h_{R_1}^{3/2}(\vec{k})$ are the effective Hamiltonian that described the $|1/2, \pm 1/2\rangle$ and $|3/2, \pm 1/2\rangle$ effective states, respectively. The phenomenological analysis of the band structure behavior does not provide information about the interaction Hamiltonian between these states, $\mathcal{H}_{int}(\vec{k})$.

Scattering rate

In order to quantify the probability of backscattering, we calculate the scattering rate due to a single coulomb impurity considering the bare coulomb potential[40], $\mathcal{S}_{\vec{k}'n',\vec{k}n} = \frac{2\pi}{\hbar}\frac{q_e^4}{4A^2\kappa^2\beta^2}(1 - cos\theta_{\vec{k}',\vec{k}})\boldsymbol{I}_{\vec{k}',n',\vec{k},n}\delta(E_n - E_{n'})$. Here, A is the unit area, q_e is the single-electron charge, κ is the static dielectric constant and $\beta = |\vec{k} - \vec{k}'|$ and $I_{\vec{k}',n_1,\vec{k},n_2} = |\langle\psi_{E_{n_1}}(\vec{k}')|\psi_{E_{n_2}}(\vec{k})\rangle|^2$ is the overlap integral, which is calculated using the normalized wavefunction,

$$\psi_{E_{n_\lambda}}(\vec{k}) = \sqrt{N}\begin{pmatrix} 1 \\ -i\frac{k_+}{\alpha_{R_1}k^2}\frac{(\varepsilon-\xi k^2)^2-E_{n_\lambda}^2+\gamma^2k^2}{\varepsilon-\xi k^2-E_{n_\lambda}} \\ i\frac{\gamma}{\alpha_{R_1}}\frac{(\varepsilon-\xi k^2)^2-E_{n_\lambda}^2+\gamma^2k^2}{(\varepsilon-\xi k^2-E_{n_\lambda})^2} \\ \frac{-\gamma k_+}{(\varepsilon-\xi k^2-E_{n_\lambda})} \end{pmatrix}, \tag{5.19}$$

where $N = \frac{|\varepsilon-\xi k^2-E_{n_\lambda}|^2}{2[(\varepsilon-\xi k^2-E_{n_\lambda})^2+\alpha_{int}k^2]}$. We verify that $I_{-\vec{k}',n_1,\vec{k},n_2} = I_{-\vec{k},n_\lambda,\vec{k},n_\lambda} = 0$ and therefore the scattering rates $\mathcal{S}_{-\vec{k}',n_1,\vec{k},n_2}$ and $\mathcal{S}_{-\vec{k},n_\lambda,\vec{k},n_\lambda}$ are null, proving that backscattering processes are unlikely. On the other hand, in an ordinary out-plane spin polarized Rashba material, such as the thin films of the BiTeI 3D topological insulator[27], in an energy plane below(above) the band crossing the bands have opposite(same) in-plane chiral spin texture (Fig 5.6a) and therefore, the elastic backscattering S_3 is forbidden. Different from PbBiI, in a Rashba semiconductor, below the band crossing the inelastic backscattering S_2 is allowed and $I_{-\vec{k}',n_1,\vec{k},n_2} \approx 1$[16, 42], as represented by the green arrows in Fig 5.6a.

Using the found wavefunction we analytically show that the bulk bands scattering from k to $-k$ is forbidden for an arbitrary k-point. To address this issue, we calculate the overlap integral $\boldsymbol{I}_{-\vec{k},n,\vec{k},n} = |\sum_{\alpha=1}^{4} c_{n,\alpha}^*(-\vec{k})c_{n,\alpha}(\vec{k})|^2$ (with $|\psi_n(\vec{k})\rangle = \sum_{\alpha=1}^{4} c_{n,\alpha}(\vec{k})|Bi_{J_\alpha}, j_z\rangle$), which is proportional to the scattering rate. In the bare Coulomb potential approximation the scattering rate due to a single Coulomb impurity is written as

$$\mathcal{S}_{-\vec{k}n,\vec{k}n} = \frac{\pi}{\hbar}\frac{q_e^4}{4A^2\kappa^2\beta^2}\boldsymbol{I}_{-\vec{k},n,\vec{k},n}\delta(E_n - E_{n'}), \tag{5.20}$$

where A is the unit area, q_e is the single-electron charge, κ is the static dielectric constant and $\beta = |\vec{k} - \vec{k}'|$.

In order to find an analytic expression for $\mathcal{S}_{\vec{k}'n',\vec{k}n}$ we solved the eigensystem $\mathcal{H}\psi_n(\vec{k}) = E_n\psi_n(\vec{k})$. Only to solve an illustrative example we consider the simplification $\varepsilon_{1/2} = \varepsilon_{3/2} = \varepsilon$ and $\xi_{1/2} = \xi_{3/2} = \xi$. Thus, for a arbitrary energy E_n,

$$\det(\mathcal{H}(\vec{k})) = [(\varepsilon - \xi k^2)^2 - E_n^2 + \gamma^2k^2]^2 - \alpha_{R_1}^2k^2(\varepsilon - \xi k^2 - E_n)^2 = 0 \tag{5.21}$$

$$\Rightarrow \frac{(\varepsilon - \xi k^2)^2 - E_{n_\lambda}^2 + \gamma^2k^2}{\alpha_{R_1}k(\varepsilon - \xi k^2 - E_{n_\lambda})} = (-1)^\lambda. \tag{5.22}$$

Therefore, the energies for the valence and conduction bands are

$$E_{v,n_\lambda} = (-1)^\lambda \frac{\alpha_{R_1} k}{2} - \frac{1}{2}\{(\alpha_{R_1} k)^2 - 4[(-1)^\lambda \alpha_{R_1} k(\varepsilon - \xi k^2) - (\varepsilon - \xi k^2)^2 - \gamma k^2]\}^{1/2} \quad (5.23)$$

and

$$E_{c,n_\lambda} = (-1)^{\lambda+1} \frac{\alpha_{R_1} k}{2} + \frac{1}{2}\{(\alpha_{R_1} k)^2 - 4[(-1)^{\lambda+1} \alpha_{R_1} k(\varepsilon - \xi k^2) - (\varepsilon - \xi k^2)^2 - \alpha_{int} k^2]\}^{1/2}, \quad (5.24)$$

respectively. These functions qualitatively reproduce the DFT band structure, as shown in Fig **??**. Since just $\varepsilon_{1/2}$ and $\varepsilon_{3/2}$ define the energy gap, we do not consider the simplification $\varepsilon_{1/2} = \varepsilon_{3/2} = \varepsilon$ to plot the energies E_{c,n_λ} and E_{v,n_λ}.

Using this expression for the wavefunction $\psi_{E_{n_\lambda}}(\vec{k})$ and its time reversal $\mathcal{T}\psi_{E_{n_\lambda}}(\vec{k}) = \psi^*_{E_{n_\lambda}}(-\vec{k})$ we find that

$$\langle \psi^*_{E_{n_\lambda}}(-\vec{k}) | \psi_{E_{n_\lambda}}(\vec{k}) \rangle = \frac{(\varepsilon - \xi k^2 - E_{n_\lambda})^2}{2((\varepsilon - \xi k^2 - E_{n_\lambda})^2 + \gamma k^2)} \left[1 - \frac{((\varepsilon - \xi k^2)^2 - E^2_{n_\lambda} + \alpha^2 k^2)^2}{\alpha^2_{R_1} k^2 (\varepsilon - \xi k^2 - E_{n_\lambda})^2} \right.$$
$$\left. + \frac{\gamma^2((\varepsilon - \xi k^2)^2 - E^2_{n_\lambda} + \alpha^2 k^2)^2}{\alpha^2_{R_1}(\varepsilon - \xi k^2 - E_{n_\lambda})^4} - \frac{\gamma^2 k^2}{(\varepsilon - \xi k^2 - E_{n_\lambda})^2} \right]. \quad (5.25)$$

Substituting Eq. 5.22 into Eq. 5.25, we obtain

$$\langle \psi^*_{E_{n_\lambda}}(-\vec{k}) | \psi_{E_{n_\lambda}}(\vec{k}) \rangle = \frac{(\varepsilon - \xi k^2 - E_{n_\lambda})^2}{2((\varepsilon - \xi k^2 - E_{n_\lambda})^2 + \gamma k^2)}$$
$$\left[1 - 1 + \frac{\gamma^2 k^2}{(\varepsilon - \xi k^2 - E_{n_\lambda})^2} - \frac{\gamma^2 k^2}{(\varepsilon - \xi k^2 - E_{n_\lambda})^2} \right] = 0, \quad (5.26)$$

which evidences that for any energy level and any $\vec{k}$-point the elastic backscattering processes are forbidden in valence and conduction bands of the bulk band structure. Therefore, the scattering rates $\mathcal{S}_{-\vec{k},n_2,\vec{k},n_2}$ and $\mathcal{S}_{-\vec{k},n_1,\vec{k},n_1}$ for the PbBiI system in the presence of Coulomb scattering center are zero.

To calculate the scattering rate for inelastic backscattering process $S_{-\vec{k}',n_1,\vec{k},n_2}$, we consider $-\vec{k}' = -\vec{k}/\Delta$. There is always a value of $\Delta(E_i) = \Delta_i$ for which $E_{v,n_1}(-\vec{k}/\Delta) = E_{v,n_2}(\vec{k})$. Thus, we obtain

$$\langle \psi^*_{E_{n_1}}(-\vec{k}/\Delta) | \psi_{E_{n_2}}(\vec{k}) \rangle = \frac{(\varepsilon' - \xi k^2 - E_{n_1})(\varepsilon - \xi k^2 - E_{n_2})}{2[(\varepsilon' - \xi k^2 - E_{n_1})^2 + \gamma' k^2]^{1/2}[(\varepsilon - \xi k^2 - E_{n_2})^2 + \gamma k^2]^{1/2}}$$
$$\left[1 - \frac{[(\varepsilon' - \xi k^2)^2 - E^2_{n_1} + \alpha'^2_{int} k^2][(\varepsilon - \xi k^2)^2 - E^2_{n_2} + \alpha^2_{int} k^2]}{\alpha'_{R_1} \alpha_{R_1} k^2 (\varepsilon' - \xi k^2 - E_{n_1})(\varepsilon - \xi k^2 - E_{n_2})} \right.$$
$$\left. + \frac{\gamma' \gamma((\varepsilon' - \xi k^2)^2 - E^2_{n_1} + \alpha'^2 k^2)((\varepsilon - \xi k^2)^2 - E^2_{n_\lambda} + \alpha^2 k^2)}{\alpha'_{R_1} \alpha_{R_1} (\varepsilon' - \xi k^2 - E_{n_1})^2 (\varepsilon - \xi k^2 - E_{n_2})^2} - \frac{\alpha'_{int} \gamma k^2}{(\varepsilon' - \xi k^2 - E_{n_1})(\varepsilon - \xi k^2 - E_{n_2})} \right]. \quad (5.27)$$

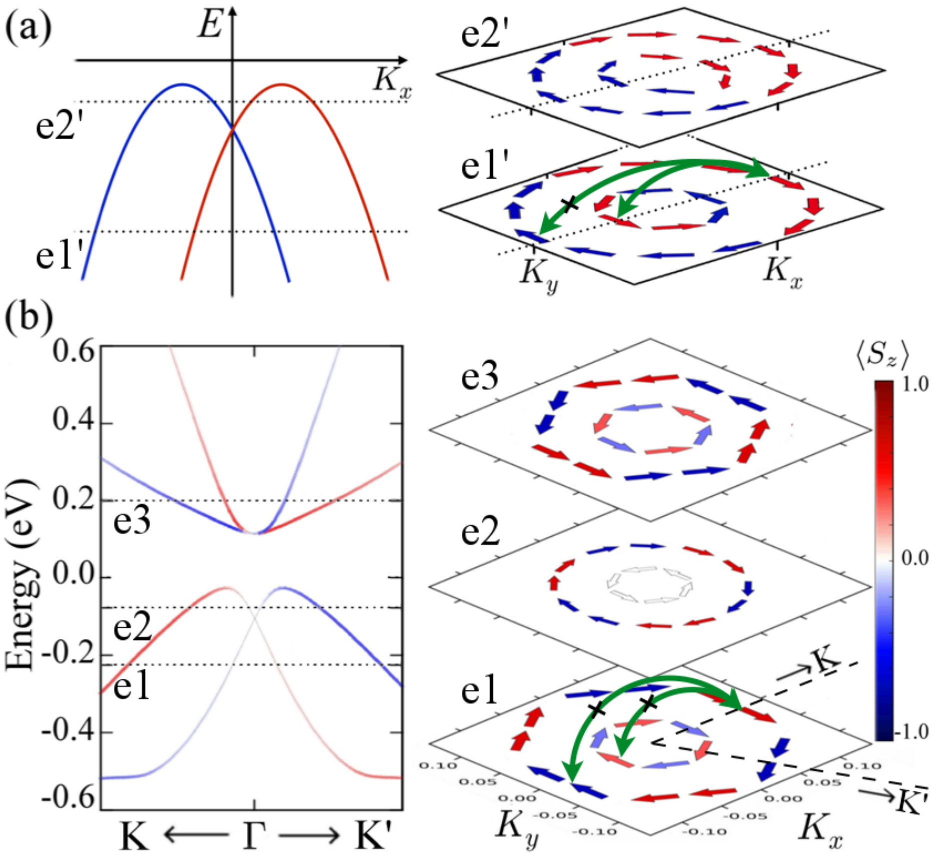

Figure 5.6 - Band structure and spin texture of (a) an out-plane spin polarized Rashba material and (b) the PbBiI system. The dotted lines in the band structure represent the energy planes (e1-e3 and e1'-e2') in which we show the in-plane spin texture, whose magnitudes are represented by the size of the arrows. In this arrows and in the band structure, the color code stands for the normalized $\langle S_z \rangle$ spin polarization. The backscattering processes S_2 and S_3 are represented by green arrows.

Using Eq. 5.22 we have that:

$$\langle \psi^*_{E_{n_1}}(-\vec{k}/\Delta)|\psi_{E_{n_2}}(\vec{k})\rangle = \frac{(\varepsilon' - \xi k^2 - E_{n_1})(\varepsilon - \xi k^2 - E_{n_2})}{2[(\varepsilon' - \xi k^2 - E_{n_1})^2 + \gamma' k^2]^{1/2}[(\varepsilon - \xi k^2 - E_{n_2})^2 + \gamma k^2]^{1/2}}[1 - 1$$

$$- \frac{\alpha'_{int}\gamma k^2}{(\varepsilon' - \xi k^2 - E_{n_1})(\varepsilon - \xi k^2 - E_{n_2})} + \frac{\alpha'_{int}\gamma k^2}{(\varepsilon' - \xi k^2 - E_{n_1})(\varepsilon - \xi k^2 - E_{n_2})}\Bigg] = 0, \tag{5.28}$$

where $\gamma' = a\gamma$, $\alpha'_{R_1} = a\alpha_{R_1}$ and $\varepsilon' = a^2\varepsilon$. Now, it is evident that the inelastic scattering process S_2 is forbidden. In contrast with an ordinary Rashba semiconductor in which $I_{-\vec{k}',n_1,\vec{k},n_2} \approx 1$, in the PbBiI system we obtain $I_{-\vec{k}',n_1,\vec{k},n_2} = 0$. Therefore, the inelastic backscattering process $S_{-\vec{k}',n_1,\vec{k},n_2}$ is very unlikely.

Far from the Γ point, the R_3 symmetry breaking generates nonlinear terms in the SOC such as the three order Rashba term $h_{R_3}(\vec{k})$, which induces $\langle S_z \rangle$ spin polarization and hexagonal warping effect in the bulk states[43, 44], as represented in Fig 5.6b. Although

S_z spin-polarized increases, the expected value of S_z is still near zero. Because the $\langle S_x \rangle$ and $\langle S_y \rangle$ spin flips are required so that the inelastic scattering process $\mathcal{S}_{-\vec{k}',n_1,\vec{k},n_2}$ occurs (see Fig 5.6b), the overlap integral $I_{-\vec{k}',n_1,\vec{k},n_2}$ is still small compared to the value found in an ordinary Rashba semiconductors and the probability that the scattering process S_2 occurs remains low. Analogous to the surface states of $\mathrm{Bi_2Te_3}$[44], near the Γ point, the $\langle S_z \rangle$ spin-polarization and the warping hexagonal tend to zero and the only contribution coming from the lack of inversion symmetry is the first order Rashba term, $h_{R_1}(\vec{k})$. Thus, to obtain the unconventional spin texture near the Γ point is only enough to consider both Rashba effect and band inversion, as it was done in eq. 5.16. According to our DFT results, the Rashba spin-splitting is about 60 meV, which are huge compared with the values found in semiconductors and surprisingly is among the highest found in 3D systems[21, 22, 20, 23, 24, 27]. This value can be increased up to $E_R \approx 90$ meV applying large compressive strain (see Supplemental Material).

On the other hand, since the out-plane spin polarization oscillates according to the C_{3v} symmetry, as occurs in thin films of $\mathrm{Bi_2Te_3}$[44], at the $\Gamma \rightarrow M$ symmetry path, the S_z spin component is zero (see Fig 5.6) and therefore, inelastic backscattering processes are completely suppressed. The armchair nanoribbon BZ is parallel to the $\Gamma \rightarrow M$ symmetry path at the k_y axis of the hexagonal BZ. Thus, scattering processes are dominated by the S_x spin component and hence, the elastic and inelastic backscattering is forbidden for bulk and edge states, as shown in Fig 5.7. Similarly, the zigzag nanoribbon BZ is parallel to the k_x axis and therefore, $\langle S_x \rangle = 0$. Because of the non-zero $\langle S_z \rangle$ spin components, there is a low probability of inelastic backscattering in accordance with the bulk behavior discussed above (see Supplemental Material). Because of the strong SOC, the spin and momentum are constrained to be perpendicular. This spin-momentum locking implies that Dirac cones of different edges are required to have the same S_x spin texture and different S_z spin texture of spin in the armchair nanoribbon, as represented in Fig 5.7c.

The protected bulk states near the Γ point only appear in the energy region in which the Rashba effect and the band inversion point take place. This energy region overlaps with the bottom of the conduction band, which is at $\Gamma \rightarrow M$ symmetry path, as shown inf Fig 5.7b. The bottom of the conduction band and hence, the energy range in which the unusual spin texture is present can be modified by applying tensile strain (see Supplemental Material). Indeed, the inverted bandgap at Γ can be equal to the bandgap E_g when strain is applied.

It is well established that the Bi-Pb alloy can be realized experimentally maintaining the $R\bar{3}m$ space group [45, 46]. The Pb-Bi rhombohedral alloy along the [111] direction can be considered as a stack of PbBi honeycomb lattices that are weakly bonded (mainly ruled by Van der Waals type interaction) to each other, similarly to the bismuth bilayers[47]. The dangling bonds that appear at the Pb-rich PbBi surface can be eliminated by bonding

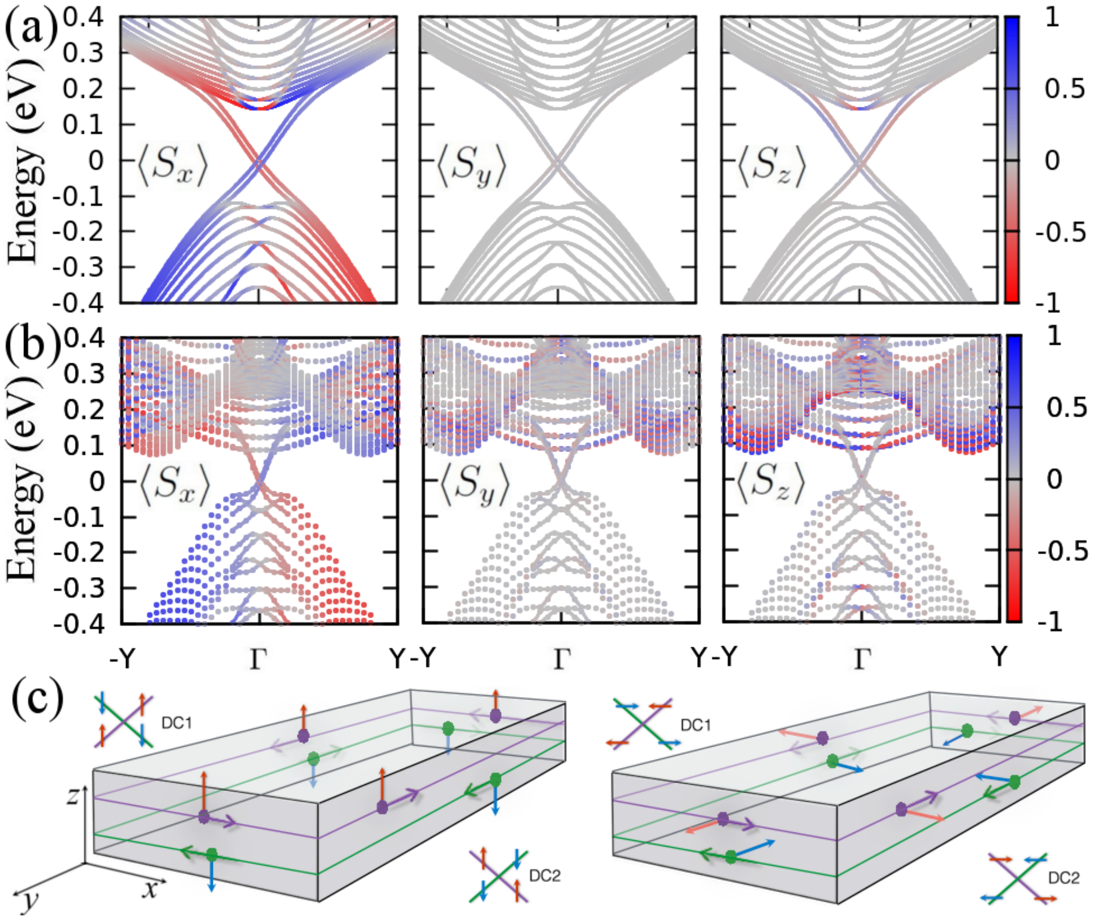

Figure 5.7 - (a) Tight-binding and (b) DFT spin-texture band structure of an armchair nanoribbon with 98.7 Å wide. The color code stands for the spin polarization. (c) Pictorial representation of edge states with $\langle S_z \rangle$ (left) and $\langle S_x \rangle$ (right) spin polarization.

to iodine atoms and hence, the proposed spin texture could be observed in the PbBiI system via STM experiments analogously to the observation of Bi-bilayers' edge states[47].

The C_{3v} symmetry in the PbBiI system leads to a interaction term different from the BHZ model used to describe the QHS phase in HgTe/CdTe quantum wells[48]. Although the BHZ model considering the Rashba effect has been used to describe asymmetric InAs/GaSb/AlSb quantum wells[49], the consequences of a huge Rashba spin-splitting and the three order Rashba term in a bulk inverted band gap, such as the unconventional spin texture reported here, have been ignored.

In summarizing, the simultaneous presence of a huge Rashba effect and a inverted bandgap in systems with C_{3v} symmetry leads to conduction and valence bands with a Rashba-like spin-splitting with the same helical in-plane spin texture and with null S_z spin-polarization at the $\Gamma \rightarrow M$ symmetry paths. Thus, the spin texture in the nanoribbons depends on its orientation. We find that bulk states are protected by the TR symmetry and contrary to what happens in most doped QSH systems, the bulk states do not contribute to the backscattering, opening the way for realizing novel applications of topological edge states. Additionally, we proposed a new honeycomb-lattice QSH insulator mechanically stable - the PbBiI system, which has a large Rashba splitting of 60 meV, a large nontrivial gap of 0.14 eV and hence, it presents the predicted unconventional spin texture. As far as we know, the PbBiI system is the first system that has such spin texture properties in its bulk band structure.

Bibliography

[1] D. Pesin and A. H. MacDonald, Nat Mater **11**, 409 (2012).

[2] A. Brataas, A. D. Kent, and H. Ohno, Nat Mater **11**, 372 (2012).

[3] T. Liang, Q. Gibson, M. N. Ali, M. Liu, R. J. Cava, and N. P. Ong, Nat Mater **14**, 280 (2015), letter.

[4] L. Liu, O. J. Lee, T. J. Gudmundsen, D. C. Ralph, and R. A. Buhrman, Phys. Rev. Lett. **109**, 096602 (2012).

[5] M. Z. Hasan and C. L. Kane, Rev. Mod. Phys. **82**, 3045 (2010).

[6] X.-L. Qi and S.-C. Zhang, Rev. Mod. Phys. **83**, 1057 (2011).

[7] C. Brune, A. Roth, H. Buhmann, E. M. Hankiewicz, L. W. Molenkamp, J. Maciejko, X.-L. Qi, and S.-C. Zhang, Nat Phys **8**, 485 (2012).

[8] L. V. Kulik, A. V. Gorbunov, A. S. Zhuravlev, V. B. Timofeev, S. Dickmann, and I. V. Kukushkin, Sci. Rep. **5** (2015), article.

[9] S. Maekawa, S. O. Valenzuela, E. Saitoh, and T. Kimura, **Spin Current** (Series on Semiconductor Science and Technology 17, Oxford University Pres, 2012).

[10] R. Jansen, Nat Mater **11**, 400 (2012).

[11] A. Manchon, H. C. Koo, J. Nitta, S. M. Frolov, and R. A. Duine, Nat Mater **14**, 871 (2015).

[12] D. Bercioux and P. Lucignano, Reports on Progress in Physics **78**, 106001 (2015).

[13] C. L. Kane and E. J. Mele, Phys. Rev. Lett. **95**, 146802 (2005).

[14] M. König, S. Wiedmann, C. Brüne, A. Roth, H. Buhmann, L. W. Molenkamp, X.-L. Qi, and S.-C. Zhang, Science **318**, 766 (2007).

[15] E. B. Olshanetsky, Z. D. Kvon, G. M. Gusev, A. D. Levin, O. E. Raichev, N. N. Mikhailov, and S. A. Dvoretsky, Phys. Rev. Lett. **114**, 126802 (2015).

[16] Y. A. Bychkov and E. I. Rashba, JETP Lett **39**, 78 (1984).

[17] S. LaShell, B. A. McDougall, and E. Jensen, Phys. Rev. Lett. **77**, 3419 (1996).

[18] C. R. Ast, J. Henk, A. Ernst, L. Moreschini, M. C. Falub, D. Pacilé, P. Bruno, K. Kern, and M. Grioni, Phys. Rev. Lett. **98**, 186807 (2007).

[19] Y. M. Koroteev, G. Bihlmayer, J. E. Gayone, E. V. Chulkov, S. Blügel, P. M. Echenique, and P. Hofmann, Phys. Rev. Lett. **93**, 046403 (2004).

[20] J. Nitta, T. Akazaki, H. Takayanagi, and T. Enoki, Phys. Rev. Lett. **78**, 1335 (1997).

[21] T. Hirahara, T. Nagao, I. Matsuda, G. Bihlmayer, E. V. Chulkov, Y. M. Koroteev, P. M. Echenique, M. Saito, and S. Hasegawa, Phys. Rev. Lett. **97**, 146803 (2006).

[22] S. Mathias, A. Ruffing, F. Deicke, M. Wiesenmayer, I. Sakar, G. Bihlmayer, E. V. Chulkov, Y. M. Koroteev, P. M. Echenique, M. Bauer, and M. Aeschlimann, Phys. Rev. Lett. **104**, 066802 (2010).

[23] H. Yuan, M. S. Bahramy, K. Morimoto, S. Wu, K. Nomura, B.-J. Yang, H. Shimotani, R. Suzuki, M. Toh, C. Kloc, X. Xu, R. Arita, N. Nagaosa, and Y. Iwasa, Nat Phys **9**, 563 (2013), article.

[24] J. H. Dil, F. Meier, J. Lobo-Checa, L. Patthey, G. Bihlmayer, and J. Osterwalder, Phys. Rev. Lett. **101**, 266802 (2008).

[25] Z.-H. Zhu, G. Levy, B. Ludbrook, C. N. Veenstra, J. A. Rosen, R. Comin, D. Wong, P. Dosanjh, A. Ubaldini, P. Syers, N. P. Butch, J. Paglione, I. S. Elfimov, and A. Damascelli, Phys. Rev. Lett. **107**, 186405 (2011).

[26] Y. Zhang, K. He, C.-Z. Chang, C.-L. Song, L.-L. Wang, X. Chen, J.-F. Jia, Z. Fang, X. Dai, W.-Y. Shan, S.-Q. Shen, Q. Niu, X.-L. Qi, S.-C. Zhang, X.-C. Ma, and Q.-K. Xue, Nat Phys **6**, 584 (2010).

[27] K. Ishizaka, M. S. Bahramy, H. Murakawa, M. Sakano, T. Shimojima, T. Sonobe, K. Koizumi, S. Shin, H. Miyahara, A. Kimura, K. Miyamoto, T. Okuda, H. Namatame, M. Taniguchi, R. Arita, N. Nagaosa, K. Kobayashi, Y. Murakami, R. Kumai, Y. Kaneko, Y. Onose, and Y. Tokura, Nat Mater **10**, 521 (2011).

[28] M. S. Bahramy, B. J. Yang, R. Arita, and N. Nagaosa, Nat Commun **3**, 679 (2012).

[29] T. Das and A. V. Balatsky, Nat Commun **4** (2013).

[30] J.-J. Zhou, W. Feng, Y. Zhang, S. A. Yang, and Y. Yao, Scientific Reports **4**, 3841 EP (2014).

[31] J. M. Soler, E. Artacho, J. D. Gale, A. García, J. Junquera, P. Ordejón, and D. Sánchez-Portal, Journal of Physics: Condensed Matter **14**, 2745 (2002).

[32] G. Kresse and J. Furthmüller, Phys. Rev. B **54**, 11169 (1996).

[33] C. M. Acosta, M. P. Lima, R. H. Miwa, A. J. R. da Silva, and A. Fazzio, Phys. Rev. B **89**, 155438 (2014).

[34] L. Fernandez-Seivane, M. A. Oliveira, S. Sanvito, and J. Ferrer, J. of Phys.: Condens. Matter **18**, 7999 (2006).

[35] J. P. Perdew and A. Zunger, Phys. Rev. B **23**, 5048 (1981).

[36] J. P. Perdew, K. Burke, and M. Ernzerhof, Phys. Rev. Lett. **77**, 3865 (1996).

[37] R. Yu, X. L. Qi, A. Bernevig, Z. Fang, and X. Dai, Phys. Rev. B **84**, 075119 (2011).

[38] A. A. Soluyanov and D. Vanderbilt, Phys. Rev. B **83**, 035108 (2011a).

[39] A. A. Soluyanov and D. Vanderbilt, Phys. Rev. B **83**, 235401 (2011b).

[40] G. Yin, D. Wickramaratne, Y. Zhao, and R. K. Lake, Applied Physics Letters **105**, 033118 (2014).

[41] Ishizaka K., Bahramy M. S., Murakawa H., Sakano M., Shimojima T., Sonobe T., Koizumi K., Shin S., Miyahara H., Kimura A., Miyamoto K., Okuda T., Namatame H., Taniguchi M., Arita R., Nagaosa N., Kobayashi K., Murakami Y., Kumai R., Kaneko Y., Onose Y., and Tokura Y., Nat Mater **10**, 521–526 (2011), 10.1038/nmat3051.

[42] K. Sakamoto, T.-H. Kim, T. Kuzumaki, B. Müller, Y. Yamamoto, M. Ohtaka, J. R. Osiecki, K. Miyamoto, Y. Takeichi, A. Harasawa, S. D. Stolwijk, A. B. Schmidt, J. Fujii, R. I. G. Uhrberg, M. Donath, H. W. Yeom, and T. Oda, Nat Commun **4** (2013).

[43] S. Vajna, E. Simon, A. Szilva, K. Palotas, B. Ujfalussy, and L. Szunyogh, Phys. Rev. B **85**, 075404 (2012).

[44] L. Fu, Phys. Rev. Lett. **103**, 266801 (2009).

[45] N. Gokcen, Journal of Phase Equilibria **13**, 21 (1992).

[46] H. C. W. Huang and C. M. Serrano, Journal of Vacuum Science and Technology A **1**, 1409 (1983).

[47] I. K. Drozdov, A. Alexandradinata, S. Jeon, S. Nadj-Perge, H. Ji, R. J. Cava, B. Andrei Bernevig, and A. Yazdani, Nat Phys **10**, 664 (2014).

[48] B. A. Bernevig, T. L. Hughes, and S.-C. Zhang, Science **314**, 1757 (2006).

[49] C. Liu, T. L. Hughes, X.-L. Qi, K. Wang, and S.-C. Zhang, Phys. Rev. Lett. **100**, 236601 (2008).

6. A transistor model: Spin-filtering breaking the mirror symmetry in two-dimensional dual topological insulator

Introduction

The quantum geometrical description of the insulator state gave rise to a breakthrough in the understanding of the topological phases in solids [1, 2, 3, 4]. Topological invariants, e.g., the Z_2-invariant and the Chern number $\mathcal{C}_n$, classify insulators according to the preserved symmetries and the "symmetry-charge" pumped to the boundary [5]. Systems featuring non-zero topological invariant, i.e., topological insulators (TIs), support dissipationless metallic boundary (edge/surface) states protected by a specific crystal symmetry on a bulk insulator [6]. For instance, quantum spin Hall insulators (QSHIs) and topological crystalline insulators (TCIs) are two-dimensional materials (2D) characterized by $Z_2 = 1$ [7, 8, 9] and a non-zero mirror Chern number [10, 11, 12], $\mathcal{C}_M$, respectively. In QSHIs, the edge states are protected by the time-reversal (TR) symmetry, while in TCIs, by either point or mirror symmetries. Topological transitions are typically related to band inversions [13]: the transition from normal insulators to either QSHIs or TCIs with $\mathcal{C}_M = \pm 1$ requires odd number of band inversions, while TCIs with $\mathcal{C}_M = \pm 2$ exhibit even band inversions. Naturally, $\mathcal{C}_M \neq 0$ or ± 1 intrinsically avoid the QSH state ($Z_2 = 1$).

In materials with a dual topological character (DTC), i.e., systems that are simultaneously QSHIs (TIs in three-dimensions) and TCIs [14], external electric and magnetic fields perpendicular to the mirror plane allow the topological states control. Naturally, this intrinsic property arises form the effect of external fields in QSHIs [15, 16, 17] and TCIs [18, 19, 20], e.g., the spin-polarization control and ban-gap size engineering. For instance, although the magnetic field breaks the TR-symmetry, the edge states could still be protected by the mirror symmetry. In the opposite way, an external electric field can break the mirror symmetry but preserves the TR-symmetry. The DTC requires both $Z_2 = 1$ and $\mathcal{C}_M = \pm 1$, which imposes a condition: it must occurred only odd number of band inversion at k-points preserving both the mirror and the TR-symmetry. Since the TR invariant momentum (TRIM) points always come in pairs, this condition is only satisfied by the Γ point.

Since 2D-TCIs are typically systems with $\mathcal{C}_M = \pm 2$, e.g., SnTe multilayers [11, 21], monolayers of SnSe, PbTe, PbSe [22, 23, 24], TlSe [25], and SnTe/NaCl quantum wells [26], DTC in 2D compounds have been predicted only for Na_3Bi layers [27] and graphene [18, 7]. Three dimensional materials exhibiting DTC not only have been predicted in Bi_2Te_3 [14],

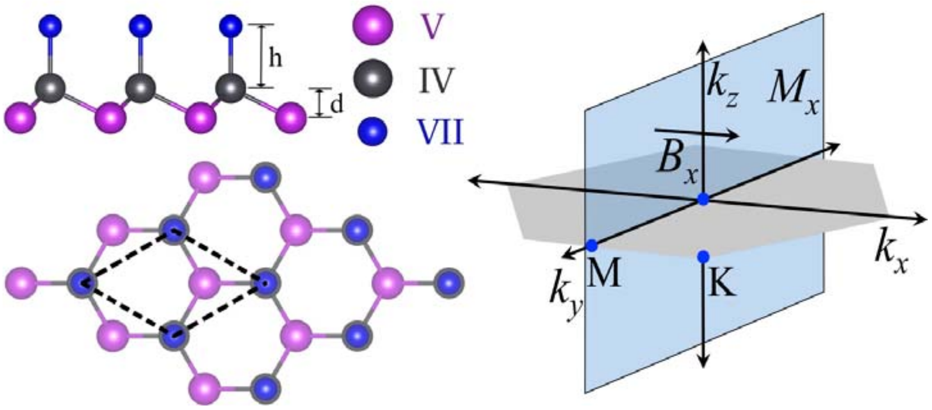

Figure 6.1 - (left) Side and top view of the HF honeycomb lattice compounds. Unit cell is represented by the dashed lines. Atoms of the IV, V, and VII group of the periodic table are presented in gray, purple, and blue, respectively. (right) The respective Brillouin Zone is represented in gray. There are three equivalent reflection planes containing the line connecting two TR equivalent M-points. For illustrative proposal, we only show the plane giving the reflection $x \to -x$ (blue plane).

Bi_4Se_3 [28], and Bi_{1-x} Sb_x [29], but also experimentally observed in the stoichiometric superlattice $[Bi2]_1[Bi2Te3]_2$ [30]. A natural way to search for novel 2D materials featuring DTC is to look for TCIs among the already predicted QSHIs in which band inversion takes place at the Γ point. In half functionalized (HF) group-IV hexagonal materials, an intrinsic magnetic moment spoils the QSHI state, giving rise to the quantum anomalous Hall effect [31]. However, HF IV-V hexagonal-lattices materials feature the QSH and giant Rashba effects [32]. Since, the this effect allows the spin-polarization control, search for non-centrosymmetric systems featuring DTC and their potential for device application is desired for the development of spintronics.

In this letter, we show that HF honeycomb lattice materials can exhibit DTC (See Fig. 6.1), allowing the spin-polarization control through an external electric field breaking the mirror symmetry, i.e., the field induces a spin-polarization parallel to the mirror plane. Based on this effect, we propose a transistor model using the spin-direction as a switch. We confirm that $\mathcal{C}_M = 1$, using the tight-binding effective model we proposed in Ref. [32] to described the QSHIs in HF-hexagonal materials. We also find that a in-plane magnetic field $B = B_x\hat{x}$, breaking the TR-symmetry and preserving the mirror symmetry M_x, leads to a displacement of the Dirac point formed by the edge states in the reciprocal space, confirming the topological mirror symmetry protection. Additionally, a band-gap size engineering can be performed by breaking both TR and mirror symmetries applying an external magnetic field parallel to the mirror plane.

Bulk mirror protection

The HF-honeycomb lattice is formed by two triangular sub-lattices, one consisting of a AX-dimer and the other of atoms B (See Fig 6.1), thus this lattice satisfies the symmetry operations: i) three-fold rotation symmetry $\mathcal{R}_3$ along the z axis, ii) TR symmetry $\mathcal{T}$, and iv) mirror symmetry M_x $(x \rightarrow -x)$ in the yz plane, which is schematically represented in Fig 6.1. The TCI phase is protected by the reflection symmetry respect to the three planes that are perpendicular to the lattice and contain the lines connecting the nearest neighbors in the honeycomb lattice. If the lattice lies in the xy-plane, this mirror symmetry corresponds to the plane M_x in the reciprocal space, as represented in Fig. 6.1.

The HF-honeycomb lattice materials can display an inverted band character, as confirmed by our *ab initio* calculations (See Fig. 6.2). In the inverted order, the valence band maximum has a p-orbital character, mainly dominated by p_z-orbitals of the Bi atoms, whereas the conduction band mainly consists of $p_{x,y}$ Bi orbitals, as shown in Fig 6.2. At the Γ point, the valence (conduction) band is described by the effective states $\{|\mathrm{Bi}_J, j_z\rangle\}$ with the total angular momentum $J = 3/2$ $(J = 1/2)$. Hence, the Hamiltonian in the full SOC basis $\{|\mathrm{Bi}_{1/2}, \pm 1/2\rangle, |\mathrm{Bi}_{3/2}, \pm 1/2\rangle\}$ reads [32]

$$\mathcal{H}(\vec{k} \rightarrow \Gamma) = \begin{pmatrix} -\varepsilon + \xi k^2 & i\alpha k_- & 0 & \gamma k_- \\ -i\alpha k_+ & -\varepsilon + \xi k^2 & \gamma k_+ & 0 \\ 0 & \gamma k_- & \tilde{\varepsilon} - \tilde{\xi} k^2 & 0 \\ \gamma k_+ & 0 & 0 & \tilde{\varepsilon} - \tilde{\xi} k^2 \end{pmatrix}, \tag{6.1}$$

where $k_\pm = k_x \pm k_y$ and $k_2 = k_x^2 + k_y^2$. Here, α_R is the Rhasba parameter, and γ is the interaction term between the $J = 1/2$ and $J = 3/2$ states. The on-site energy (mass term) and kinetic term for states with $J = 1/2$ $(J = 3/2)$ are represented by ε and ξ ($\tilde{\varepsilon}$ and $\tilde{\xi}$), respectively. The band inversion is then introduced only by considering different signs in these terms, i.e., the inverted band-gap at the Γ point is defined by the difference between the mass terms, i.e., $E_g(\vec{k} \rightarrow \Gamma) = \tilde{\varepsilon} + \varepsilon$.

The Hamiltonian describing QSHIs with inversion symmetry breaking (Eq. 6.1) leads to parabolic bands with the same helical in-plane spin texture, forbidding the backscattering in the bulk states (See Fig 6.2) [32]. This spin texture was also observed in the metallic alloy Bi/Cu(111) [37]. We find that the scattering processes are not only limited by the spin texture. Specifically, for $k_x = 0$ the wave-function $|\psi_n^s(\vec{k})\rangle$ (with $s = \uparrow, \downarrow$) can also be indexed with the eigenvalues of the mirror operator $\mathcal{M}_x$, m_J. This is a consequence of commutation relation $[\mathcal{H}(k_x = 0), \mathcal{M}_x]$, which can be easily verified using the matrix representation $\mathcal{M}_x = -i\tau_z \otimes \sigma_x$., i.e., the mirror operator transforms the orbitals as $\mathcal{M}_x|\mathrm{Bi}_{1/2}, \pm 1/2\rangle = -i|\mathrm{Bi}_{1/2}, \mp 1/2\rangle$ and $\mathcal{M}_x|\mathrm{Bi}_{3/2}, \pm 1/2\rangle = i|\mathrm{Bi}_{3/2}, \mp 1/2\rangle$. Using this

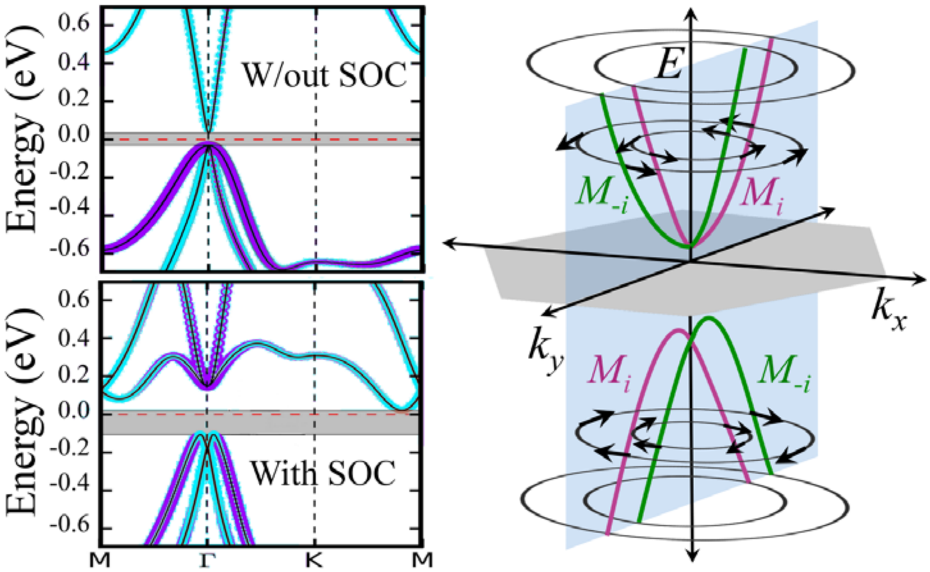

Figure 6.2 - (left) DFT calculation of the band structure with and without SOC for the compound PbBiI. The SOC inverts the states with the total angular momentum $J = 1/2$ and $J = 3/2$, to which the p_z (cian) and p_{xy} (purple) orbitals from Bi meanly contribute, respectively. The band gap is represented by gray areas. (right) Band structure calculated from Eq. 6.1 for $\vec{k}$-points in the mirror plane M_x (blue plane). Then bands are disciminated by the mirror symmetry operator eigenvalues M_i and M_{-i}, which are represented in green and purple, respectively. The arrows at the energy cuts in the valence and conduction bands represent the in-plane spin texture.

representation, we find the eigenvalues $m_{1/2} = \pm i$ and $m_{3/2} = \pm i$, and eigenvectors

$$\phi^{\pm i}_{m_{1/2}} = \begin{pmatrix} 1 \\ \mp 1 \\ 0 \\ 0 \end{pmatrix} \quad \text{and} \quad \phi^{\pm i}_{m_{3/2}} = \begin{pmatrix} 0 \\ 0 \\ 1 \\ \pm 1 \end{pmatrix}. \tag{6.2}$$

The Hamiltonian can be rewritten in the basis of these eigenvectors $\phi^{\pm i}_{m_J}$, by considering the unitary transformation $\overline{\mathcal{H}}(\vec{k}) = U^{-1}\mathcal{H}(\vec{k})U$, where

$$U = \frac{1}{\sqrt{2}} \begin{pmatrix} i\sigma_y + \mathbb{1} & 0 \\ 0 & \sigma_z + \mathbb{1} \end{pmatrix}. \tag{6.3}$$

This leads to a block diagonal matrix,

$$\tilde{\mathcal{H}}(\vec{k})\Big|_{k_x=0} = \mathbb{1} \otimes h_0 + \tau_z \otimes (h - h_R), \tag{6.4}$$

Table 6.1 - Winding number for the one-dimensional Hamiltonians $h_{\pm i}$. Without loss of generality, we impose that $\xi > 0$ and $\alpha > 0$.

	$\delta^{\pm i}_{k=\Gamma}$	$\delta^{\pm i}_{k=M}$	$\mathcal{C}_{\pm i}$
$4 > \varepsilon/\xi$	$\mp$	$\pm$	0
$0 < \varepsilon/\xi < 4$	$\mp$	$\mp$	± 1
$\varepsilon/\xi < 0$	$\pm$	$\mp$	0

where $h = \sigma_y \gamma k$ and $h_R = (\mathbb{1} + \sigma_z)\alpha k/2$, and

$$h_0(k) = \begin{pmatrix} -\varepsilon + \xi k^2 & 0 \\ 0 & \tilde{\varepsilon} - \tilde{\xi} k^2 \end{pmatrix}. \tag{6.5}$$

The blocks of the Hamiltonian related to the eigenvalues of the mirror symmetry operator $\pm i$ are written as $h_{\pm i} = h_0 \pm (h - h_R)$, respectively. The Hamiltonian $h_{\pm i}$ leads to the band structure discriminating mirror eigenvalues, as represented in Fig. 6.2. Naturally, the matrix $U^{-1}\mathcal{M}_x U$ is diagonal.

The Zeeman term associated to magnetic fields perpendicular to the mirror plane, $\mathcal{H}_{B_x} = \tau_z \otimes \sigma_x B_x$, commutes with the mirror operator $\mathcal{M}_x$ (See Fig. 6.1). By taking the unitary transformation $U^{-1}\mathcal{H}_{B_x}U = -\tau_z \otimes \mathbb{1} B_x$, we verify that only diagonal terms are introduced in the Hamiltonian $\tilde{\mathcal{H}}(\vec{k})$. Specifically, band with different mirror eigenvalues are shifted due to the Zeeman term $\mathcal{H}_{B_x}$, i.e., $h_{\pm i} \to h_{\pm i} \mp \mathbb{1} B_x$ (See Fig. 6.3), leading to a Dirac semi-metal for $B_x > 2.85 \cdot 10^{-2} \mu_B$ eV [**?**]. The external magnetic field breaks the TR symmetry, splitting the up and down spin states at the TR invariant-momentum points. The QSH effect is then spoiled, i.e. $Z_2 = 0$, but the band structure is still protected by the mirror symmetry $\mathcal{M}_x$. On the other hand, an external magnetic field parallel to the mirror plane $\mathcal{H}_{B_\parallel} = \mathbb{1} \otimes (\sigma_y B_y + \sigma_z B_z)$ gives rise to a coupling term between h_i and h_{-i}, breaking both TR and mirror symmetries. The magnetic field also induces a spin-polarization in the direction in which is applied. For instance, the spin has non-zero components in the y-axis when the magnetic field $U\mathcal{H}_{B_y}U^{-1}$ is considered, while the out-plane spin component is still zero, as apparent from Fig. 6.3.

Mirror Chern number

In 2D-TCIs protected by a mirror plane parallel to the structure, the mirror Chern number and Hall conductivity are calculated through the Berry phase $\Omega^{\pm i}_n(k_x, k_y)$[10, 25]. Here, since the mirror plane is perpendicular to the plane containing the 2D structure, the mirror Chern number $\mathcal{C}_M$ is calculated via the winding numbers $\mathcal{C}_{\pm i}$, which are essentially the Zak phase for the one-dimensional effective Hamiltonian $h_{\pm i}$ [38, 39, 40]. To better understand the mirror symmetry protection, we explicitly calculate this winding numbers by considering the lattice model given by the substitutions $ka \to \sin ka$ and $(ka)^2 \to$

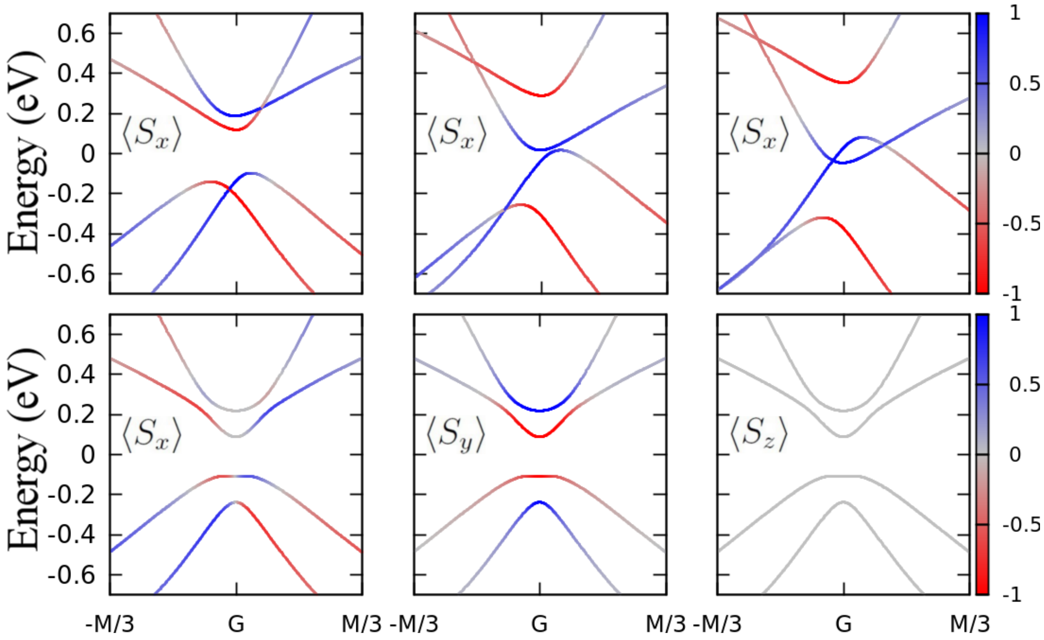

Figure 6.3 - (top) Expected values of the S_x spin operators for the bulk band structure in a magnetic field of 0.065, 0.136, and 0.200 $10^{-2}\mu_B$ eV in the x. The band-gap closes for $B_x > 2.85 \cdot 10^{-2}\mu_B$ eV. (Bottom) Spin texture for the bulk band structure in a magnetic field of $0.065 \cdot 10^{-2}\mu_B$ eV in the y direction. The color code stands for the spin orientation.

$2(1 - \cos ka)$, i.e.,

$$h_{\pm i} = \sigma_z(\overline{\varepsilon} \pm \overline{\alpha}) \pm (\sigma_y \overline{\gamma} - \mathbb{1}\overline{\alpha}), \tag{6.6}$$

where $\overline{\varepsilon} = -\varepsilon + 2\xi(1 - \cos ak)/a^2$, $\overline{\gamma} = \gamma \sin(ak)/a$, and $\overline{\alpha} = \alpha \sin(ak)/2a$. The winding number is then directly related to band indexes $\delta_k^{\pm i} = \operatorname{sgn}(\overline{\varepsilon} \pm \overline{\alpha}) \operatorname{sgn}(\pm\overline{\gamma})$ of the states involved in the band inversion at the symmetry points $k = \Gamma, M$ in the mirror plane, as calculated for one-dimensional topological insulators [41],

$$\mathcal{C}_{\pm i} = -\frac{1}{2}\left(\delta_{k=\Gamma}^{\pm i} + \delta_{k=M}^{\pm i}\right). \tag{6.7}$$

The conditions leading to a non-zero winding number are summarized in Table 6.1. For $0 < \varepsilon/\xi < 4$ the mirror Chern number is $\mathcal{C}_M = \frac{1}{2}(\mathcal{C}_i - \mathcal{C}_{-i})$=1, indicating that HF-honeycomb materials are DTIs protected by both the TR-symmetry and the mirror symmetry operator $\mathcal{M}_x$. This can also be verified from [38, ?],

$$\mathcal{C}_i = \frac{1}{2\pi}\int_0^{2\pi} dk \frac{h_z \partial_y h_y - h_y \partial_z h_z}{h_z^2 + h_y^2}, \tag{6.8}$$

where we consider the unitary transformation $\chi h_i(k)\chi^{-1} = h_0\mathbb{1} + h_z\sigma_x + h_y\sigma_y$, with $\chi = i\sigma_y/\sqrt{2}$. Naturally, external magnetic and electric fields can be used to remove this topological protection, which would allow to control the nano-ribbon electronic structure, e.g., the band-gap and spin texture, as we show below.

Transistor model: transverse external electric field

Metallic edge states, the most interesting feature in both TCIs and QSHIs, are computed by considering open boundary conditions in the tight-binding model of Ref. [32]. First, we confirm the presence of edge states preserving the TR symmetry, i.e., anti-propagating spin current in each edge. The spin is forced to be oriented in the x-axis to preserved the mirror symmetry in armchair nano-ribbons, as shown in Fig. 6.4a. Therefore, different from the out-plane spin polarized edge states in the known QSHIs, the states spatially localized in different edge and with the same momentum also have the same spin direction (See Fig. 6.4c). The spin-flip is then required for scattering processes involving state spatially localized in different edges. This spin texture has been also observed in curve QSHIs [42]. In zigzag nanoribbons, the mirror symmetry is intrinsically broken and hence, the spin is not only oriented in the x-axis [32].

An external electric field breaking the mirror symmetry $\mathcal{M}_x$ can be introduced by modifying the on-site term, i.e., $\tilde{\varepsilon}_n(\vec{k}) = \varepsilon(veck) + naeE_0/N$, where n is the index of the Bi atoms in a nanoribbon whose unit cell is formed by N cells along the x-axis, a is the lattice constant, and e is the electron charge. We find that this field induces a non-zero out-plane spin-polarization, as represented in Fig. 6.4. The electric field effect can be understood using the phenomenological model describing the Rashba effect in inversion symmetry braking systems: the electric field $\vec{E}$ induces an momentum-dependent Zeeman energy $\vec{\phi}_{eff} = -\mu_B \vec{\mathcal{B}}_{eff} \cdot \sigma$ with $\vec{\mathcal{B}}_{eff} = \vec{E} \times \hbar\vec{k}/m_e c^2$ [43, 44]. In our particular case, the momentum carried by the electrons at the edge is oriented along the y-axis and the electric field is transverse to the nanoribbon $\vec{E} = E_0\hat{x}$, resulting in a effective field along the z-axis $\vec{\mathcal{B}}_{eff} = (\mu_B/m_e c^2)E_0 k_y \hat{z}$. This odd-in-$k$ effective field, i.e., $\vec{\mathcal{B}}_{eff}(k) = -\vec{\mathcal{B}}_{eff}(-k)$, only appears when the mirror symmetry is broken, exactly in the same way that the Rashba effect depends on the inversion symmetry breaking [44, 45]. The odd dependence on k imposes that the total spin-polarization component vanishes, preserving the TR-symmetry, which is consistent with the spin-polarization observed in Fig. 6.4b. Although Rashba-split surface states coexists with surface states in the 3D TIs due to the band bending and structural inversion asymmetry [46, 47, 48], the consequences of the Rashba effect and transverse electric fields in the edge states have not been widely explored [49]. However, the control of the spin-polarization in non-topological ferromagnetic graphene nanoribbons has been recently proposed [50]. The proposed spin-polarization control is different form the dynamic spin-orbit torque in anti- and ferromagnetic 2D and 3D TIs [51, 52, 53, 54, 55], since the effective field $\vec{\mathcal{B}}_{eff}$ appears for the equilibrium carrier spin density configuration and does not required magnetic order.

The change of spin orientation suggests that a simple transistor model can be con-

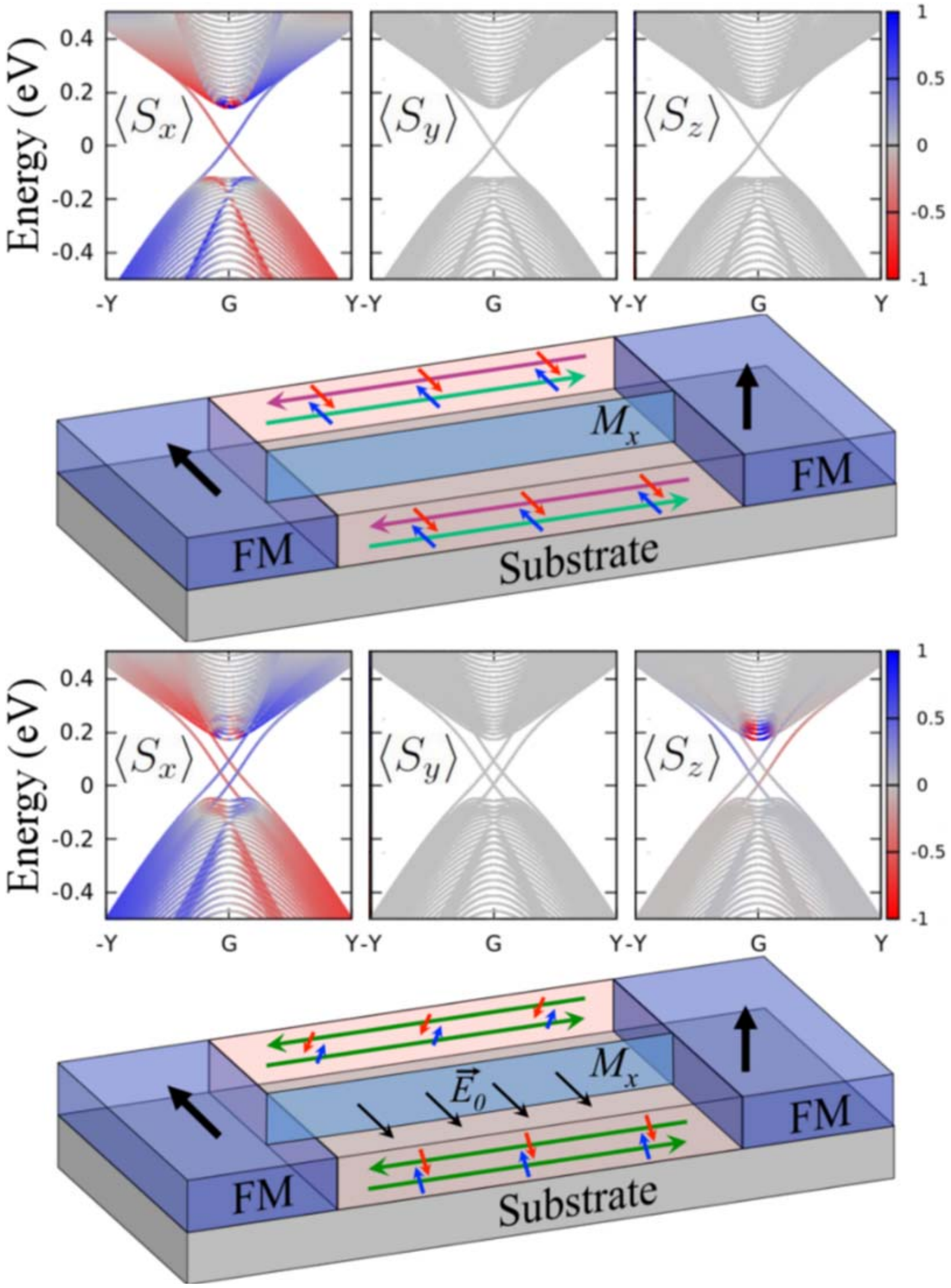

Figure 6.4 - Expected values of the spin operator for the band structure of a nanoribbon 33.6 nm width armchair terminated for (top) $E_0 = 0eV/\text{Å}$ and (bottom) $E_0 = 2 \cdot 10^{-2} eV/\text{Å}$. Here, E_0 is an external electric field breaking the mirror symmetry $\mathcal{M}_x$ (blue plane). The color code stands for the spin orientation. The spin texture is also schematically represented in a transistor model: a nanoribbon connected to two ferromagnetic contacts (FM). This structure is deposited in a substrate (gray area). States with eigenvalue symmetry operator $\pm i$, which are only defined for $E_0 = 0$, are represented by purple and green, respectively.

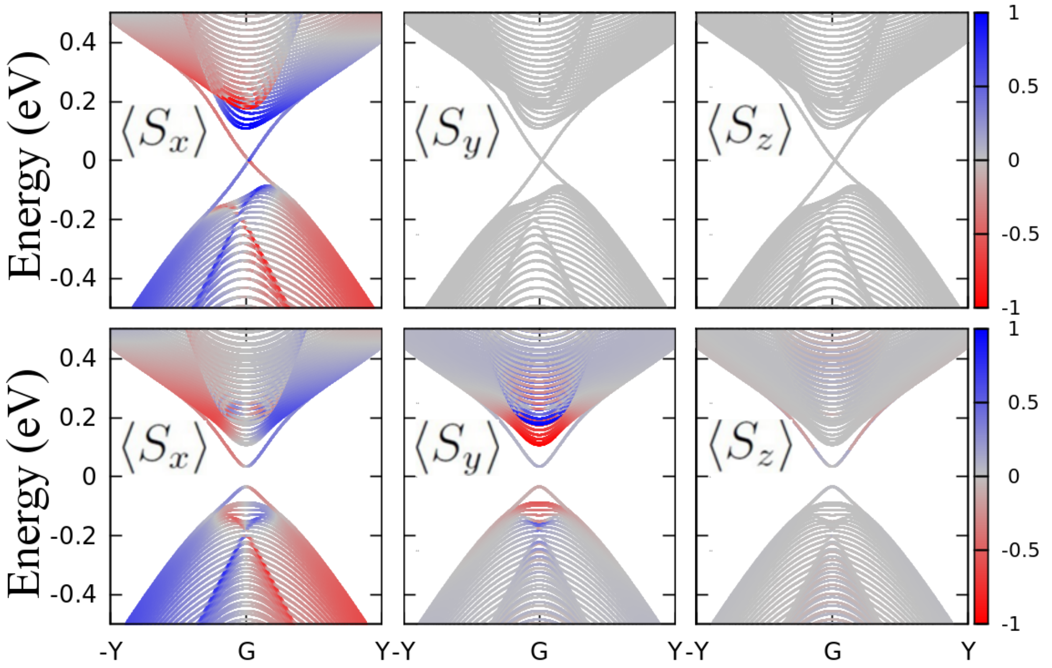

Figure 6.5 - Expected values of the S_x and S_z spin operators for the band structure of a nanoribbon 33.6 nm width armchair terminated for magnetic field of 0.035 in the (top) x and (bottom) y direction. The color code stands for the spin orientation.

structed. Specifically, if the armchair nano-ribbon is connected to ferromagnetic electrodes, the electrons in the edge states are not detected by a drain whose magnetic moment is oriented along either z- or y-axis, as schematicaly represented in Fig. 6.4. This corresponds to the Off of the transistor. If an electric field perpendicular to the mirror plane is turned on, the electrons in the edge states have a non-zero probability of being detected by the electrode (See Fig. 6.4). Different from the transistors based on TCIs, in the proposed DTC insulators, the switch is not defined by the band-gap opening, but the spin direction.

Finally, we verify the mirror symmetry protection in the bulk states by looking at the spin texture of the nanoribbon band structure for different direction of a applied magnetic field. For magnetic fields perpendicular to the mirror plane, edge states are still gapless, but the Dirac point is shifted from the Γ to k-points preserving the mirror symmetry. Naturally, band-gap size engineering can also be achieved by applying an external magnetic field that breaks both TR and mirror symmetries, as represented in Fig. 6.5. For instance, a magnetic field applied in the y-direction opening the band-gap in the edge states, leads to a normal insulating behavior.

Conclusion

Summarizing, we proposed a transistor model using the spin-direction as a switch, based on the fact an external electric field breaking the mirror symmetry induces a spin-polarization parallel to the mirror plane in HF honeycomb lattice materials. Using DFT calculation, tight-binding model, and topological invariant calculation, we found that these systems can exhibit DTC leading to edge states protected by the TR and mirror symmetry. An in-plane magnetic fields $B = B_x\hat{x}$, breaking the TR-symmetry and preserving the mirror symmetry M_x, leads to a displacement of the Dirac point formed by the edge states in the reciprocal space, also confirming the topological mirror symmetry protection. Additionally, an band-gap sizes engineering can be performed by breaking both TR and mirror symmetries applying and external magnetic field parallel to the mirror plane.

Bibliography

[1] D. J. Thouless, M. Kohmoto, M. P. Nightingale, and M. den Nijs, Phys. Rev. Lett. **49**, 405 (1982).

[2] R. Resta, The European Physical Journal B **79**, 121 (2011).

[3] R. Resta, EPL (Europhysics Letters) **22**, 133 (1993).

[4] M. Z. Hasan and C. L. Kane, Rev. Mod. Phys. **82**, 3045 (2010).

[5] L. Fu and C. L. Kane, Phys. Rev. B **74**, 195312 (2006).

[6] X.-L. Qi and S.-C. Zhang, Rev. Mod. Phys. **83**, 1057 (2011).

[7] C. L. Kane and E. J. Mele, Phys. Rev. Lett. **95**, 226801 (2005a).

[8] C. L. Kane and E. J. Mele, Phys. Rev. Lett. **95**, 146802 (2005b).

[9] L. Fu and C. L. Kane, Phys. Rev. B **76**, 045302 (2007).

[10] L. Fu, Phys. Rev. Lett. **106**, 106802 (2011).

[11] T. H. Hsieh, H. Lin, J. Liu, W. Duan, A. Bansil, and L. Fu, Nature Communications **3**, 982 EP (2012).

[12] Y. Ando and L. Fu, Annual Review of Condensed Matter Physics **6**, 361 (2015), https://doi.org/10.1146/annurev-conmatphys-031214-014501 .

[13] A. Bansil, H. Lin, and T. Das, Rev. Mod. Phys. **88**, 021004 (2016).

[14] T. Rauch, M. Flieger, J. Henk, I. Mertig, and A. Ernst, Phys. Rev. Lett. **112**, 016802 (2014).

[15] X. Qian, J. Liu, L. Fu, and J. Li, Science **346**, 1344 (2014), http://science.sciencemag.org/content/346/6215/1344.full.pdf .

[16] K. Olejnik, J. Wunderlich, A. C. Irvine, R. P. Campion, V. P. Amin, J. Sinova, and T. Jungwirth, Phys. Rev. Lett. **109**, 076601 (2012).

[17] D. Nanclares, L. R. F. Lima, C. H. Lewenkopf, and L. G. G. V. D. da Silva, Phys. Rev. B **96**, 155302 (2017).

[18] J. Liu, T. H. Hsieh, P. Wei, W. Duan, J. Moodera, and L. Fu, Nature Materials **13**, 178 EP (2013).

[19] Y. Okada, M. Serbyn, H. Lin, D. Walkup, W. Zhou, C. Dhital, M. Neupane, S. Xu, Y. J. Wang, R. Sankar, F. Chou, A. Bansil, M. Z. Hasan, S. D. Wilson, L. Fu, and V. Madhavan, Science **341**, 1496 (2013), http://science.sciencemag.org/content/341/6153/1496.full.pdf .

[20] P. Dziawa, B. J. Kowalski, K. Dybko, R. Buczko, A. Szczerbakow, M. Szot, E. Łusakowska, T. Balasubramanian, B. M. Wojek, M. H. Berntsen, O. Tjernberg, and T. Story, Nature Materials **11**, 1023 EP (2012).

[21] Y. Tanaka, Z. Ren, T. Sato, K. Nakayama, S. Souma, T. Takahashi, K. Segawa, and Y. Ando, Nature Physics **8**, 800 EP (2012).

[22] E. O. Wrasse and T. M. Schmidt, Nano Letters **14**, 5717 (2014), pMID: 25198344, https://doi.org/10.1021/nl502481f .

[23] J. Liu, X. Qian, and L. Fu, Nano Letters **15**, 2657 (2015), pMID: 25741907, https://doi.org/10.1021/acs.nanolett.5b00308 .

[24] C. Niu, P. M. Buhl, G. Bihlmayer, D. Wortmann, S. Blugel, and Y. Mokrousov, Phys. Rev. B **91**, 201401 (2015a).

[25] C. Niu, P. M. Buhl, G. Bihlmayer, D. Wortmann, S. Blügel, and Y. Mokrousov, Nano Letters **15**, 6071 (2015b), pMID: 26241305, https://doi.org/10.1021/acs.nanolett.5b02299 .

[26] C. Niu, P. M. Buhl, G. Bihlmayer, D. Wortmann, S. Blügel, and Y. Mokrousov, 2D Materials **3**, 025037 (2016).

[27] C. Niu, P. M. Buhl, G. Bihlmayer, D. Wortmann, Y. Dai, S. Blugel, and Y. Mokrousov, Phys. Rev. B **95**, 075404 (2017).

[28] A. P. Weber, Q. D. Gibson, H. Ji, A. N. Caruso, A. V. Fedorov, R. J. Cava, and T. Valla, Phys. Rev. Lett. **114**, 256401 (2015).

[29] J. C. Y. Teo, L. Fu, and C. L. Kane, Phys. Rev. B **78**, 045426 (2008).

[30] M. Eschbach, M. Lanius, C. Niu, E. Młyńczak, P. Gospodarič, J. Kellner, P. Schüffelgen, M. Gehlmann, S. Döring, E. Neumann, M. Luysberg, G. Mussler, L. Plucinski, M. Morgenstern, D. Grützmacher, G. Bihlmayer, S. Blügel, and C. M. Schneider, Nature Communications **8**, 14976 EP (2017).

[31] S.-C. Wu, G. Shan, and B. Yan, Phys. Rev. Lett. **113**, 256401 (2014).

[32] C. Mera Acosta, O. Babilonia, L. Abdalla, and A. Fazzio, Phys. Rev. B **94**, 041302 (2016).

[33] J. M. Soler, E. Artacho, J. D. Gale, A. García, J. Junquera, P. Ordejón, and D. Sánchez-Portal, Journal of Physics: Condensed Matter **14**, 2745 (2002).

[34] C. M. Acosta, M. P. Lima, R. H. Miwa, A. J. R. da Silva, and A. Fazzio, Phys. Rev. B **89**, 155438 (2014).

[35] L. Fernandez-Seivane, M. A. Oliveira, S. Sanvito, and J. Ferrer, J. of Phys.: Condens. Matter **18**, 7999 (2006).

[36] J. P. Perdew, K. Burke, and M. Ernzerhof, Phys. Rev. Lett. **77**, 3865 (1996).

[37] H. Mirhosseini, J. Henk, A. Ernst, S. Ostanin, C. T. Chiang, P. Yu, A. Winkelmann, and J. Kirschner, Phys. Rev. B **79**, 245428 (2009).

[38] L. Li, C. Yang, and S. Chen, EPL (Europhysics Letters) **112**, 10004 (2015a).

[39] J. Zak, Phys. Rev. Lett. **62**, 2747 (1989).

[40] M. Atala, M. Aidelsburger, J. T. Barreiro, D. Abanin, T. Kitagawa, E. Demler, and I. Bloch, Nature Physics **9**, 795 EP (2013).

[41] M. Okamoto, Y. Takane, and K.-I. Imura, Phys. Rev. B **89**, 125425 (2014).

[42] B. Huang, K.-H. Jin, B. Cui, F. Zhai, J. Mei, and F. Liu, Nature Communications **8**, 15850 EP (2017).

[43] Y. A. Bychkov and E. I. Rashba, JETP Lett **39**, 78 (1984).

[44] A. Manchon, H. C. Koo, J. Nitta, S. M. Frolov, and R. A. Duine, Nat Mater **14**, 871 (2015).

[45] S. Vajna, E. Simon, A. Szilva, K. Palotas, B. Ujfalussy, and L. Szunyogh, Phys. Rev. B **85**, 075404 (2012).

[46] M. Bianchi, D. Guan, S. Bao, J. Mi, B. B. Iversen, P. D. C. King, and P. Hofmann, Nature Communications **1**, 128 EP (2010).

[47] P. D. C. King, R. C. Hatch, M. Bianchi, R. Ovsyannikov, C. Lupulescu, G. Landolt, B. Slomski, J. H. Dil, D. Guan, J. L. Mi, E. D. L. Rienks, J. Fink, A. Lindblad, S. Svensson, S. Bao, G. Balakrishnan, B. B. Iversen, J. Osterwalder, W. Eberhardt, F. Baumberger, and P. Hofmann, Phys. Rev. Lett. **107**, 096802 (2011).

[48] H. M. Benia, A. Yaresko, A. P. Schnyder, J. Henk, C. T. Lin, K. Kern, and C. R. Ast, Phys. Rev. B **88**, 081103 (2013).

[49] G. Liu, G. Zhou, and Y.-H. Chen, Applied Physics Letters **99**, 222111 (2011), https://doi.org/10.1063/1.3664776 .

[50] M. R. Rezapour, J. Yun, G. Lee, and K. S. Kim, **The Journal of Physical Chemistry Letters**, The Journal of Physical Chemistry Letters **7**, 5049 (2016).

[51] I. Mihai Miron, G. Gaudin, S. Auffret, B. Rodmacq, A. Schuhl, S. Pizzini, J. Vogel, and P. Gambardella, Nature Materials **9**, 230 EP (2010).

[52] S. Ghosh and A. Manchon, Phys. Rev. B **95**, 035422 (2017).

[53] Y. Wang, P. Deorani, K. Banerjee, N. Koirala, M. Brahlek, S. Oh, and H. Yang, Phys. Rev. Lett. **114**, 257202 (2015).

[54] H. Kurebayashi, J. Sinova, D. Fang, A. C. Irvine, T. D. Skinner, J. Wunderlich, V. Novák, R. P. Campion, B. L. Gallagher, E. K. Vehstedt, L. P. Zârbo, K. Výborný, A. J. Ferguson, and T. Jungwirth, Nature Nanotechnology **9**, 211 EP (2014).

[55] H. Li, H. Gao, L. P. Zârbo, K. Výborný, X. Wang, I. Garate, F. Doğan, A. Čejchan, J. Sinova, T. Jungwirth, and A. Manchon, Phys. Rev. B **91**, 134402 (2015b).

7. Microscopic origin of bulk-states near the Dirac-point in rhombohedrical topological insulators

Topological insulator (TI) materials have attracted a lot of attention over the recent years [1, 2, 3]. Their unusual metallic surface electronic structure on an inverted bulk band gap and the time reversal (TR) topological protection of these states, which forbids the backscattering, make TIs very fascinating materials [4, 5, 6]. Due to the advances in synthesis techniques[7] and their simple mathematical [8] and computational modeling[9], Bi_2Se_3-like materials have been referred as the "hydrogen atom" of the 3DTI[10]. These systems have been proposed as platforms for spintronic devices based on the control of induced magnetic moment direction [11], surface barriers[12], and single-atom magnetoresistance[13].

In addition to the metallic surface topological protected states in a insulating bulk, experiments find that Bi_2Se_3-like materials exhibit electronic scattering channels, attributed to the presence of bulk states near in energy to the Dirac point[1, 5, 14]. These ubiquitous bulk states are believed to prevent the observation of the expected unusual electronic and transport properties governed by surface states in 3DTIs[14, 15, 16].

First principles GW calculations for surface states [17, 18, 19] show that bulk states of Bi_2Se_3 thin films are shifted below the Dirac point, while this is not the case for Bi_2Te_3. In contrast, other bulk band structure calculations show that there is barely any energy separation between the Dirac point and the bulk valence band maximum [19, 20, 21]. This is at odds with recent experimental results [16] that, by investigating Shubnikov-de Haas oscillations in this material, showed the coexistence of surface states and bulk channels with high mobility.

In order to obtain insight on this problem and understand the experimentally observed magnetotransport properties of thin films of rhombohedral TI materials, one needs an effective model capable of describing both the topological surface states as well as the bulk ones over the whole Brillouin zone. In addition, the effective Hamiltonian has to account for the presence of external magnetic fields and be amenable to model disorder effects, which is beyond the scope of first principle methods. The main purpose of this paper is to put forward a tight-binding model that fulfills these characteristics.

Based on symmetry properties and $\boldsymbol{k} \cdot \boldsymbol{p}$ perturbation theory, Zhang and collaborators [8] derived a Dirac-like Hamiltonian model describing the low energy band structure around the Γ-point of Bi_2Se_3-like 3DTIs. Subsequently[22], a tight-binding effective model

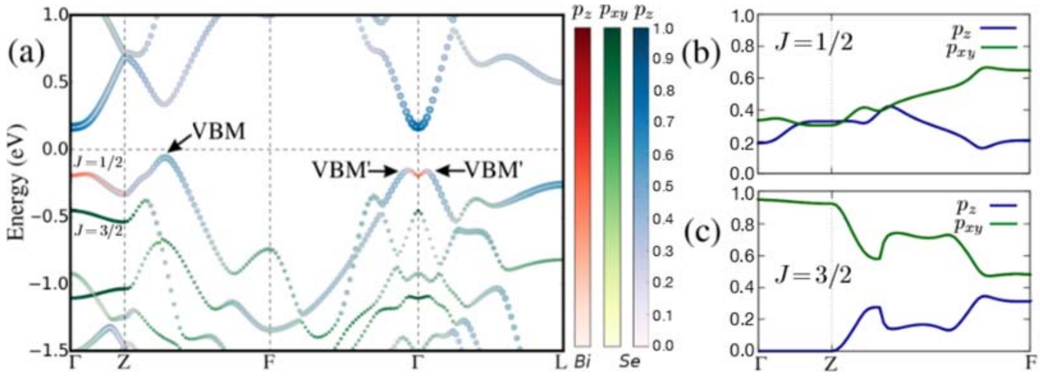

Figure 7.1 - (a) Bulk band structure of Bi_2Se_3. The color code stands for the projections of the p_z Bi orbitals (red), p_xp_y Se orbitals (blue), and p_z Se orbitals (green) in the wave function. The maximum and local maxima of the valence band are denoted by VBM and VBM', respectively. Panels (b) and (c) give the p_z and p_xp_y contributions of the $J = 1/2$ and $J = 3/2$ bands, respectively.

has been proposed to describe the Brillouin of these systems, realizing both strong and weak TIs. However, the basis set used in such works fails to account for bulk states in the energy vicinity of the Dirac point and, hence, their effect on the electronic properties.

Here, we propose an effective tight-binding model that provides insight on the above mentioned bulk states close to the Fermi energy that potentially spoil the bulk-boundary duality. In the presence of disorder these states can mix with the surface ones, quenching the topological properties of the material. We also use our model to discuss some known mechanisms to cause an energy shift of the bulk states, such as, stacking faults [23] and applying an external electric field [24].

7.1 Tight-binding effective model

We begin this section by reviewing the key symmetry arguments that allow one to obtain a simple effective tight-binding model for Bi_2Se_3-like 3DTIs. Next, we present the *ab initio* electronic structure calculations on which our effective tight-binding model is based.

The crystalline structure of Bi_2Se_3-like 3DTIs is formed by Quintuple-Layers (QL) characterized by $D^5_{3d}(R\overline{3}m)$ point group symmetries [5]. The Bi_2Se_3 QL unit cell is composed by two bismuth and three selenium atoms [5]. The QL-QL interaction is weak, mainly ruled by the Van der Waals-like interaction [5, 8, 23]. This allows one to model each QL unit cell by a triangular lattice site. Following the approach presented in Ref. [8], the Bi_2Se_3 hexagonal unit cell is conveniently described by three triangular lattice layers stacked in the z direction, instead of considering three QL unit cells. This simple model preserves the symmetries of the $D^5_{3d}(R\overline{3}m)$ point group, namely: *i*) threefold rotation symmetry R_3 along the z axis, *ii*) twofold rotation symmetry R_2 along the x axis, *iii*) inversion symmetry $\mathcal{P}$, and *iv*) time-reversal symmetry $\mathcal{T}$.

It is well established [8, 5] that the bulk wave function at the Γ point can be accurately described by a set of few effective states $\{|\Lambda^{\tau}_{J}, j_z\rangle\}$. Here, τ is the state parity, J is the total angular momentum with projection j_z on the z axes, and Λ labels the Bi and Se orbital contributions. We use these states to obtain an effective Hamiltonian that reproduces the bulk states of rhombohedral TIs calculated using *ab initio* methods.

The first-principle calculations are performed within the Density Functional Theory (DFT) framework[25], as implemented in the SIESTA code[26], considering the on-site approximation for the spin-orbit coupling[27, 28]. The Local Density Approximation (LDA)[29] is used for the exchange-correlation functional.

Figure 7.1 summarizes our *ab initio* results for Bi_2Se_3. The color code represents the contribution of the Bi and Se p_z orbitals and the Se p_xp_y atomic orbitals to the electronic structure. The main orbital contributions are associated with p orbitals corresponding to $J = 3/2, 1/2$ and $j_z = \pm 3/2, \pm 1/2$ states (Fig. 7.1a). To conserve the total angular momentum the $|\Lambda^{\pm}_{3/2}, \pm 3/2\rangle$ effective states must be a linear combination of p_x and p_y orbitals, whereas the $|\Lambda^{\pm}_{J}, \pm 1/2\rangle$ states correspond to a linear combination of all p orbitals (Fig. 7.1b and Fig. 7.1c). The symmetry properties of the $|\Lambda^{\tau}_{J}, j_z\rangle$ states are discussed below.

The bulk Valence Band Maximum (VBM) is located along the $Z \to F$ symmetry path, as shown in Fig. 7.1a. In addition, one finds two local maxima, denoted by VBM', along the $F \to \Gamma$ and $\Gamma \to L$ lines, both close to the Γ-point. In line with previous results[22], we observe that both VBM and VBM' have a strong p_z Se orbital character. However, we find that the so far neglected p_xp_y orbitals play a key role for an accurate description of the orbital composition of the valence band maxima, as we discuss below.

Along the $\Gamma \to Z$ symmetry line, the R_3 symmetry is preserved. Thus, the $|\Lambda_{1/2}, \pm 1/2\rangle$ and $|\Lambda_{3/2}, \pm 3/2\rangle$ effective states do not mix. In contrast, in the $\Gamma \to L$ and $\Gamma \to F$ paths the R_3 symmetry is broken. This allows for the hybridization of p_z atomic orbitals with p_x and p_y ones. We find that this hybridization can be rather large, as clearly shown by Figs. 7.1b and 7.1c, where we present the Se orbital composition of the $J = 1/2$ and $J = 3/2$ bands along the Brillouin zone.

Since the valence band maxima do not belong to the $\Gamma \to Z$ symmetry line, their orbital composition is a superposition of all p Se-atomic orbitals. As a consequence, a minimal Hamiltonian aiming to effectively describe VBM and VBM' needs to take into account the states associated with the p_x and p_y orbitals, instead of including just the states with p_z character [8, 22].

To calculate the surface electronic structure in the presence of surface projected bulk states, we consider a tight-binding model with eight states, namely, the $|\mathrm{Se}^{-}_{1/2}, \pm 1/2\rangle$ and $|\mathrm{Bi}^{+}_{1/2}, \pm 1/2\rangle$ states responsible for the band inversion, and $|\mathrm{Se}^{-}_{3/2}, \pm 3/2\rangle$ and $|\mathrm{Se}^{+}_{3/2}, \pm 3/2\rangle$ that dominate the most energetic $J = 3/2$ band. Using this basis, we write the 8×8 Hamiltonian:

$$\mathcal{H}(\boldsymbol{k}) = \begin{pmatrix} \mathcal{H}_{1/2}(\boldsymbol{k}) & \mathcal{H}_{\mathrm{int}}(\boldsymbol{k}) \\ \mathcal{H}^{\dagger}_{\mathrm{int}}(\boldsymbol{k}) & \mathcal{H}_{3/2}(\boldsymbol{k}) \end{pmatrix}, \tag{7.1}$$

where $\mathcal{H}_{1/2}(\boldsymbol{k})$ is the standard 4×4 Hamiltonian discussed in the literature [8, 22], that considers only $|\mathrm{Bi}^{+}_{1/2}, \pm 1/2\rangle$ and $|\mathrm{Se}^{-}_{1/2}, \pm 1/2\rangle$ states [1] Our model introduces $\mathcal{H}_{3/2}(\boldsymbol{k})$, a 4×4 Hamiltonian associated with the $|\mathrm{Se}^{-}_{3/2}, \pm 3/2\rangle$ and $|\mathrm{Se}^{+}_{3/2}, \pm 3/2\rangle$ states, and $\mathcal{H}_{\mathrm{int}}(\boldsymbol{k})$ the corresponding coupling term.

For a given total angular momentum J the matrix elements in $\mathcal{H}(\boldsymbol{k})$ read

$$[\mathcal{H}(\boldsymbol{k})]_{ii'} = \varepsilon_{ii'}(\boldsymbol{k})\delta_{ii'} + \sum_{\nu} \left(t^{ii'}_{\boldsymbol{a}_\nu} e^{i\boldsymbol{k}\cdot\boldsymbol{a}_\nu} + t^{ii'}_{\boldsymbol{b}_\nu} e^{i\boldsymbol{k}\cdot\boldsymbol{b}_\nu} \right), \tag{7.2}$$

where the states are labeled by $i = (\Lambda, J, \tau, j_z)$, $\varepsilon_{ii}(\boldsymbol{k})$ are on-site energy terms, and $t^{ii'}_{\boldsymbol{c}} = \langle \boldsymbol{n}, \Lambda^{\tau}_{J}, j_z | H | \boldsymbol{n} + \boldsymbol{c}, \Lambda'^{\tau'}_{J'}, j'_z \rangle$ are the corresponding nearest neighbor QL hopping terms, with $\boldsymbol{n}_\nu$ and τ indicating lattice site and orbital parity, respectively. Here $\boldsymbol{c} = \boldsymbol{a}_\nu$ or $\boldsymbol{b}_\nu$, where $\pm\boldsymbol{a}_\nu$ stands for the 6 intra-layer nearest neighbor vectors of each triangular lattice, namely, $\boldsymbol{a}_1 = (a, 0, 0), \boldsymbol{a}_2 = (-a/2, \sqrt{3}a/2, 0), \boldsymbol{a}_3 = (-a/2, -\sqrt{3}a/2, 0)$, while $\pm\boldsymbol{b}_\nu$ denotes the 6 inter-layer nearest neighbors vectors, $\boldsymbol{b}_1 = (0, \sqrt{3}a/3, c/3), \boldsymbol{b}_2 = (-a/2, -\sqrt{3}a/6, c/3), \boldsymbol{b}_3 = (a/2, -\sqrt{3}a/6, c/3)$ with $a = 4.14$ Å and $c = 28.70$ Å [5].

Exploring the system symmetries, we find constraints relating the nearest neighbors QL hopping terms $t^{ij}_{\boldsymbol{c}}$, thereby reducing the total number of possible hopping terms from 432 to 30 independent ones. The corresponding 30 tight-binding parameters are determined by fitting the tight-binding model bulk band structure to the one calculated with DFT, shown in Fig 7.2. We present the complete Hamiltonian and provide more details on the fitting procedure in the next section.

The proposed Hamiltonian captures the low-energy *ab initio* band dispersion, even for k-points far from Γ, overcoming an intrinsic limitation of the $\boldsymbol{k}\cdot\boldsymbol{p}$ models proposed in the literature to describe the band inversion at the Γ point. We show in the next section how to reduce our model to a $\boldsymbol{k}\cdot\boldsymbol{p}$ Hamiltonian by taking the approximation $k \to \Gamma$ and relating, for instance, the hopping terms $t^{ii'}_{\boldsymbol{a}_\nu}$ and $t^{ii'}_{\boldsymbol{b}_\nu}$ to the perturbation theory parameters of Ref. [8]. The inclusion of additional bands does not affect the band inversion, for instance, the $J = 3/2$ bands have much lower energies than the $J = 1/2$

---

[1] We note that Ref. [8] presents an 8×8 Hamiltonian, which is slightly different from ours, but does not explore its consequences of the additional bands. The focus of this seminal paper is the study of $\mathcal{H}_{1/2}(\boldsymbol{k})$.

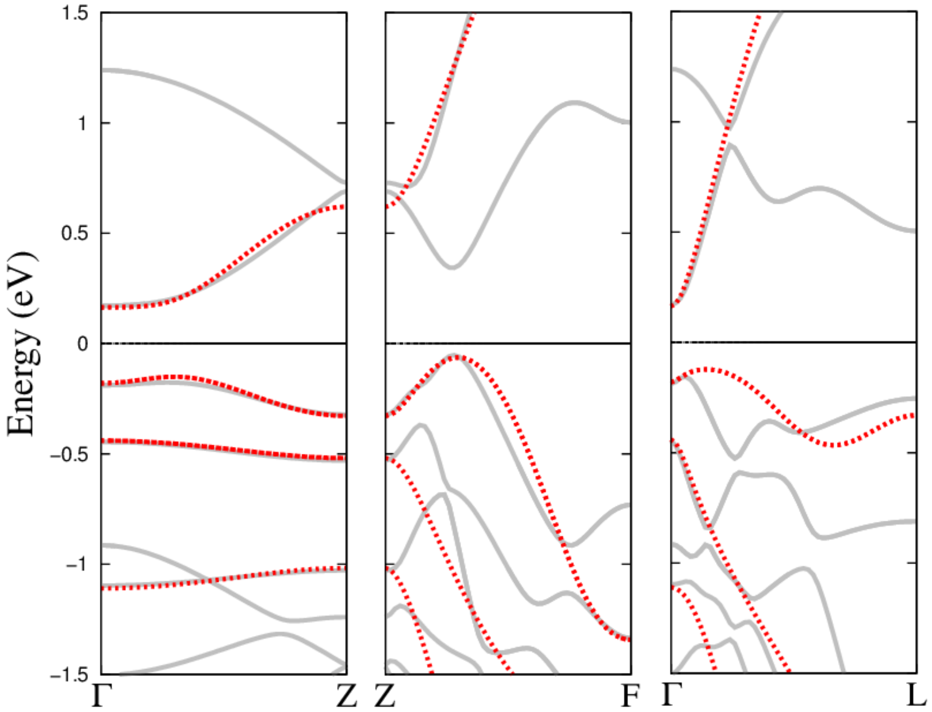

Figure 7.2 - Comparison between the DFT (gray solid lines) and the tight-binding model (red dotted lines) bulk band structure of Bi_2Se_3.

bands.

7.2 Full effective Hamiltonian and model parameters

The form of proposed effective Hamiltonian is obtained by considering symmetry arguments only, which allows one to address the complete family of rhombohedral materials. In turn, the model parameters are determined by fitting the electronic properties obtained from a given first principle calculation.

In this section we discuss in detail the reasoning behind the construction of the model and present explicit expressions for the matrix elements of the resulting effective Hamiltonian. We also present the model parameters for both Bi_2Se_3 and Bi_2Te_3 compounds.

Let us begin recalling that the effective Hamiltonian $\mathcal{H}(\boldsymbol{k})$, Eq. (7.1) reads

$$\mathcal{H}(\boldsymbol{k}) = \begin{pmatrix} \mathcal{H}_{1/2}(\boldsymbol{k}) & \mathcal{H}_{\text{int}}(\boldsymbol{k}) \\ \mathcal{H}^{\dagger}_{\text{int}}(\boldsymbol{k}) & \mathcal{H}_{3/2}(\boldsymbol{k}) \end{pmatrix}. \tag{7.3}$$

The states with effective angular moment $J = 3/2$ are combination of two representations of the double group $D^5_{3d}(R3m)$. Therefore, we consider the states with defined representation:

$$\left|\Lambda^{\pm},\Gamma_4\right\rangle = \frac{1}{\sqrt{2}}\left(|\Lambda^{\pm}_{3/2},3/2\rangle + |\Lambda^{\pm}_{3/2},-3/2\rangle\right), \tag{7.4}$$

and

$$\left|\Lambda^{\pm},\Gamma_5\right\rangle = \frac{1}{\sqrt{2}}\left(|\Lambda^{\pm}_{3/2},3/2\rangle - |\Lambda^{\pm}_{3/2},-3/2\rangle\right). \tag{7.5}$$

The states $\{|\Lambda^{\tau}_{J},j_z\rangle\}$ are transformed by the symmetries operator as

1. *Threefold rotation* R_3:

$$\begin{aligned}\left|\Lambda^{\pm},\Gamma_{4,5}\right\rangle &\rightarrow -\left|\Lambda^{\pm},\Gamma_{4,5}\right\rangle,\\ \left|\Lambda^{\pm},\pm 1/2\right\rangle &\rightarrow e^{\pm\frac{i\pi}{3}}\left|\Lambda^{\pm},\pm 1/2\right\rangle.\end{aligned}$$

2. *Twofold rotation* R_2:

$$\begin{aligned}\left|\Lambda^{\pm},\Gamma_4\right\rangle &\rightarrow \pm\, i\left|\Lambda^{\pm},\Gamma_4\right\rangle,\\ \left|\Lambda^{\pm},\Gamma_5\right\rangle &\rightarrow \mp\, i\left|\Lambda^{\pm},\Gamma_5\right\rangle,\\ \left|\Lambda^{+},\pm 1/2\right\rangle &\rightarrow i\left|\Lambda^{+},\mp 1/2\right\rangle,\\ \left|\Lambda^{-},\pm 1/2\right\rangle &\rightarrow -\, i\left|\Lambda^{-},\mp 1/2\right\rangle.\end{aligned}$$

3. *Inversion* $\mathcal{P}$:

$$\begin{aligned}\left|\Lambda^{\pm},\Gamma_{4,5}\right\rangle &\rightarrow \pm\left|\Lambda^{\pm},\Gamma_{4,5}\right\rangle,\\ \left|\Lambda^{\pm},\alpha\right\rangle &\rightarrow \pm\left|\Lambda^{\pm},\alpha\right\rangle \quad \text{with} \quad \alpha = \pm 1/2.\end{aligned}$$

4. *Time reversal* $\mathcal{T}$:

$$\begin{aligned}\left|\Lambda^{\pm},\Gamma_{4,5}\right\rangle &\rightarrow -\left|\Lambda^{\pm},\Gamma_{5,4}\right\rangle,\\ |\Lambda,\pm 1/2\rangle &\rightarrow \pm\,|\Lambda,\mp 1/2\rangle.\end{aligned}$$

These symmetry transformations relate the hopping terms to each other, as shown for $t^{11}_{\boldsymbol{c}_\nu} = \langle 0,\mathrm{Bi}^{+}_{1/2},1/2|H|\boldsymbol{c}_\nu,\mathrm{Bi}^{+}_{1/2},+1/2\rangle$ in Table 7.1.

These relations allow us to write the matrix elements in a simplified way. For instance, the matrix element $[\mathcal{H}(\boldsymbol{k})]_{11}$, Eq. (7.2), is written as

$$[\mathcal{H}(\boldsymbol{k})]_{11} = \varepsilon_{11}(\boldsymbol{k}) + \alpha_{11}(\boldsymbol{k}), \tag{7.6}$$

Table 7.1 - Symmetry operations on the hopping matrix element $t^{11}_{\boldsymbol{c}_\nu} = \langle 0, \mathrm{Bi}^+_{1/2}, +1/2|H|\boldsymbol{c}_\nu, \mathrm{Bi}^+_{1/2}, +1/2\rangle$, where $\boldsymbol{c}_\nu = \boldsymbol{a}_\nu$ or $\boldsymbol{b}_\nu$, and $\nu = 1, 2$ or 3. (For completeness, we recall that $t^{22}_{\boldsymbol{c}_\nu} = \langle 0, \mathrm{Bi}^+_{1/2}, -1/2|H|\boldsymbol{c}_\nu, \mathrm{Bi}^+_{1/2}, -1/2\rangle$.)

	$t^{11}_{a_1,b_1}$	$t^{11}_{a_2,b_2}$	$t^{11}_{a_3,b_3}$	$t^{11}_{-a_1,-b_1}$	$t^{11}_{-a_2,-b_2}$	$t^{11}_{-a_3,-b_3}$
$\mathcal{T}$	$t^{22*}_{a_1,b_1}$	$t^{22*}_{a_2,b_2}$	$t^{22*}_{a_3,b_3}$	$t^{22*}_{-a_1,-b_1}$	$t^{22*}_{-a_2,-b_2}$	$t^{22*}_{-a_3,-b_3}$
$\mathcal{P}$	$t^{11}_{-a_1,-b_1}$	$t^{11}_{-a_2,-b_2}$	$t^{11}_{-a_3,-b_3}$	$t^{11}_{a_1,b_1}$	$t^{11}_{a_2,b_2}$	$t^{11}_{a_3,b_3}$
R_3	$t^{11}_{a_3,b_3}$	$t^{11}_{a_1,b_1}$	$t^{11}_{a_2,b_2}$	$t^{11}_{-a_3,-b_3}$	$t^{11}_{-a_1,-b_1}$	$t^{11}_{-a_2,-b_2}$
R_2	$t^{22}_{a_1,b_1}$	$t^{22}_{a_3,b_3}$	$t^{22}_{a_2,b_2}$	$t^{22}_{-a_1,-b_1}$	$t^{22}_{-a_3,-b_3}$	$t^{22}_{-a_2,-b_2}$

with

$$\begin{aligned}\alpha_{11}(\boldsymbol{k}) =& \sum_{\nu=1}^{6} \left(t^{11}_{\boldsymbol{a}_\nu} e^{i\boldsymbol{k}\cdot\boldsymbol{a}_\nu} + t^{11}_{\boldsymbol{b}_\nu} e^{i\boldsymbol{k}\cdot\boldsymbol{b}_\nu} \right) \\ =& \sum_{\nu=1}^{3} \left(t^{11}_{\boldsymbol{a}_\nu} e^{i\boldsymbol{k}\cdot\boldsymbol{a}_\nu} + t^{11}_{-\boldsymbol{a}_\nu} e^{-i\boldsymbol{k}\cdot\boldsymbol{a}_\nu} \right. \\ & \left. + t^{11}_{\boldsymbol{b}_\nu} e^{i\boldsymbol{k}\cdot\boldsymbol{b}_\nu} + t^{11}_{-\boldsymbol{b}_\nu} e^{-i\boldsymbol{k}\cdot\boldsymbol{b}_\nu} \right). \end{aligned} \tag{7.7}$$

Using Table 7.1, $\alpha_{11}(\boldsymbol{k})$ can be rewritten as

$$\begin{aligned}\alpha_{11} =& \sum_{\nu=1}^{3} \left[t^{11}_{\boldsymbol{a}_\nu} (e^{i\boldsymbol{k}\cdot\boldsymbol{a}_\nu} + e^{-i\boldsymbol{k}\cdot\boldsymbol{a}_\nu}) + t^{11}_{\boldsymbol{b}_\nu} (e^{i\boldsymbol{k}\cdot\boldsymbol{b}_\nu} + e^{-i\boldsymbol{k}\cdot\boldsymbol{b}_\nu}) \right] \\ =& 6 \left(t^{11}_a \cos \boldsymbol{k}\cdot\boldsymbol{a}_\nu + t^{11}_b \cos \boldsymbol{k}\cdot\boldsymbol{b} \right). \end{aligned} \tag{7.8}$$

Time-reversal symmetry $\mathcal{T}$ and the two-fold rotation R_2 impose the relation $t^{11}_{\boldsymbol{a}_1} = t^{22*}_{\boldsymbol{a}_1} = t^{22}_{\boldsymbol{a}_1}$, which in turn requires $t^{11}_{\boldsymbol{a}_1}$ be real. A symmetry analysis, expanding Table 7.1 to other ij values, shows that $t^{ij}_{\boldsymbol{a}_\nu} = t^{ij}_a$ and $t^{ij}_{\boldsymbol{b}_\nu} = t^{ij}_b$.

In the same way, we use the symmetry operations to calculate all terms for the Hamiltonian matrix elements describing rhombohedral TIs, which also imposes the sign and imaginary phases of the hopping terms, as presented below.

The 4×4 Hamiltonian $\mathcal{H}_{1/2}(\boldsymbol{k})$, associated with the $|\mathrm{Se}^-_{1/2}, \pm 1/2\rangle$ and $|\mathrm{Bi}^+_{1/2}, \pm 1/2\rangle$ states, reads

$$\mathcal{H}_{1/2}(\boldsymbol{k}) = \begin{pmatrix} \varepsilon_1 + \alpha_{11} & 0 & i\alpha_{13} & i\alpha_{14} \\ & \varepsilon_1 + \alpha_{11} & -i\alpha^*_{14} & i\alpha^*_{13} \\ \text{H.c.} & & \varepsilon_3 + \alpha_{33} & 0 \\ & & & \varepsilon_3 + \alpha_{33} \end{pmatrix}, \tag{7.9}$$

where the diagonal α_{ii} matrix elements are given by

$$\alpha_{ii} = 2t_a^{ii} \sum_{\nu=1}^{3} \cos(\boldsymbol{k} \cdot \boldsymbol{a}_\nu) + 2t_b^{ii} \sum_{\nu=1}^{3} \cos(\boldsymbol{k} \cdot \boldsymbol{b}_\nu) \tag{7.10}$$

while the off-diagonal ones read

$$\alpha_{13} = -i2t_a^{13} \sum_{j=1}^{3} \sin(\boldsymbol{k} \cdot \boldsymbol{a}_j) + 2t_b^{13} \sum_{j=1}^{3} \sin(\boldsymbol{k} \cdot \boldsymbol{b}_j) \tag{7.11}$$

$$\begin{aligned} \alpha_{14} = 2t_a^{14}[&\sin(\boldsymbol{k} \cdot \boldsymbol{a}_1) + e^{-i2\pi/3} \sin(\boldsymbol{k} \cdot \boldsymbol{a}_2) \\ &+ e^{-i4\pi/3} \sin(\boldsymbol{k} \cdot \boldsymbol{a}_3)] + 2t_b^{14}[e^{-i\pi/2} \sin(\boldsymbol{k} \cdot \boldsymbol{b}_1) \\ &+ e^{i5\pi/6} \sin(\boldsymbol{k} \cdot \boldsymbol{b}_2) + e^{i\pi/6} \sin(\boldsymbol{k} \cdot \boldsymbol{b}_3)]. \end{aligned} \tag{7.12}$$

The 4×4 Hamiltonian, $H_{3/2}(\boldsymbol{k})$, associated with the $|\mathrm{Se}^-_{3/2}, \pm 3/2\rangle$ and $|\mathrm{Bi}^+_{3/2}, \pm 3/2\rangle$ states is written as

$$\mathcal{H}_{3/2}(\boldsymbol{k}) = \begin{pmatrix} \varepsilon_5 + \beta_{55} & 0 & i\beta_{57} & i\beta_{58} \\ & \varepsilon_5 + \beta_5 & -i\beta_{58}^* & i\beta_{57}^* \\ \text{H.c.} & & \varepsilon_7 + \beta_{77} & 0 \\ & & & \varepsilon_7 + \beta_{77} \end{pmatrix}, \tag{7.13}$$

where

$$\beta_{ii} = 2t_a^{ii} \sum_{j=1}^{3} \cos(\boldsymbol{k} \cdot \boldsymbol{a}_j) + 2t_b^{ii} \sum_{j=1}^{3} \cos(\boldsymbol{k} \cdot \boldsymbol{b}_j) \tag{7.14}$$

$$\beta_{57} = 2t_b^{57} \sum_{j=1}^{3} \sin(\boldsymbol{k} \cdot \boldsymbol{b}_j) \tag{7.15}$$

$$\beta_{58} = 2t_a^{58} \sum_{j=1}^{3} \sin(\boldsymbol{k} \cdot \boldsymbol{a}_i). \tag{7.16}$$

The diagonal on-site energies ε_i of the matrices $H_{1/2}(\boldsymbol{k})$ and $H_{3/2}(\boldsymbol{k})$ are given in Table 7.2.

Finally, the interaction matrix $H_{\mathrm{int}}(\boldsymbol{k})$ is parametrized in block form as

$$\mathcal{H}_{\mathrm{int}}(\boldsymbol{k}) = \begin{pmatrix} \boldsymbol{\gamma}_{15} & \boldsymbol{\gamma}_{17} \\ \boldsymbol{\gamma}_{35} & \boldsymbol{\gamma}_{37} \end{pmatrix}, \tag{7.17}$$

where the $\boldsymbol{\gamma}$'s are $2\times$ 2 matrices given by

$$\boldsymbol{\gamma}_{15} = i\begin{pmatrix} \gamma^{a}_{15}+\gamma^{b}_{15} & \gamma^{a*}_{15}-\gamma^{b*}_{15} \\ -\gamma^{a}_{15}+\gamma^{b}_{15} & \gamma^{a*}_{15}+\gamma^{b*}_{15} \end{pmatrix}, \tag{7.18}$$

$$\boldsymbol{\gamma}_{17} = \begin{pmatrix} \gamma^{a}_{17}+\gamma^{b}_{17} & -\gamma^{a*}_{17}-\gamma^{b*}_{17} \\ \gamma^{a}_{17}+\gamma^{b}_{17} & \gamma^{a}_{17}+\gamma^{b*}_{17} \end{pmatrix}, \tag{7.19}$$

$$\boldsymbol{\gamma}_{35} = \begin{pmatrix} \gamma^{a}_{35}+\gamma^{b}_{35} & -\gamma^{a*}_{35}-\gamma^{b*}_{35} \\ \gamma^{a}_{35}+\gamma^{b}_{35} & \gamma^{a*}_{35}+\gamma^{b*}_{35} \end{pmatrix}, \tag{7.20}$$

$$\boldsymbol{\gamma}_{37} = i\begin{pmatrix} \gamma^{a}_{37}+\gamma^{b}_{37} & \gamma^{a*}_{37}-\gamma^{b*}_{37} \\ \gamma^{a}_{37}-\gamma^{b}_{37} & \gamma^{a*}_{37}+\gamma^{b*}_{37} \end{pmatrix}. \tag{7.21}$$

Let us define

$$\Phi_c(\boldsymbol{k}) = \sum_{\nu=1}^{3}(-1)^{\nu-1}e^{-i(\nu-1)\pi/3}\sin(\boldsymbol{k}\cdot\boldsymbol{c}_\nu) \tag{7.22}$$

and

$$\Psi_c(\boldsymbol{k}) = \sum_{\nu=1}^{3}(-1)^{\nu-1}e^{-i(\nu-1)\pi/3}\cos(\boldsymbol{k}\cdot\boldsymbol{c}_\nu), \tag{7.23}$$

where $c = a$ or b, to write

$$\gamma^{a(b)}_{15} = 2t^{15}_{a(b)}\Phi_{a(b)}(\boldsymbol{k}), \tag{7.24}$$

$$\gamma^{a(b)}_{35} = 2t^{35}_{a(b)}\Psi_{a(b)}(\boldsymbol{k}), \tag{7.25}$$

$$\gamma^{a(b)}_{17} = 2t^{17}_{a(b)}\Psi_{a(b)}(\boldsymbol{k}), \tag{7.26}$$

$$\gamma^{a(b)}_{37} = 2t^{37}_{a(b)}\Phi_{a(b)}(\boldsymbol{k}). \tag{7.27}$$

Table 7.2 - On-site energies ε_i (in eV).

	ε_1	ε_3	ε_5	ε_7
Bi_2Se_3	1.602	-1.374	-1.050	-2.100
Bi_2Te_3	0.805	-0.572	-0.9304	-1.900

Symmetry considerations allow us to reduce the number of the model parameters to 30 independent ones. The latter are determined by a least-square fitting the bulk band structure obtained from the DFT calculation described in Sec. 7.1 for Bi_2Se_3 and Bi_2Te_3 rhombohedral materials. The obtained on-site matrix elements are given in Table 7.2, while the hopping matrix elements are shown in Table 7.3.

The important parameters for the TI nature of the material are contained in the $\mathcal{H}_{1/2}$ Hamiltonian. The role of the mass term (on-site term) in the band inversion is very well established in the literature, as well as all remaining matrix elements in $\mathcal{H}_{1/2}$ [22, 8]. The novelty here are the additional states that correctly account for surface projected

Table 7.3 - Non-zero hopping matrix elements t_c^{ij} with $c = a, b$ in eV. The superscripts ij listed by the first column correspond to all (symmetry) independent non vanishing hopping terms.

	Bi_2Se_3		Bi_2Te_3	
ij	t_b^{ij} (eV)	t_a^{ij}(eV)	t_b^{ij} (eV)	t_a^{ij} (eV)
11	-0.067	-0.240	-0.027	-0.130
33	0.040	0.211	0.015	0.120
55	0.0066	0.095	0.007	0.095
77	-0.0097	0.181	-0.012	0.171
13	0.045	0.210	-0.025	0.210
14	$i0.190$	-0.170	$i0.210$	-0.270
15	0.008	0.100	0.012	0.171
17	-0.008	$-0.120 + i0.006$	-0.012	$-0.140 + i0.008$
35	-0.082	0.152	-0.093	0.092
37	-0.090	0.210	-0.110	0.190
57	$< 10^{-3}$	0.005	$< 10^{-3}$	0.009
58	0.008	$< 10^{-3}$	0.012	$< 10^{-3}$

bulk states, in which we have focused our discussion and are represented by $\mathcal{H}_{3/2}$. As discussed in Fig. 7.1b and Fig. 7.1c, we do not use an energy criterion, but rather the total angular momentum and atomic orbitals projection to select the suitable basis to describe the band interaction giving the shift in the bulk states. For instance, in Ref. [8] the basis is $\{|\mathrm{Se}^-_{1/2}, \pm1/2\rangle$, $|\mathrm{Bi}^+_{1/2}, \pm1/2\rangle$, $|\mathrm{Se}^-_{3/2}, \pm3/2\rangle$, and $|\mathrm{Se}^+_{3/2}, \pm1/2\rangle\}$. In our work we use $\{|\mathrm{Se}^-_{1/2}, \pm1/2\rangle$,$|\mathrm{Bi}^+_{1/2}, \pm1/2\rangle$, $|\mathrm{Se}^-_{3/2}, \pm3/2\rangle$, and $|\mathrm{Se}^+_{3/2}, \pm3/2\rangle\}$. It is possible to compare the Hamiltonian matrix elements in Ref. [8] with the ones obtained in this work only for the common elements, as shown in Table 7.4.

Table 7.4 - Relation between the $\boldsymbol{k} \cdot \boldsymbol{p}$ perturbation theory parameters reported in Ref. [8] with the hopping matrix elements.

$\boldsymbol{k} \cdot \boldsymbol{p}$ parameters	tight-binding parameters
$F_{i(ij)}$	$-(a^2/2)(3t_a^{ii} + t_b^{ii})$
$K_{i(ij)}$	$-3c^2 t_b^{ii}$
Q_1	$6ct_b^{13}$
P_1	$a(3t_a^{14} - i\sqrt{3}t_b^{14})$
$P_2 = Q_2$	$a(3t_a^{15} + i\sqrt{3}t_b^{15})$
$\overline{P}_3 = \overline{Q}_3$	$a(3t_a^{17} + i\sqrt{3}t_b^{17})$
U_{35}	$(a^2/4)(\frac{3}{4}t_a^{35} + t_b^{35})$
V_{35}	$(i\sqrt{3}act_b^{35})$
$\overline{U}_{37}$	$-(a^2/2)(3t_a^{37} + t_b^{37})$
$\overline{V}_{37}$	$-3c^2 t_b^{37}$

7.3 Thin films

In this section we calculate the electronic band structure of rhombohedral TI thin films. We take the QLs parallel to the xy-plane and define the z-axis as the stacking

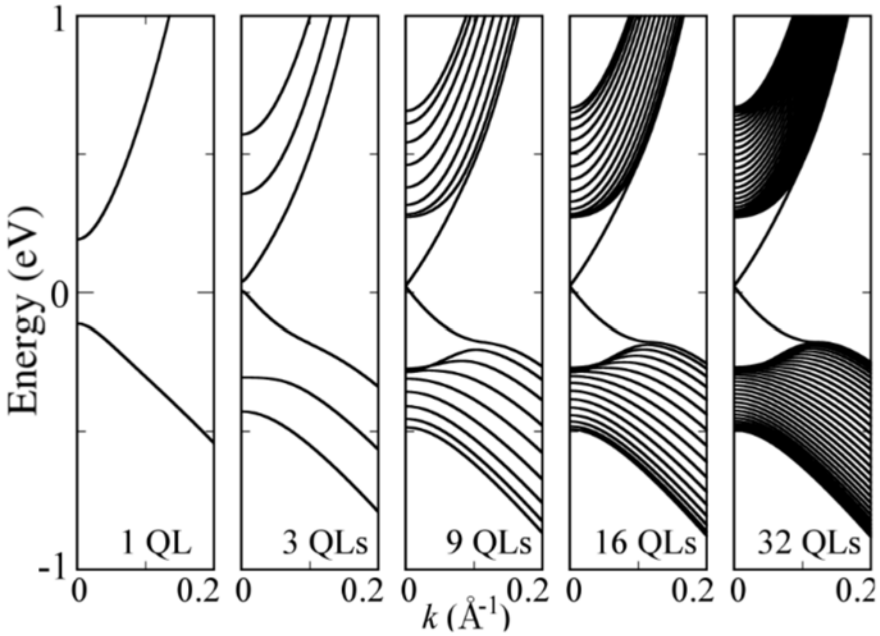

Figure 7.3 - Band structure along the $\Gamma \rightarrow M$ symmetry line, without considering $J = 3/2$-states, for different film thicknesses of Bi_2Se_3.

direction. The thickness of the films is given in terms of N_{QL}, the number of stacked QLs. The surface corresponds to the outermost QLs. The surface states correspond to the ones spatially localized in these QLs.

We modify the bulk tight-binding Hamiltonian defined in Eq. (7.1) to account for a finite number of layers. The slab Hamiltonian consists of intra- and inter-layer terms, namely [30]

$$\mathcal{H}_{\mathrm{slab}} = \sum_{n=1}^{N_{\mathrm{QL}}} c_n^\dagger \mathcal{H}_0 c_n + \sum_{n=1}^{N_{\mathrm{QL}}-1} \left(c_n^\dagger \mathcal{H}_z c_{n+1} + \mathrm{H.c.} \right) . \tag{7.28}$$

The basis is given by $|n, k_x, k_y, \Lambda_J^\tau, j_z\rangle$ with corresponding creation (annihilation) operators given in compact notation by $c_n^\dagger$ (c_n). The intra-layer matrix elements read

$$[\mathcal{H}_0(\boldsymbol{k})]_{ii'} = \varepsilon_i(\boldsymbol{k})\delta_{ii'} + \sum_{\nu=1}^{6} t_{\boldsymbol{a}_\nu}^{ii'} e^{i\boldsymbol{k}\cdot\boldsymbol{a}_\nu} . \tag{7.29}$$

The latter are similar to those of Eq. (7.2), but restricted to two-dimensions, namely, $\boldsymbol{k} = (k_x, k_y)$. In turn, the inter-layer term,

$$[\mathcal{H}_z]_{ii'} = \sum_{\nu} t_{\boldsymbol{b}_\nu}^{ii'} , \tag{7.30}$$

provides the coupling between nearest neighbor QLs planes.

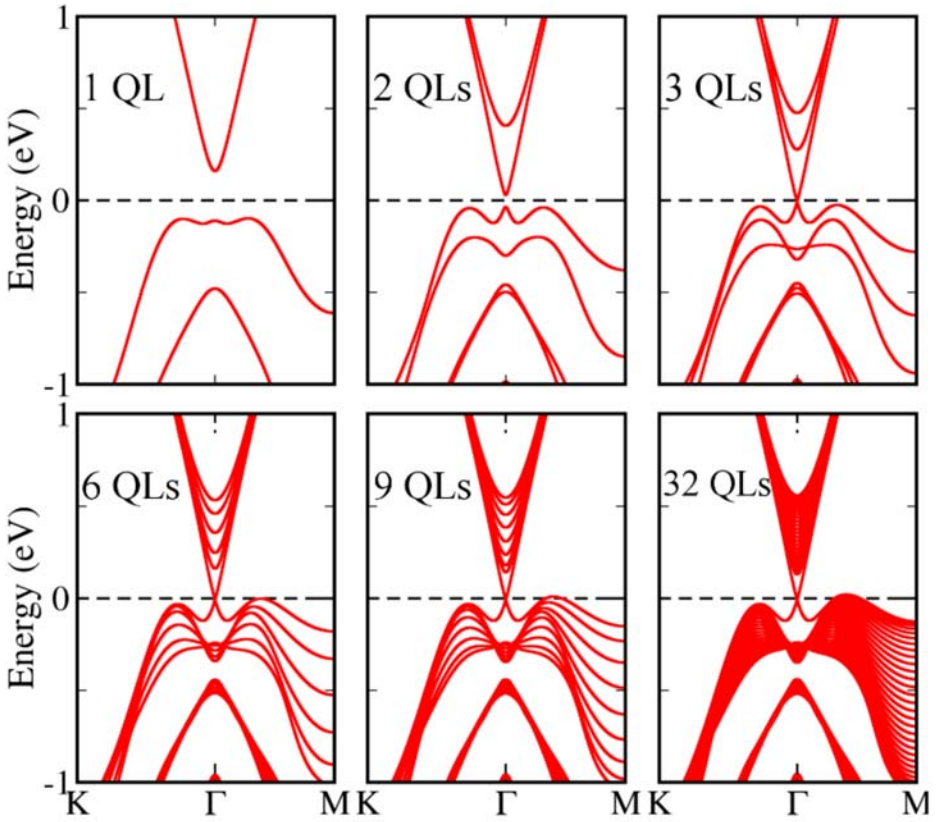

Figure 7.4 - Band structure of a Bi_2Se_3 thin film for different thickness values, $N_{\mathrm{QL}} = 1, 2, 3, 6, 9$, and 32, using our 8×8 tight-binding effective model.

It is well established that a bulk band inversion occurs between states dominated by p_z Se and Bi atomic orbitals with different parities [5]. The four states $|\mathrm{Se}^-_{1/2}, \pm 1/2\rangle$ and $|\mathrm{Bi}^+_{1/2}, \pm 1/2\rangle$ form a good basis to describe the surface states at the k-points near the Γ point [8, 22]. However, similarly to bulk systems, this reduced basis also fails to correctly describe the bulk states close in energy to the Dirac point in thin Bi_2Se_3 films.

To better understand the importance of the $J = 3/2$ states, let us first consider a thin film described by the Hamiltonian $\mathcal{H}_{1/2}(\boldsymbol{k})$ projected out from $\mathcal{H}_{\mathrm{slab}}$. Figure 7.3 shows the finite size effects and how the band structure is modified by increasing N_{QL}[30]. For $N_{\mathrm{QL}} \geqslant 3$ one clearly observes the appearance of surface states and the formation of a Dirac cone. For $N_{\mathrm{QL}} \gg 1$ the bulk band gap is recovered. We stress that without the $J = 3/2$ states, the model does not show VBM bulk states close to the Fermi level, as expected from the analysis of bulk band structure (see, for instance, Fig. 7.1). Moreover, within this simple model the band structure close to the Dirac point along the $\Gamma \to K$ and $\Gamma \to M$ paths are identical, which is a rather unrealistic symmetry feature.

The $J = 3/2$ states modify significantly the electronic band structure. Figure 7.4 summarizes the results we obtain for the 8×8 total effective Hamiltonian, Eq. (7.1).

Even for a few QLs, the shape of the surface band structure reproduces the qualitative behavior observed in the bulk LDA-DFT calculations. Figure 7.4 shows that as N_{QL} is increased, the Dirac cone is formed and bulk states appear in the vicinity of the Fermi level turning the system into a metal.

7.4 Application: Bulk states engineering

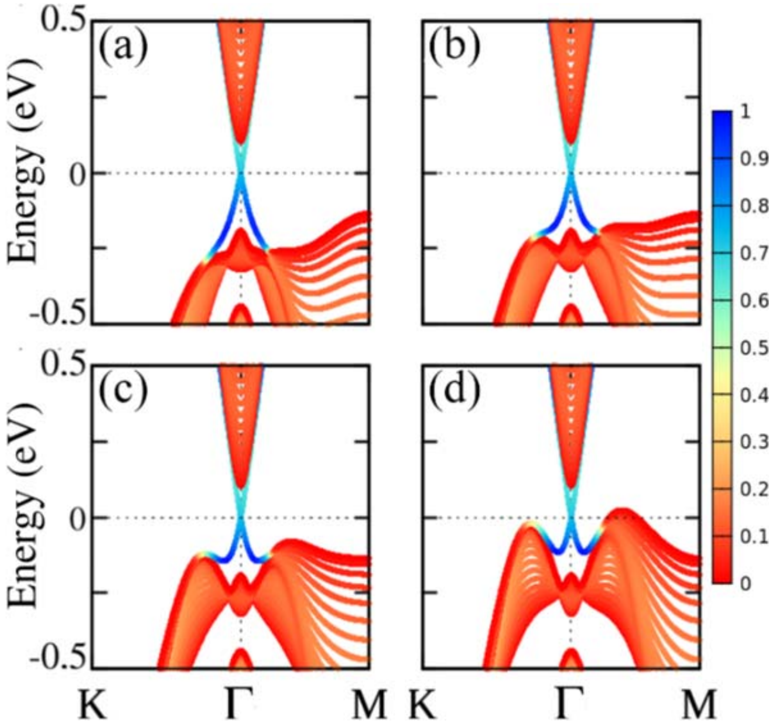

Figure 7.5 - Surface band structure for $N_{\mathrm{QL}} = 20$ calculated using the eight bands effective model with hopping term (repulsion parameter) (a) $t_b^{ij} = 1.2$ eV, (b) $t_b^{ij} = 1.5$ eV, (c) $t_b^{ij} = 1.8$ eV, and (d) $t_b^{ij} = 2.1$ eV, where $i = (\mathrm{Se}^{-}_{1/2}, \pm 1/2)$, and $j = (\mathrm{Se}^{+}_{3/2}, \pm 3/2)$. The color code stands for the magnitude of the projection of the orbitals at the outermost (surface) QLs. Pure surface states are indicated by blue, whereas bulk states are depicted in red.

Several strategies have been proposed and used to suppress the scattering channels associated with the continuous bulk states, like for instance, alloy stoichiometry [31, 32, 33, 34], application of an external electric field[24], stacking faults[23], and strain[35, 36].

Let us now use the effective model put forward in the previous section to discuss some of these known strategies to shift the bulk band states away from the Dirac point energy, defined as $\varepsilon = 0$.

Our analysis is based on the observation that the energy of the bulk states along the $\Gamma \rightarrow M$ symmetry path depends very strongly on the in-plane interaction between $|\mathrm{Se}^{-}_{1/2}, \pm 1/2\rangle$ and $|\mathrm{Se}^{+}_{3/2}, \pm 3/2\rangle$ states. We find that by increasing the matrix elements associated with the mixture of the above states the bulk states are shifted up in energy, as shown by Fig. 7.5.

Hence, as previously proposed [34], one way to engineer the VBM and VBM′ states is by substituting the Se atoms by chemical elements that do not spoil the topological properties of the material and reduce the interaction between $|\mathrm{Se}^{-}_{1/2}, \pm 1/2\rangle$ and $|\mathrm{Se}^{+}_{3/2}, \pm 3/2\rangle$ states. This effect can be described by a simple model in terms of the direct modification of the matrix element t_b^{ij} that mixes the $|\mathrm{Se}^{-}_{1/2}, \pm 1/2\rangle$ and $|\mathrm{Se}^{+}_{3/2}, \pm 3/2\rangle$ states. In fact, the band structures obtained for several values of t_b^{ij} shown in Fig. 7.5 qualitatively describe the first-principles calculations for $\mathrm{Bi_2(Se_{1-x}S_x)_3}$ alloys [34].

Alternatively, the double degenerate surface-state bands due to the presence of two [111] cleavage surfaces in a slab geometry can be removed by applying a perpendicular electric field $E_0\hat{z}$ [24]. The Dirac cone associated with the surface at the highest potential energy can be shifted above the VBM, leading to a suppression of the scattering channels between the topologically protected metallic surface states and the bulk states. We describe this effect using our tight-binding effective model by modifying the on-site term $\varepsilon(\boldsymbol{k})\delta_{ij}$ in the inter-layer matrix elements associated with each QL. As a result, Eq. (7.29) becomes

$$[\mathcal{H}_0(k_x, k_y)]_{n,ij} = \tilde{\varepsilon}_n(\boldsymbol{k})\delta_{ij} + \sum_{\nu} t^{ij}_{\boldsymbol{a}_\nu} e^{i\boldsymbol{k}\cdot\boldsymbol{a}_\nu}, \qquad (7.31)$$

where $\tilde{\varepsilon}_n(\boldsymbol{k}) = \varepsilon(\boldsymbol{k}) + nceE_0/N_{QL}$, n is the layer index, and e is the electron charge. This simple approach captures the shift of the Dirac cone located at the surfaces corresponding to the QL with $n = N_{QL}$ and $n = 0$. Figure 7.6a show the effect of an electric field of $E = 5 \times 10^{-3}$ V/Å on a thin film of $N_{\mathrm{QL}} = 9$.

Another band engineering strategy has been suggested by *ab-initio* atomistic investigations on the role played by extended defects, like stacking faults, on the structural and electronic properties of 3D topological insulators [23]. In $R\bar{3}m$ structures the typical stacking is a ABCABC configuration, that is, each QL is rotated with respect to its adjacent QL by 120^o. When a QL is "removed" leading to a ACABCA, ABABCA, or ABCBCA stacking configuration, the defects is called an intrinsic stacking fault. The inter-QLs distance decreases as a consequence of these stacking faults, making the Van der Waals inter-QLs interaction weaker and changing the on-site potential of the QLs in which the structural defect is located [23]. Thus, it is relatively easy to account for this effect within our model, namely, we rewrite the on-site energy and the inter band interaction as $\varepsilon_n(\boldsymbol{k}) - \delta\varepsilon_0$ and $t^{ij}_{\boldsymbol{b}_\nu} - \delta t$.

Stacking faults nearby the surface layers of $\mathrm{Bi_2Se_3}$ give rise to a positive energy shift of the bulk states with respect to their energy in a pristine system[23]. This shift is typically about 75 meV. Thus, we obtain a qualitative description of the stacking faults effect by

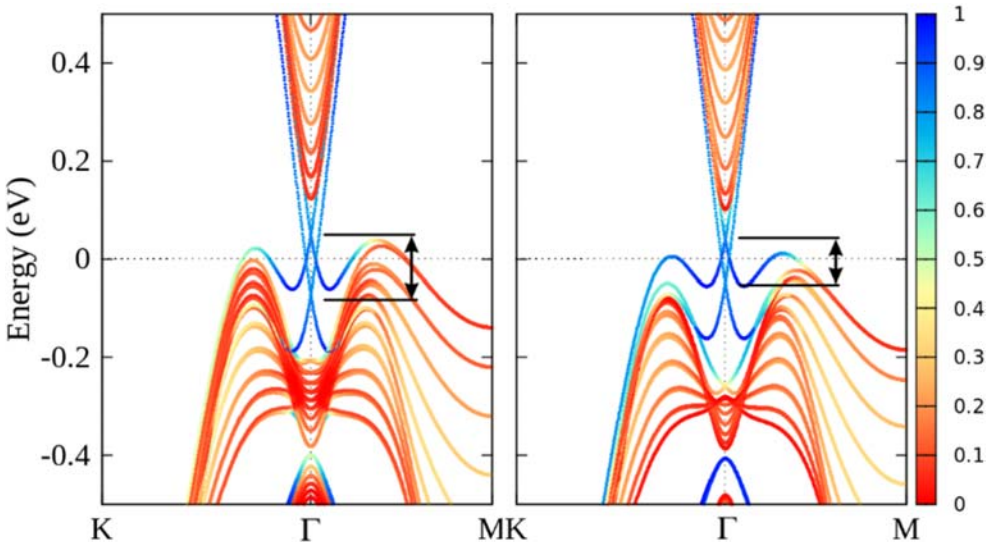

Figure 7.6 - Electric field (left) and stacking faults (right) effect of the band structure of a Bi_2Se_3 thin film of 9QLs. The splitting between the Dirac cones associated with different surfaces is represented by the arrow. The color code quantifies the surface/bulk character of the electronic states, see caption of Fig. 7.5.

fitting $\delta\varepsilon_0$ and δt to the DFT results only for the QLs with this structural defect, see Fig. 7.6. Our simplified model and description allows for the study of thin films with a large number of QLs.

7.5 Scattering Rates

Rhombohedral topological insulators such as Bi_2Se_3 have demonstrated surface state mobilities about of 10^4 $\mathrm{cm^2V^{-1}s^{-1}}$. When the thickness of a 3D TI thin film is reduced to several quintuple layers (QLs), the high mobility is suppressed to $10^2 - 10^3$ $\mathrm{cm^2V^{-1}s^{-1}}$. The suppression of the mobility in the low temperature transport measurements has been attributed to the strong scattering from the p-type dopants that are required to move the Fermi level close to the Dirac point and charged surface adsorbates. Theoretical studies focused on scattering between topological states in opposite surfaces show that the Intersurface coupling in thin-film topological insulators can reduce the surface state mobility by an order of magnitude in low-temperature transport measurements. The reduction is caused by a reduction in the group velocity and an increased S_z component of the surface-state spin which weakens the selection rule against large-angle scattering. the effect of inhomogeneities on the transport of TI surface states on a single surface.

The surface states of 3D TI thin films couple and hybridize the opposite spins of the top and the bottom surface states. As a consequence of this, the original momentum-spin (k-s) relation that prohibits back-scattering of surface states is broken. However, this effect does not explain fully the reduction in the carrier mobility in TI thin films compared

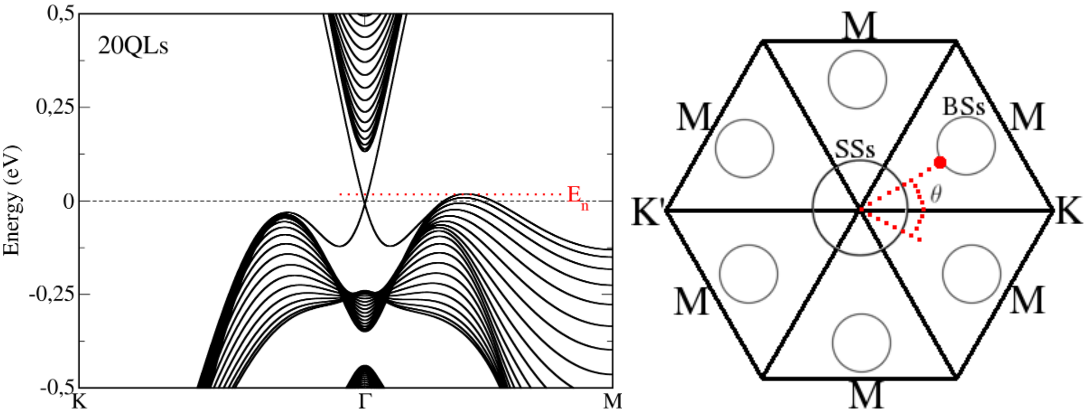

Figure 7.7 - Band structure for 4QLs (left) and 20QLs (right). E_n represented the energy label in which the scattering rate is calculated.

to the expected value of bulk surface states. According to experimental results, bulks states near the Fermi energy can be detrimental to topological conductivity conductivity. In plain words, continuous bulk states can be coupled to the topological surface states. the majority of 3D topological insulators materials despite of support helical metallic surface states on an insulating bulk, forming topological Dirac fermions protected by the time-reversal symmetry, exhibit electronic scattering channels due to the presence of residual continuous bulk states near the Dirac-point[1, 5]. G_0W_0 and GW calculations show that in the particular case of Bi_2Se_3, the bulk states are near the Dirac cone instead of being in the same energy level of this, as other rhombohedral TI systems[20, 21].

When the thickness of a 3D TI thin film is reduced to several quintuple layers (QLs), the scattering processes caused by coulomb impurities allow electronic transitions between the continuous bulk states and the surfaces states, and the order of magnitude of these transitions are of the order of those found when the opposite spins of the top and the bottom surface states are hybridize. We calculated the scattering rate for electronic transitions from the surface states to residual bulk states for several values of QLs. We also find that for high temperatures, the conductivity has the same behavior of native bulk conductivity.

To consider the effect of bulk states, we use the previously proposed Hamiltonian model, in which are included the effective states with total angular moment $J = 3/2$. Far from the Γ point, such states and the $J = 1/2$ effective states, which are involves in the band inversion, are mixed. This interaction leads to a band repulsion depending on the number of QLs forming the TI thin film. In Fig 7.7a we shown the surface band structure for 20 QLs calculated with the tight-binding model and energy plane, E_n, that cuts the surface states and the continuous bulk states. The $k_x k_y$ band profile showing the surface states around the Γ point and the bulk states in the $\Gamma \rightarrow M$ symmetry

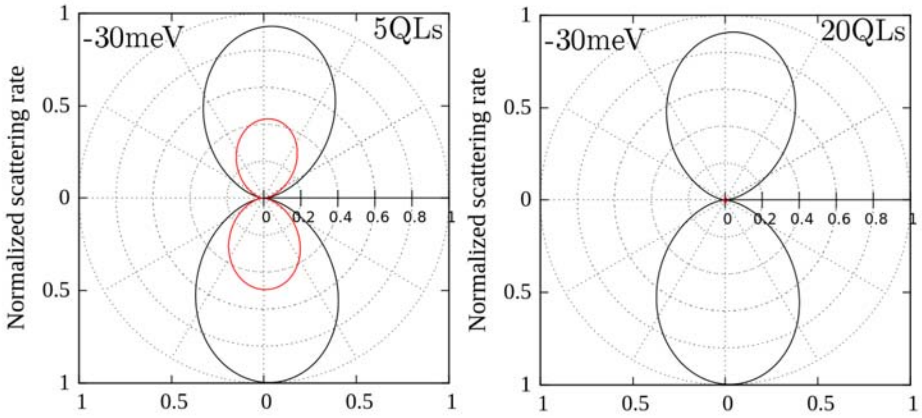

Figure 7.8 - Normalized scattering rate for 5QLs (left) and 20QLs (right) for -30meV and the coulonm impurity in the surface top. The black line represent the scattering rate for the Dirac cone in the surface top, whereas the red line represent the scattering rate for the Dirac cone in the surface bottom.

path are represented in the 7.7b. An electron in the surface states (SS), $|\psi_{k_{SS},n}\rangle$, can be scattered in a elastic processes to the bulks states (BS), $|\psi_{k_{BS},n}\rangle$, where $\vec{k}_{SS}$ and $\vec{k}_{BS}$ are the momentum of the surface and bulk states, respectively. These k-points form a θ angle at a constant energy plane, $E_n = E_{n'}$, where n is the band index.

To quantitatively determine the mobility in TI thin films, a four-band semi-classical calculation is carried out. For a screened Coulomb scattering center at layer j, the Hamiltonian matrix element between states $|\psi_{k_x,k_y,n}\rangle$ and $|\psi_{k'_x,k'_y,n'}\rangle$, is written as,

$$H^{j}_{\vec{k}',n',\vec{k},n} = \frac{1}{A}\sum_{i}^{N}\sum_{\alpha=1}^{8} c^{n'*}_{i,\alpha}(\vec{k}')c^{n}_{i,\alpha}(\vec{k})\frac{q_e^2 e^{-\sqrt{q_0^2+\beta^2}|z|}}{2\kappa\sqrt{q_0^2+\beta^2}} \tag{7.32}$$

where A is the unit area, q_e is the single-electron charge, $\kappa = 100\epsilon_0$ is the static dielectric constant, $\beta = |\vec{k} - \vec{k}'|$, and $z = |i - j|\Delta$ is the vertical distance between site i and the layer of the Coulomb scattering center j. The discretization length $\Delta = 0.3nm$. Equation 7.32 results from the 2D Fourier transform of the screened Coulomb potential $\frac{q^2 e^{q_0 r}}{4\pi\kappa r}$. The inverse screening length q_0 is given by $q_0 = \frac{2\pi q_e^2}{\kappa}\frac{d\rho}{d\epsilon_F}$, where ρ is the 2-dimensional (2D) charge density and ϵ_F is the Fermi energy.

Using the bare Coulomb potential, the scattering rate due to each impurity on layer j is,

$$S_{\vec{k}'\vec{k}} = \frac{2\pi}{\hbar}\frac{q_e^4}{4A^2\kappa^2\beta^2}\vec{I}_{\vec{k}',\vec{k}}(1 - cos(\theta))\delta(E - E'), \tag{7.33}$$

where

$$\boldsymbol{I}_{\vec{k}',\vec{k}} = |\sum_{i}^{N}\sum_{\alpha=1}^{8} c^{p'*}_{i,\alpha}(\vec{k}')c^{p*}_{i,\alpha}(\vec{k})|^2. \tag{7.34}$$

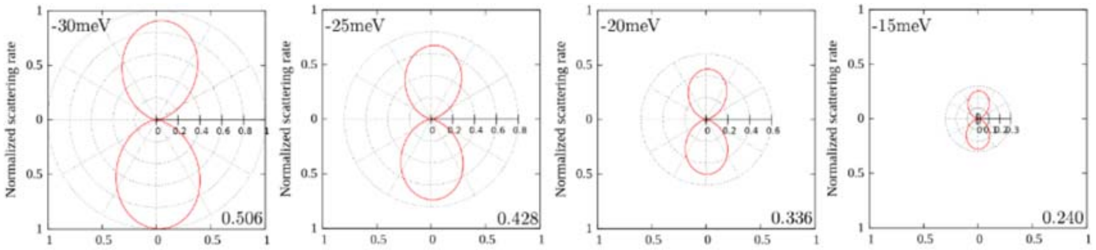

Figure 7.9 - Normalized scattering rate for 20QLs varying the energy label (using the same normalization parameter). The Coulumb impurity is in the surface bottom. According to Fig. 7.8. the surface contribution (lower right side) decrease with increasing the energy label.

First we study the behavior of dimensionless overlap integral, $\boldsymbol{I}_{\vec{k}',\vec{k}}$, for different constant energy planes and before we consider different thickness of a 3D TI thin film in terms of a number of QLs.

For few QLs, the Coulomb scattering impurity couples the bulk states and the surface states. Thus, the scattering rate for transitions from $|\psi_{k_{SS},n}\rangle$ to $|\psi_{k_{BS},n}\rangle$ for topological surface states coming from the top surface has the same order of magnitude that the scattering rate involving states located on the bottom surface. That is, since for few QLs the surface are coupled, the scattering processes involves the bulk states affects similarly both bottom and top surface states. Therefore, scattering processes $|\psi_{k_{SS},n}\rangle \rightarrow |\psi_{k_{SS},n}\rangle$ are as important as the scattering $|\psi_{k_{SS},n}\rangle \rightarrow |\psi_{k_{BS},n}\rangle$, and hence, for few QLs these scattering processes can be detrimental to the electronic transport.

In systems formed by a large number of QLs, only when the layer of the Coulomb scattering center, j, is near the top (bottom) surfaces, the electrons can be scattered from surface states to the bulk states and hence, the scattering processes $|\psi_{k_{SS},n}\rangle \rightarrow |\psi_{k_{BS},n}\rangle$ are relevant. In plain words, the elastic scattering processes in electronic transitions from spatially distant surfaces states of Coulomb impurity to the bulk states are negligible, whereas for surface states near the Coulomb impurity the scattering rate have the same order of magnitude of the surface-surface scattering processes for systems with few QLs, as shown in Fig 7.8.

At a energy plane very near the Fermi energy, the scattering rate is negligible for any thickness, any values of $\vec{k}_{SS}$ and $\vec{k}_{BS}$, and any position of the Coulomb scattering center. For energy planes above energy Fermi the scattering rate is very small, which is expected because in this energies the surface states do not have any mixing with the bulk states. In contrast, when the energy plane is below the Fermi energy, the scattering rate increases as the position of the energy plane relative to the Fermi energy decreases. For instance, when the energy plane is in the $E_n = -30$ meV, the order of magnitude of the scattering rate increases by four times, as shown in Fig 7.9. This suggest that the temperature

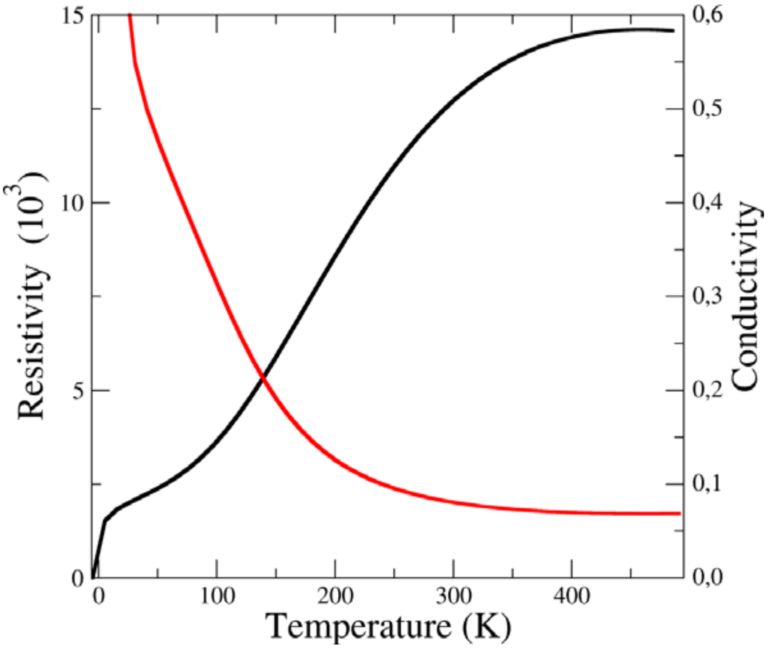

Figure 7.10 - The conductivity (red line) and resistivity (black line) as function of the temperature.

can induce elastic scattering processes associated with electronic transitions from surface states to continuous bulk states. To study the effective current associated with electronic transitions $|\psi_{k_{SS},n}\rangle \rightarrow |\psi_{k_{BS},n}\rangle$, we consider a semiclassical model,

$$\sigma_{|\psi_{k_{SS},n}\rangle \rightarrow |\psi_{k_{BS},n}\rangle}(T) = \int_{-\infty}^{\infty} S_{\vec{k}'\vec{k}}(E) \frac{df(E,T)}{dE}, \tag{7.35}$$

where $f(E,T)$ is the Fermi-Dirac distribution. The resistivity $R_{SS\rightarrow BS} = 1/\sigma_{|\psi_{k_{SS},n}\rangle \rightarrow |\psi_{k_{BS},n}\rangle}(T)$ increase as the temperature increase. Since, this resistivity is associated with electronic transition between bulk and surface states, it represents the detriment of the topological current caused by such scattering processes. Thus, at low temperatures the electronic transport is dominated by the topological current. However, when the temperature increase the surface-bulk transitions increase by one order of magnitude. At room temperature, the resistivity reaches a constant value, and hence, it is expected that the conductivity decrease by one order of magnitude. this suggest that the surface-bulk transition can be explain the experimental reduction of the topological current (See Fig. 7.10).

7.6 Conclusion

We have revisited the band structure calculations of rhombohedral topological insulators, both bulk and thin films, and investigated the occurrence of bulk states at the Fermi level. Based on *ab initio* calculations, we construct a simplified tight-binding model considering the states with angular momentum $J = 1/2$ and $J = 3/2$ and therefore, taking explicitly into account the $p_x p_y$ Se orbitals contributions.

Our model shows that the energy of bulk states near the Dirac-point is associated with a band mixing, which is mainly ruled by the hopping term between p_z and $p_x p_y$ states. The valence band maximum appears in the symmetry path in which the R_3 symmetry is broken. In this situation, the $J = 3/2$ states can mix with the $J = 1/2$ ones.

We illustrate the versatility of our tight-binding model by studying some strategies to eliminate and/or shift the bulk states away from the Fermi surface. We show that the band structures obtained using our simple model reproduce qualitatively very well computationally costly *ab initio* calculations found in the literature.

In summary, we show that our simple effective model captures the main surface band structure features, allowing to explore strategies to perform a continuous bulk states engineering and opening the possibility to model disorder, which is ubiquitous in rhombohedral TIs and beyond the scope of *ab initio* calculations.

We also investigated the relevance of electronic transitions between surface and bulk states in electronic transport in a thin film of rhombohedral TI. Through a effective Hamiltonian considering the bulk states near the Fermi energy, we calculated the amplitude of elastic scattering processes for several temperatures, thickness of the slab and angles between the initial and final momentum. In a semiclassica model for the current associated with this processes, we find that the resistivity for low temperature is near zero and for high values of temperature increase by one order of magnitude, which can be explain the reduction in the topological current. We find that the limit temperature to obtain a clean topological current is about 10K. This results allow understand experimental results and contribute to the understanding of the fundamental physics of the topological insulator materials.

Bibliography

[1] M. Z. Hasan and J. E. Moore, Annu. Rev. Condens. Matter Phys. **2**, 55 (2011).

[2] X.-L. Qi and S.-C. Zhang, Rev. Mod. Phys. **83**, 1057 (2011).

[3] M. Z. Hasan and C. L. Kane, Rev. Mod. Phys. **82**, 3045 (2010).

[4] J. Maciejko, X.-L. Qi, H. D. Drew, and S.-C. Zhang, Phys. Rev. Lett. **105**, 166803 (2010).

[5] H. Zhang, C.-X. Liu, X.-L. Qi, X. Dai, Z. Fang, and S.-C. Zhang, Nat. Phys. **5**, 438 (2009).

[6] C. Mera Acosta, O. Babilonia, L. Abdalla, and A. Fazzio, Phys. Rev. B **94**, 041302 (2016).

[7] S. V. Eremeev, G. Landolt, T. V. Menshchikova, B. Slomski, Y. M. Koroteev, Z. S. Aliev, M. B. Babanly, J. Henk, A. Ernst, L. Patthey, A. Eich, A. A. Khajetoorians, J. Hagemeister, O. Pietzsch, J. Wiebe, R. Wiesendanger, P. M. Echenique, S. S. Tsirkin, I. R. Amiraslanov, J. H. Dil, and E. V. Chulkov, Nat. Commun. **3**, 635 (2012).

[8] C. X. Liu, X. L. Qi, H. J. Zhang, X. Dai, Z. Fang, and S. C. Zhang, Phys. Rev. B **82**, 045122 (2010).

[9] K. Yang, W. Setyawan, S. Wang, M. Buongiorno Nardelli, and S. Curtarolo, Nat. Mater. **11**, 614 (2012).

[10] Y. Xia, D. Qian, D. Hsieh, L. Wray, A. Pal, H. Lin, A. Bansil, D. Grauer, Y. S. Hor, R. J. Cava, and M. Z. Hasan, Nat. Phys. **5**, 398 (2009).

[11] J. Henk, M. Flieger, I. V. Maznichenko, I. Mertig, A. Ernst, S. V. Eremeev, and E. V. Chulkov, Phys. Rev. Lett. **109**, 076801 (2012).

[12] A. Narayan, I. Rungger, A. Droghetti, and S. Sanvito, Phys. Rev. B **90**, 205431 (2014).

[13] A. Narayan, I. Rungger, and S. Sanvito, New J. Phys. **17**, 033021 (2015).

[14] S. Kim, M. Ye, K. Kuroda, Y. Yamada, E. E. Krasovskii, E. V. Chulkov, K. Miyamoto, M. Nakatake, T. Okuda, Y. Ueda, K. Shimada, H. Namatame, M. Taniguchi, and A. Kimura, Phys. Rev. Lett. **107**, 056803 (2011).

[15] M. Brahlek, N. Koirala, N. Bansal, and S. Oh, Solid State Commun. **215-Äì216**, 54 (2015).

[16] E. K. de Vries, S. Pezzini, M. J. Meijer, N. Koirala, M. Salehi, J. Moon, S. Oh, S. Wiedmann, and T. Banerjee, Phys. Rev. B **96**, 045433 (2017).

[17] O. V. Yazyev, E. Kioupakis, J. E. Moore, and S. G. Louie, Phys. Rev. B **85**, 161101 (2012).

[18] T. Förster, P. Krüger, and M. Rohlfing, Phys. Rev. B **92**, 201404 (2015).

[19] T. Förster, P. Krüger, and M. Rohlfing, Phys. Rev. B **93**, 205442 (2016).

[20] I. A. Nechaev, R. C. Hatch, M. Bianchi, D. Guan, C. Friedrich, I. Aguilera, J. L. Mi, B. B. Iversen, S. Blügel, P. Hofmann, and E. V. Chulkov, Phys. Rev. B **87**, 121111 (2013).

[21] I. Aguilera, C. Friedrich, G. Bihlmayer, and S. Blügel, Phys. Rev. B **88**, 045206 (2013).

[22] S. Mao, A. Yamakage, and Y. Kuramoto, Phys. Rev. B **84**, 115413 (2011).

[23] L. Seixas, L. B. Abdalla, T. M. Schmidt, A. Fazzio, and R. H. Miwa, J. Appl. Phys. **113**, 023705 (2013).

[24] O. V. Yazyev, J. E. Moore, and S. G. Louie, Phys. Rev. Lett. **105**, 266806 (2010).

[25] K. Capelle, Braz. J. Phys. **36**, 1318 (2006).

[26] J. M. Soler, E. Artacho, J. D. Gale, A. García, J. Junquera, P. Ordejón, and D. Sánchez-Portal, J. Phys.: Condens. Matter **14**, 2745 (2002).

[27] L. Fernández-Seivane, M. A. Oliveira, S. Sanvito, and J. Ferrer, J. Phys.: Condens. Matter **18**, 7999 (2006).

[28] C. M. Acosta, M. P. Lima, R. H. Miwa, A. J. R. da Silva, and A. Fazzio, Phys. Rev. B **89**, 155438 (2014).

[29] J. P. Perdew and A. Zunger, Phys. Rev. B **23**, 5048 (1981).

[30] K. Ebihara, K. Yada, A. Yamakage, and Y. Tanaka, Physica E **44**, 885 (2012).

[31] J. Zhang, C. Z. Chang, Z. Zhang, J. Wen, X. Feng, K. Li, M. Liu, K. He, L. Wang, X. Chen, Q. K. Xue, X. Ma, and Y. Wang, Nat. Commun. **2**, 574 (2011).

[32] T. Arakane, T. Sato, S. Souma, K. Kosaka, K. Nakayama, M. Komatsu, T. Takahashi, Z. Ren, K. Segawa, and Y. Ando, Nature Communications **3**, 636 (2012).

[33] Z. Ren, A. A. Taskin, S. Sasaki, K. Segawa, and Y. Ando, Phys. Rev. B **84**, 165311 (2011).

[34] L. B. Abdalla, E. Padilha José, T. M. Schmidt, R. H. Miwa, and A. Fazzio, J. Phys.: Condens. Matter **27**, 255501 (2015).

[35] Y. Liu, Y. Y. Li, S. Rajput, D. Gilks, L. Lari, P. L. Galindo, M. Weinert, V. K. Lazarov, and L. Li, Nat. Phys. **10**, 294 (2014).

[36] S. H. Park, J. Chae, K. S. Jeong, T. H. Kim, H. Choi, M. H. Cho, I. Hwang, M. H. Bae, and C. Kang, Nano Lett. **15**, 3820 (2015).

8. Conclusions

Throughout this work we use different strategies for the study of systems with topological boundary states protected by the time-reversal symmetry. Specifically, we integrate the use of DFT calculations and tight-binding approximations to obtain models describing these systems. These models are indispensable for the study of electronic transport and the effect of external potentials, e.g., electric and magnetic fields. We believe that the systematic use of this methodology and the new models found in this work are a great contribution not only in the understanding of topologically protected systems, but also in the methodologies used for the study of these systems.

We believe that there are new ways to use the spin-texture of topologically protected boundary states: instead of looking for new materials with a large enough gap size, we propose the use of bulk states, which in principle would exhibit a much more robust spin-texture. Thus, we find that it is possible to obtain bulk states with a spin texture that prohibits backscattering. We believe that this could generate a future research area. However, from our point of view, the most important result of this work is the proposal of a new transistor model in dual topological insulators. This model is based on the mirror symmetry breaking and the resulting Rashba effect. The break of this symmetry is achieved through an external electric field applied perpendicular to the mirror plane, generating a new spin-polarization orientation. The proposed spin-polarization control is similar to spin-orbit torque, but here the induction of spin charge is not dynamic. The possible implication of a dual topological protection has been scarcely explored, for this reason we believe that our work could open a new possibility for future research in this area. In fact, we are studying not only the effect of the breaking of this symmetry for planes oriented in other directions, but also the effect of the rotational symmetry breaking in systems not only protected by the time-reversal symmetry.

Despite this main proposal, we also invest time in finding a systematic way to predict new topological insulators. Specifically, we find that there is a simple way to find the topological invariant, i.e., using the metalicty as a property defining the band inversion before including the spin-orbit. This never-before-reported relationship allows the topological classification of crystalline systems using only atomic properties of the elements forming the system. Undoubtedly, this bring a new understanding of topological properties as an emergent phenomena.

Since we also study the interaction between bulk states and topologically protected states, we believe that we have provided a broad vision of how to approach problems in theoretical observation and even in the use of systems with non-zero topological invariants. Our constant focus throughout this work was to find new phenomena or systems that allow the use of spin as a basic element in a transistor. Thus, the next step is to study in depth the properties of electronic transport. In principle, the proposed models would help in this type of studies. Additionally, we are also using the proposed methodology for machine learning to understand and study other physical properties, such as the thermal stability of two-dimensional systems.